Inaugural dissertation

for

obtaining the doctoral degree

of the

Combined Faculty of Mathematics, Engineering and Natural Sciences of the

Ruprecht - Karls - University

Heidelberg

Presented by

M.Sc. Elvira Magdalena Criado Moronati

born in: Salamanca, Spain

Oral examination: 09.09.2024

Characterization of tumor-infiltrating $CD8^+$ T cells towards clinical application

Referees:

Prof. Dr. Rienk Offringa

Prof. Dr. Viktor Umansky

“Without the love of research,

mere knowledge and intelligence

cannot make a scientist.”

Irène Joliot-Curie

The experimental work of the following PhD thesis was performed between April 2017 and December 2020 at Miltenyi Biotec (Bergisch Gladbach) under the supervision of Dr. Bianca Kaiser-Heemskerk and Dr. Andrzej Dzionek in the R&D Reagents department of Personalized Immunotherapy.

Summary

Tumor-infiltrating lymphocytes (TILs) have been successfully used in adoptive cell therapies (ACT) for various cancer types. However, only a small fraction of TILs mediates antitumor responses. Therefore, the enrichment of tumor-reactive TILs prior to the *ex vivo* expansion during cell manufacturing for ACT may improve their clinical efficacy. An enrichment based on an *a priori* tumor-reactive T cell phenotype represents an appealing approach as it is independent of the target antigen. Therefore, my PhD project aimed to identify a cell surface marker that can enrich tumor-reactive $CD8^+$ TILs for clinical use.

For this purpose, I comprehensively characterized $CD8^+$ TILs using different technologies. First, I screened the expression of activation/exhaustion surface markers as a proxy for tumor reactivity on TILs from freshly dissociated tumors by flow cytometry. I focused on CD39 as this population contained higher frequencies of activated/exhausted TILs than their negative counterpart. I developed a pre-sorting workflow to sort $CD39^+$ and $CD39^-$ TIL subsets, which were expanded to test their tumor reactivity *in vitro*. The co-culture of TILs and autologous tumor cells revealed the presence of a small population of cytokine-secreting, tumor-reactive $CD8^+$ TILs in the $CD39^+$ subset in one out of three tumor samples tested, whereas $CD39^-$ TILs showed no reactivity in any sample. These results suggest that CD39 can select for tumor-reactive T cells, but it needs to be further confirmed in a larger cohort of patients. The combined analysis of TCR repertoire and gene expression by single-cell RNA sequencing showed that dominant clonotypes in the expanded $CD39^+$ T cell subset had in the tumor an activated, dysfunctional state and exhibited tumor-reactive T cell transcriptome signatures. Last, I studied the phenotype of TILs in close proximity to tumor cells in tissues as a potential indicator of tumor recognition. To this end, I used our newly developed multiplexed MACSima imaging cyclic staining (MICS) technology to examine the spatial distribution of not only TIL subsets but also other cell types in the tumor microenvironment. CD39 was highly expressed on non-T cell types such as endothelium and fibroblasts which overlapped with T cells, challenging the identification of *bona fide* $CD39^+$ T cells. Therefore, I used other activation/exhaustion markers that correlated with CD39 expression, including CD137, PD1, and CD103, to label potential tumor-reactive $CD8^+$ TILs. These TIL subsets tended to be in close proximity to tumor cells compared to stromal areas or tertiary lymphoid structures, supporting that T cells expressing those markers may be interacting with or recognizing tumor cells.

In summary, the data presented in my PhD thesis highlights the potential of CD39 as a marker of tumor-reactive $CD8^+$ TILs. Future studies are needed to validate these findings in a larger cohort of patients and tumor types, enabling the development of improved manufacturing processes of tumor-reactive TILs for ACT.

Zusammenfassung

Tumorinfiltrierende Lymphozyten (TILs) wurden erfolgreich in adoptiven Zelltherapien (ACT) für verschiedene Krebsarten eingesetzt. Allerdings vermittelt nur ein kleiner Teil der TILs eine Antitumorreaktion. Daher kann, während der Zellherstellung für ACT, die Anreicherung von tumorreaktiven TILs vor der *ex-vivo* Expansion die klinische Wirksamkeit verbessern. Eine Anreicherung auf der Grundlage eines *a priori* tumorreaktiven T-Zell-Phänotyps ist ein attraktiver Ansatz, da sie unabhängig vom Zielantigen ist. Ziel meines Promotionsprojekts war es daher, einen Zelloberflächenmarker zu identifizieren, der tumorreaktiver $CD8^+$ TILs für den klinischen Einsatz anreichern kann.

Zu diesem Zweck habe ich $CD8^+$ TILs mithilfe verschiedener Technologien umfassend charakterisiert. Zunächst untersuchte ich die Expression von Aktivierungs-/Erschöpfungsoberflächenmarkern als Stellvertreter für die Tumorreaktivität auf TILs aus frisch dissoziierten Tumoren mittels Durchflusszytometrie. Ich konzentrierte mich auf CD39, da diese Population eine höhere Häufigkeit von aktivierten/erschöpften TILs enthielt als ihr negatives Gegenstück. Ich entwickelte einen Arbeitsablauf zur Vorsortierung, um $CD39^+$ und $CD39^-$ TIL-Gruppen zu sortieren, die dann expandiert wurden, um ihre Tumorreaktivität in vitro zu testen. Die Co-Kultur von TILs und autologen Tumorzellen bestätigte das Vorhandensein einer kleinen Population von Zytokin-sekretierend tumorreaktiven $CD8^+$ TILs in der $CD39^+$ Gruppe in einer von drei getesteten Tumorproben, während $CD39^-$ TILs in keiner Probe eine Reaktivität zeigten. Diese Ergebnisse deuten darauf hin, dass CD39 für tumorreaktive T-Zellen selektieren kann, was jedoch in einer größeren Patientenkohorte noch bestätigt werden muss. Die kombinierte Analyse des TCR-Repertoires und der Genexpression durch Einzelzell-RNA-Sequenzierung zeigte, dass dominante Klonotypen in der erweiterten $CD39^+$ T-Zell-Gruppe zunächst im Tumor einen aktivierten und dysfunktionalen Zustand hatten und tumorreaktive T-Zell-Transkriptomsignaturen aufwiesen. Schließlich untersuchte ich den Phänotyp von TILs in unmittelbarer Nähe von Tumorzellen in Geweben als potenziellen Indikator für die Tumorerkennung. Zu diesem Zweck verwendete ich unsere neu entwickelte Multiplex-MACSima-Imaging-Cyclic-Staining-Technologie (MICS), um die räumliche Verteilung nicht nur von TIL-Gruppen, sondern auch von anderen Zelltypen in der Tumormikroumgebung zu untersuchen. CD39 wurde in hohem Maße auf Nicht-T-Zelltypen wie Endothel und Fibroblasten exprimiert, die sich mit T-Zellen überschnitten, was die Identifizierung echter $CD39^+$ T-Zellen erschwerte. Daher verwendete ich andere Aktivierungs-/Erschöpfungsmarker, die mit der CD39-Expression korrelierten, darunter CD137, PD1 und CD103, um potenziell tumorreaktive $CD8^+$ TILs zu markieren. Diese TIL-Gruppen befanden sich tendenziell in unmittelbarer Nähe von Tumorzellen im Vergleich zu stromalen Bereichen oder tertiären

lymphatischen Strukturen, was dafür spricht, dass T-Zellen, die diese Marker exprimieren, möglicherweise mit Tumorzellen interagieren oder diese erkennen.

Zusammenfassend lässt sich sagen, dass die in meiner Dissertation vorgestellten Daten das Potenzial von CD39 als Marker für tumorreaktive $CD8^+$ TILs unterstreichen. Zukünftige Studien sind erforderlich, um diese Ergebnisse in einer größeren Kohorte von Patienten und Tumorarten zu validieren und die Entwicklung verbesserter Herstellungsverfahren von tumorreaktiven TILs für ACT zu ermöglichen.

Acknowledgements

My most sincere thanks goes to my supervisor, **Dr. Bianca Kaiser-Heemskerk**, for her guidance and enthusiasm. Thank you for teaching me everything about TILs and for always being there, professionally and personally. I would also like to thank **Dr. Andrzej Dzionek** for giving me the chance to work on this project at Miltenyi, for his insightful suggestions, thoughtful feedback, and his support.

I am grateful to my academic supervisors, **Prof. Dr. Rienk Offringa** and **Prof. Dr. Viktor Umansky**, for their constructive comments and scientific input. I would like to thank all the members of Prof. Offringa and Prof. Platten´s groups for welcoming me during my internship in Heidelberg. Particularly, to **Kyle** for his bioinformatic support, and to **Julian** for his expertise on TLS and his always encouraging words. I wish to extend my special thanks to the rest of my thesis examination committee, **Prof. Dr. Nina Papavasiliou** and **Prof. Dr. Benedikt Brors**, for reading and evaluating this thesis.

I wish to show my appreciation to the whole MICS team. To **Lara**, **Vanessa**, and **Nadine** for introducing me to MICS. To **Jan**, **Christiane**, and **Max** for handling the TECAN. To **Silvia** for organizing the teams. To **Karo** and **Jona** for our initial experiments on single-cell MICS. To **Lea** and **Telma** for sharing their knowledge about microscopy with me. Last, thank you, **Apu**, for sharing with me many MICS runs as well as lots of fun and deep conversations—especially during endless pipetting hours.

I would also like to express my gratitude to the Bioinformatics team. My special thanks goes to Andre, for your InspectorCell tool and for being a good friend and roommate. A great thank you to **Werner**, **Ali**, **Jutta**, **Michail**, and **Paurush** for their insights and suggestions on the MICS analysis.

Special thanks to the Tyto team, particularly to **Polina** and **Alina**, who assisted me in performing the Tyto sorts and who always tried their best, regardless of the challenge.

I am deeply grateful to the NGS team for their outstanding work on performing the 10x Genomics experiments. **Ruth**, **Nadine**, **Lilian**, **Nojan**, **Katha** and **Adriana**, thank you all for your time, especially for those long evenings. Thank you, **Stefan**, for pre-processing the data and being always available for questions.

I would like to thank Bianca´s team, **Christina**, **Lisa**, **Sophia**, and **Laura**, for their constructive comments, assistance in the laboratory, and for sharing the PDAC data with me. I would like to offer my special thanks to **Martina**, for her support and trust on me. Thank you, **Emre**, for reading and commenting this thesis, and for your scientific and emotional support.

This work would not have been possible without the generosity and resilience of many **cancer patients** and their **medical staff** who fight every day to find a cure. Hope is the last thing to lose.

I am glad to have met wonderful people who are not only my colleagues, but also my friends. To **Bettina** and **Nicole** for being always there, in good and bad times. To **Julia** for being the sunshine that I miss from Spain. To **Philipp** for his expertise on MQuants, which saved me many times. To **Marta** and **Josi**, for being the perfect roommates. To **Christin**, the first person who welcomed me at Miltenyi. To **Inés**, **Shakhlo**, **Johanna**, **Tümay**, and the rest of **H13 crew** for their unconditional support and friendship. To all members of the **StudiClub** and many more, who have made this time unforgettable.

I cannot find words to express my gratitude to my family and friends. A mis **Raviolis**, que siempre han estado y estarán ahí, compartiendo risas y lloros. A **Eli**, porque su alegría contagiosa me ha sacado adelante en muchas ocasiones. A **Virginia**, que me ha enseñado a ser resiliente. Thank you to the Tübingen crew, **Jen**, **Betül**, **Marco** and **Astrid**, for being supportive and sharing my love for science (and wizard). Thank you to my german family, **Birgit**, **Uwe**, **Jens**, and **Helmuth**. Vielen Dank, dass Sie mich mit offenen Armen empfangen und dafür gesorgt haben, dass ich mich wie zu Hause fühle. Nada de esto hubiera sido posible sin el apoyo incondicional de toda mi familia, incluidas las personas que ya no están con nosotros pero que nunca nos abandonan. **Papá**, **mamá**, estoy eternamente en deuda con vosotros por darme esta y muchas otras oportunidades. Es gracias a vosotros que estoy aquí. **Marita**, gracias por ser tan buena hermana y escucharme cada vez que te necesito. Muchas gracias, **Tavi**, por tus consejos y risas. Y muchas gracias, **Carmen**, por tu apoyo y tus jerséis que me han mantenido viva en el inverno alemán. Os quiero y os echo mucho de menos.

And last but not least, to **Sven**. Your optimism has always been an inspiration to me. You have been my rock during the last 10 years, and I cannot imagine my life without you. Thanks for your support, love, and all those virtual hugs which gave me strength every single day.

Table of Contents

List of Figures

List of Tables

List of Abbreviations

7-AAD	7-Aminoactinomycin D
ACT	Adoptive cell therapy
AMP	Adenosine monophosphate
APC	Antigen presenting cell
ATP	Adenosine triphosphate
BCL6	B-cell lymphoma 6
CAF	Cancer-associated fibroblast
CAR	Chimeric antigen receptor
ccRCC	Clear cell renal cell carcinoma
cDC2	Conventional dendritic cell type 2
CODEX	Co-detection by indexing
CRC	Colorectal carcinoma
CTL	Cytotoxic T lymphocyte
CTLA4	Cytotoxic T-lymphocyte antigen number 4
CTR	Control
CxCa	Cervical squamous cell carcinoma
CXCL13	C-X-C motif chemokine ligand 13
CyTOF	Cytometry by time of flight
DC	Dendritic cell
DCR	Dead cell removal kit
DNA	Deoxyribonucleic acid
ENTPD1	Ectonucleoside triphosphate diphosphohydrolase 1
EOMES	Eomesodermin
EtOH	Ethanol
FACS	Fluorescence-activated cell sorting
FasL	FAS ligand
FBS	Fetal bovine serum
FDA	Food and Drug Administration
FDC	Follicular dendritic cell
FITC	Fluorescein
FoxP3	Forkhead box protein P3
FRC	Fibroblastic reticular cells
GC	Germinal center

GEMs	Gel Bead-in Emulsions
GEX	Gene expression
GMP	Good manufacturing practice
GNLY	Granulysin
GZM	Granzyme
h	Hours
H&E	Hematoxylin and eosin
HEV	High endothelial cell
HGSOC	High-grade serous ovarian cancer
HNSCC	Head and neck squamous cell carcinoma
HPV	Human papillomavirus
HSP	Heat shock protein
hTSE	Human tandem signal enhancer
ICB	Immune checkpoint blockade
ICOS	Inducible T cell co-stimulator
IF	Immunofluorescence
IFNγ	Interferon ɣ
IL-2	Interleukin-2
LAG3	Lymphocyte activation gene 3
LN	Lymph node
LuCa	Lung carcinoma
MACS	Magnetic cell separation
metCRC	Metastatic colorectal carcinoma
MDSC	Myeloid-derived suppressor cell
MFI	Mean fluorescent intensity
MHC	Major histocompatibility complex
MIBI-TOF	Ion beam imaging by time-of-flight
MICS	MACSima imaging cyclic staining
min	Minutes
mRNA	Messenger RNA
MTRNR	Mitochondrially encoded RNA
ND	Not determined
NK	Natural killer cell
NSCLC	Non-small cell lung cancer
OPSCC	Oropharyngeal squamous cell carcinoma

OvCa	Ovarian carcinoma
PBL	Peripheral blood lymphocyte
PBMC	Peripheral blood mononuclear cell
PBS	Phosphate-buffered saline
PC	Plasma cell
PCA	Principal component analysis
PD1	Programmed cell death protein 1
PDAC	Pancreatic ductal adenocarcinoma
PE	Phycoerythrin
PI	Propidium iodide
pMHC	Peptide-MHC
RBC	Red blood cell
REP	Rapid expansion protocol
rh-IL-2	Recombinant human interleukin-2
RNA	Ribonucleic acid
ROI	Region of interest
RT	Room temperature
scRNA-seq	Single-cell mRNA sequencing
SD	Standard deviation
SNN	Shared nearest neighbor
TAM	Tumor-associated macrophage
TAN	Tumor-associated neutrophil
T-BET	T-box expressed in T cells
TCF1	T cell-specific transcription factor 1
T_{CM}	Central memory T cell
TCR	T cell receptor
TDK	Tumor dissociation kit
T_{EM}	Effector memory T cell
T_{EX}	Exhausted T cell
T_{FH}	Follicular helper T cell
TGFβ	Transforming growth factor β
T_H	Helper T cell
TIGIT	T cell immunoreceptor with immunoglobulin and ITIM domains
TIL	Tumor-infiltrating lymphocyte
TIM3	T cell immunoglobulin domain and mucin domain protein 3

TLS	Tertiary lymphoid structure
TME	Tumor microenvironment
TNFα	Tumor necrosis factor α
TNFRSF9	Tumor necrosis factor receptor superfamily member 9
TOX	Thymocyte selection-associated high mobility group box protein
T_{PEX}	Pre-exhausted T cell
TRA	TCR alpha chain
TRAIL	TNF-related apoptosis inducing ligand
TRB	TCR beta chain
T_{reg}	Regulatory T cell
T_{RM}	Tissue-resident memory T cell
tSNE	t-distributed stochastic neighbor embedding
UMAP	Uniform manifold approximation and projection
VEGF	Vascular endothelial growth factor
VISTA	V-domain immunoglobulin suppressor of T cell activation
VSCC	Vulvar squamous cell carcinoma

1 Introduction

1.1 The pillars of cancer therapy

Cancer is a devastating disease and leading cause of death, accounting for 20 million new cases and 9.7 million deaths globally in 2022 according to the World Health Organization[1]. And yet, the number of cases is still on the rise, and over 35 million new cancer cases are estimated worldwide for 2050[1]. Therefore, a great effort in many aspects, such as prevention, diagnosis, and treatment, is necessary. Cancer is caused by the uncontrolled growth of cells upon acquisition of certain mutations during the cell life cycle. It can virtually appear in any organ of the body, creating tumors that can compromise the functions of tissues and invade other body parts in a process termed metastasis. In adults, the most common cancers are solid tumors of epithelial origin, such as lung (12.4% of total cases), breast (11.6%), colorectal (9.6%), and prostate (7.3%) cancers[1]. Consequently, cancer is not one but a collection of diseases with diverse characteristics that requires diverse treatments.

1.1.1 The evolution of cancer treatments

The origins of cancer are embedded within the human evolution. The oldest description of cancer dates to 3,000 BC in ancient Egypt[2]. For centuries, surgical removal of tumors has been the only possible cure[3]. But in the last 70 years, immense progress in medicine and a deep understanding of cancer have led to the development of new therapeutic options. Sophisticated surgical interventions and the discoveries of radiotherapy in the early 20th century and chemotherapy in the 1950s were remarkable steps in cancer therapy history. These methods aim to harm malignant cells by causing DNA damage and thus inducing cell death. Although they can control or cure cancer, they may also damage non-malignant cells and cause severe side effects[4]. Therefore, the search for more targeted and safer therapies continues today.

Immunotherapy has recently become a therapeutic option for cancer patients and constitutes the fourth pillar in cancer treatment—after surgery, radiotherapy, and chemotherapy[5]. The aim of this treatment is to harness the natural defenses of the body—the immune system—to fight cancer. For more than a century, observations in cancer patients whose tumors spontaneously regressed after viral or bacterial infections opened on to the idea of unleashing the host immune system to eliminate cancer[6]. However, it was not until recently that a deeper knowledge of the interactions between cancer and the immune system allowed the flourishment of immunotherapy. A breakthrough was the use of immune checkpoint inhibitors, drugs that were able to interrupt the inhibitory signals of T cells which tumor cells exploit to escape immune cell attacks[7]. The first checkpoint inhibitor approved by the US

Food and Drug Administration (FDA) to treat metastatic melanoma was ipilimumab, an antibody targeting the cytotoxic T-lymphocyte antigen number 4 (CTLA4) expressed on T cells. In 2014, three years later, nivolumab, which targets the programmed cell death protein 1 (PD1), was also authorized. As of February 2023, nine agents have been FDA-approved for immune checkpoint blockade (ICB) therapy for a wide range of cancer types[8]. Although remarkable and durable responses have been observed in a subset of patients, a large majority (estimated to be 87% of cancer patients[9]) does not respond or are not eligible to ICB therapy yet[10]. Therefore, other immunotherapy modalities have also risen in the last decades, such as cancer vaccines or adoptive cell therapies.

1.1.2 Adoptive cell therapies

Adoptive cell therapy (ACT) is based on the transfer of sufficient numbers of *ex vivo* expanded antitumor immune cells, commonly T cells, into cancer patients after a lymphodepleting regimen (generally nonmyeloablative chemotherapy). The presence of large numbers of tumor-reactive T cells in a manipulated host environment that favors the engraftment of infused cells enables the mediation of cancer regression[11]. Autologous or allogeneic T cells are used for ACT, and they can be composed of naturally occurring tumor-reactive T cells, normally obtained from autologous tumor-infiltrating lymphocytes (TILs), or genetically engineered peripheral blood lymphocytes (PBLs). PBLs can be engineered with either T cell receptors (TCRs) targeting tumor antigens presented via major histocompatibility complexes (MHCs), or chimeric antigen receptors (CARs) detecting tumor-associated molecule structures on the surface of tumor cells in a non-MHC-restricted manner.

Adoptive cell therapies still face many challenges to become effective immunotherapies for a widespread application, especially for solid malignancies. Not only the search for tumor-specific targets is of high importance, but also other limitations, such as the trafficking of T cells into the tumor or the immune suppressive tumor microenvironment (TME), need to be considered[12]. The study of TILs offers a promising opportunity to understand the biological interactions and the diverse states of immune cells in the TME. On the one hand, TILs are enriched with tumor-reactive T cells, which is not only a suitable source of antitumor TCRs, but also of T cells that can be used in adoptive cell transfers. On the other hand, the phenotypic and functional states of TILs are shaped by the TME they reside in. Therefore, the study of TILs in the context of its TME could shed light into the mechanisms of antitumor immune responses, and thus facilitating the development of successful immunotherapies.

1.2 The tumor microenvironment and TILs

Tumors are not only composed of cancer cells, but of a miscellany of cells and molecules that together comprise the tumor microenvironment. It can be composed of immune cells, stromal cells, and extracellular matrix[13]. The immune cell compartment commonly consists of both adaptive immune cells, such as T and B cells, and innate immune cells like natural killer (NK) cells, macrophages, neutrophils, and dendritic cells (DCs)[13]. In addition, the TME has been divided into three categories based on the immune infiltrate: 1) infiltrated-excluded TMEs, in which $CD8^+$ T cells are unable to penetrate the tumor mass, accumulating in the periphery and having generally decreased functionality; 2) infiltrated-inflamed TMEs, characterized by high infiltration of cytotoxic $CD8^+$ T lymphocytes which are homogenously distributed throughout the tumor; and 3) infiltrated-TLS, a class defined by the presence of tertiary lymphoid structures (TLSs)[14] (Illustration 1). Stromal cells (e.g., endothelium and fibroblasts) are recruited by cancer cells to support its growth and invasion[13]. Last, a network of non-cellular components, such as collagen, fill up the physical space of the extracellular matrix, providing cell support and signals to promote tumor cell dissemination[13].

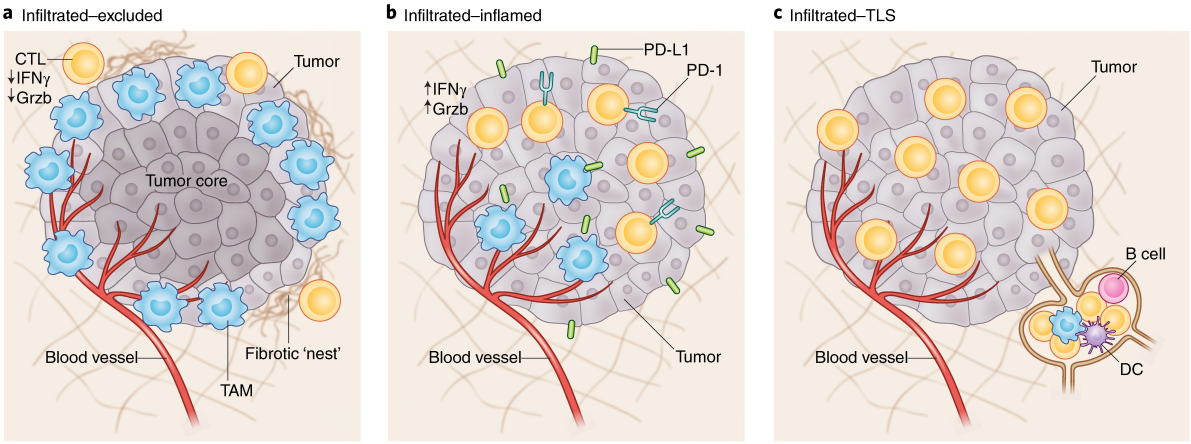

Illustration 1. Classification of tumor microenvironments based on the immune infiltrate
TMEs can be classified into a) infiltrated-excluded, in which cytotoxic CD8+ T lymphocytes (CTLs) are excluded from the tumor core; b) infiltrated-inflamed, characterized by the infiltration of activated CTLs; and c) infiltrated-TLS, defined by the presence of tertiary lymphoid structures (TLSs). TAM: tumor-associated macrophage. DC: dendritic cell. Re-used from Binnewies et al. 2018[14] with permission (license number 5804731315211).

The complexity of the TME is evident by the reciprocal crosstalk between all its components and their spatial organization in the tumor. The generation of antitumor responses in TLSs and the effects of the TME on TIL activities, especially those of $CD8^+$ TILs, are of relevance in the context of TIL ACT therapy.

1.2.1 Tertiary lymphoid structures

The generation of an effective antitumor response occurs not only in secondary lymphoid organs, such as lymph nodes (LNs), but also in tertiary lymphoid structures—organized ectopic structures that resemble LNs and can be found in the stroma, invasive margins and/or core of some tumors[15]. The formation of TLSs is thought to be mediated by diverse cytokines and chemokines under inflamed conditions. One of the most relevant chemokines is C-X-C motif chemokine ligand 13 (CXCL13), a potent B cell chemoattractant. Interestingly, exhausted PD1^{hi} CD8^{+} TILs upregulate CXCL13, possibly to mediate immune cell recruitment to TLSs[16,17]. TLS formation is a complex process and different subtypes have been described based on its developmental stage: 1) immature or early TLSs, where T cell and B cells form aggregates in the absence of B cell follicles and follicular dendritic cells (FDCs); 2) intermediate mature or primary follicle-like TLSs, which contain FDCs in the B cell-rich area but lack germinal center (GC) reactions; and 3) fully mature or secondary follicle-like TLSs, which have active GCs where B cells undergo maturation processes leading to the generation of antigen-producing plasma cells (PCs) and memory B cells[15,18]. In addition, fully mature TLSs contain in the T cell-rich zone follicular helper CD4^{+} T cells (T_{FH}) that support both B and T cell activation[19], fibroblastic reticular cells (FRCs), and mature DCs that play key roles during priming and activation of T cells[20]. PCs and macrophages can be found in the B cell area[15]. To sustain the migration and extravasation of immune cells into the developing TLS, high endothelial venules (HEVs) are formed, which are special blood vessels found in lymphoid organs[21] (Illustration 2).

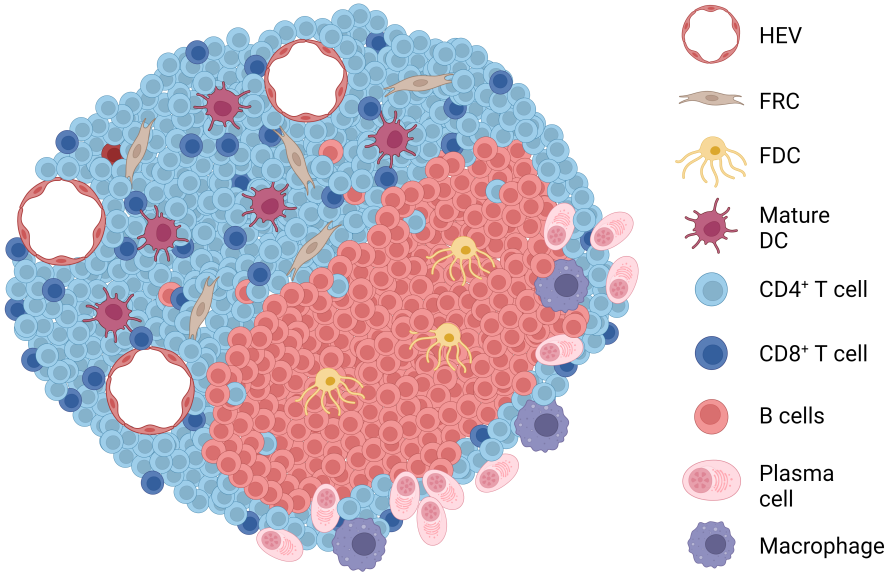

Illustration 2. Cell composition and structure of a TLS
TLSs are organized ectopic structures composed of a T cell zone containing fibroblastic reticular cells (FRCs) and mature dendritic cells (DCs), and a B cell zone with follicular DCs (FDCs) that form the germinal center, in which plasma cells are generated. Macrophages and high endothelial vessels (HEVs) are also found in the TLS. Inspired by Domblides et al. 2021[22] and created with BioRender.com by Elvira Criado-Moronati.

Overall, TLSs are considered to be “antitumor schools” where both tumor-specific T and B cells are locally trained to fight cancer[22]. The presence of TLSs has usually been associated with favorable clinical outcomes in several solid tumors[15] and with responses to anti-PD1 therapy in non-small cell lung cancer[17]. The impact of TLSs is noticeable by the correlation between TLS abundance and increased frequencies of activated $CD8^+$ TILs in tumors[23]. Nonetheless, once T cells leave TLSs and migrate to tumors, they encounter a hostile TME that hamper their cytotoxic activity.

1.2.2 Effects of the TME on TILs

T cells are one of the major components of immune infiltrates in tumors. Tumor-infiltrating $CD8^+$ T cells recognize tumor-specific antigens presented via MHC class I molecules on tumor cells. They mediate tumor destruction by two methods: 1) secretion of cytotoxic molecules, such as perforin and granzymes; and 2) expression of death ligands like Fas ligand (FasL) and tumor necrosis factor (TNF)-related apoptosis inducing ligand (TRAIL)[24]. Both pathways result in cell death by triggering apoptosis in target cells[24]. Moreover, they release pro-inflammatory cytokines upon activation, such as interferon γ (IFNγ) and TNFα[25]. The functionality of $CD8^+$ TILs is, however, suboptimal in cancer. First, tumor cells develop intrinsic immune escape mechanisms that protect them from T cell attacks, such as downregulation of MHC molecules or upregulation of inhibitory ligands like PD1 ligand 1 (PD-L1)[26]. Second, TME components that support tumor growth may impair cytotoxic T cells.

Regulatory $CD4^+$ T cells (T_{reg}) are characterized by the expression of CD25 (the α chain of the high-affinity interleukin-2 [IL-2] receptor), and the transcription factor forkhead box protein P3 (FoxP3). They suppress $CD8^+$ TILs by diverse mechanisms like secretion of immune suppressive cytokines (IL-10, IL-35 and transforming growth factor β [TGFβ]), or deprivation of IL-2—a potent growth and survival factor of T cells[27]. In contrast, conventional helper $CD4^+$ T cells, especially type 1 (T_{H1}), support $CD8^+$ T cells by promoting T cell priming through CD40 stimulation on DCs[28], and can even directly lyse or induce senescence on MHC class II-expressing tumor cells[29]. NK cells are innate lymphoid cells that have similar roles as cytotoxic $CD8^+$ T cells but without antigen-MHC specificity and can thus eliminate tumors that have downregulated MHC molecules[30]. In tumors, cells from the myeloid lineage, such as DCs, tumor-associated macrophages (TAMs), myeloid-derived suppressor cells (MDSCs), or tumor-associated neutrophils (TANs), exhibit complex phenotypes and functions. Some of them support antitumor T cell responses by functioning as antigen presenting cells (APCs), such as DCs. Others like MDSCs promote immunosuppression by multiple means, such as expression of regulatory molecules or depletion of relevant metabolites for T cells[31]. For TAMs and TANs, both anti- and pro-tumorigenic subtypes known as M1/N1 or M2/N2, respectively, have been observed. For example, M1 TAMs produce IFNγ, express high levels of MHC class II and costimulatory molecules and secrete recruiting

chemokines[32]. In contrast, M2 TAMs promote immunosuppression through the secretion of TGFβ and IL-10, and expression of inhibitory molecules such PD-L1[33]. In addition, they are found in hypoxic regions and blood vessels, stimulating angiogenesis by the expression of vascular endothelial growth factor (VEGF), resulting in the formation of unmature, leaky vasculature, essential to maintain the rapid development of tumor cells[33]. Nevertheless, the M1/M2 or N1/N2 classification does not accurately represent all the activation states of these cells but rather the ends of a large spectrum[34]. Last, cancer-associated fibroblasts (CAFs) are a class of activated fibroblasts that play tumor-promoting roles. They not only stimulate angiogenesis and mediate the epithelial-mesenchymal transition that cancer cells need to metastasize, but also suppress T cell recruitment and activation by secreting immunosuppressive molecules and forming a dense intra-tumoral stroma, which functions as a physical barrier and hinders the movement of TILs within the tumor[35]. As a result of this inhibitory environment, together with a persistent antigen stimulation, TILs are rendered unfunctional, also known as T cell exhaustion or dysfunction.

1.2.3 Dysfunctional TILs in tumors

The term exhaustion was first defined in chronic viral infections as the progressive loss of T cell functions due to viral persistence. Exhausted $CD8^+$ T cells were characterized by reduced proliferative capacity, loss of cytokine production (e.g., IL-2, TNFα, and IFNγ) and increased expression of inhibitory receptors[36]. As in chronic viral infections, target antigens are persistent in cancer, and similar hyporesponsive $CD8^+$ TILs have also been identified in tumors. However, recent advances in single-cell technologies allowed the in-depth characterization of exhausted $CD8^+$ TILs, bringing new insights into the definition of exhaustion or dysfunction in cancer. Emerging data suggests that the development of dysfunction in TILs is a continuum rather than a discrete process[37,38]. After $CD8^+$ T cells are activated, a subset of pre-exhausted $CD8^+$ T cells is formed. These cells have qualities of stem-like cells, such as self-renewal, proliferative capacity, and multipotency. They represent a small fraction of the bulk TIL population that serves as a reservoir of long-lived progenitors that give rise to more differentiated, short-lived exhausted $CD8^+$ TILs[39], which have higher cytotoxic capabilities and are thought to be important in the elimination of tumor cells.

The concepts of activation and exhaustion are fairly intermingled since exhaustion is the result of activation, and thus the upregulation of inhibitory molecules, which naturally occurs upon T cell activation to cease immune responses, is a characteristic feature of exhausted T cells as well. Different studies have shown that the more exhausted $CD8^+$ TILs are, the higher the expression of immune checkpoint molecules is. Terminally dysfunctional TILs tend to express high levels of PD1, CTLA4, CD39, CD160, CD244 (2B4), T cell immunoglobulin domain and mucin domain protein 3 (TIM3), lymphocyte

activation gene 3 (LAG3), inducible T cell co-stimulator (ICOS), and T cell immunoreceptor with immunoglobulin and ITIM domains (TIGIT)[37], whereas earlier dysfunctional states are characterized by low expression of PD1 and lack of CD39 or TIM3, among others[40,41]. On a transcriptional level, various signatures have been described[37]. The transcription factors T-box expressed in T cells (T-BET), eomesodermin (EOMES), T cell-specific transcription factor 1 (TCF1), and thymocyte selection-associated high mobility group box protein (TOX) are master regulators involved in $CD8^+$ T cell differentiation and dysfunctionality, arising in different stages[37]. For instance, TCF1 promotes stemness and it is associated with pre-dysfunctional, stem-like T cell states. On the contrary, TOX sustains high expression of inhibitory molecules and drives early dysfunctional $CD8^+$ T cells into terminal exhaustion by coordinating the irreversible fixed chromatin states of terminally dysfunctional T cells[42]. Intriguingly, transcriptional, epigenetic, and metabolic signatures distinguish exhaustion from effector or memory T cell states present during acute infections and in healthy tissues[43,44], underlaying the importance of the TME in controlling the fate of $CD8^+$ TILs (Illustration 3).

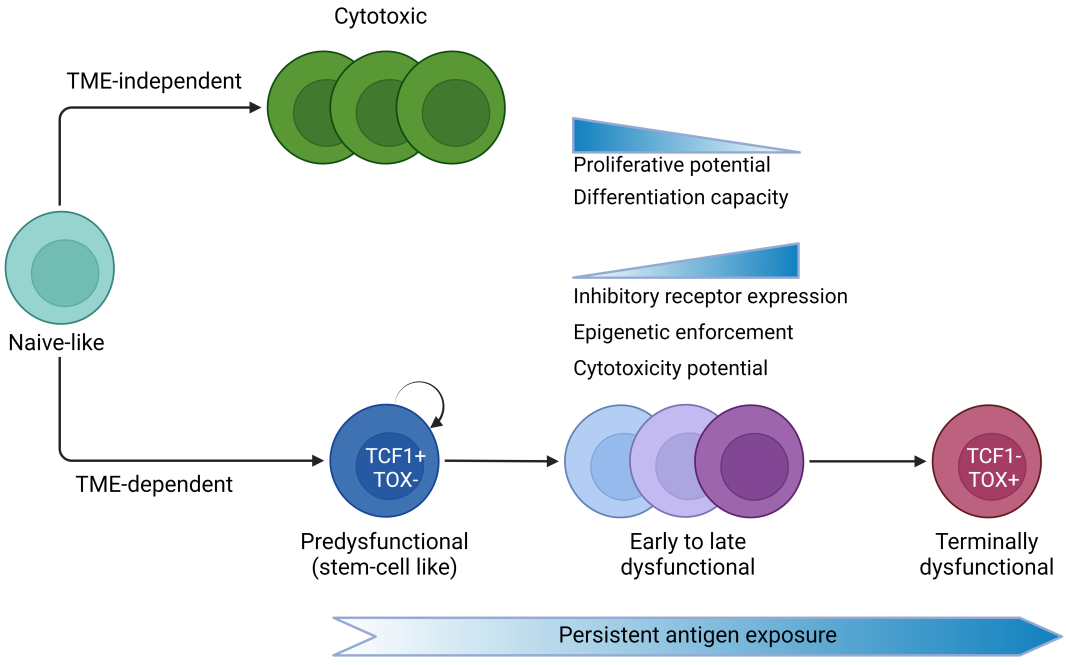

Illustration 3. Dysfunctional states of TILs
Dysfunctionality is predominantly driven by persistent antigen exposure and/or TME-specific factors, whereas cytotoxic states, also present in healthy tissues, follows other differentiation processes independent of the TME. Dysfunctional states are a continuum from $TCF1^+$ TOX^- stem-cell like progenitors to $TCF1^-$ TOX^+ terminally dysfunctional cells, which vary in several phenotypic and functional aspects. Inspired by Blank et al. 2019[45] and van der Leun et al. 2020[37], and created with BioRender.com by Elvira Criado-Moronati.

In short, T cell dysfunction is a continuum of transcriptional, epigenetic, and metabolic states driven by the persistent antigen exposure and/or a suppressive TME. Although dysfunctional $CD8^+$ TILs have initially been seen as unresponsive, recent discoveries highlight the potential and relevance of certain T cell subsets, such as the stem-like $TCF1^+$ $CD8^+$ T cell population, in different immunotherapy settings[46]. Importantly, dysfunction can be used as an indicator of tumor reactivity[37]. Therefore, this knowledge can be exploited in the development of effective TIL therapies.

1.3 Therapeutic applications of TILs

The use of TILs as source of naturally occurring tumor-reactive T cells was first used by Rosenberg et al. in the late 1980s, when they reported several studies demonstrating an accumulation of T cells in TILs from melanoma patients that were capable of recognizing and lysing tumor cells *in vitro*[47]. This led to the first successful ACT using autologous TILs (together with infusions of IL-2) in 1988, which mediated objective regressions in 11 out of 20 metastatic melanoma patients[48]. In the following years, more clinical evidence highlighted the potential of TIL therapy to treat metastatic melanoma[49–52]. Despite that, the use of this therapy to non-melanoma cancers has been less successful, with some modest clinical responses in patients with gastrointestinal[53], advanced breast[54], and head and neck[55] cancers. The most evident limitation is the surgical inaccessibility of some types of cancer, but other factors may also play a role. Therefore, understanding which features effective TIL products must have and optimizing current protocols to obtain them are crucial steps to increase the success of TIL therapy in a wider range of cancers.

1.3.1 Generation of effective TIL products

The conventional protocol to grow TILs for cancer treatment is based on the Rapid Expansion Protocol (REP) developed by Rosenberg and colleagues[56]. Tumor single-cell suspensions (digests) or tumor fragments are initially cultured in 24-well plates in the presence of high IL-2 concentrations, which favors the growth of T cells. After 2-3 weeks, T cells have outgrown and eliminated tumor cells, known as “outgrown TILs”. Cells are then rapidly expanded in the REP, which involves a polyclonal T cell activation by soluble anti-CD3 antibody (OKT3) in a culture with high doses of IL-2 and an excess of irradiated feeder cells derived from allogeneic donor´s peripheral blood mononuclear cells (PBMCs). In the period of 14 days, TILs expand to eligible numbers for clinical use, which are formulated and infused into the nonmyeloablative lymphodepleted patient, followed by IL-2 administration. This protocol is capable of expanding TILs to clinical doses in a relative short period of time. However, recent studies underline its negative effects on T cell fitness, including their functionality and proliferative capacity, and on the frequency of tumor-reactive T cells after the expansion.

Improving the fitness of tumor-reactive TILs

The fitness of expanded TILs is a key factor for therapeutic effectiveness. In 2020, Krishna et al. found that infused TIL products from complete responders in metastatic melanoma had a higher percentage of $TCF1^+$ stem-like $CD8^+$ TILs compared to non-responders, and that the lack of CD39 and CD69 was one of their characteristic features[39]. Therefore, approaches intended to enhance the presence of stem-like $CD8^+$ T cells on TIL products are under investigation[57]. Some include alterations in the metabolic pathways of T cells, such as triggering caloric restriction by increased extracellular potassium ion[43]. Others incorporate different cytokines into the expansion medium, such as IL7, IL-15, or IL-21, known to favor the formation and retention of memory phenotypes[58]. Next generation strategies involve genetic modification or reprogramming of T cells to increase stemness[57].

Increasing the frequency of tumor-reactive TILs

The frequency of tumor-reactive T cells is highly relevant in the context of TIL therapy as it varies among tumor types and patients. Melanoma is one of the cancers with the highest mutational burden as a result of the exposure to mutagens (e.g., ultraviolet light)[59]. Consequently, private *de novo* antigens termed neoantigens, which are solely found in tumor cells, are generated. They are excluded from immune tolerance and are thus potentially highly immunogenic[60]. Several studies suggest that melanoma TILs targeting neoantigens are responsible for an effective TIL therapy[61] and are the targets of ICB therapy[62]. The percentage of neoantigen-specific T cells in other tumor types is generally much lower due to the poorer mutated landscape[63], such as in brain[64], ovarian[65,66] or pancreatic cancers[67], explaining the poor response rates seen in these cancers.

Nonetheless, not only the low starting number of tumor-reactive T cells is challenging, but also the loss of relevant clonotypes during the expansion protocol. T cells unspecific for tumor antigens (referred as bystander) may hold greater proliferative capacity than exhausted, antigen-experienced T cells and they can thus outgrow them during the *ex vivo* culture, decreasing the numbers of tumor-reactive TILs in the final product[68,69]. Several approaches have aimed to support the growth of tumor-reactive T cells. On the one hand, the activation/exhaustion states of these cells have been used as an advantage in targeted strategies. For instance, the targeting of costimulatory molecules such as 4-1BB (CD137) or OX40 (CD134) by agonistic antibodies have shown an augmented cytolytic function and enhanced antitumor activity[70]. In a similar way, the blockade of immune checkpoints, such as CTLA4 or PD1, had the potential to unleash the proliferative capacity of exhausted TILs[71,72]. The most promising approach so far is the enrichment of tumor-reactive T cells prior to the expansion, which can also shorten the *ex vivo* expansion time (Illustration 4). However, the main challenges reside on

the identification of tumor-reactive T cells and the clinical applicability of the chosen enrichment strategy.

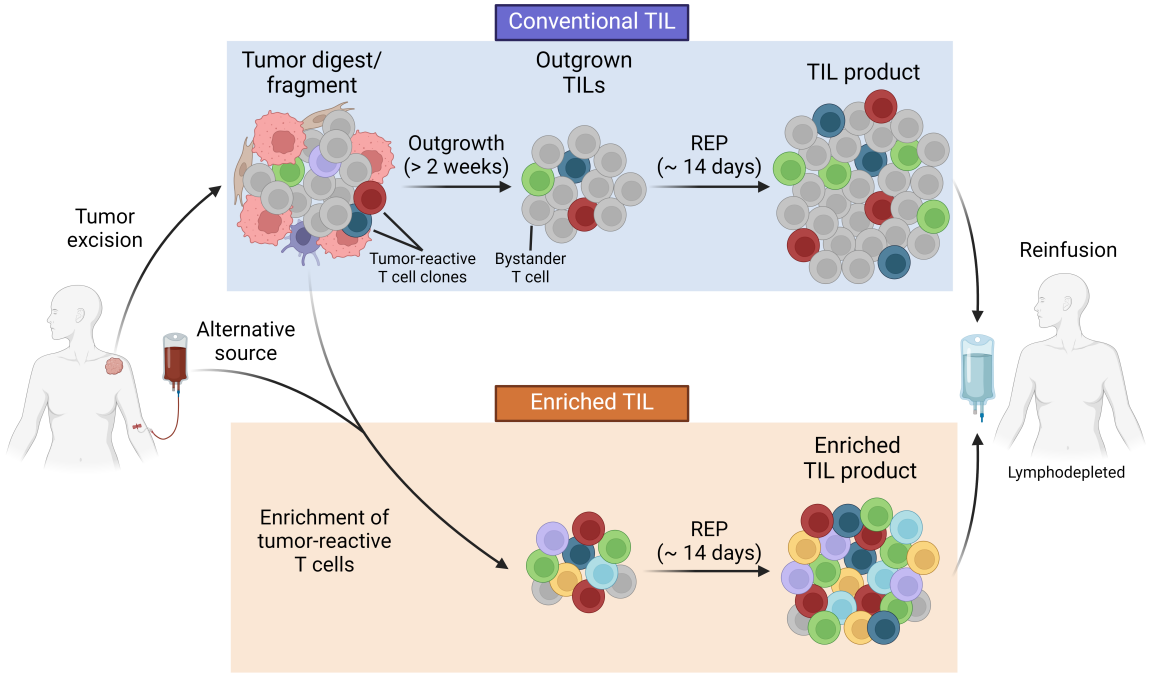

Illustration 4. Enrichment of tumor-reactive T cells to improve the generation of TIL products
The conventional protocol to generate TILs for ACT relies on the outgrowth of bulk TILs from tumor digests (or pieces) followed by a rapid expansion (REP) to obtain large numbers of TILs for reinfusion into the lymphodepleted patient. The addition of an enrichment step of tumor-reactive T cells directly from tumor digests (or alternative sources as blood) and prior to the REP constitutes a potential improvement to obtain a TIL product enriched in tumor reactivity. Created with BioRender.com by Elvira Criado-Moronati.

1.3.2 Identification and enrichment of tumor-reactive T cells

Several methods have been proposed for the selection of tumor-reactive T cells. The chosen approach depends on whether the tumor antigens are known or not. The development of next generation sequencing and novel bioinformatic tools have enabled the systematic identification of neoantigens in multiple cancer types[73]. The accuracy of *in silico* predictions is a major factor in the efficacy of this process, and although new algorithms are being developed[74], it still remains a challenge. The direct identification of peptides bound to MHC molecules on the surface of tumor cells by mass spectrometry have shown to be advantageous to find *bona fide* neoantigens, although large amounts of biological material are required[75]. Therefore, enrichment strategies that are independent on tumor antigen identification constitute promising alternatives.

Isolation methods via fluorescent-activated cell sorting (FACS) and magnetic cell separation (MACS) technologies are under investigation, such as peptide-MHC (pMHC) multimers, activation-based and phenotype-based approaches (Illustration 5).

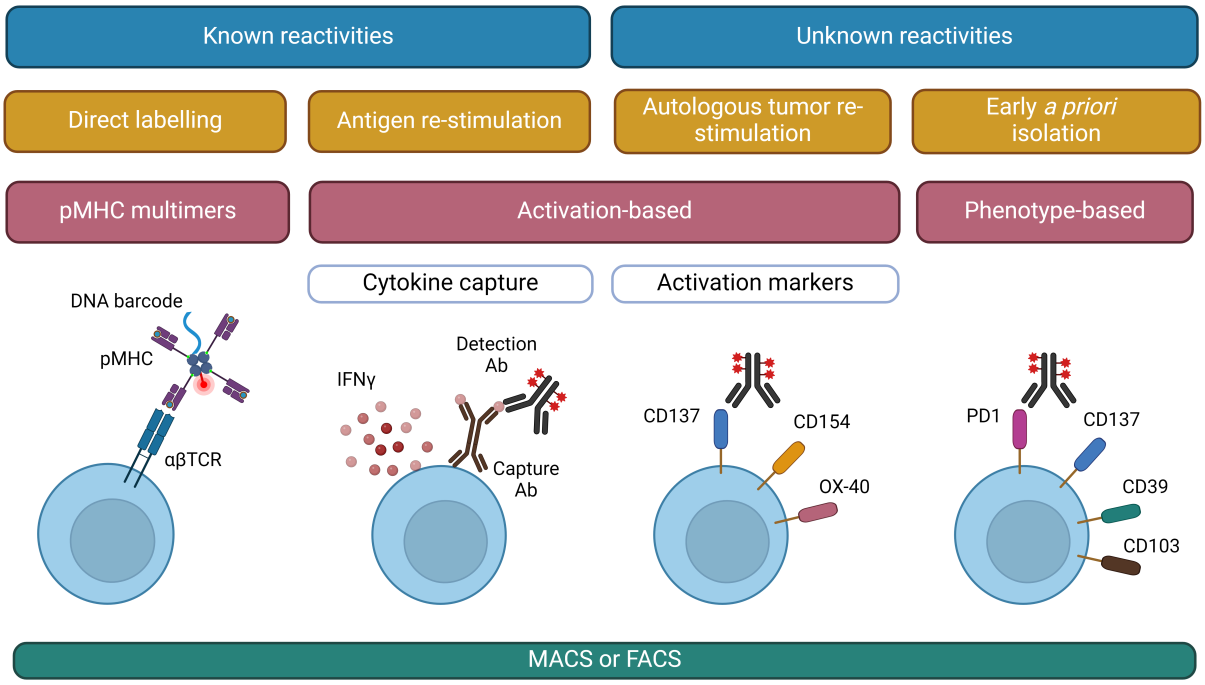

Illustration 5. Enrichment strategies for tumor-reactive T cells
Based on the targeting of either known or unknown specificities, different strategies can be pursued. The direct labelling of specific TCRs requires the identification of tumor antigens and production of pMHC multimers. Targeting activated cells upon re-stimulation with antigens or autologous tumor can be achieved by using reagents that either target cytokine-producing T cells or activation markers. The identification of tumor-reactive phenotypes can be exploited to isolate cells based on specific activation/exhaustion markers. The enrichments can be developed for MACS or FACS technologies. Inspired by Bianchi et al. 2020[76] and created with BioRender.com by Elvira Criado-Moronati.

pMHC Multimers

Multimers are complexes formed of fluorochrome-conjugated pMHC molecules that are multimerized to allow stable binding to their cognate TCR, enabling the detection and selection of peptide-specific T cells. In recent years, multimer technologies have been improved towards increased sensitivity and larger number of T cell clones that can be simultaneously detected, from the use of combinatorial staining approaches for flow[77] and mass cytometry[78], to DNA barcode-labeled MHC multimers[79]. Several of these technologies have been used to isolate and study neoantigen-specific T cells in cancer patients[80,81]. However, various intrinsic factors limit their clinical application. First, the difficulties associated with the production of MHC class II molecules and the prediction of MHC class II-restricted peptides to form stable MHC complexes[82] result in the exclusion of tumor-reactive $CD4^+$ T cells. Second,

the engagement of TCR by multimers can cause activation-induced T cell death[83]. Third, the generation of a library of MHC multimers for each patient under Good Manufacturing Practice (GMP) conditions for clinical implementation may constitute a time-consuming as well as cost prohibitive process[76].

Activation-induced methods

In contrast to multimers, which allow for a direct labeling of antigen-specific T cells, other approaches exploit the activation of T cells upon antigen-specific TCR engagement. Consequently, these methods require a transient stimulation prior to the enrichment. When neoantigens have been identified, a restimulation of T cells with antigen-pulsed APCs can be performed. Alternatively, the use of autologous tumor cells as targets can cover a broader range of naturally presented tumor antigens. Regardless of the stimulation approach, activated T cells respond by secreting cytokines and upregulating activation markers on their cell surface.

Cytotoxic cytokines, such as TNFα and IFNγ, can be retained on the cell surface by a capture matrix and be sorted by FACS or MACS[84]. IFNγ secretion has been associated with the identification of tumor-reactive T cells in previous studies[85,86] as well as TNFα in colorectal cancer[87]. The availability of clinical grade reagents and uncomplicated protocols allows this technique to be rapidly implemented in the clinic[88]. Despite this, T cells are functionally diverse and cannot be defined by a single cytokine[89], which might be restricted to particular T cell subsets[89,90]. Therefore, the cytokine-based enrichment may not represent the whole pool of tumor-reactive T cells.

The use of activation-induced surface markers represents a more suitable approach to isolate antigen-specific T cells as it is independent of cytokine production ability. One of the most common markers employed is CD137, the tumor necrosis factor receptor superfamily member 9 (TNFRSF9). This surface glycoprotein is transiently expressed on activated $CD8^+$ and $CD4^+$ T cells upon TCR engagement and it is constitutively expressed on intratumoral T_{reg} cells[91]. Its costimulatory and anti-apoptotic functions mediate T cell proliferation, activation, and survival[92]. CD137 has been shown to enrich tumor-reactive T cells from PBLs and TILs with heterogenous functional profiles after a restimulation period (24-48 hours) with tumor-associated antigens[93] and neoantigens[94], as well as with autologous tumor cells[95,96]. Other activation-induced markers, such as CD154 and CD134, have particularly been used for the recognition of conventional $CD4^+$ T cell responses[97], and efforts have been undertaken to distinguish them from activated regulatory $CD4^+$ T cells[98].

Phenotype-based methods

Dysfunctional T cell phenotypes, together with highly clonal TCR repertoires, are generally hallmarks of an antigen-specific expansion[37]. Naturally occurring tumor-reactive TILs, either targeting neoantigens or shared tumor-associated antigens, may thus exhibit a characteristic phenotype profile that differentiates them from bystander T cells. Consequently, the expression of a distinct set of cell surface activation/exhaustion markers could be exploited to directly isolate tumor-reactive T cells without the need of either tumor antigen identification or *ex vivo* stimulation methods. This strategy has become a collective and challenging effort among groups in the field, aiming to find the marker, or combination thereof, that could enrich the highest fraction of tumor-reactive T cells.

Studies in melanoma, which generally contains significant frequencies of tumor-reactive TILs, were the pioneers in finding marker expression patterns of tumor-reactive $CD8^+$ T cells. The co-inhibitory molecule PD1 (CD279) was identified as a surrogate marker for tumor reactivity in $CD8^+$ TILs from melanoma patients[99,100]. Gros et al. found that $PD1^+$ $CD8^+$ TILs, which co-expressed other exhaustion markers such as TIM3 and LAG3, were highly clonal and recognized autologous tumor cells[101]. In addition, a small proportion of $PD1^+$ $CD8^+$ TILs upregulated the activation marker CD137. Although the frequencies of $CD137^+$ TILs are generally low, they have been correlated to increased tumor reactivity in melanoma and ovarian cancer[95]. Particularly, the tumor reactivity of the $PD1^+$ population is restricted to the highly expressing PD1 ($PD1^{hi}$) $CD8^+$ TILs, as emphasized in several studies in ovarian[102] and triple-negative breast cancers[103]. All in all, PD1 and CD137 are two of the most relevant markers for tumor-reactive T cells, although other markers have gained importance in recent years, especially in low immunogenic tumors.

CD103 (ITGAE) is an integrin ($\alpha E\beta 7$) expressed on tissue-resident memory $CD8^+$ T cells (T_{RM}), among others, which mediates cell adhesion and migration of immune cells through interaction with the epithelial marker E-cadherin, improving their retention in peripheral epithelial tissues[104]. CD103 upregulation is not only correlated with E-cadherin expression, but also antigen recognition in the presence of TGF-$\beta 1$[105–108]. $CD103^+$ $CD8^+$ T cell infiltration has been correlated with overall survival in multiple studies[109–112], especially after anti-PD1 therapy[105,113]. As a result, several groups have investigated the tumor reactivity of this subset and found that it is enriched with tumor-reactive $CD8^+$ T cells in various tumor types[108–111,113,114]. Interestingly, CD103 expression increases TCR antigen sensitivity and migration of $CD8^+$ T cells, leading to a faster and more efficient tumor recognition and killing[108].

Remarkably, CD39 has become the new contestant in this game. CD39, also known as ectonucleoside triphosphate diphosphohydrolase 1 (*ENTPD1*), is an enzyme that hydrolyzes extracellular ATP

(adenosine triphosphate), generating AMP (adenosine monophosphate), which is further converted into adenosine by CD73[115]. Decreased extracellular ATP and increased adenosine levels create an immunosuppressive environment for T cells. Consequently, CD39 and CD73 are considered to be inhibitory molecules[116]. CD39 is widely expressed on several immune cells, among those regulatory cell populations like $CD4^+$ T_{reg}, as well as in non-immune cells, such as endothelial cells[116]. In $CD8^+$ T cells, CD39 is upregulated upon prolonged TCR stimulation[107] and, similarly to PD1, has been linked to T cell exhaustion in several studies in TILs[117]. Simoni et al. discovered that bystander cells, such as virus-specific T cells, lack CD39 expression[118].

Other markers have been suggested, especially those related to exhaustion or dysfunctional states, such as the co-inhibitory receptor TIGIT, expressed on $CD8^+$, conventional and regulatory $CD4^+$ T cells, and NK cells[119]. Neuropilin-1 (CD304), generally found in subsets of $CD4^+$ T_{reg} cells in LNs and TILs, has been identified in a $CD8^+$ TIL population which expressed high levels of PD1 and is enriched with tumor-reactive T cells in non-small cell lung cancer[120]. Furthermore, Philip et al. demonstrated that the co-upregulation of CD38 and CD101, two molecules considered as co-stimulatory, and downregulation of CD5, an inhibitor of TCR-mediated signaling[121], defined the epigenetic imprinted, fixed dysfunctional state of tumor-reactive $PD1^{hi}$ $CD8^+$ TILs in mouse models[42].

In summary, the enrichment of tumor-reactive T cells based on *a priori* phenotype before the *ex vivo* expansion has the advantage of being independent of the antigen targeted, which can accelerate and cheapen manufacturing processes. However, the search for a cell surface marker, or a combination thereof, that could enrich tumor-reactive T cells is a very dynamic and controversial research field. Several markers, particularly PD1, CD137, CD39, or CD103, have been proposed, but no consensus has been reached yet despite the increasing accumulation of data over the past years (Table 1).

Table 1. Overview of proposed tumor-reactive $CD8^+$ TIL phenotypes (until 2021)

Proposed phenotype	**Cancer type (*Reference*)**
$PD1^+$	Melanoma (*Ahmadzahed 2009*[102]*; Inozume 2010*[100]*; Fourcade 2009*[122]*; Gros 2014*[101])
	HPV^+ HNSCC (*Eberhardt 2021*[123])
$PD1^{high}$	Ovarian cancer (*Salas-Benito 2021*[102])
	Triple-negative breast cancer (*Guo 2020*[103])
$CD137^+$	Ovarian cancer, melanoma (*Ye 2014*[95] , Seliktar-Ofir 2017[96])
$CD103^+$	Melanoma (*Malik 2017*[111])
	Lung cancer (*Djenidi 2015*[109]*; Ganesan 2015*[110]*; Corgnac 2020*[124]*; Hamid 2020*[108])

Proposed phenotype	Cancer type (*Reference*)
CD103$^+$ CD69$^+$	NSCLC (*De Groot 2019*[114])
CD103$^+$ PD1$^+$	Ovarian cancer (*Webb 2015*[125])
CD39$^+$	Colorectal and lung cancer (*Simoni 2018*[118])
CD39$^+$ CD103$^+$	HNSCC, melanoma, lung, ovarian, rectal, colon cancers (*Duhen 2018*[107])
	Endometrial cancer (*Workel 2020*[126])
	CxCa, VSCC, OPSCC (*Kortekaas 2020*[127])
TIGIT$^+$ PD1$^+$ CD39$^+$ CD103$^+$	HGSOC (*Laumont 2021*[128])
Neuropilin-1$^+$	NSCLC (*Leclerc 2019*[120])

CxCa: cervical squamous cell carcinoma; HGSOC: high-grade serous ovarian cancer; HNSCC: head and neck squamous cell carcinoma; HPV: human papillomavirus; NSCLC: non-small cell lung cancer; OPSCC: oropharyngeal squamous cell carcinoma; VSCC: vulvar squamous cell carcinoma

1.4 Multiplexed imaging techniques

Multiplexed single-cell technologies, such as single-cell RNA sequencing and cytometry by time of flight (CyTOF), have opened a new horizon in the study of tumor immunology. However, these methods neglect the spatial dimension of tumor tissues as they rely on single-cell suspensions. The TME is a dynamic ecosystem in which distinct cell types are organized into cellular neighborhoods with different functions that communicate across each other, leading to a pro- or anti-tumor environment[129]. Therefore, spatial organizations and relationships have become important in understanding biological processes and in clinically stratifying solid cancer patients[130]. The limited number of features simultaneously analyzed on a single section in conventional immunohistochemistry reduces the view of the diversity and complexity of the TME. New cutting-edge technologies are emerging as promising tools, capable of highly multiplexed analyses at the single-cell level while preserving the tissue spatial context, offering us to study the TME in unprecedented ways.

1.4.1 State of the art

Fluorescence microscopy has faced limitations in the number of fluorophores that can be simultaneously imaged due to spectral overlaps[131]. Iterative methods based on cycles of antibody staining and stripping have increased the number of parameters that can be measured on a single tissue section. However, handling these technologies requires a certain degree of automation.

Several platforms have been developed in recent years. One of the first multiplexed fluorescent microscopy methods was presented by Gerdes et al. in 2013, which is now commercialized in a fully

automated instrument by Leica Microsystems as Cell DIVE. It involves iterative cycles in which the chemically inactivation of the fluorescent dye enables the re-use of the same dye conjugated to a different antibody in the next cycle[132]. In 2018, Goltsev et al. first described the cyclic imaging technique termed CODEX® (co-detection by indexing)[133], which relies on the conjugation of antibodies with DNA barcodes. This technology has the advantage of simultaneously co-stain tissues with a mixture of tagged antibodies, which are targeted in each cycle by a polymerization reaction with complementary fluorescent-labelled nucleotides. The CODEX technology was licensed to Akoya Biosciences® and is commercially available as PhenoCycler®. Alternative to optical imaging, TOF mass spectrometry-based technologies overcome the limitations of fluorochromes by labelling antibodies to stable metal isotopes. Keren et al. developed the ion beam imaging by time-of-flight (MIBI-TOF) technology. Tissues are simultaneously co-stained with metal-tagged antibodies, which are rastered by a focused ion beam, producing secondary ions that are measured by TOF mass spectrometry[134]. Bondenmiller´s group established a protocol to simultaneously detect both mRNA and proteins in tissues based on TOF mass spectrometry [135]. In addition, companies like 10x Genomics and NanoString offer commercially available platforms for sequencing-based, spatial resolved transcriptomics and proteomics.

Overall, spatial multi-omics has the potential to become a relevant tool not only in immuno-oncology, but also in other areas, and hence it has been selected one of the seven technologies to watch in 2022 by the scientific journal Nature[136]. At Miltenyi Biotec, we have developed our own multiplexed imaging: the MICS technology.

1.4.2 The MICS technology

MICS (MACSima™ imaging cyclic staining) is a new ultrahigh content imaging technology that, together with the fully automated MACSima instrument platform, has been developed for almost a decade at Miltenyi Biotec. MICS is an iterative-based technique that is capable to measure more than a hundred markers on a single tissue section. Each cycle is composed of the following steps: 1) staining with fluorochrome-conjugated antibodies; 2) image acquisition; and 3) fluorescent signal removal. As of 2023, three different methods for the removal of fluorochromes have been developed. Initial versions of the instrument utilized photobleaching, a process in which fluorophores are chemically destroyed upon exposure to excitation light, permanently losing the ability to fluoresce[137]. In this case, antibodies are conjugated with fluorochromes that are highly sensitive to photobleaching, such as phycoerythrin (PE) or fluorescein (FITC)[138]. More recently, the use of REAdyelease™ and REAlease® fluorochrome-conjugated antibodies allows the chemically controlled release of fluorochromes and antibody complexes, respectively. This method constitutes a gentler mechanism and can erase the signal of the

whole tissue section, in contrast to the photobleaching-based process, which needs to raster through different areas of interest. Nevertheless, both technologies can be combined in one experiment (Illustration 6).

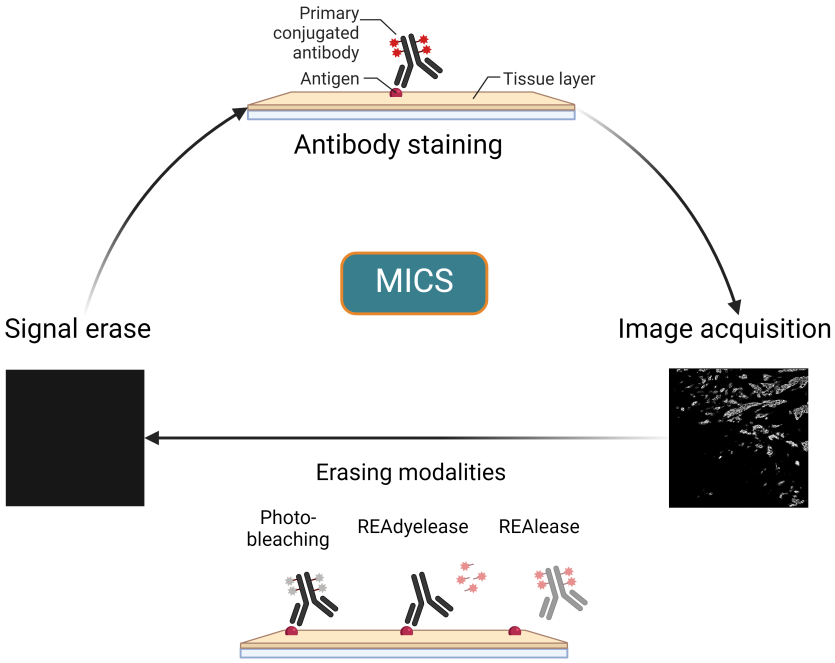

Illustration 6. Schematic representation of the MICS technology
The MICS technology is a multiplexed fluorescent imaging approach that consist of iterative cycles in which tissues are incubated with fluorochrome-conjugated antibodies and imaged. Consecutively, fluorochrome signals are erased either by photobleaching, stripping of fluorophores (REAdyelease) or of the full antibody complex (REAlease) in order to allow subsequent staining cycles. Created with BioRender.com by Elvira Criado-Moronati.

In summary, the MICS technology offers the possibility to screen hundreds of markers in a single tissue section in a fully automated manner with the MACSima imaging platform, enabling the characterization of tumor tissues on a deeper level.

1.5 Aim of PhD project

The necessity to improve TIL products for the effective adoptive cell therapy for cancers other than melanoma has been highlighted by the modest outcomes seen in these patients[53–55]. One of the most attractive approaches to increase the frequency of naturally occurring tumor-reactive TILs in cell products is their enrichment prior to the *ex vivo* expansion during cell manufacturing. Of all methods described, the *a priori* isolation of TILs based on a tumor-reactive T cell phenotype holds great promise as it is independent on the antigen recognized and there is thus no need for the identification of private tumor antigens, significantly shortening the time for patients to receive the treatment. In addition, the enriched product represents a polyclonal tumor-reactive T cell population that can potentially improve clinical outcomes. Therefore, my PhD project aims to identify a cell surface marker, or combination thereof, that can potentially be used to enrich tumor-reactive $CD8^+$ TILs for clinical use.

First, I will dissociate fresh tumor samples into single cell suspensions for two purposes. On the one hand, to characterize by flow cytometry the cell surface expression of markers related to activation and exhaustion as a proxy of tumor reactivity and evaluate their potential to be used in enrichment strategies. On the other hand, to establish an optimal workflow for the isolation of tumor-reactive $CD8^+$ TIL populations from tumor digests. Ultimately, I will expand the enriched $CD8^+$ TIL subsets and co-culture them with autologous tumor cells to validate their tumor reactivity *in vitro*.

Second, I will complement the characterization of TILs using single-cell RNA sequencing. I will investigate the TCR repertoires of pre- and post- expanded T cell subsets to understand clonal overlaps between samples and clonotype shifts over the *in vitro* culture. Additionally, gene expression profiles will shed light on the different states of T cell populations in the tumor, particularly those of relevant clonotypes, such as dominant TCRs in the tumor as a surrogate of tumor-specific TCRs as well as those TCRs found in post-expanded T cell subsets that exhibit tumor reactivity.

Lastly, I will examine the spatial distribution of relevant $CD8^+$ TIL subsets in the tumor microenvironment to confirm the identified phenotype of tumor-reactive $CD8^+$ TILs. For this purpose, I will study the composition, spatial location, and phenotypes of cell types, especially $CD8^+$ T cells, in the TME and complex structures like TLSs in selected tumor tissues using our newly developed MICS technology. Particularly, I will focus on the expression of relevant activation and exhaustion markers on T cells in close proximity to tumor cells, which may presumably be interacting with or recognizing tumor cells, in comparison with T cells in stromal areas or TLSs.

By characterizing TILs at different levels and using diverse technologies, I aim to contribute to the discovery of marker(s) that can be exploited in the development of clinical processes to generate tumor-reactive TILs for ACT.

2 Materials and Methods

2.1 Materials

2.1.1 Human material

Table 2. Human tumor samples

Cancer Type	Subtype	Patient ID	Tissue ID	Gender	Age	Matched blood	Source
Colorectal	-	CRC1	TS20180829	F	82	No	1
Colorectal	-	CRC2	TS20190919	M	77	No	1
Colorectal	Adenocarcinoma	CRC3	TS20200428	M	45	Yes	6
Colorectal	Adenocarcinoma	CRC4	TS20200714	F	74	Yes	6
Colorectal Met	Metastasis in ovary	metCRC5*	TS20180615	F	72	No	2
Lung	Squamous cell lung carcinoma	LuCa1	TS20180815	M	71	No	1
Ovarian	-	OvCa2	TS20180914	F	-	No	2
Ovarian	-	OvCa3	TS20180926	F	-	No	2
Ovarian	-	OvCa4	TS20181009	F	-	No	2
Ovarian	-	OvCa5	TS20181114	F	-	No	2
Ovarian	-	OvCa6	TS20181214	F	45	No	2
Ovarian	Sex cord-stromal tumor	OvCa7	TS20190524	F	57	No	2
Ovarian	-	OvCa8	TS20190806	F	-	No	4
Ovarian	Endometrial carcinoma	OvCa9	TS20191114	F	-	No	4
Ovarian	-	OvCa10	TS20191122	F	-	No	3
Ovarian	-	OvCa11	TS20200108	F	-	No	3
Ovarian	Serous carcinoma	OvCa12	TS20200514	F	60	Yes	6
Ovarian	Cystadenocarcinoma	OvCa13	TS20200708	F	61	Yes	6
Ovarian	Serous carcinoma	OvCa17*	TS20150707	F	73	No	2
Pancreatic	Ductal adenocarcinoma	PaCa1	TIPc375	-	-	No	4
Pancreatic	Ductal adenocarcinoma	PaCa2	TIPc377	M	70	No	4
Pancreatic	Ductal adenocarcinoma	PaCa4	KUM2	M	67	Yes	5
Pancreatic	Ductal adenocarcinoma	PaCa5	KUM3	M	79	Yes	5
Pancreatic	Ductal adenocarcinoma	PaCa6	KUM5	M	71	Yes	5
Pancreatic	Ductal adenocarcinoma	PaCa7	KUM6	M	80	Yes	5

Gender: F (Female), M (Male); **Source:** 1: Prof. Dr. med. Philipp Ströbel, Institute of Pathology, University Medical Center Göttingen; 2: Dr. med. Peter Mallmann and Michael Mallmann, Department of Obstetrics and Gynecology, Faculty of Medicine, University of Cologne; 3: Prof. Dr. Jolanda de Vries, Department of

Tumor Immunology, Radboud University Medical Center, Nijmegen; 4: Prof. Dr. Rienk Offringa, Department of Molecular Oncology of Gastrointestinal Tumors, DKFZ, Heidelberg; 5: Prof. Dr. Stefan Böck, Medical Clinic and Polyclinic II, University Hospital of Munich (KUM); 6: Trans-Hit Bio, Quebec, Canada; -: not available; *Sample tissues used for MICS.

Human samples, either cryopreserved or fresh, were obtained in the context of collaborations with academic or clinical sites (sources 1 to 5) within different departments at Miltenyi Biotec, following the approved ethical guidelines of the corresponding local ethics committees and written informed consent of patients, except for samples from source 3, which were anonymized leftover biomaterial, and thus no explicit ethical approval nor informed consent from patients were necessary according to the code of conduct established by the collaborating Dutch universities and the COREON (Committee for Regulation of Research) that was in placed during the period of time the samples were received (2019/2020). Fresh samples from the company Trans-Hit Bio (source 6), now Azenta Life Sciences—a biospecimen collector—were acquired in compliance with ethical and quality control standards.

The OC12 tumor cell line —derived from an ovarian cancer patient and kindly provided by the group of Dr. Olaf Hardt at Miltenyi Biotec— was the only tumor cell line used in this PhD project.

Healthy peripheral blood mononuclear cells (PBMCs) were obtained from anonymous internal volunteers at Miltenyi Biotec upon written informed consent.

2.1.2 Laboratory equipment

Table 3. Laboratory equipment

Laboratory Equipment	Provider
Centrifuge 5424 R	Eppendorf, Hamburg, Germany
CoolCell™ LX Freezer Container	Biocision Azenta Inc., Chelmsford, MA, USA
Cryostat CM1860 UV	Leica Biosystems, Wetzlar, Germany
Cytation 3 Cell Imaging Multi-Mode Reader	BioTek Instruments, Winooski, VT, USA
EP Research® plus Pipettes, 10-1000 µL	Eppendorf, Hamburg, Germany
gentleMACS™ Octo Dissociator with Heaters	Miltenyi Biotec B.V. & Co. KG, Bergisch Gladbach, Germany
IN Cell Analyzer 2000	GE Healthcare, Chicago, IL, USA
Leica DM IL LED Inverted Microscope	Leica Microsystems GmbH, Wetzlar, Germany
MACS® Separator	Miltenyi Biotec B.V. & Co. KG, Bergisch Gladbach, Germany
MACSQuant® Analyzer 10, 16, X	Miltenyi Biotec B.V. & Co. KG, Bergisch Gladbach, Germany
MACSQuant® Tyto® Cell Sorter	Miltenyi Biotec B.V. & Co. KG, Bergisch Gladbach, Germany
Milli-Q® E-POD®	Millipore, Merck KGaA, Darmstadt, Germany
Multifuge™ X3R	Thermo Fisher Scientific, Waltham, MA, USA
NextSeq™ 550	Illumina, San Diego, CA, USA

S1 Pipet Fillers	Thermo Fisher Scientific, Waltham, MA, USA
RS-2000 Irradiator	RadSource, Buford, GA, USA
SensoScope® BrightROI Microscope	Miltenyi Imaging GmbH, Radolfzell, Germany
Sysmex XP-300	Sysmex Corporation, Jobe, Japan
TECAN Freedom EVO 200	Tecan Group AG, Männedorf, Switzerland
Vortex-Genie® 2	Scientific Industries, Inc., Bohemia, NY, USA

2.1.3 Consumables

Table 4. Consumables

Consumable	Provider
24-Well No-Bottom Plates	Zell-Kontakt GmbH, Nörten-Hardenberg, Germany
6-Well, 24-Well, 48-Well Plates	Corning Inc., Corning, NY, USA
96-Well U-Bottom Microtest Plates, 1.2 mL	LVL technologies GmbH & Co. KG, Crailsheim, Germany
96-Well U-Bottom Plates	Corning Inc., Corning, NY, USA
ART™ Wide Bore Filtered Pipette Tips	Thermo Fisher Scientific, Waltham, MA, USA
C-Chip Neubauer Improved Disposable Hemocytometer	NanoEntek, Seoul, South Korea
CellStar® Tissue Culture Dishes	Greiner Bio-One, Kremsmünster, Austria
Coverglass Plates, 76 x 111 mm	Zell-Kontakt GmbH, Nörten-Hardenberg, Germany
Cryovials (2 mL)	Thermo Fisher Scientific, Waltham, MA, USA
Disposable Syringes	BD Biosciences, Franklin Lakes, NJ, USA
Epredia™ SuperFrost Plus™ Adhesion Slides	Fisher Scientific GmbH, Schwerte, Germany
Falcon® Tubes, 15-50 mL	Corning Inc., Corning, NY, USA
gentleMACS™ C Tubes	Miltenyi Biotec B.V. & Co. KG, Bergisch Gladbach, Germany
LS Columns	Miltenyi Biotec B.V. & Co. KG, Bergisch Gladbach, Germany
MACS® SmartStrainers, 70 µm	Miltenyi Biotec B.V. & Co. KG, Bergisch Gladbach, Germany
MACSQuant® Tyto® Cartridge	Miltenyi Biotec B.V. & Co. KG, Bergisch Gladbach, Germany
Microcentrifuge Tubes, 0.5-2 mL	Starlab International GmbH, Hamburg, Germany
Millex-GV Filter, 0.22 µm	Millipore Merck KGaA, Darmstadt, Germany
Nunc™ Thermanox™ Coverslips	Fisher Scientific GmbH, Schwerte, Germany
PFE Latex Gloves	Kimberly-Clark Kimtech, Irving, TX, USA
Pierceable Film	Brooks Life Sciences, Chelmsford, MA, USA
Pre-Separation Filters, 30 µm	Miltenyi Biotec B.V. & Co. KG, Bergisch Gladbach, Germany

Sakura Finitek™ Tissue-Tek™ Cryomold™ Biopsy Molds	Fisher Scientific GmbH, Schwerte, Germany
Serological Pipettes, 5-50 mL	Sarstedt Inc., Nümbrecht, Germany
Storage Bottles, 250-500 mL	Corning Inc., Corning, NY, USA
Tips without Filter, 10-1000 µL	Starlab International GmbH, Hamburg, Germany
Tissue Culture Flasks, T25, T75	Corning Inc., Corning, NY, USA

2.1.4 Kits

Table 5. Kits

Kit	Provider
Chromium Next GEM Chip G Single Cell Kit	10x Genomics, Pleasanton, CA, USA
Chromium Next GEM Single Cell 5' Library and Gel Bead Kit	10x Genomics, Pleasanton, CA, USA
Chromium Single Cell 5' Library Construction Kit	10x Genomics, Pleasanton, CA, USA
Chromium Single Cell V(D)J Enrichment Kit, Human T Cell	10x Genomics, Pleasanton, CA, USA
Dead Cell Removal Kit	Miltenyi Biotec B.V. & Co. KG, Bergisch Gladbach, Germany
Inside Stain Kit	Miltenyi Biotec B.V. & Co. KG, Bergisch Gladbach, Germany
NextSeq™ 500/550 Mid or High Output Kit	Illumina, San Diego, CA, USA
REAlease® CD4/CD8 (TIL) MicroBead Kit, human	Miltenyi Biotec B.V. & Co. KG, Bergisch Gladbach, Germany
REAlease® CD45 (TIL) MicroBead Kit, human	Miltenyi Biotec B.V. & Co. KG, Bergisch Gladbach, Germany
REAlease® CD8 (TIL) MicroBead Kit, human	Miltenyi Biotec B.V. & Co. KG, Bergisch Gladbach, Germany
Tumor Dissociation Kit, human	Miltenyi Biotec B.V. & Co. KG, Bergisch Gladbach, Germany

2.1.5 Chemicals and solutions

Table 6. Chemicals and solutions

Chemical/Solution	Provider
2-Methylbutane	Sigma-Aldrich Chemie GmbH, Munich, Germany
37% Hydrochloric Acid (HCl)	Sigma-Aldrich Chemie GmbH, Munich, Germany
Accutase® Solution	Sigma-Aldrich Chemie GmbH, Munich, Germany
Acetone	Sigma-Aldrich Chemie GmbH, Munich, Germany
Albumin, human	Octapharma GmbH, Langenfeld, Germany
Antibiotic-Antimycotic (Anti-Anti) (100X)	Gibco Thermo Fisher Scientific, Waltham, MA, USA

AutoMACS™ Running Buffer	Miltenyi Biotec B.V. & Co. KG, Bergisch Gladbach, Germany
BD GolgiPlug™ (1000X)	BD Biosciences, Franklin Lakes, NJ, USA
BD GolgiStop™ (1500X)	BD Biosciences, Franklin Lakes, NJ, USA
Cell Stimulation Cocktail (500X)	eBioscience, San Diego, CA, USA
CliniMACS® PBS/EDTA Buffer	Miltenyi Biotec B.V. & Co. KG, Bergisch Gladbach, Germany
Dimethyl Sulfoxide (DMSO)	Sigma-Aldrich Chemie GmbH, Munich, Germany
Erythrosin B Dye	Sigma-Aldrich Chemie GmbH, Munich, Germany
Ethanol Absolute (EtOH)	Merck KGaA, Darmstadt, Germany
Fetal Bovine Serum (FBS) Maximus	Catus Biotech GmbH, Tutzing, Germany
Fluorescence Mounting Medium	Agilent, Santa Clara, CA, USA
Giemsa's Azur Eosin Methylene Blue Solution	Sigma-Aldrich Chemie GmbH, Munich, Germany
Human IL-2 IS Premium Grade	Miltenyi Biotec B.V. & Co. KG, Bergisch Gladbach, Germany
Human Serum Type AB, male (AB serum)	Sigma-Aldrich Chemie GmbH, Munich, Germany
L-Glutamine, 200 mM	Lonza Group Ltd, Basel, Switzerland
MACS® BSA Stock Solution	Miltenyi Biotec B.V. & Co. KG, Bergisch Gladbach, Germany
MACS® GMP CD3 Pure (OKT3)	Miltenyi Biotec B.V. & Co. KG, Bergisch Gladbach, Germany
MACS® Tissue Storage Solution	Miltenyi Biotec B.V. & Co. KG, Bergisch Gladbach, Germany
MACSQuant® Tyto® Running Buffer	Miltenyi Biotec B.V. & Co. KG, Bergisch Gladbach, Germany
Ovarian TumorMACS™ Medium	Miltenyi Biotec B.V. & Co. KG, Bergisch Gladbach, Germany
Pancoll, human	PAN-Biotech GmbH, Aidenbach, Germany
Pancreas TumorMACS™ Medium	Miltenyi Biotec B.V. & Co. KG, Bergisch Gladbach, Germany
PBS pH 7.4	Gibco Thermo Fisher Scientific, Waltham, MA, USA
ROTI® Histokitt II	Carl Roth GmbH + Co. KG, Karlsruhe, Germany
RPMI 1640 w/o L-Glutamine	Biowest, Nuaillé, France
Sterile Water	Miltenyi Biotec B.V. & Co. KG, Bergisch Gladbach, Germany
TexMACS™ GMP Medium, 1L	Miltenyi Biotec B.V. & Co. KG, Bergisch Gladbach, Germany
Tissue Freezing Medium	Leica Biosystems Nussloch GmbH, Nussloch, Germany
Trypsin-EDTA Solution	Sigma-Aldrich Chemie GmbH, Munich, Germany
Wigert´s Iron Hematoxylin Solution	Sigma-Aldrich Chemie GmbH, Munich, Germany
Xylol	Sigma-Aldrich Chemie GmbH, Munich, Germany

2.1.6 Cell culture media and buffers

Table 7. Prepared cell culture media and buffers

Medium/Buffer	Composition
Cell line freezing medium	90% FBS (heat inactivated) 10% DMSO
Freezing medium	40% TexMACS GMP medium 50% AB-serum 10% DMSO
Ovarian TumorMACS medium	Ovarian TumorMACS medium + 1% Anti-Anti
Pancreas TumorMACS medium	Pancreas TumorMACS medium + 1% Anti-Anti
REP medium	TexMACS GMP medium + 5% AB-serum (heat inactivated) + 1% Anti-Anti + 3000 IU/mL rh-IL-2
Tumor culture medium	RPMI 1640 medium + 10% FBS (heat inactivated) + 1% Anti-Anti + 2 mM L-glutamine
MACS buffer	CliniMACS PBS/EDTA buffer + 0.5% HSA

2.1.7 Antibodies

Table 8. Tumor panel (flow cytometry)

Specificity	Fluorochrome	Dilution	Clone	Isotype	Cat #	Provider
CD326 (EpCAM)	VioBlue	1:50	REA764	rh-IgG1	130-111-004	Miltenyi Biotec
CD235a (GlyA)	VioGreen	1:50	REA175	rh-IgG1	130-120-477	Miltenyi Biotec
CD90	FITC	1:50	REA897	rh-IgG1	130-114-859	Miltenyi Biotec
CD31	FITC	1:50	REA730	rh-IgG1	130-110-668	Miltenyi Biotec
CD163	PE	1:50	REA812	rh-IgG1	130-112-128	Miltenyi Biotec
CD14	PE	1:50	REA599	rh-IgG1	130-110-519	Miltenyi Biotec
CD45	PE-Vio770	1:50	REA747	rh-IgG1	130-110-634	Miltenyi Biotec
CD3	APC	1:50	REA613	rh-IgG1	130-113-135	Miltenyi Biotec
CD19	APC-Vio770	1:50	REA675	rh-IgG1	130-113-643	Miltenyi Biotec
CD138	APC-Vio770	1:50	44F9	m-IgG1κ	130-119-837	Miltenyi Biotec

Table 9. Immunophenotyping panel (flow cytometry)

Specificity	Fluorochrome	Dilution	Clone	Isotype	Cat #	Provider
CD45	VioBlue	1:50	REA747	rh-IgG1	130-110-637	Miltenyi Biotec
CD4	VioGreen	1:50	REA623	rh-IgG1	130-113-230	Miltenyi Biotec
CD3	FITC	1:50	REA613	rh-IgG1	130-113-138	Miltenyi Biotec
CD56	PE	1:50	REA196	rh-IgG1	130-113-312	Miltenyi Biotec
CD16	PE	1:50	REA423	rh-IgG1	130-113-393	Miltenyi Biotec
CD138	PE-Vio770	1:50	44F9	m-IgG1κ	130-119-842	Miltenyi Biotec
CD20	PE-Vio770	1:50	REA780	rh-IgG1	130-111-340	Miltenyi Biotec
CD14	APC	1:50	REA599	rh-IgG1	130-110-520	Miltenyi Biotec
CD8	APC-Vio770	1:50	REA734	rh-IgG1	130-110-681	Miltenyi Biotec

Table 10. T cell phenotyping panel, extracellular (flow cytometry)

Specificity	Fluoro-chrome	Dilution	Clone	Isotype	Cat #	Provider	MQ10 Panel	MQ16 Panel
CD278 (ICOS)	VioBlue	1:10	REA192	rh-IgG1	130-100-737	Miltenyi Biotec		A
CD5	VioBlue	1:50	REA782	rh-IgG1	130-110-995	Miltenyi Biotec		C, E
CD64	VioBlue	1:50	REA978	rh-IgG1	130-116-202	Miltenyi Biotec		D
CD69	VioBlue	1:50	REA824	rh-IgG1	130-112-610	Miltenyi Biotec		B
CD8	VioBlue	1:50	REA734	rh-IgG1	130-110-683	Miltenyi Biotec	A-I	
CD223 (LAG3)	BV650	1:20	11C3C65	m-IgG1κ	369316	BioLegend		A
CD25	BV650	1:20	BC96	m-IgG1κ	302634	BioLegend		D
CD28	BV650	1:20	CD28.2	m-IgG1κ	302946	BioLegend		C
CD38	BV650	1:20	HB-7	m-IgG1κ	356620	BioLegend		B, E
CD103	FITC	1:50	Ber-ACT8	m-IgG1κ	130-128-222	Miltenyi Biotec	A	
CD11a	FITC	1:50	REA378	rh-IgG1	130-124-886	Miltenyi Biotec	I	
CD154	FITC	1:50	REA238	rh-IgG1	130-113-612	Miltenyi Biotec	G	
CD161	FITC	1:50	REA631	rh-IgG1	130-113-598	Miltenyi Biotec	F	
CD278 (ICOS)	FITC	1:10	REA192	rh-IgG1	130-100-732	Miltenyi Biotec	B	

CD28	vFITC	1:50	REA612	rh-IgG1	130-118-792	Miltenyi Biotec	E	
CD64	FITC	1:50	REA978	rh-IgG1	130-116-195	Miltenyi Biotec	H	
CD69	FITC	1:50	REA824	rh-IgG1	130-112-612	Miltenyi Biotec	C	
CD94	FITC	1:50	REA113	rh-IgG1	130-123-678	Miltenyi Biotec	D	
CD3	PerCP-Vio770	1:50	REA613	rh-IgG1	130-113-141	Miltenyi Biotec	A-I	A-E
CD137	PE	1:50	REA756	rh-IgG1	130-110-763	Miltenyi Biotec	B	A
CD152 (CTLA4)	PE	1:50	REA1003	rh-IgG1	130-116-810	Miltenyi Biotec	E	C
CD160	PE	1:20	BY55	m-IgMκ	341206	BioLegend	D	B
CD223 (LAG3)	PE	1:50	REA351	rh-IgG1	130-120-470	Miltenyi Biotec	A	
CD304	PE	1:50	REA774	rh-IgG1	130-111-893	Miltenyi Biotec	F	
CD38	PE	1:50	REA572	rh-IgG1	130-113-431	Miltenyi Biotec	C	
CD7	PE	1:50	REA1244	rh-IgG1	130-124-931	Miltenyi Biotec	G	
CD82	PE	1:10	REA221	rh-IgG1	130-101-306	Miltenyi Biotec	I	E
VISTA	PE	1:20	B7H5DS8	rh-IgG1	12-1088-41	eBioscience	H	D
CD101	PE-Vio615	1:50	REA954	rh-IgG1	130-115-835	Miltenyi Biotec		B
CD103	PE-Vio615	1:50	REA803	rh-IgG1	130-111-837	Miltenyi Biotec		A
CD154	PE-Vio615	1:50	REA238	rh-IgG1	130-123-039	Miltenyi Biotec		D
CD278 (ICOS)	PE-Vio615	1:10	REA192	rh-IgG1	130-107-458	Miltenyi Biotec		E
TIGIT	PE-Vio615	1:50	REA1004	rh-IgG1	130-116-816	Miltenyi Biotec		C
CD279 (PD1)	PE-Vio770	1:50	PD1.3.1.3	m-IgG2bκ	130-117-698	Miltenyi Biotec	A-I	A-E
CD101	APC	1:50	REA954	rh-IgG1	130-115-831	Miltenyi Biotec	C	
CD150	APC	1:10	REA151	rh-IgG1	130-099-674	Miltenyi Biotec	I	E
CD226	APC	1:50	REA1040	rh-IgG1	130-117-490	Miltenyi Biotec	H	D

CD244 (2-B4)	APC	1:10	REA112	rh-IgG1	130-099-072	Miltenyi Biotec	B	
CD25	APC	1:50	REA945	rh-IgG1	130-115-535	Miltenyi Biotec	G	
CD270	APC	1:10	REA247	rh-IgG1	130-101-609	Miltenyi Biotec	D	B
CD366 (TIM3)	APC	1:50	REA635	rh-IgG1	130-119-781	Miltenyi Biotec	A	A
CD5	APC	1:50	REA782	rh-IgG1	130-110-991	Miltenyi Biotec	F	
CD7	APC	1:50	REA1244	rh-IgG1	130-124-932	Miltenyi Biotec		C
TIGIT	APC	1:50	REA1004	rh-IgG1	130-116-815	Miltenyi Biotec	E	
CD39	APC-Vio770	1:50	REA739	rh-IgG1	130-110-653	Miltenyi Biotec	A-I	A-E
CD8	AF700	1:20	SK1	m-IgG1κ	344724	BioLegend		A-E

Table 11. Intracellular cytokine staining (ICS) panel (flow cytometry)

Specificity	Fluorochrome	Dilution	Clone	Isotype	Cat #	Provider
CD107a**	VioBlue	1:50	REA792	rh-IgG1	130-111-620	Miltenyi Biotec
CD8	FITC	1:50	REA734	rh-IgG1	130-110-677	Miltenyi Biotec
CD3	PerCP-Vio770	1:50	REA613	rh-IgG1	130-113-141	Miltenyi Biotec
CD137*	PE	1:50	REA756	rh-IgG1	130-110-763	Miltenyi Biotec
TNFα*	PE-Vio770	1:50	cA2	h-IgG1	130-120-492	Miltenyi Biotec
CD154*	APC	1:50	REA238	rh-IgG1	130-113-610	Miltenyi Biotec
IFNɣ*	APC-Vio770	1:50	REA600	rh-IgG1	130-113-496	Miltenyi Biotec

*Intracellular antibodies; ** Added 1h after cell stimulation

Table 12. Basic T cell panel (Tc) and FACS sort panel (F) (flow cytometry)

Specificity	Fluorochrome	Dilution	Clone	Isotype	Cat #	Provider	Panel
CD8	VioBlue	1:50	REA734	rh-IgG1	130-110-683	Miltenyi Biotec	Tc, F
CD39	FITC	1:50	MZ18-23C8	m-IgG1κ	130-125-094	Miltenyi Biotec	F
CD279	PE	1:50	PD1.3.1.3	m-IgG2bκ	130-117-384	Miltenyi Biotec	F
CD366	APC	1:50	REA635	rh-IgG1	130-119-781	Miltenyi Biotec	F
CD3	FITC	1:50	BW264/56	rh-IgG1	130-113-128	Miltenyi Biotec	Tc
CD4	VioGreen	1:50	REA623	rh-IgG1	130-113-230	Miltenyi Biotec	Tc
CD56	APC	1:50	REA196	rh-IgG1	130-113-310	Miltenyi Biotec	Tc

Table 13. General MICS panel (MACSima)

Specificity	Fluorochrome	Dilution	Clone	Isotype	Cat #	Provider
BAFFR	PE	1:50	REA1115	rh-IgG1	130-119-297	Miltenyi Biotec
CD10	PE	1:50	REA877	rh-IgG1	130-114-502	Miltenyi Biotec
CD101	PE	1:50	REA954	rh-IgG1	130-115-830	Miltenyi Biotec
CD103	PE	1:50	REA803	rh-IgG1	130-111-832	Miltenyi Biotec
CD105	PE	1:50	43A4E1	m-IgG1κ	130-117-696	Miltenyi Biotec
CD11a	PE	1:50	REA378	rh-IgG1	130-128-076	Miltenyi Biotec
CD137	PE	1:50	REA756	rh-IgG1	130-110-763	Miltenyi Biotec
CD138	PE	1:50	REA929	rh-IgG1	130-127-978	Miltenyi Biotec
CD14	PE	1:50	REA599	rh-IgG1	130-110-519	Miltenyi Biotec
CD141	PE	1:50	REA674	rh-IgG1	130-113-662	Miltenyi Biotec
CD151	PE	1:10	REA265	rh-IgG1	130-103-662	Miltenyi Biotec
CD152 (CTLA4)	PE	1:50	REA1003	rh-IgG1	130-116-810	Miltenyi Biotec
CD161	PE	1:50	REA631	rh-IgG1	130-113-596	Miltenyi Biotec
CD162	PE	1:50	REA319	rh-IgG1	130-128-075	Miltenyi Biotec
CD163	PE	1:50	REA812	rh-IgG1	130-112-128	Miltenyi Biotec
CD183	PE	1:50	REA232	rh-IgG1	130-120-452	Miltenyi Biotec
CD19	PE	1:50	REA675	rh-IgG1	130-113-646	Miltenyi Biotec
CD1c	PE	1:50	REA694	rh-IgG1	130-110-536	Miltenyi Biotec
CD20	PE	1:50	REA780	rh-IgG1	130-111-338	Miltenyi Biotec
CD21	PE	1:10	HB5	m-IgG2aκ	130-101-716	Miltenyi Biotec
CD22	PE	1:50	REA340	rh-IgG1	130-123-245	Miltenyi Biotec
CD23	PE	1:50	REA1222	rh-IgG1	130-124-105	Miltenyi Biotec
CD24	PE	1:50	REA832	rh-IgG1	130-112-656	Miltenyi Biotec
CD244 (2-B4)	PE	1:10	REA112	rh-IgG1	130-099-051	Miltenyi Biotec
CD25	PE	1:50	REA945	rh-IgG1	130-115-534	Miltenyi Biotec
CD26	PE	1:50	FR10-11G9	m-IgG2aκ	130-126-362	Miltenyi Biotec
CD27	PE	1:50	M-T2T1	m-IgG1κ	130-113-630	Miltenyi Biotec
CD274 (PDL1)	PE	1:50	29E.2A3	m-IgG2bκ	329706	BioLegend
CD278 (ICOS)	PE	1:50	REA192	rh-IgG1	130-120-069	Miltenyi Biotec
CD279 (PD1)	PE	1:50	PD1.3.1.3	m-IgG2bκ	130-117-384	Miltenyi Biotec
CD28	PE	1:50	REA612	rh-IgG1	130-123-782	Miltenyi Biotec
CD3	PE	1:50	BW264/56	m-IgG2aκ	130-113-129	Miltenyi Biotec

CD304	PE	1:50	REA774	rh-IgG1	130-111-893	Miltenyi Biotec
CD31	PE	1:50	REA730	rh-IgG1	130-110-669	Miltenyi Biotec
CD326 (EpCAM)	FITC	1:50	REA764	rh-IgG1	130-110-998	Miltenyi Biotec
CD34	PE	1:50	REA1164	rh-IgG1	130-120-515	Miltenyi Biotec
CD35	PE	1:50	REA1133	rh-IgG1	130-119-510	Miltenyi Biotec
CD366 (TIM3)	PE	1:50	REA635	rh-IgG1	130-119-785	Miltenyi Biotec
CD38	PE	1:50	REA572	rh-IgG1	130-113-431	Miltenyi Biotec
CD39	PE	1:50	REA739	rh-IgG1	130-110-650	Miltenyi Biotec
CD4	PE	1:50	REA623	rh-IgG1	130-113-225	Miltenyi Biotec
CD40	PE	1:50	REA733	rh-IgG1	130-110-946	Miltenyi Biotec
CD45	PE	1:50	REA747	rh-IgG1	130-110-632	Miltenyi Biotec
CD45RA	PE	1:50	T6D11	m-IgG2b	130-113-356	Miltenyi Biotec
CD45RO	PE	1:50	REA611	rh-IgG1	130-113-559	Miltenyi Biotec
CD49a	PE	1:50	REA1106	rh-IgG1	130-119-306	Miltenyi Biotec
CD5	PE	1:50	UCHT2	m-IgG1κ	130-119-855	Miltenyi Biotec
CD50	PE	1:50	REA905	rh-IgG1	130-115-203	Miltenyi Biotec
CD52	PE	1:50	REA164	rh-IgG1	130-123-743	Miltenyi Biotec
CD53	PE	1:10	REA259	rh-IgG1	130-101-782	Miltenyi Biotec
CD54	PE	1:50	REA266	rh-IgG1	130-120-711	Miltenyi Biotec
CD56	PE	1:50	REA196	rh-IgG1	130-113-312	Miltenyi Biotec
CD57	PE	1:50	REA769	rh-IgG1	130-111-810	Miltenyi Biotec
CD58	PE	1:10	TS2/9	m-IgG1κ	130-101-193	Miltenyi Biotec
CD64	PE	1:50	REA978	rh-IgG1	130-116-196	Miltenyi Biotec
CD68	PE	1:50	REA886	rh-IgG1	130-114-460	Miltenyi Biotec
CD69	PE	1:50	REA824	rh-IgG1	130-112-613	Miltenyi Biotec
CD7	PE	1:50	CD7-6B7	m-IgG2aκ	130-123-247	Miltenyi Biotec
CD79a	PE	1:50	REA1142	rh-IgG1	130-119-722	Miltenyi Biotec
CD8	PE	1:50	BW135/80	m-IgG2aκ	130-113-158	Miltenyi Biotec
CD83	PE	1:50	REA714	rh-IgG1	130-110-503	Miltenyi Biotec
CD86	PE	1:50	REA968	rh-IgG1	130-116-160	Miltenyi Biotec
CD9	PE	1:50	SN4 C3-3A2	m-IgG1κ	130-123-761	Miltenyi Biotec
CD90	PE	1:60	DG3	m-IgG1κ	130-117-388	Miltenyi Biotec
HLA-ABC	PE	1:50	REA230	rh-IgG1	130-120-055	Miltenyi Biotec
HLA-DQ	PE	1:50	REA303	rh-IgG1	130-123-765	Miltenyi Biotec
HLA-DR	PE	1:60	REA805	rh-IgG1	130-111-789	Miltenyi Biotec
IgD	PE	1:50	REA740	rh-IgG1	130-110-643	Miltenyi Biotec

IgM	PE	1:10	PJ2-22H3	m-IgG1	130-093-077	Miltenyi Biotec
Ki67	PE	1:50	REA183	rh-IgG1	130-120-417	Miltenyi Biotec
MECA-79	AF488	1:50	MECA-79	rat-IgM	53-6036-82	eBioscience
TSPAN8	PE	1:50	REA443	rh-IgG1	130-117-391	Miltenyi Biotec
Vimentin	PE	1:50	REA409	rh-IgG1	130-123-774	Miltenyi Biotec

Table 14. Dyes and other reagents for flow cytometry/MACSima

Reagent	Dilution	Cat #	Provider
7-AAD Staining Solution	1:10	130-111-568	Miltenyi Biotec
FcR Blocking Reagent, human	1:5	130-059-901	Miltenyi Biotec
Hoechst 33258 Dye	1:100	94403	Sigma-Aldrich
Propidium Iodide (PI)	1:100	130-093-233	Miltenyi Biotec
Tandem Signal Enhancer, human (hTSE)	1:10	130-099-888	Miltenyi Biotec
Viobility™ Fixable Dye 405/520	1:100	130-109-814	Miltenyi Biotec

Antibody Isotypes: recombinant human (**rh-**); mouse (**m-**), rabbit (**rbt-**), rat (**rat-**).

Antibody Providers: **Miltenyi Biotec** B.V. & Co. KG, Bergisch Gladbach, Germany; **BioLegend**, San Diego, CA, USA; **eBioscience,** Waltham, MA, USA; **Cell Signaling Technology,** Danvers, MA, USA; **Sigma-Aldrich** Chemie GmbH, Munich, Germany.

2.1.8 Software

Table 15. Software

Software	Developer
10x Genomics Cell Ranger 4.0.0	10x Genomics, Pleasanton, CA, USA
BioRender	BioRender.com
CellProfiler 4.2.1	McQuin et al. 2018[139]
FigureJ 1.36	Mutterer et al. 2013[140]
Fiji/ImageJ 2.3.0	Schindelin et al. 2012[141]
FlowJo™ 10.6.2	FlowJo LLC, Ashland, OR, USA
FlowLogic™ 7.0	Inivai, Mentone VIC, Australia
ggplot2 3.3.5	https://ggplot2.tidyverse.org[142]
GraphPad Prism 9.2.0	GraphPad Software Inc., La Jolla, CA, USA
InspectorCell 0.2	https://gitlab.com/InspectorCell[143]
MACS iQ View Analysis 1.2.0	Miltenyi Biotec B.V. & Co. KG, Bergisch Gladbach, Germany

Microsoft Office 365	Microsoft, Redmond, WA, USA
Orange 3.30.2	Demšar et al. 2013[144]
ProjecTILs 3.3.0	Andreatta et al. 2021[145]
R 4.3.1	R Core Team (2021). R: A language and environment for statistical computing. R Foundation for Statistical Computing, Vienna, Austria https://www.r-project.org
Rstudio 2023.09.1	RStudio Team (2021). RStudio: Integrated Development Environment for R. RStudio, PBC, Boston, MA, USA https://www.rstudio.com
scDblFinder 1.15.4	Germain et al, 2022[146]
scRepertoire 1.11.0	Borcherding et al. 2020[147]
Seurat 5.0.1	Hao et al. 2021[148]
UCell 2.6.2	Andreatta & Carmona, 2021[149]

2.2 Methods

2.2.1 Sample preparation

Tumor tissue dissociation

I dissociated tumor samples into single cell suspensions by combining mechanical force and enzymatic digestion with the human Tumor Dissociation Kit (Miltenyi) following the manufacturer's protocol. A reduction of enzyme R to 20% of the recommended concentration or total exclusion of the enzyme was performed when indicated in order to avoid the degradation of sensitive epitopes to this enzyme. A gentleMACS Octo Dissociator with Heaters (Miltenyi) with the program 37C_h_TDK_2 or 3 (depending on the softness of the sample) was used for the dissociation. Afterwards, I resuspended the tumor digest in approximately 5-10 mL RPMI 1640 medium (Biowest) per gram of tissue and performed a cell count and composition analysis by flow cytometry (see 2.2.4)

Isolation of peripheral blood mononuclear cells

I isolated peripheral blood mononuclear cells (PBMCs) from whole blood by density gradient centrifugation. Briefly, blood was diluted 1:1 with PBS (Miltenyi) and up to 35 mL were carefully layered onto 15 mL Pancoll solution (Pan-Biotech) in a 50 mL Falcon tube without mixing the phases. After a centrifugation step (800xg, 20 min, RT, acceleration/deceleration: 1/1), the layer containing mononuclear cells and platelets was carefully aspired with a 5 mL pipette and transferred into a 50 mL Falcon for a wash with PBS (300xg, 10 min, RT, acceleration/deceleration: 9/9). The supernatant was discarded and PBMCs were resuspended in an appropriate volume of TexMACS GMP medium (Miltenyi) for further experiments. I counted cells in a Sysmex XP-300 Hematology Analyzer (Sysmex) and analyzed the cell composition by flow cytometry (see 2.2.4)

Dead Cell Removal

I performed a clean-up of tumor digests with poor viability prior to further processing with the Dead Cell Removal Kit (Miltenyi), which depletes dead cells by magnetic labeling, following the manufacturer's instructions. LS columns were always preferred.

Cryopreservation and thawing of cells

I cryopreserved cells ($1x10^6$-$1x10^8$ cells/vial, 1 mL/vial) by resuspending the cell pellet after centrifugation (300xg, 10 min, RT) in freezing medium (Table 7). The cryovials were transferred into a

CoolCell LX freezer container (Biocision) at -80 °C for at least 24 h and transferred into the liquid nitrogen tank for long-term preservation. I froze down established tumor cell lines in tumor cell line freezing medium (Table 7).

I thawed cells by warming up the vial on hands till a small ice clump was present. The cell suspension was slowly transferred into a suitable Falcon tube containing 1 mL of human AB-serum (Sigma) per vial and filled in with TexMACS GMP medium + 10% human AB-serum. After gentle centrifugation (200xg, 10 min, RT, acceleration-break: 5-5), the pellet was resuspended in a suitable medium depending on downstream applications.

2.2.2 Cell isolations

Enrichment of leukocytes from tumor digests

In order to isolate leukocytes from tumor digests, I performed a positive selection of $CD45^+$ cells following the manufacturer's instructions in the REAlease CD45 (TIL) MicroBead Kit (Miltenyi). MACS buffer (Table 7) was freshly prepared and kept sterile. LS columns were always preferred. In addition, pre-separation filters (30 µm) (Miltenyi) were used before applying the cell suspension into the column to avoid clogging. After the separation, the MicroBeads were released according to the protocol to allow subsequent magnetic isolations, if applicable.

Enrichment of T cells from tumor digests

I magnetically enriched tumor-infiltrating $CD4^+$/$CD8^+$ or only $CD8^+$ T cells from tumor digests by using a positive selection following the REAlease CD4/8 (TIL) MicroBead Kit and the REAlease CD8 (TIL) MicroBead Kit (both from Miltenyi), respectively. The manufacture's protocol was followed, but the amount of biotinylated antibody was double increased to ensure high yields of target cells. MACS buffer was freshly prepared and kept sterile. LS columns were always preferred. In addition, pre-separation filters (30 µm) were used before applying the cell suspension into the column to avoid clogging. After the separation, the MicroBeads were released according to the protocol to allow subsequent magnetic isolations, if applicable.

Fluorescence-activated cell sorting

Subsets of T cells were sorted by fluorescence-activated cell sorting (FACS) in the MACSQuant Tyto Cell Sorter (Miltenyi), which allows sterile, serial sorts in a closed system.

I stained T cells (1-5x10^6 cells) with the FACS sort panel (Table 12) in MACSQuant Tyto running buffer (Miltenyi) for 10 min in the dark at 4 °C. Cells were diluted to 5-7 mL in MACSQuant Tyto running buffer and loaded into a MACSQuant Tyto cartridge (Miltenyi).

The instrument was set up with the assistance of Dr. Polina Zjablovskaja and Alina Kurowski from the Tyto team at Miltenyi, following the manufacturer´s recommendations. Briefly, the V1 violet channel (CD8-VioBlue) was used for triggering and the B1 blue channel (CD39-FITC) for determining cell speed. The sort gate was defined as $CD8^+$ $CD39^+$ cells. The valve opening time was 50 µs. No compensation was required.

After the isolation, I harvested the sort and non-sort fractions, which were used for *in vitro* expansions (see 2.2.3) and —if enough cells— single-cell mRNA sequencing (see 2.2.5).

2.2.3 Cell culture and functional assays

Rapid expansion of T cells

I expanded *in vitro* sorted T cells following a Rapid Expansion Protocol (REP) as previously described[150]. Briefly, a cell count was carried out using Erythrosin B (Sigma-Aldrich) as live/dead exclusion dye and a C-Chip Neubauer Improved hemocytometer (NanoEntek), following manufacturer´s instructions. TILs were adjusted to 1x10^4 cells/mL in REP medium (Table 7). Fresh or frozen PBMCs from 2 or 3 healthy volunteers were pooled in TexMACS GMP medium and irradiated at 40 Gy in a RS-2000 irradiator (RadSource). After determining the cell count, PBMCs were centrifuged (300xg, 10 min, RT) and the pellet was resuspended in REP medium at a cell concentration of 4x10^6 cells/mL. OKT3 (Miltenyi) was added at 60 ng/mL (final concentration in the well of 30 ng/mL) in the feeder cell suspension. Finally, 1 mL of TILs (1x10^4) and 1 mL of feeder cells (4x10^6) were added into a well of a 24-well plate (1:400 TIL to feeder ratio) and incubated at 37 °C in a humidified atmosphere (5% CO_2).

After 5 days, I performed a ¾ medium exchange. Every 2-3 days, ½ medium was exchanged, and cells were split to maintain cell densities at around 1x10^6 cells/mL. After 14 days of the initiation of the REP, I harvested cells and determined the viability, cell count, and percentages of $CD3^+$, $CD4^+$, and $CD8^+$ by flow cytometry (see 2.2.4).

Cultivation of tumor cells

To establish primary tumor cell cultures, I used tumor digests and other tumor sources, such as the MACS Tissue Storage Solution (Miltenyi) in which samples are transported as well as the pieces which did not pass the strainers during tumor dissociation. Approximately 2x10^5 total cells/cm^2 were seeded

in 48-well or 24-well plates (1 mL/well) in tumor medium and cultured at 37 °C in a humidified atmosphere (5% CO_2). For ovarian and pancreatic tumors, Ovarian TumorMACS medium and Pancreas TumorMACS medium (both from Miltenyi) were used, respectively. In order to generate cell lines, I followed the guideline of the manufacturer ("Guide for the initiation of primary tumor cell culture", Miltenyi). Briefly, cultures were observed every 2-3 days and ½ medium was exchanged if turned yellow. When 70-80% confluent, adherent cultures were split by removing the medium, washing once with PBS and briefly incubating cells at 37 °C in trypsin-EDTA or accutase (both Sigma-Aldrich) until cells were detached. The reaction was stopped by adding the corresponding tumor culture medium and cells were collected, centrifuged (300xg, 5 min, RT) and then subcultured at 1:2 split ratio. In the case of fibroblast outgrowth, cells were treated with accutase for a short period of time (1-2 min) to induce the detachment of fibroblasts but not of the tumor cells, washing them away from the culture.

For the established OC12 tumor cell line, cells were cultivated in Ovarian TumorMACS medium in 6-well plates or T25/T75 culture flasks at 37 °C in in a humidified atmosphere (5% CO_2). When 70-80% confluent, I split cultures as described above.

Reactivity assay

I co-cultured TILs after REP expansion with autologous tumor cells in order to determine their tumor reactivity by measuring T cell activation. For this, TILs were washed twice (300xg, 10 min, RT) with TexMACS GMP medium prior to the assay in order to remove remaining IL-2. Cells were counted by flow cytometry (see 2.2.4) and adjusted to $2x10^6$ cells/mL in TexMACS GMP medium + 5% AB-serum + 1% P/S.

As no tumor cell lines were established from patients at the time of the reactivity assays, I used 14 days-cultured or thawed tumor digests ("tumor target") for the co-cultures. When the percentage of $CD45^+$ cells in the tumor target sample was >20%, I depleted leukocytes with the REAlease CD45 (TIL) MicroBead Kit (see 2.2.2). The tumor target was adjusted to $2x10^6$ cells/mL in the corresponding tumor medium. The co-culture was set up in 96-well U-bottom plates by adding 50 µL of TILs ($1x10^5$) and 50 µL of tumor target ($1x10^5$). For each well, 30 µL of TexMACS GMP medium + 5% AB-serum + 1% P/S with CD107a-VioBlue antibody was added.

As negative controls, a co-culture with a tumor cell line from the same cancer type but different patient ("irrelevant tumor"), a condition with only tumor targets ("Tumor only"), and a condition with only TILs ("TIL only") were set up.

As positive control, 50 µL of 1X Cell Stimulation Cocktail (eBioscience) in TexMACS GMP medium + 5% AB-serum + 1% P/S were added to 100 µL ($2x10^5$) of TILs per well.

All conditions were set up as duplicates or, if enough cells, triplicates. After 1 h incubation at 37 °C in a humidified atmosphere (5% CO_2), 20 µL of 1X GolgiPlug + 1X GolgiStop (both BD Bioscience) in TexMACS GMP medium + 5% AB-serum + 1% P/S per well was added to block the secretion of cytokines, allowing their accumulation and detection in intracellular compartments. After 12 h of incubation at 37 °C in a humidified atmosphere (5% CO_2), the plate was transferred to 4 °C and the intracellular cytokine staining was performed (see 2.2.4)

2.2.4 Flow cytometry

Count and composition of cell samples by flow cytometry

I carried out cell counts and composition analysis of tumor samples by flow cytometry using two different panels: the tumor panel (Table 8) for defining different cell types in the tumor microenvironment, such as leukocytes, tumor cells and stroma cells; and the immunophenotyping panel (Table 9) for diverse subtypes of immune cells. For cell counts of PBMCs by flow cytometry, only the immunophenotyping panel was used. T cells, such as REP expanded, were stained with the T cell panel (Table 12) to identify $CD4^+$/$CD8^+$ T cell ratios after expansion.

For the staining, 50 µL of the sample were mixed with 50 µL of MACS buffer with the corresponding antibodies, human Tandem Signal Enhancer (hTSE) (Miltenyi) and the dead/live exclusion dye 7-AAD (Miltenyi) in a 1.5 mL Eppendorf tube. Cells were incubated for 10 min in the dark at 4 °C. For the tumor panel sample, a wash with 1 mL MACS buffer (300xg, 5 min, 4 °C) was performed. The supernatant was carefully discarded, and the pellet resuspended in 300 µL of MACS buffer for acquisition in the MACSQuant Analyzer 10 (Miltenyi). For the immunophenotyping panel, no wash was performed, and the sample was diluted with MACS buffer to 500 µL for acquisition.

For cell counting, 100-200 µL of the sample were acquired at medium speed in the MACSQuant Analyzer 10. This instrument can calculate the cell concentration (cells/mL), which then was multiplied by the corresponding dilution factor to obtain the final concentration.

In some cases, only viable cell counts were needed. For this, an aliquot of the sample was taken and propidium iodide (PI) (Miltenyi) was added before the acquisition.

T cell phenotyping

For extracellular stainings of different T cell markers in the MACSQuant Analyzer 10 (Panels A-I) and/or MACSQuant Analyzer 16 (Panels A-E) (Table 10), I transferred 1-10x10^5 cells/test into a 1.5 mL Eppendorf tube and washed with 1 mL PBS (300xg, 5 min, RT). To stain dead cells, the pellet was

resuspended in 100 µL (up to $1x10^7$ cells) of PBS-diluted Viobility Fixable Dye 405/520 (Miltenyi) and incubated for 15 min in the dark at RT. Cells were washed with 1 mL PBS (300xg, 5 min, 4 °C) and the supernatant was discarded. Cells were resuspended in 50 µL of MACS buffer per test and transferred into a 96-well U-bottom plate. Cells were incubated for 10 min in the dark at 4 °C with 50 µL of MACS buffer with the corresponding antibodies and hTSE. After a wash (300xg, 5 min, 4 °C) with 100 µL of MACS buffer, I resuspended pellets in 200 µL of MACS buffer for acquisition.

For extracellular stainings, I used a "FMO" control sample in which only CD8, CD3, and CD39 were stained in order to assist gating during data analysis.

Intracellular cytokine staining (ICS)

Cells in a 96-well U-bottom plate, which I previously activated overnight (see 2.2.3), were spun down (300xg, 5 min, 4 °C) and washed with 200 µL PBS (300xg, 5 min, 4 °C). Afterwards, cells were resuspended in PBS-diluted Viobility Fixable Dye 405/520 for live/dead exclusion and incubated for 15 min in the dark at RT. Cells were washed with 100 µL of PBS (300xg, 5 min, 4 °C). Extracellular markers were stained by adding 100 µL of MACS buffer with the corresponding antibodies (Table 11) except for CD107a-Vioblue, which I already added during the activation phase. After an incubation of 10 min in the dark at 4 °C, cells were washed with 100 µL MACS buffer (300xg, 5 min, 4 °C). For the intracellular staining, I used the Inside Fix Kit (Miltenyi). For cell fixation, 100 µL of 1:2 diluted Inside Fix in MACS buffer was added to the wells and the plate was incubated for 20 min in the dark at RT. Cells were centrifuged (400xg, 5 min, 4 °C) and supernatant was discarded. Two sequential washes with 200 µL MACS buffer and 200 µL Inside Perm solution for permeabilization were performed (400xg, 5 min, 4 °C), respectively. Afterwards, cells were stained with 100 µL of Inside Perm solution containing the intracellular antibodies (Table 11) and hTSE, and incubated for 20 min in the dark at 4 °C. I performed a final wash with 100 µL of Inside Perm solution (400xg, 5 min, 4 °C) and resuspended cells in 200 µL MACS buffer for acquisition in the MACSQuant X (Miltenyi).

Flow cytometry and statistical analysis

I analyzed flow cytometry data with the software FlowLogic 7.0 (Inivai) and FlowJo 10.6.2 (FlowJo LLC). I generated plots and performed statistical analysis, when specified in the plot legends, with GraphPad Prism 9.2.0 (GraphPad).

2.2.5 Single cell mRNA sequencing (10x Genomics)

Sample preparation

I prepared cells under sterile conditions to minimize contaminations and on ice. Cells were transferred into a 1.5 mL Eppendorf and washed twice (300xg, 5 min, RT) with 1 mL of freshly prepared PBS + 0.04% MACS BSA stock solution (Miltenyi) using wide-bore pipette tips to avoid cell damage. I determined cell counts and viability manually by Erythrosin B staining in a Neubauer Improved hemocytometer. I adjusted cells to 1000 total cells/µL in PBS + 0.04% MACS BSA stock solution. If cell clumps were present, a cell strainer (70 µm) was used. Viability should be higher than 85% for optimal results.

10x Genomics workflow and Illumina sequencing

The following steps were performed by Dr. Ruth Kläver, Nadine Preiß, Nojan Jelveh, Katharina Lamfried, and Adriana Gerick from the in-house Next Generation Sequencing Facility at Miltenyi Biotec. The Chromium (Next GEM) Single Cell V(D)J Reagent Kits (10x Genomics) were used following the manufacturer´s instructions (user guide CG000086 Rev H and CG000208 Rev E).

In short, Gel Bead-in Emulsions (GEMs) were generated and a barcoded full-length cDNA from poly-adenylated mRNA was produced. After GEMs were broken, pooled, and cleaned up, cDNA was amplified. For TCR libraries, the V(D)J cDNA segments were enriched by PCR with primers specific to the TCR constant regions. No targeted enrichment was performed for 5' Gene Expression (GEX) analysis. cDNA was enzymatically fragmented, and size excluded prior to library construction. The libraries were sequenced with a NextSeq 500/550 Mid/High Output kit (Illumina) on a NextSeq550 sequencer (Illumina). The recommended minimum sequencing depth was 5,000 pair reads/targeted cell for V(D)J and 20,000 pair reads/cells for GEX.

Sequencing data analysis

Raw sequencing data was pre-processed with the 10x Genomics Cell Ranger 4.0.0 pipeline (10x Genomics) by Dr. Stefan Tomiuk from the in-house Bioinformatic team at Miltenyi Biotec.

For TCR analysis, I loaded the “filtered_contig_annotations.csv” file onto RStudio and used the R package scRepertoire[147] for analysis. Tables from duplicate samples were merged and a sample prefix was added to each cell barcode. Multiple cells had either only a TCR α chain (TRA) or a TCR β chain (TRB) or multiple TRA and TRB. For this reason, I defined TCR clonotypes based on TRB only. During the creation of an object containing the V(D)J genes and CDR3 sequences by cell barcode, I applied the

following parameters: *removeNA = FALSE* – cells with 1 NA value in at least one of the chains are included; *removeMulti = FALSE* – cells with more than 2 chains are included; *filterMulti = TRUE* – the top 2 expressed chains are isolated in cell barcodes with multiple chains. In addition, cells with only TRA were excluded. The *cloneCall* used along the pipeline was the amino acid sequences of the CDR3 region.

For GEX analysis, I loaded the "filtered_feature_bc_matrix" folder onto RStudio and used the R package Seurat[148] for analysis. I merged matrices from duplicate samples and added a sample prefix to each cell barcode. First, I removed cells with less than 200 features and features in less than 3 cells. Cells were further filtered out during the first quality control steps based on doublet detection by the R package scDblFinder[146], percent of mitochondrial genes, number of molecules detected per cell, and number of unique genes per cell. I performed normalization and variance stabilization by SCTransform v2[151], regressing the proliferation, mitochondrial, ribosomal, and heat shock protein genes, as well as excluding TCR and BCR genes from the variable genes (list of TCR/BCR genes from Minervina et al, 2022[152]). I applied dimensionality reduction by principal component analysis (PCA), followed by a shared nearest neighbor (SNN) based clustering (dimensions = 25-30 based on Elbow plot, resolution = 0.8). Data was visualized by running a non-linear dimensional reduction, in this case uniform manifold approximation and projection (UMAP). After an initial cell type annotation based on cell lineage marker genes, I subset T cell clusters—expressing *CD3E*—and repeated the previous steps from normalization to clustering (dimensions = 25-35, resolution = 1-1.5) on the raw counts. Expression of selected genes among clusters was visualized by heatmaps, dot plots, violin plots, or UMAP plots. Additionally, I calculated gene signatures related to TIL states (gene list from Andreatta et al, 2021[145]) and tumor-reactive T cell (TRT) states (gene lists obtained from Supplementary Table 1C in Wischnewski et al, 2023[153]) with the R package UCell[149]. To aid in the annotation of the clusters, the R package ProjecTILs was used to automatically assign labels to individual cells based on the human CD4 and CD8 TIL reference atlases available in the package[145].

In order to combine datasets with paired TCR and GEX data, I merged the TCR clonotype information from the scRepertoire object with the Seurat object with the function *combineExpression* (*cloneCall* = "aa", *chain* = "TRB") from the scRepertoire package as previously described in the vignette from Dr. Nick Borcherding (scRepertoire package) and the pipeline published by Andreatta et al, 2023[154].

2.2.6 Microscopy methods

Snap freezing and cryosection of tumor tissues

I embedded tumor pieces of approximately 2-3 mm in diameter in Tissue Freezing Medium (Leica) in a Tissue-Tek™ Cryomold™ (Fisher Scientific), "snap" frozen in liquid nitrogen in the presence of 2-methylbutane (Sigma) to slow down the freezing process, and stored at -80 °C.

I sectioned tissue blocks at 8 µm using a Cryostat (Leica) and loaded into Epredia™ SuperFrost Plus™ Adhesion slides (Fisher Scientific) for hematoxylin and eosin (H&E) staining and immunofluorescence staining, and into 76 x 111 mm glass slides (Zell-Kontakt) coated with silane for the MACSima experiment. Sections were immediately fixed in -20 °C-cold acetone (Sigma) for 10 min and used for the corresponding stainings. Alternatively, a shorter fixation (3 min) was performed prior to storage at -80 °C and, after thawing, sections were re-fixed in acetone for 10 min before the staining procedure.

Hematoxylin and eosin (H&E) staining

I washed tissue slides with PBS and then immersed them in running tap water x3 for 1 min. Afterwards, sections were stained in previously filtered hematoxylin solution (Sigma) for 7 min and then transferred to warm water for 5 min. After a short immersion in 1% hydrochloric acid (HCl, Sigma) in 70% EtOH (Sigma), sections were washed with water and stained in eosin solution (Sigma) for 5 min. I dehydrated the tissues in 70% EtOH x3 for 30 s, then in 96% EtOH x3 for 30 s, and finally in 100% EtOH x3 for 30 s. Tissues were x6 immersed in xylol (Sigma) and dry for a few seconds. A couple of drops of Roti-Histokitt II (Carl Roth) were added on the slide to mount the coverslip (Fisher Scientific). Slides were kept in the dark at 4 °C till image acquisition in a SensoScope BrightROI Microscope (Miltenyi).

Immunofluorescence (IF) staining

In order to select relevant tissue samples as well as regions of interest (ROIs), I stained tissues with a FITC-conjugated antibody for tumor cells (e.g., CD326 or cytokeratin for tumor of epithelial origin) and a PE-conjugated antibody for leukocytes (e.g., CD45). Shortly, tissue slices were washed x2 with autoMACS running buffer (Miltenyi). The staining was performed with the mix of antibodies, Hoechst (Sigma) for nuclei detection, and FcR blocking reagent (Miltenyi) in autoMACS running buffer for 10 min at RT in the dark. Afterwards, tissues were washed x3-5 with autoMACS running buffer. A coverslip was placed on top of the tissue with fluorescence mounting medium (Agilent) and I acquired images in a Cytation 3 (BioTek) for pre-screening relevant samples. For selecting regions of interest, the stained tissues were kept in autoMACS running buffer and imaged in the MACSima platform.

MACSima imaging

I glued the glass plates with acetone-fixed sections into 24-well no-bottom plates (Zell-Kontakt) (one section per well). I performed an optional 2-color IF staining with relevant markers to assist in the selection of ROIs for imaging. In order to prepare the reagents for the MACSima experiment, I manually pipetted each antibody into a well of a 96-well U-bottom microtest plate (LVL technologies) at the corresponding titer (Table 16) in autoMACS running buffer supplemented with FcR blocking reagent. Every 4th well, I added Hoechst to re-stain the nuclei. A final volume of 300 µL reagent per tissue section was prepared. The reagent plate was covered with a pierceable film (Brooks) to avoid evaporation.

Most of the MACSima experiments in this PhD project were performed in the prototype of the current instrument, handled by Jan Drewes, Max Schulze, and Christiane Oleszynski from the MACSima Team at Miltenyi. It was composed of a TECAN robot (Tecan Group AG) coupled with a IN Cell Analyzer 2000 (GE Healthcare), which was programmed to proceed with the MICS (MACSima Imaging Cyclic Staining) steps (Table 16). The microscope set the autofocus on each cycle based on the nuclei staining. Each cycle lasted about 45 min for one tissue section and 2-4 ROIs. The images were acquired in 20x magnification and with a pixel size of 0.379 µm per pixel.

Table 16. MICS steps

	STEPS	
1	MANUAL SELECTION OF REGIONS OF INTEREST	
2	IMAGE ACQUISITION OF AUTOFLUORESCENCE/PRE-IF STAINING	
3	PHOTOBLEACHING OF AUTOFLUORESCENCE/PRE-IF STAINING	
4	ANTIBODY ADDITION TO TISSUE SECTION	96 CYCLES
5	INCUBATION FOR 10 MIN	
6	WASHING	
7	IMAGE ACQUISITION OF STAINING	
8	PHOTOBLEACHING OF ANTIBODY FLUOROPHORE	
9	IMAGE ACQUISITION OF BLEACHING BACKGROUND	

2.2.7 Image analysis

Image processing

Images were processed in two subsequent steps for image analysis. First, Jan Drewes, Max Schulze, or Christiane Oleszynski processed the images with a custom pipeline generated by the MACSima Team at Miltenyi, which consisted of four steps: 1) dark-frame subtraction to correct noise and pixel errors of the CCD camera chip during acquisition; 2) flat-ROI correction to mitigate image artifacts caused by

uneven illumination; 3) image registration to transform the images of all cycles into one coordinate system based on the nuclei staining for each cycle; and 4) bleach correction to remove residual fluorescence signals from previous cycles by subtracting the bleaching image of the previous cycle from the fluorescent image of the current cycle. Second, I selected a common exposure time for all the images based on a visual inspection in Fiji[141] and excluded blurred images and images with uncorrectable artifacts from the analysis. I performed a background correction (ball radius = 30) followed by a median filter (radius = 2) in Fiji since it showed improved downstream analysis (data not shown). Images were saved in 16-bit TIFF files with a size of 2048 x 2048 pixel. I generated image composites in the MACS iQ View Analysis (Miltenyi). I further discarded not usable images (e.g., blurred or no stainings, large artifacts), and annotated smaller artifacts in the images to exclude them from the analysis.

Image segmentation

I segmented images using CellProfiler 4.2.1[139] or MACS iQ. In CellProfiler, nuclei were detected using the *IdentifyPrimaryObjects* module. The Hoechst image was used as input image and regions with annotated artifacts were excluded. The typical diameter of objects was set to a minimum-maximum of 9-50 pixels. The thresholding method was minimum cross-entropy (globally applied), with the default settings. The nuclei segments were expanded 2 pixels in the *IdentifySecondaryObjects* module in order to define cell boundaries. In MACS iQ, I used the advanced morphology for tissue method to detect nuclei with a minimum-maximum cell diameter of 9-50 pixels and a separation force between 40-70%. The Hoechst image was the reference channel. Cells situated in regions with bright or dark artifacts and at the edges were excluded. To detect the cytoplasm, I selected the constrained donut method with multiple constrain channels to improve cell boundary identification. The donut width was 4 pixels and the detection sensitivity between 100-120%. All parameters were adjusted per dataset, if required.

Segment correction and annotation

In certain cases, especially to investigate the phenotypes of single T cells, a very accurate cell segmentation was needed. For this purpose, I manually corrected the segmented image (generated in CellProfiler with the *ConvertObjectsToImage* module) with a Python-based platform named InspectorCell, created by Andre Gosselink (Miltenyi) and Tatsiana Hofer (University of Vienna)[143] (https://gitlab.com/InspectorCell/inspectorcell). This application is built as add-on in the bioinformatic software Orange 3.30.2[144]. InspectorCell´s graphic interface is composed of a synchronized view of up to 20 markers to aid during segment correction. Furthermore, annotations can also be simultaneously

added on individual cell segments, such as marker positivity based on visual screening. I manually annotated relevant markers of T cells to validate the bioinformatic analysis of $CD8^+$ T cells (see below). These annotations also served as training data by Andre Gosselink to develop supervised machine learning methods in the course of his PhD project. In addition, I automatically annotated tumor areas (defined by CD326 expression) and enlargements of 20 µm from the previous region with a self-written custom Fiji macro. I manually defined TLSs areas based on CD45 staining. I systematically extracted the XY coordinates of each area with the Fiji macro and used a self-written R pipeline to label cells based on their location in the tissue (e.g., tumor area and 20, 40, 80, 100, >100 µm distance from tumor area).

Bioinformatic analysis

The mean fluorescent intensity, cell ID, and XY coordinates were extracted per cell segment into a csv file by the software MACS iQ. If the segments were corrected and annotated, feature extraction was performed by the software InspectorCell. For the analysis of $CD8^+$ T cell phenotypes, I loaded the extracted data into FlowJo and performed a manual gating to extract the frequency of cells expressing markers of interest. The gates for each marker were set with the aid of the manual annotations performed in InspectorCell, which were visualized in FlowJo as a separate variable. I generated graphs in GraphPad Prism. In addition, I used the mean intensity marker expression of gated $CD8^+$ T cells (excluding outliers by a local outlier factor method with a contamination factor of 5% in Orange) to perform dimension reduction (tSNE) in the software Orange. Marker expression was visualized in tSNE plots and heatmaps using a self-written custom R pipeline. The mean intensity values were transformed to log10 scale in tSNE plots and Z-normalization was used for heatmaps.

3 Results

3.1 Identification of a CD8$^+$ T cell phenotype that is predictive of tumor reactivity

To identify a phenotype capable of distinguishing tumor-reactive CD8$^+$ tumor-infiltrating lymphocytes (TILs) from tumor-unrelated T cells for the development of enrichment strategies for clinical purposes, I first performed a flow cytometry-based screening of extracellular markers related to T cell activation and exhaustion as a proxy for tumor reactivity in TILs from tumor digests.

3.1.1 The proportion of TILs in tumor digests was variable across and within cancer types

Freshly digested tumor samples from ovarian carcinoma (OvCa), colorectal carcinoma (CRC), and pancreatic ductal adenocarcinoma (PDAC) patients were used for the identification of tumor-reactive CD8$^+$ TILs[FN1]. To ascertain whether sufficient numbers of TILs could be isolated from tumor digests to perform phenotypic characterizations and T cell subset enrichments, I first determined the cellular composition and total number of T cells for each sample.

First, the frequencies of tumor, stromal, and immune cells were calculated. Cells expressing EpCAM, a marker upregulated in cancer cells of epithelial origin[155], were abundant in CRC samples (median = 73% of viable cells) and less frequent in PDAC samples (median = 13%; Figure 1A). Studies have shown that PDAC tissues have on average a smaller proportion of tumor cells compared to other cancer types (26% vs 81.1%, respectively[156]), which results in a high heterogeneous PDAC tumor microenvironment[157]. In line with this observation, the stromal component (CD90$^+$ fibroblasts and CD31$^+$ blood vessels) of PDAC samples was more pronounced (median = 4% of viable cells) than in other cancer types (medians = 1% and 0.3% in OvCa and CRC samples, respectively; Figure 1A). The CD45$^+$ immune population was variable among samples (Figure 1A) and included: 1) T cells, with high heterogenous fractions ranging from 0.7% to 85% of CD45$^+$ cells in OvCa samples, 22% to 67% in CRC, and 0% to 58% in PDAC (Figure 1B), and within the T cell fraction, CD8$^-$ T cells were more prevalent than CD8$^+$ T cells (Figure 1C); 2) CD14$^+$ myeloid cells, which were present at variable levels, especially in OvCa samples (6% to 46% of CD45$^+$ cells; Figure 1B); and 3) B cells, which were generally rare (medians = 0.4% and 1.2% in OvCa and CRC, respectively; Figure 1B). The cell composition of each individual sample is shown in Supplementary Figure 1.

[FN1] Lung cancer (LuCa) was also used for the enrichment of tumor-reactive T cells (see following section 3.2). However, I excluded it from this section as only one LuCa patient sample was processed and characterized.

The number of CD8$^+$ T cells obtained from tumor digests ranged between 1.3 x 10^4 and 1.3 x 10^7 cells (Figure 1D). Generally, PDAC samples had fewer T cells than OvCa or CRC samples, which correlated with a lower average weight of PDAC samples (median = 0.9 g) compared to OvCa (median = 2.1 g) and CRC (median = 4.8 g) samples. The recovery of viable cells depends on the digestion protocol[158], and while testing different concentrations of enzyme R in the Tumor Dissociation Kit (Miltenyi) due to its influence on epitope degradation (see Results section 3.1.2.), I observed that a reduction of enzyme R to 20% of the recommended dose decreased cell viability in the tested sample metCRC5 (82% to 57%; Supplementary Figure 2A). This, together with data generated in the Sample Preparation Group led by Dr. Carsten Poggel at Miltenyi Biotec (data not shown), suggests that using the recommended amount of enzyme R can maintain the overall sample viability. Therefore, the chosen concentration of enzyme R may rely on a compromise between cell viability/yield and epitope preservation on target cells for each individual application. Nonetheless, viabilities greatly varied among samples digested with the same protocol (Supplementary Figure 2A), suggesting that patient heterogeneity and other factors, such as surgical resection or transport, may also have an impact on sample viability.

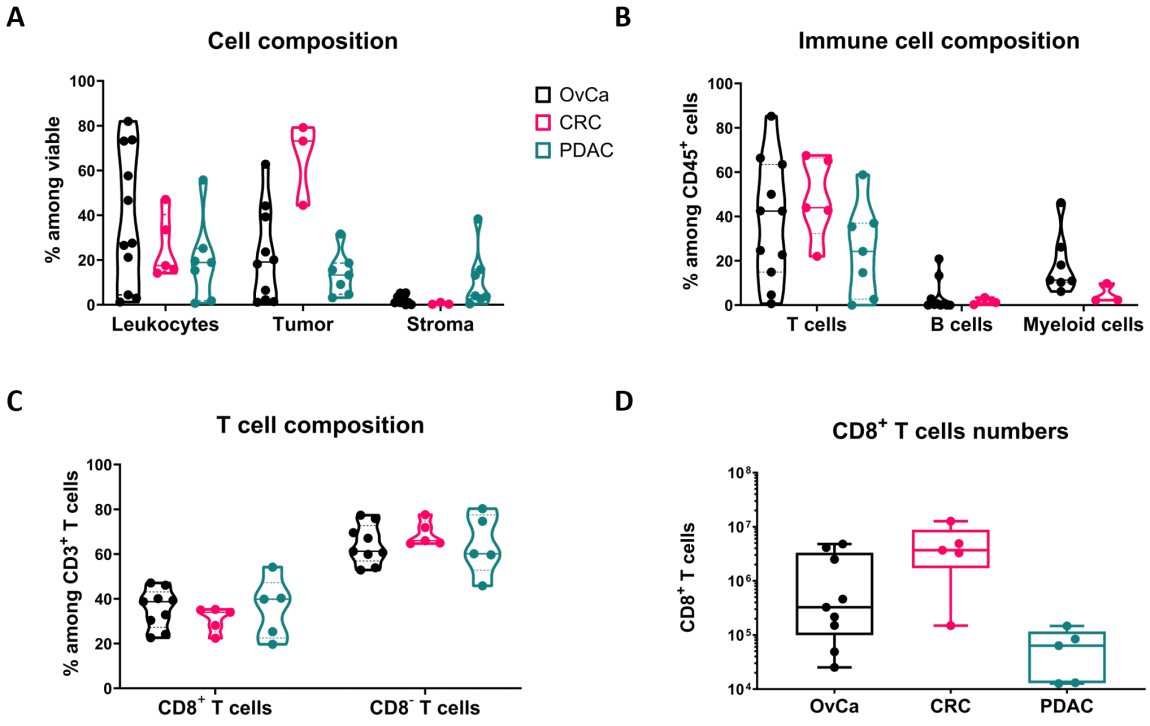

Figure 1. Cell composition of digested tumor samples
(A to C) Percentage of (A) leukocytes (CD45$^+$), tumor cells (EpCAM$^+$), and stromal cells (CD31$^+$ and CD90$^+$) among viable cells, (B) T cells (CD3$^+$), B cells (CD19$^+$), and myeloid cells (CD14$^+$) among CD45$^+$ immune cells, and (C) CD8$^+$ and CD8$^-$ T cells among CD3$^+$ T cells. B cells and CD14$^+$ myeloid cells were not screened in PDAC samples. **(D)** Total CD8$^+$ T cell numbers obtained per cancer type. Ovarian carcinoma (OvCa, n = 7 to 11), colorectal carcinoma (CRC, n = 3 to 5), and pancreatic ductal adenocarcinoma (PDAC, n = 5 to 7). Violin plots show the median (line) and quartiles (dotted line). Box plots show the median (line), quartiles (box), and minimum and maximum values (whiskers). Each dot represents a sample.

In summary, I dissociated several tumor samples to obtain TILs for the identification of tumor-reactive $CD8^+$ TILs. The characteristics of each sample in terms of cell composition and number of T cells after dissociation were variable across and within cancer types: colorectal carcinoma samples offered the highest number of TILs, ovarian carcinoma samples were highly heterogenous, and pancreatic samples generally yielded low TIL counts.

3.1.2 CD39 as a potential marker of tumor-reactive $CD8^+$ TILs

T cell activation and exhaustion have been considered surrogates of tumor reactivity in TILs due to chronic antigen stimulation in an immunosuppressive tumor microenvironment[159]. To investigate which markers could be used to enrich tumor-reactive $CD8^+$ T cells from tumor digests, I screened the cell surface expression of 25 markers associated with T cell activation and exhaustion by flow cytometry (antibody panels are summarized in Table 10 of Methods section 2.2.4, and a description of the most relevant markers can be found in Introduction section 1.3.2). I focused on $CD8^+$ TILs, but an overview of $CD8^-$ TIL phenotypes is depicted in Supplementary Figure 3. PDAC-derived TILs were excluded from most of the following analyses due to insufficient number of T cells.

The degree of T cell activation and exhaustion varied among samples (Figure 2 and Supplementary Figure 4). Some markers, such as the T cell receptor (TCR) inhibitory molecule CD5, the costimulatory molecules CD7 and CD38, and the early activation and tissue retention marker CD69, were expressed by most $CD8^+$ TILs in both OvCa and CRC samples (medians > 80% of T cells; Figure 2). This observation suggests that these markers alone may lack high selectivity as cancer-unrelated or bystander TILs are abundant in tumors[118], resulting in low frequencies of tumor-reactive TILs. In contrast, certain markers, such as the inhibitory molecules CTLA4, LAG3, and VISTA, were infrequently detected in $CD8^+$ TILs (median < 3% of T cells; Figure 2). This may be attributed to degradation of epitopes sensitive to the enzymes used in the tumor dissociation protocol[160], which can hinder the detection of cells expressing these markers, especially those with low expression levels. Therefore, I tested the expression of all markers in my screening panels after enzymatic digestion in activated peripheral blood mononuclear cells (PBMCs) from healthy donors[FN2]. ICOS, CD25, CD7, and TIM3 were negatively affected by enzyme R, while LAG3 was sensitive to other enzymes in the kit (Supplementary Figure 2B). As enzyme R was beneficial for maintaining cell viability (Supplementary Figure 2A), our group decided to include it in the digestion protocol but at a reduced concentration (20% of the recommended dose).

I especially focused on markers proposed as tumor-reactive surrogates in various publications at the time of this PhD project (from 2017 to 2020). The activation markers CD137 (or 4-1BB) and ICOS, as

[FN2] A list of all cell surface epitopes tested within Miltenyi can be found in this website.

well as a series of immune checkpoints (PD1, TIM3, and CD39) and tumor-residency markers (CD103 and CD69) were among the top candidates in the field (see Table 1 in Introduction section 1.3.2 for a summary of proposed tumor-reactive T cell markers with references). The expression of these markers was heterogeneous across samples. For example, the frequency of $PD1^+$ $CD8^+$ T cells broadly varied from 11.0% to 90.1% in OvCa (median = 60.5% of $CD8^+$ T cells; Figure 2A) and from 17.0% to 84.7% in CRC (median = 70.3%; Figure 2B). Gros et al. have previously proposed PD1 as a marker of tumor-reactive $CD8^+$ T cells in tumors and blood[101,161], and various publications have shown that a subset of $CD8^+$ TILs expressing high levels of PD1 ($PD1^{hi}$) was enriched for tumor reactivity compared to intermediate or low PD1-expressing $CD8^+$ T cells[17,102,103]. $PD1^{hi}$ $CD8^+$ TILs reached frequencies up to 28.8% in OvCa samples (median = 12.8% of $CD8^+$ T cells; Figure 2A) and up to 33.4% in CRC samples (median = 8.0%; Figure 2B), indicating that this subset was present in most studied samples and was more restricted than PD1 alone. Therefore, using PD1 without distinguishing between high and low PD1 expressing-T cells in tumors may lead to a cell subset with a significant fraction of tumor-unrelated or bystander T cells. CD137 is an activation-induced marker that was expressed in a small portion of cells in most OvCa (median = 4.2% of $CD8^+$ T cells; Figure 2A) and CRC samples (median = 4.3%; Figure 2B). As CD137 is an early activation marker that peaks after 24 hours of activation and returns to baseline levels after 72 hours[162], it may only identify recently activated T cells in the tumor, potentially missing a fraction of tumor-reactive T cells. This is supported by the upregulation of CD137 in TILs after an overnight incubation in the presence of tumor cells[95]. Moreover, CD137 was slightly sensitive to epitope degradation by enzyme R (Supplementary Figure 2A), which may hinder the enrichment of this T cell subset after enzymatic dissociation.

CD39 is an ectonucleotidase that hydrolyzes extracellular ATP, creating an immunosuppressive environment in the tumor. As such, CD39 has been considered an inhibitory molecule that is upregulated upon prolonged TCR stimulation[107]. Most samples contained variable frequencies of $CD39^+$ $CD8^+$ TILs (Figure 3A), but they were more predominant in CRC (median = 53.1% of $CD8^+$ T cells) than OvCa (median = 15.6%) and PDAC samples (median = 11.3%). During these marker screenings in 2018, two publications by Simoni et al. and Duhen et al., respectively, proposed CD39 as a surrogate marker of tumor reactivity[107,118]. Particularly, the second publication showed that co-expression of CD39 and CD103 identified tumor-reactive $CD8^+$ T cells with a tissue-resident memory phenotype in melanoma and head and neck squamous cell carcinomas[107]. In my samples, a large frequency of $CD39^+$ $CD8^+$ TILs co-expressed CD103 (median = 91.7% of $CD39^+$ $CD8^+$ T cells in OvCa; 91.2% in CRC) compared to their $CD39^-$ counterparts (median = 19.6% of $CD39^-$ $CD8^+$ T cells in OvCa; 56.3% in CRC; Figure 3B to E). Similar to PD1, I observed cells with high expression levels of CD103 ($CD103^{hi}$), suggesting distinct $CD103^+$ $CD8^+$ TIL subsets based on its expression levels (Figure 3B). Generally, increased PD1 and CD103

expression levels were correlated with CD39 expression (Figure 3B and C), and at least for OvCa samples, the frequency of $CD103^+$ $CD8^+$ TILs, $PD1^+$ $CD8^+$ TILs, and $PD1^{hi}$ $CD8^+$ TILs was significantly higher in the $CD39^+$ subset than in $CD39^-$ T cells (Figure 3D). In addition, $CD39^+$ $CD8^+$ TILs co-expressed other activation/exhaustion markers compared to $CD39^-$ $CD8^+$ TILs, such as TIM3, LAG3, ICOS, CD137, and TIGIT (Figure 3B to E). This activated/exhausted phenotype supports the hypothesis that $CD39^+$ $CD8^+$ T cells are potentially enriched with tumor-reactive cells. Moreover, CD39 was not sensitive to any of the tumor dissociation enzymes (Supplementary Figure 2A) and its expression level was higher than the one for other markers, such as CD137 or TIM3, representing a clear population of cells that could be easily enriched by fluorescence-activated cell sorting (FACS) or magnetic cell separation (MACS) (Figure 3B).

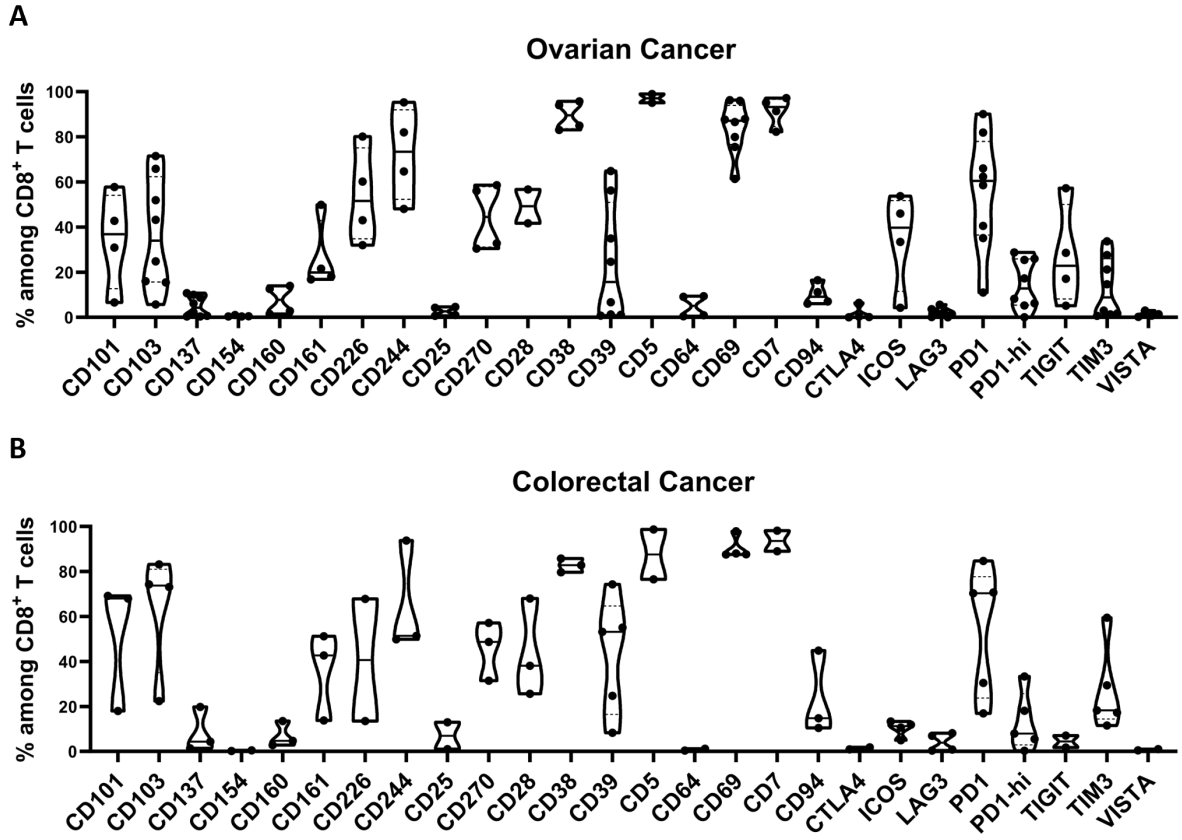

Figure 2. Phenotypic characterization of $CD8^+$ TILs in tumor patients
Several markers related to activation/exhaustion were screened in tumor patient TILs. Percentage of $marker^+$ cells among $CD8^+$ TILs are shown for **(A)** ovarian cancer (n = 3 to 9) and **(B)** colorectal cancer (n = 1 to 4). Violin plots show the median (line) and quartiles (dotted line). Each dot represents a patient.

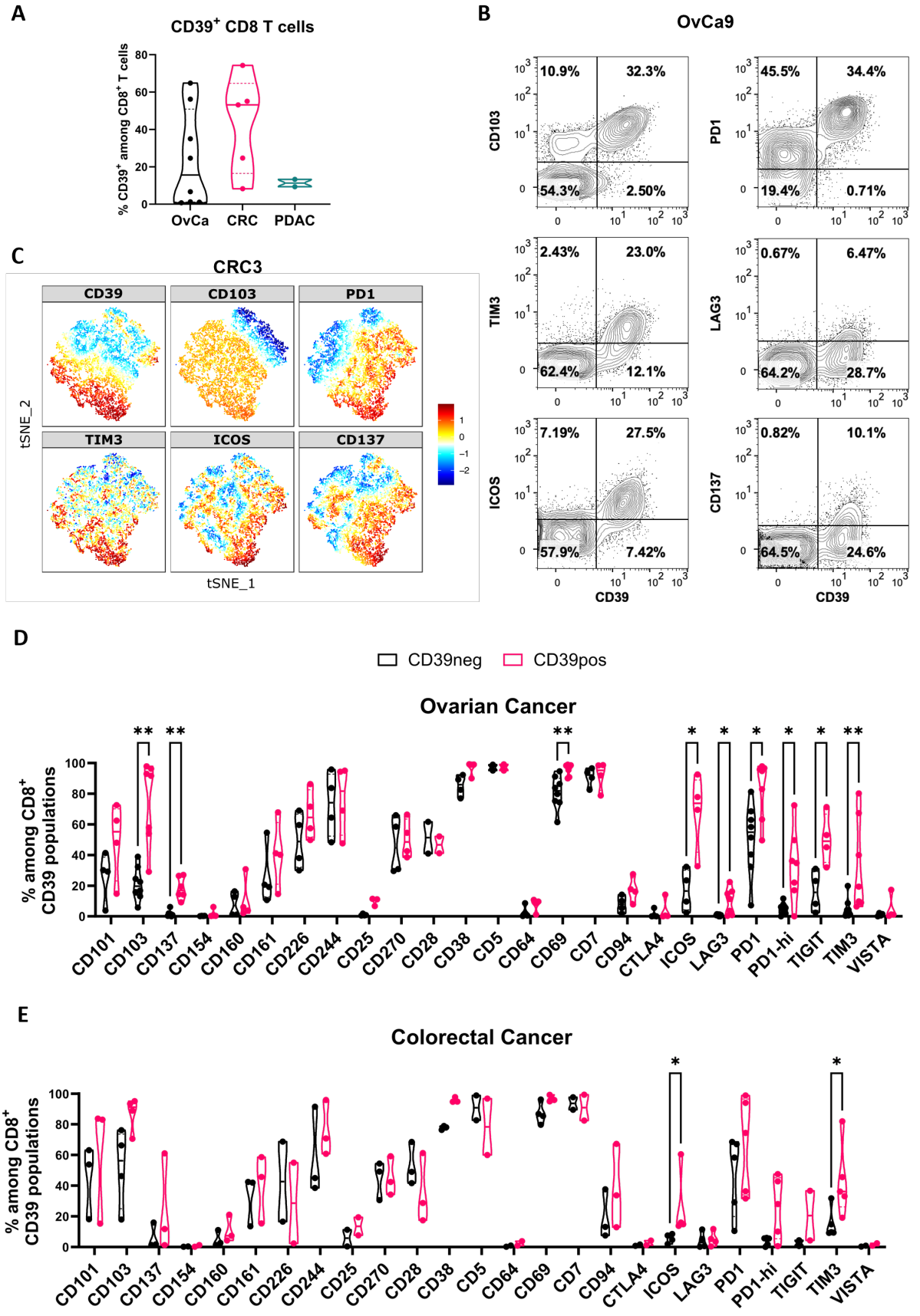
A
CD39+ CD8 T cells
% CD39+ among CD8+ T cells
OvCa
CRC
PDAC
B
OvCa9
CD103
PD1
TIM3
LAG3
ICOS
CD137
CD39
C
CRC3
CD39
CD103
PD1
TIM3
ICOS
CD137
tSNE_2
tSNE_1
D
CD39neg
CD39pos
Ovarian Cancer
% among CD8+ CD39 populations
CD101
CD103
CD137
CD154
CD160
CD161
CD226
CD244
CD25
CD270
CD28
CD38
CD5
CD64
CD69
CD7
CD94
CTLA4
ICOS
LAG3
PD1
PD1-hi
TIGIT
TIM3
VISTA
E
Colorectal Cancer

Figure 3. Phenotypic characterization of CD39$^+$ CD8$^+$ TILs in tumor samples
(A) The frequencies of CD39$^+$ cells among CD8$^+$ TILs are shown for ovarian carcinoma (OvCa, n = 8), colorectal carcinoma (CRC, n = 5), and pancreatic ductal adenocarcinoma (PDAC, n = 2) samples. **(B)** Representative FACS plots of an ovarian carcinoma sample (patient 9) depicting the co-expression of CD39 with other relevant activation/exhaustion markers. **(C)** Representative tSNE plots of CD8$^+$ TILs in a colorectal carcinoma patient (patient 3) showing the expression level of different activation/exhaustion markers by the color gradient. **(D and E)** Expression of markers related to activation/exhaustion in either CD39$^+$ or CD39$^-$ CD8$^+$ TILs for (D) OvCa (n = 3 to 8) and (E) CRC (n = 1 to 5). Violin plots show the median (line) and quartiles (dotted line). Each dot represents a patient. Unpaired, Mann-Whitney tests were performed marker-wise with no correction for multiple comparisons in D and E (** $p \leq 0.01$, * $p \leq 0.05$).

In summary, activated/exhausted CD8$^+$ TILs were detected in all samples at variable levels, and they were enriched in the CD39$^+$ subset compared to its negative counterpart. This phenotype suggests that CD39$^+$ CD8$^+$ TILs may contain tumor-reactive T cells that have undergone chronic antigen stimulation in the tumor microenvironment, in accordance with recent studies[107,117,118,163]. Therefore, I next sought to corroborate the *in vitro* reactivity of CD39$^+$ CD8$^+$ TILs in the studied patient samples.

3.2 Enrichment, expansion, and reactivity of TIL subsets

Following the identification of CD39 as a potential marker of tumor-reactive $CD8^+$ TILs, I verified the tumor reactivity of this population *in vitro* by assessing the activation of expanded $CD39^+$ $CD8^+$ TILs upon co-culture with autologous tumor cells.

3.2.1 Enrichment strategy of $CD39^+$ $CD8^+$ TILs from tumor digests

The isolation of $CD39^+$ $CD8^+$ TILs was performed by fluorescence-activated cell sorting (FACS) using the MACSQuant Tyto Sorter (Miltenyi Biotec). This instrument performs sorting in a closed cartridge system that contains three chambers: the input chamber, the positive collection chamber for the sorted fraction, and the negative collection chamber for the non-sorted fraction. On the one hand, this system enables consecutive sortings from a single sample as the negative fraction can be recovered and re-sorted, allowing for comparative analysis of multiple cell subsets. On the other hand, cells flow through microchannels in the cartridge that are prone to clogging, especially with samples containing clumps from dead cells or debris, such as tumor digests. To prevent blockages in the MACSQuant Tyto, a pre-sorting strategy of tumor digests was required and involved: 1) removing dead cells and debris with a Dead Cell Removal (DCR) kit, which is based on MACS technology; and 2) magnetic enriching T cells or $CD8^+$ T cells (CD(4)/8 MACS) to improve sorting purity by increasing the initial target cell frequency. Overall, this strategy leads to a reduced input cell number and thus a faster sorting. I tested the order of these pre-sorting steps to optimize the recovery of debris-free T cells. Figure 4 provides an overview of the complete workflow, including post-FACS cell sorting steps (expansion and reactivity test) that will be presented in the next section 3.2.2. Additionally, the characterization of TILs by single-cell RNA sequencing (scRNA-seq) is shown in the following section 3.3.

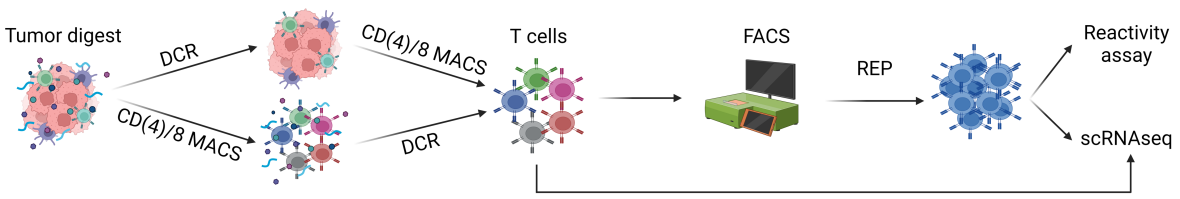

Figure 4. Workflow for the enrichment, expansion, and reactivity test of TIL subsets
Tumor digests were processed with the Dead Cell Removal (DCR) kit to remove dead cells, followed by T cell or $CD8^+$ T cell magnetic cell separation (CD(4)/8 MACS) prior to fluorescence-activated cell sorting (FACS). Alternatively, T cells were enriched first and, if needed, the DCR step was subsequently performed. Afterwards, sorted cells were expanded using the Rapid Expansion Protocol (REP)[11] and subjected to the reactivity assay. Furthermore, single-cell RNA sequencing (scRNA-seq) was performed in both pre- and post-REP subsets.

In this thesis, I present the enrichment of $CD39^+$ $CD8^+$ TILs from four different tumor samples: ovarian metastasis from colorectal cancer patient 5 (metCRC5), primary colorectal cancer patient 4 (CRC4), ovarian cancer patient 12 (OvCa12), and lung cancer patient 1 (LuCa1). The pre-sorting strategy that I followed for each sample is depicted in the cell count graphs (Figure 5A to D).

The loss of $CD8^+$ T cells during the pre-sorting steps (including washes) was substantial—over 72% loss in all samples. The most significant loss occurred during the first MACS separation, where 43% to 70% of $CD8^+$ TILs were lost irrespective of the method used (Figure 5A to D). This may be caused by non-specific binding of sticky or dead cells to microbeads and/or MACS columns, which increases the retention of cells in the column. Consequently, low numbers of $CD8^+$ T cells were available prior to the FACS cell sorting, ranging from 2×10^5 for LuCa1 to 1.9×10^6 for CRC4 (Figure 5B and D, respectively). Despite this, the purity of the target population (viable cells for DCR and T cells for CD(4)/8 MACS) was generally acceptable, with viabilities exceeding 90% after DCR for all samples except for LuCa1 (33%) (Figure 5E and F), and over 66% T cells of viable cells after CD(4)/8 MACS (Figure 5E and G). Therefore, the pre-sorting strategy led to viable ($CD8^+$) TILs free of debris that could be used in the MACSQuant Tyto Sorter.

The FACS cell sorting was performed with the assistance of Dr. Polina Zjablovskaja and Alina Kurow from the Tyto team at Miltenyi. Sorting of the $CD39^+$ $CD8^+$ population achieved high purities (over 79% in all samples; Figure 6). However, cell losses ranged from 54.8% to 76% post-sorting, yielding cell numbers between 1.3×10^4 and 2.3×10^5 $CD39^+$ $CD8^+$ TILs (Figure 6B). These cell counts were sufficient to perform expansion in all cases (minimum starting cell number was 1×10^4 cells). Only sorting of sample CRC4 resulted in sufficient cells for scRNA-seq of enriched $CD39^+$ $CD8^+$ T cells. Unfortunately, I decided to exclude this sample from further analysis due to a microbial contamination that arose early during cell culture, which is common in tissue samples from colorectal cancer[164].

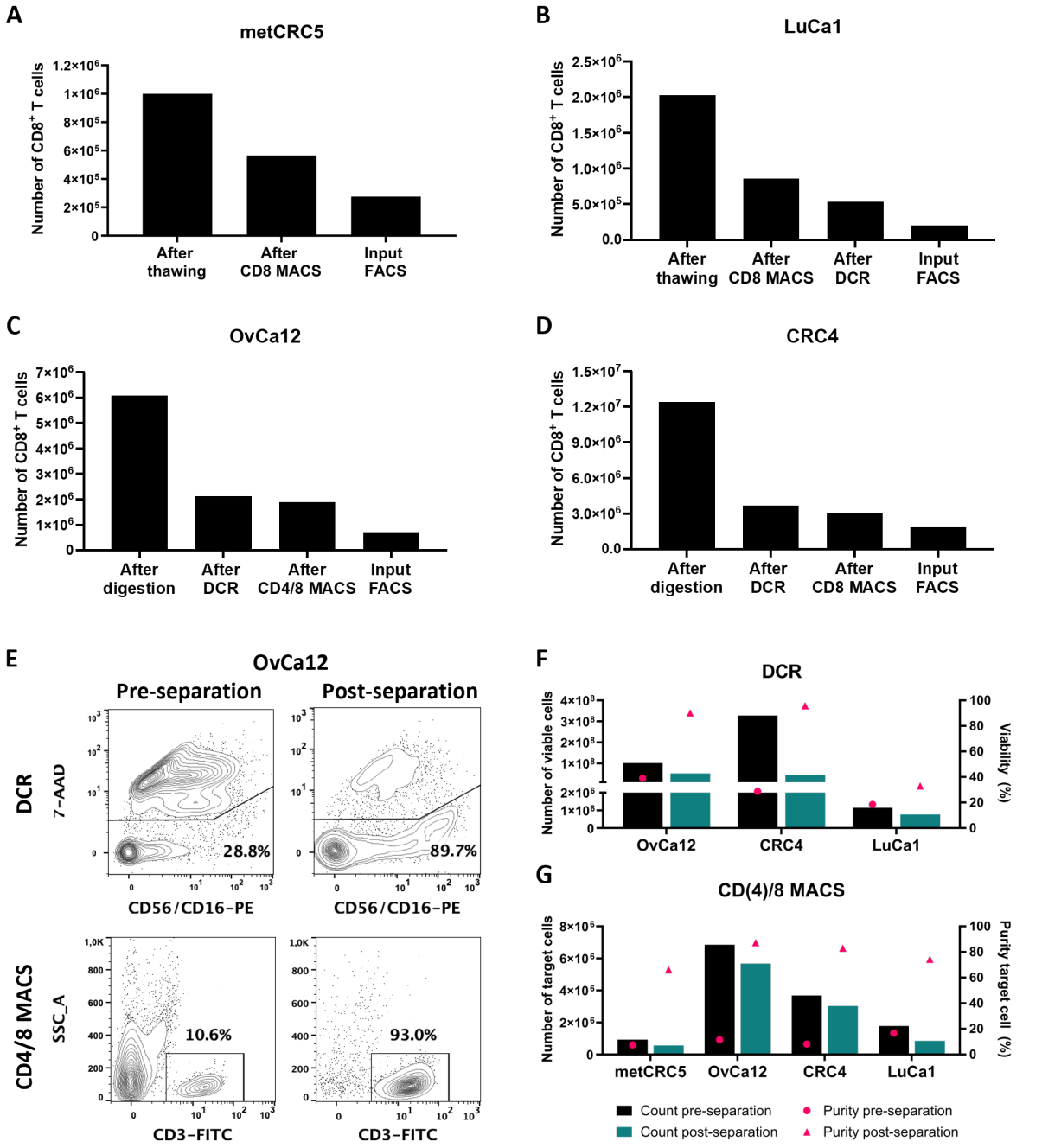

Figure 5. MACS separations used in the pre-sorting workflow

(A to D) Number of CD8$^+$ T cells during the different steps of the pre-sorting workflow for the four samples processed: (A) metCRC5, (B) LuCa1, (C) OvCa12, and (D) CRC4. **(E)** Representative density plots for patient OvCa12 showing the frequency of viable cells pre- and post-separation with the Dead Cell Removal (DCR) kit (top), and the frequency of CD3$^+$ T cells pre- and post-separation with the CD4/8 MACS kit (bottom). **(F and G)** Enrichment efficiencies of the (F) DCR and (G) CD(4)/8 MACS procedures measured by the recovered number (left axis) and purity (right axis) of target cells after the separations for each processed sample. Ovarian carcinoma (OvCa), lung carcinoma (LuCa), (metastatic) colorectal carcinoma ([met]CRC).

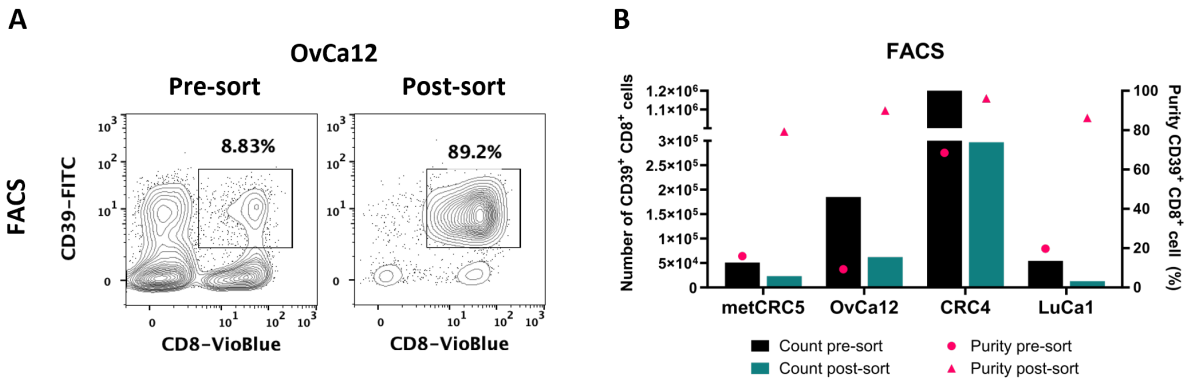

Figure 6. FACS cell sorting of CD39⁺ CD8⁺ TILs
(A) Representative density plots for patient OvCa12 showing the frequency of CD39⁺ CD8⁺ T cells pre- and post-FACS cell sorting. **(B)** Enrichment efficiencies of the FACS cell sortings measured by the recovered number (left axis) and purity (right axis) of CD39⁺ CD8⁺ T cells after sorting for each processed sample. Ovarian carcinoma (OvCa), lung carcinoma (LuCa), (metastatic) colorectal carcinoma ([met]CRC).

I calculated various parameters using the cell counts before and after the separations (excluding washing steps) to summarize the efficiency of each separation method. Magnetic-based technologies (DCR and CD(4)/8 MACS) showed higher recoveries (sum of sorted and non-sorted target cells divided by input target cells) than FACS, indicating less cell loss through the MACS columns than in the Tyto cartridge (Figure 7). In line with the recovery, the yield (sorted target cells divided by input target cells) was highest in CD(4)8/MACS, variable in DCR, and lowest in FACS sortings. Conversely, FACS, along with DCR (except for one case), resulted in higher purities of target cells.

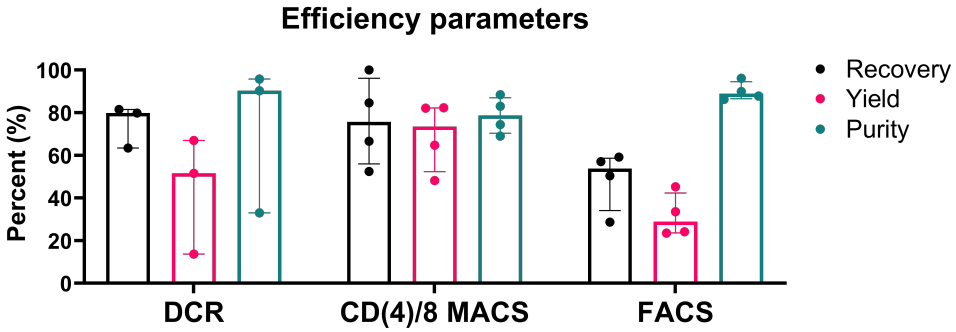

Figure 7. Efficiency parameters of the different types of separation
Summary of the efficiency of all the separation methods performed based on the recovery (number of sorted and non-sorted target cells / number of input target cells), yield (number of sorted target cells / number of input target cells), and purity (frequency of sorted target cells). Dead Cell Removal (DCR, n = 3), CD4/8 or only CD8 MACS (CD(4)/8 MACS, n = 4), and FACS sorting (n = 4). The bars represent the mean, and the bar errors the SD.

In summary, the pre-sorting workflow, consisting of debris/dead cells removal and magnetic pre-enrichment of T cells, enabled the performance of FACS sorting of tumor digests, achieving high $CD39^+$ $CD8^+$ T cell purities. Despite this improvement, cell loss during MACS isolations and FACS sorting remained a challenge, limiting subsequent experiments due to low cell numbers.

3.2.2 $CD39^+$ $CD8^+$ TILs are enriched for tumor reactivity compared to the $CD39^-$ counterparts

The reactivity of $CD39^+$ and $CD39^-$ T cell subsets as well as unsorted TILs was assessed *in vitro*. To provide sufficient cell numbers for the functional assay, I carried out a polyclonal expansion of each T cell subset using the Rapid Expansion Protocol (REP) developed by Rosenberg and colleagues[11] and described in detail in Methods section 2.2.3.

T cell fold expansions at the end of the 14-days culture ranged from 740 to 2,455-fold (Figure 8A). In the pre-sorting strategy described earlier, metCRC5 and LuCa1 tumor digests were magnetically enriched for $CD8^+$ TILs, while the separation in OvCa12 included both $CD4^+$ and $CD8^+$ TILs (Figure 5A to C). Consequently, unsorted and $CD39^-$ fractions from OvCa12 had over 60% $CD4^+$ TILs before expansion, resulting in the presence of $CD4^+$ T cells—and thus low percentage of $CD8^+$ cells—at the end of the REP expansion (Figure 8B).

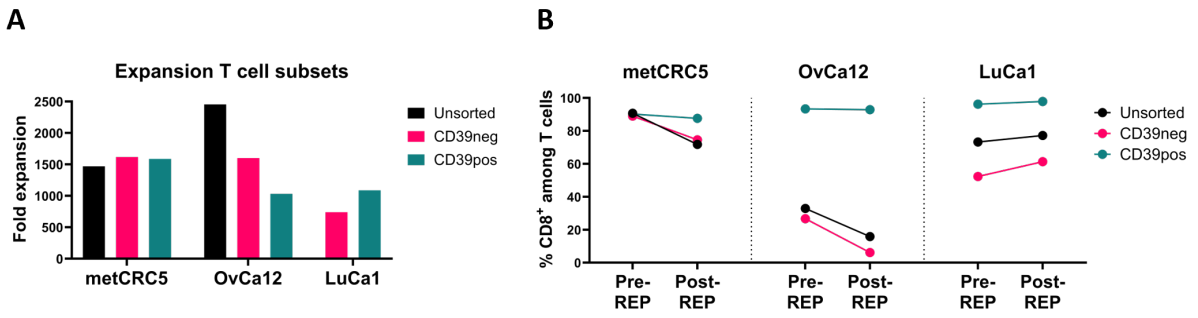

Figure 8. Rapid expansion of TIL subsets
(A) Fold expansion of each T cell subset (unsorted fraction, $CD39^-$ [CD39neg] and $CD39^+$ [CD39pos] subsets) for each tumor sample after the 14 days Rapid Expansion Protocol (REP). **(B)** Frequencies of $CD8^+$ cells among $CD3^+$ TILs pre- and post-REP for each T cell subset per tumor sample. Ovarian carcinoma (OvCa), lung carcinoma (LuCa), metastatic colorectal carcinoma (metCRC).

I assessed the tumor reactivity of each expanded population by the upregulation of activation markers (CD137 and CD154) and the secretion of cytokines (IFNγ and TNFα) and effector molecules (CD107a) upon co-culture with autologous tumor cells (see antibody panel in Table 11 of Methods section 2.2.4). Due to the absence of established tumor cell lines derived from these three patient´s tumors at the time of the functional tests, I used different autologous tumor "targets", such as CD45-depleted tumor digest (for metCRC5) or starting tumor cell cultures (for OvCa12 and LuCa1).

In metCRC5, I observed no clear responses against the autologous tumor target compared to the negative control (Figure 9A), although the data quantification after subtracting the background resulted in a small subset of $CD39^+$ $CD8^+$ T cells (0.19% of $CD8^+$ T cells) that produced $IFN\gamma^+$ and $TNF\alpha^+$ in response to the autologous tumor target (Figure 9C). No detectable T cell responses were observed against an irrelevant, allogeneic tumor control (ovarian carcinoma cell line OC-12; Figure 9C).

In OvCa12, unsorted and $CD39^+$ $CD8^+$ T cell subsets responded to the tumor target, in contrast to the $CD39^-$ $CD8^+$ TILs (Figure 9B). Among $CD8^+$ T cells, cytokine-producing cells were more frequent in the unsorted fraction than in the $CD39^+$ T cell subset (0.93% and 0.36% $IFN\gamma^+$ $TNF\alpha^+$ of $CD8^+$ T cells, respectively; Figure 9D). Due to higher frequencies of $CD8^+$ TILs in the expanded $CD39^+$ subset (Figure 8B), the total number of $IFN\gamma^+$ $TNF\alpha^+$ $CD8^+$ T cells was comparable in both $CD39^+$ and unsorted T cell subsets (around 2.4 x 10^5 cells). Consistent with previous studies emphasizing the crucial roles of $CD4^+$ T cells in antitumor responses[28,29,165], these results suggest a positive impact of $CD4^+$ T cells on the expansion of tumor-reactive $CD8^+$ T cells in the unsorted subset.

In LuCa1, I observed no responses in any TIL subset upon co-culture with autologous tumor target in comparison with negative controls, including irrelevant, allogeneic tumor cells or TILs alone (Supplementary Figure 5).

In conclusion, I detected cytokine-secreting, tumor-reactive $CD8^+$ T cells at low frequencies (0.36% of $CD8^+$ TILs) in the expanded $CD39^+$ population in OvCa12. The selection of $CD39^+$ $CD8^+$ TILs did not favor the outgrowth of tumor-reactive $CD8^+$ TILs compared to no enrichment (i.e., unsorted TILs) for this sample. However, the reactivity was lost when $CD39^+$ $CD8^+$ TILs were depleted (i.e., in the $CD39^-$ T cell subset), supporting that tumor-reactive $CD8^+$ T cells expressed CD39. The low frequencies observed in the tested samples could be a result of multiple factors, including an initial low fraction of tumor-reactive $CD8^+$ TILs in the tumor and a possible loss of tumor-reactive T cell clones during the *in vitro* culture, as previously observed[68]. To answer these questions, I next characterized TILs at the molecular level by scRNA-seq, including TCR repertoire and gene expression analyses.

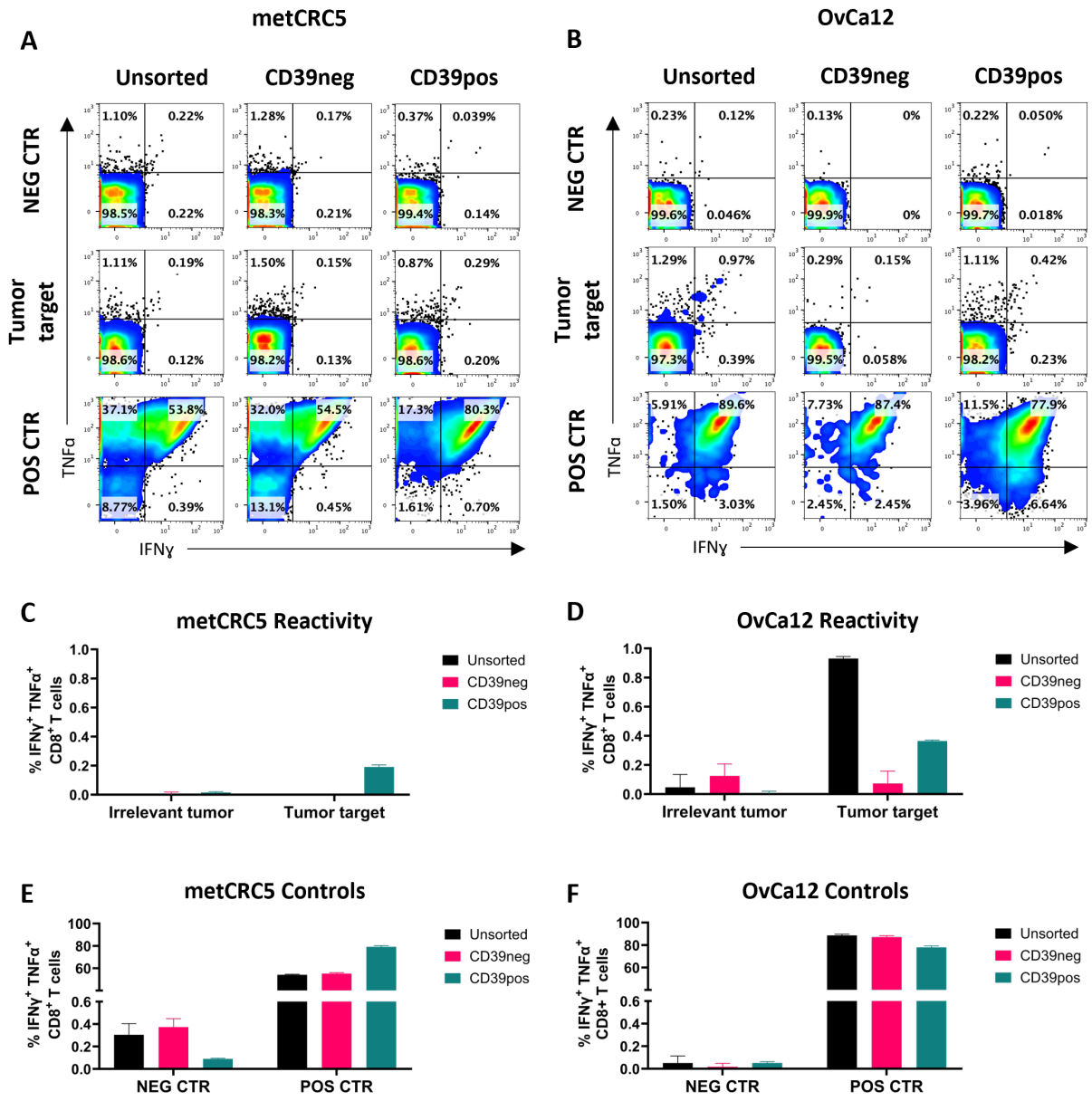

Figure 9. Reactivities of expanded CD8⁺ TILs

(A and B) Representative FACS plots of the different expanded T cell populations from (A) metastatic colorectal carcinoma 5 (metCRC5) and (B) ovarian carcinoma 12 (OvCa12) (unsorted fraction, CD39⁻ [CD39neg], CD39⁺ [CD39pos]), showing the frequency of interferon γ (IFNγ) and tumor necrosis factor α (TNFα)-secreting CD8⁺ TILs upon co-culture with tumor targets (CD45-depleted tumor digest for metCRC5 and 14-day cultured tumor cells for OvCa12). Unstimulated TILs were used as negative control (NEG CTR), whereas TILs stimulated with PMA/Ionomycin were the positive control (POS CTR). **(C and D)** Quantification of the percentage of IFNγ⁺ TNFα⁺ CD8⁺ TILs from (C) metCRC5 and (D) OvCa12 upon co-culture with an irrelevant tumor or autologous tumor target. The signal baseline of the negative control is subtracted in the graphs. **(E and F)** Quantification of the percentage of IFNγ⁺ TNFα⁺ CD8⁺ TILs from (E) metCRC5 and (F) OvCa12 in the negative and positive controls. Bars represent the mean and bar errors the SD of technical triplicates.

3.3 Molecular characterization of TIL subsets

To further determine the initial T cell frequency and differentiation state in the original tumor of relevant TCR clonotypes (i.e., tumor-dominant and CD39$^+$-expanded TCRs), I investigated the gene expression profiles of *ex vivo* TILs and the TCR repertoires of *ex vivo* TILs and post-REP TILs of two patients (metCRC5 and OvCa12) using single-cell mRNA sequencing combined with TCR sequencing.

3.3.1 Dominant TCR clonotypes in the expanded CD39$^+$ T cell subset were found in a small group of exhausted CD8$^+$ T cells in the original tumor of patient metCRC5

Dominant T cell clones in the tumor have been generally considered tumor-specific due to clonal, antigen-driven expansions[166]. However, chronic antigen stimulation of tumor-reactive TILs in an immunosuppressive tumor microenvironment often induces exhaustion, rendering them dysfunctional and with a reduced proliferative capacity *ex vivo*[167]. Consequently, the TCR repertoire in the tumor may not always be maintained after *in vitro* T cell cultures, as previously observed in TIL expansions from PDAC and melanoma patients[68]. To investigate whether high-frequent TCR clones in the tumor of patient metCRC5 were enriched and expanded in the CD39$^+$ T cell population, I compared the TCR repertoires of *ex vivo* TILs (i.e., before the expansion) and expanded TILs (unsorted, CD39$^-$, and CD39$^+$)

First, I calculated the number of unique TCR clonotypes (defined by a distinct CDR3 ammino acid sequence) and their dominance (hyperexpanded: > 10%; large: 1-10%; medium: 0.1-1%; small: 0.01-0.1%; and rare: < 0.01%) for each sample (Figure 10A and B). The TCR diversity in terms of richness (i.e., number of unique clonotypes) and evenness (i.e., relative abundance of unique clonotypes) was higher in *ex vivo* TILs than expanded subsets, with higher number of unique clonotypes (63 per 100 cells; Figure 10A) and smaller percentage of large clonotypes (3% of T cells; Figure 10B). Of note, CD39$^+$ TILs had the highest fraction of large clonotypes compared to the other expanded subsets (60% of T cells; Figure 10B). This suggests that only a small fraction of cells in the tumor was clonal, and the enrichment and/or expansion of CD39$^+$ CD8$^+$ TILs selected a few TCR clonotypes, resulting in a greater clonality.

Regarding TCR overlaps, the *ex vivo* TIL repertoire did not share many clonotypes with expanded TILs (e.g., 0.042 Morisita index between *ex vivo* and CD39$^+$ TILs). The expanded CD39$^-$ TILs had a higher overlap with unsorted than with CD39$^+$ T cell subsets (0.411 vs 0.116 Morisita indexes, respectively; Figure 10C), indicating the presence of unique clonotypes in expanded CD39$^+$ TILs. At the single clonotype level, clonal shifts during the *in vitro* culture were observed. For example, the two largest clones in the tumor (1.6% and 1.5% of T cells) did not greatly proliferate in any subset (Figure 10D to

F, black arrows). The dominant TCR clonotypes in the CD39^{+} CD8^{+} TIL subset were small or undetectable in *ex vivo* TILs and in both unsorted and CD39^{-} expanded TILs (Figure 10F and Supplementary Figure 6A and B, green arrows).

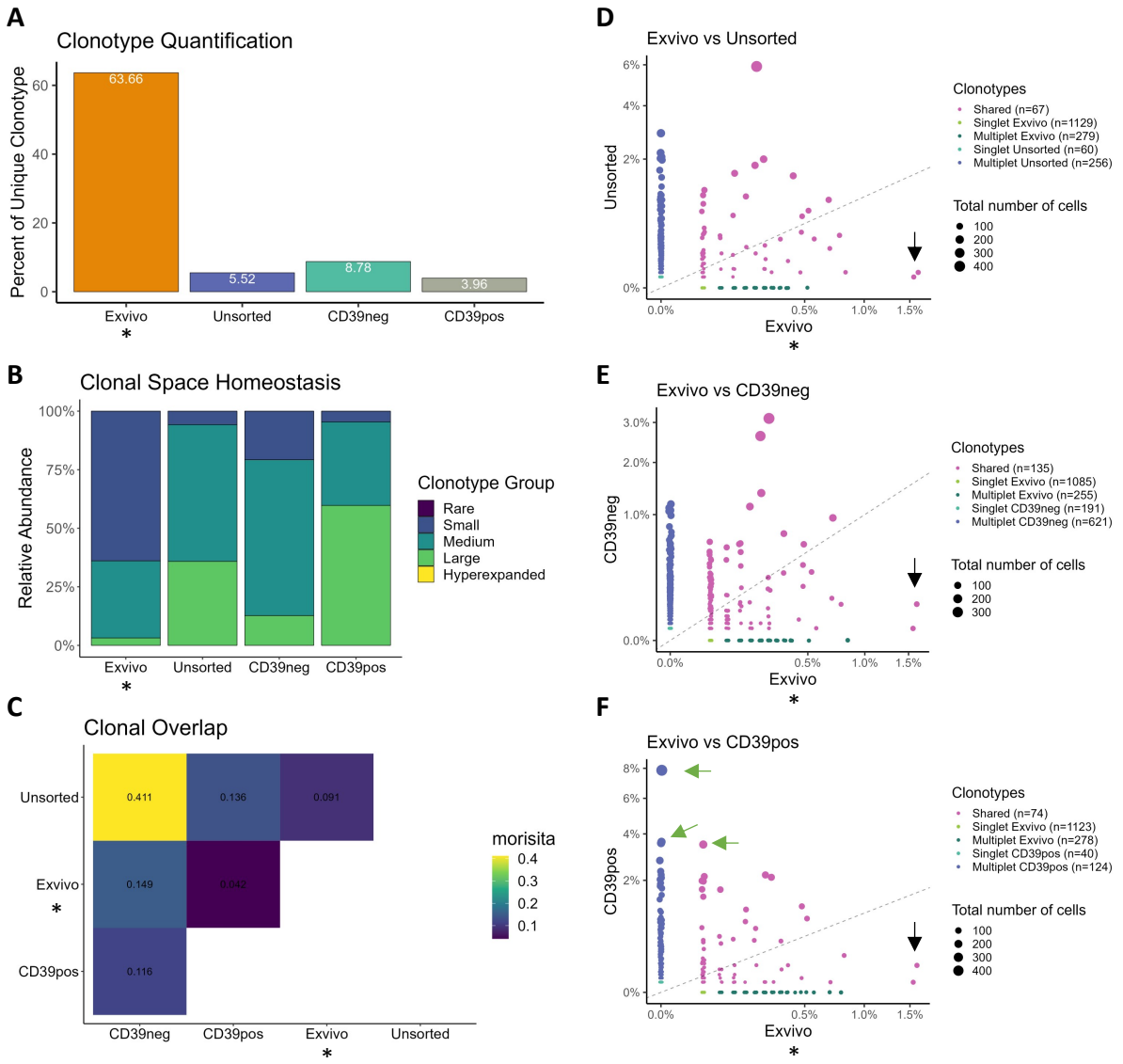

Figure 10. Characterization of the TCR repertoire in different TIL subsets from metCRC5
(A) Percentage of unique clonotypes found in TIL populations from ovarian metastasis from colorectal carcinoma patient 5 (metCRC5), including the *ex vivo* TILs (Exvivo) and the expanded subsets (Unsorted, CD39neg, and CD39pos). **(B)** The relative abundance of clonotypes grouped into classes based on its dominance per sample: hyperexpanded (>10%), large (1-10%), medium (0.1-1%), small (0.01- 0.1%) and rare (<0.01%) clones. **(C)** Clonal overlap between samples calculated by the Morisita index, where higher coefficients indicate larger overlaps. **(D to F)** Scatter plots comparing the clonotypes of *ex vivo* TILs with the expanded samples, where each dot corresponds to a unique TCR clonotype. The shared TCRs are shown in pink, the size of the circles indicates the total number of cells belonging to the clonotype, and the clonotypes closer to the diagonal are found in similar frequencies in both samples. Highlighted clonotypes are marked with arrows (black for *ex vivo* TILs and green for CD39pos). The symbol * indicates samples with 60-70% of CD4^{+} T cells.

To identify the differentiation state of T cells that gave rise to dominant clonotypes in the expanded CD39$^+$ CD8$^+$ TILs, I analyzed the gene expression profiles of *ex vivo* TILs. I identified a total of 12 T cell clusters in metCRC5 (Figure 11A). I used ProjecTILs, a computational method that uses a reference TIL atlas to infer the identity of each cell[145], to annotate each cluster (Supplementary Figure 7A). These annotations were validated through the expression of specific genes and gene signatures associated with distinct T cell subsets or states.

First, I identified naive-like T cells in clusters 0, 1, 4, and 9, and were further labeled as CD3$^+$ T cells (CD3-NaiveLike) as the distinction between CD4$^+$ and CD8$^+$ T cells was unclear (Figure 11B), probably due to low detection of *CD4* transcripts that are known to be weakly expressed in resting T cells[168]. These cells expressed genes related to naive and memory subsets, such as *IL7R*, *KLF2*, *SELL* (CD62L), and *TCF7* (Supplementary Figure 7B and C), and had high scores for naive-like gene signatures[145] (Figure 11B). Although naive and memory T cells are typically expected to be found in circulation rather than in peripheral tissues, they have been described in tumors in multiple studies and may reside in immune niches such as tertiary lymphoid structures (TLSs)[37].

Second, I observed two distinct CD4$^+$ T cell clusters: 1) Follicular helper-like T cells (2_CD4-Tfh), which upregulated genes related to this cell subset (*CXCL13*, *PDCD1* [PD1], *CD200*, *CTLA4*, and *TOX2*) and scored for the T_{FH} gene signature[145]. T_{FH} cells have been previously identified in tumors and may play a role in the formation of tertiary-lymphoid structures (TLSs)[169]; 2) regulatory T cells (3_CD4-Treg) that expressed Treg-associated genes (*FOXP3*, *BAFT*, and *IL2RA* [CD25]) and had a T_{reg} gene signature[145] (Figure 11B and Supplementary Figure 7B and D). Additionally, cells in the 3_CD4-Treg cluster upregulated *TNFRSF9* (CD137), *ICOS*, and *CTLA4*, indicative of an activated state (Figure 11E).

Third, CD8$^+$ T cells were distributed into four clusters, from more to less abundant: 1) effector memory-like CD8$^+$ T cells (6_CD8-Tem), which expressed effector genes (*CCL4*, *GZMA*, *NKG7*, and *KLRG1*) and were distinguished from the other cell subsets by the upregulation of granzyme K (*GZMK*) (Figure 11D and Supplementary Figure 7B); 2) central memory-like CD8$^+$ T cells (7_CD8-Tcm), with an effector phenotype and expression of high levels of granulysin (*GNLY*) and granzyme B (*GZMB*) (Figure 11D); 3) terminally differentiated effector memory CD8$^+$ T cells (8_CD8-Temra), which differentially expressed the effector genes *FCGR3A* and *FGFBP2* (Figure 11D), two markers that have been associated with cytotoxic states in bystander CD8$^+$ TILs[37]; and 4) exhausted CD8$^+$ T cells (11_CD8-Tex). This last cluster was characterized by the expression of effector genes (*CCL3*, *CCL4*, *GNLY*, *GZMA*, *GZMB*, and *NKG7*), effector molecules like perforin (*PRF1*), and cytokines such as interferon gamma (*IFNG*) (Figure 11D). Additionally, it had the highest score for CD8$^+$ T_{EX} gene signature[145] (Figure 11B). In line with their exhausted state, I observed that 11_CD8-Tex cells had medium to high expression levels of several immune checkpoints (*CTLA4*, *HAVCR2* [TIM3], *LAG3*, *LAYN*, *TIGIT*, and *TOX*) (Figure 11E), expressed the

proliferation gene *MKI67* (Figure 11E), and upregulated genes that have been related to tumor-reactive $CD8^+$ T cells, such as *PDCD1* (PD1), the B cell attractant chemokine *CXCL13*, and the proposed marker in this thesis: CD39, encoded by *ENTPD1* (Figure 11F). Therefore, this cluster may contain tumor-reactive $CD8^+$ T cells, which was further supported by high scores of tumor-reactive T cell (TRT) gene signatures obtained from six different publications[37,153,170–173] (Figure 11G).

After having identified the main T cell subsets in metCRC5 by their gene expression profiles, I investigated the relative abundance of TCR clonotypes per cell subset. Clusters 7_CD8-Tcm and 8_CD8-Temra had the largest proportion of large and medium TCR clonotypes, followed by cluster 11_CD8-Tex (Figure 12A and D). This is in agreement with their phenotypes as more differentiated T cells are expected to have more clonal TCR repertoires, reflecting their past or current proliferation. However, the clonal overlap among these three groups was not high (<0.044 Morisita index; Figure 12B), indicating that TCR specificity can influence the differentiation trajectory of T cells in peripheral tissues and, especially, in the tumor microenvironment. Within the $CD8^+$ T cell clusters, 11_CD8-Tex had a partial overlap with cluster 6_CD8-Tem (0.164 Morisita index; Figure 12B and C), suggesting that certain clones had transitioned from one state to the other. Some studies have described a cluster of *GZMK*-expressing $CD8^+$ T cells as pre-exhausted T cells (T_{PEX})[37], which would fit with my previous characterization of cluster 6_CD8-Tem (Figure 11D). Therefore, it may be possible that these clonotypes in pre-exhausted/effector states further differentiated into an exhausted state in the tumor as a consequence of prolonged antigen stimulation.

I next identified the differentiation states in the tumor of dominant clonotypes after expansion of TIL subsets (unsorted, $CD39^-$ and $CD39^+$; Figure 12D to G). The TCRs within the top 20 clonotypes from unsorted and $CD39^-$ TILs that were detected in *ex vivo* TILs (8 and 6 unique TCRs, respectively) did not originate from a specific T cell state but rather from several states (Figure 12E and F). The dominant clonotypes in the $CD39^+$ TILs detected in *ex vivo* TILs (6 unique TCRs) were found in cluster 11_CD8-Tex, suggesting that these TCRs may be tumor-specific based on their initial T cell phenotype.

To sum up, a small cluster of $CD8^+$ T_{EX} cells expressing *ENTPD1* (encoding CD39) exhibited a tumor-reactive T cell signature and contained TCR clonotypes that were capable of proliferating *in vitro*.

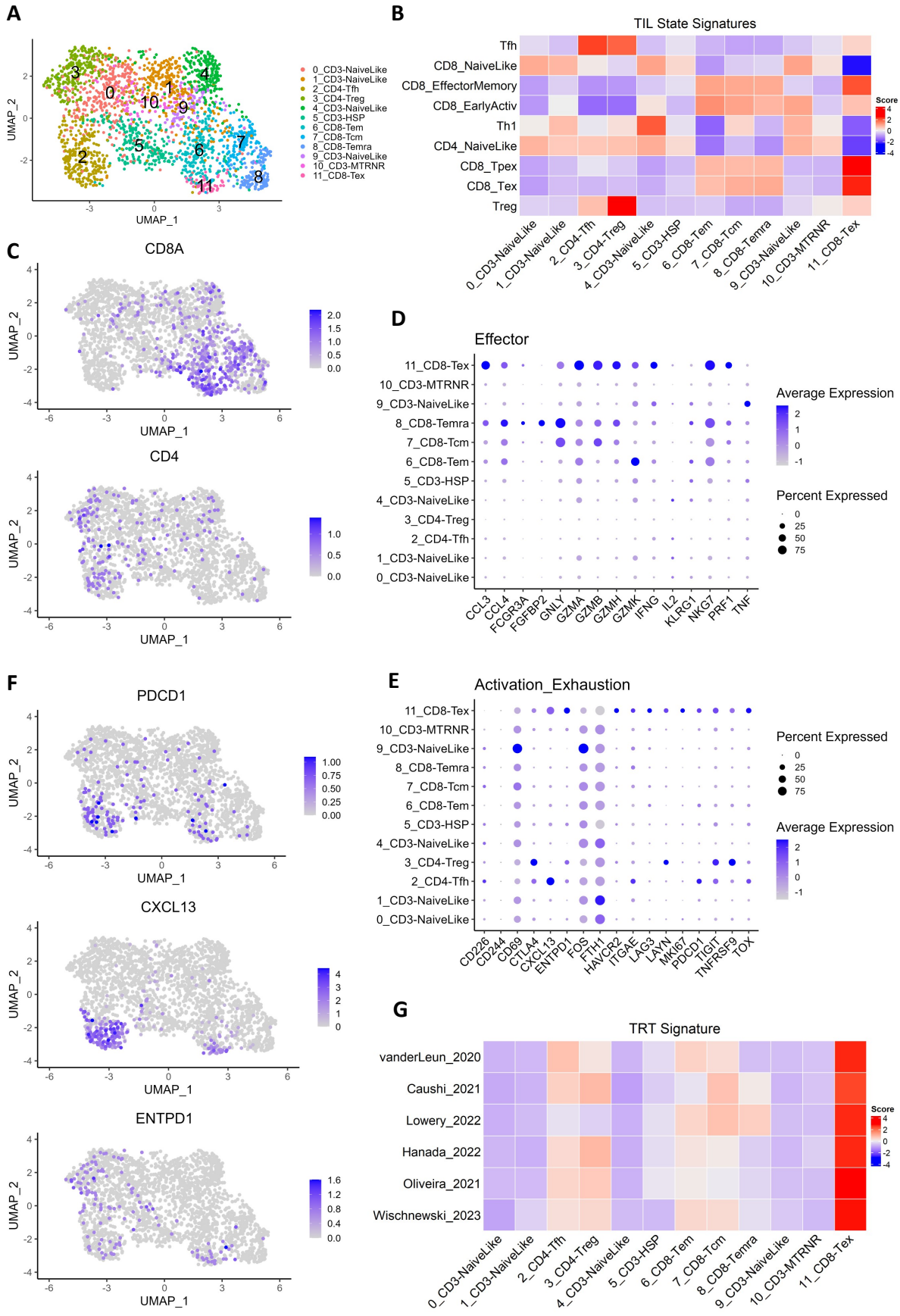
A
UMAP_2
UMAP_1
0_CD3-NaiveLike
1_CD3-NaiveLike
2_CD4-Tfh
3_CD4-Treg
4_CD3-NaiveLike
5_CD3-HSP
6_CD8-Tem
7_CD8-Tcm
8_CD8-Temra
9_CD3-NaiveLike
10_CD3-MTRNR
11_CD8-Tex
B
TIL State Signatures
Tfh
CD8_NaiveLike
CD8_EffectorMemory
CD8_EarlyActiv
Th1
CD4_NaiveLike
CD8_Tpex
CD8_Tex
Treg
Score
C
CD8A
CD4
D
Effector
Average Expression
Percent Expressed
CCL3
CCL4
FCGR3A
FGFBP2
GNLY
GZMA
GZMB
GZMH
GZMK
IFNG
IL2
KLRG1
NKG7
PRF1
TNF
E
Activation_Exhaustion
CD226
CD244
CD69
CTLA4
CXCL13
ENTPD1
FOS
FTH1
HAVCR2
ITGAE
LAG3
LAYN
MKI67
PDCD1
TIGIT
TNFRSF9
TOX
F
PDCD1
CXCL13
ENTPD1
G
TRT Signature
vanderLeun_2020
Caushi_2021
Lowery_2022
Hanada_2022
Oliveira_2021
Wischnewski_2023

Figure 11. Gene expression profiles of TILs from metCRC5

(A) *Ex vivo* TILs from ovarian metastatic colorectal carcinoma patient 5 (metCRC5) were clustered based on gene expression profiles. **(B)** Heatmap indicating the score given to each cluster for TIL state signatures based on Andreatta et al, 2021[145]. **(C)** UMAP plots showing the expression of *CD8* and *CD4*. **(D and E)** Dot plots of selected gene sets related to (D) effector and (E) activation/exhaustion states[37,174,175] and its average expression (color gradient) by cluster. The size of the dot indicates the percentage of cells expressing the gene within each cluster. **(F)** UMAP plots showing the expression of relevant genes for tumor-reactive CD8⁺ T cells. **(G)** Heatmap indicating the score given to each cluster for tumor-reactive T cell (TRT) signatures based on the stated publications in the figure[37,153,170–173].

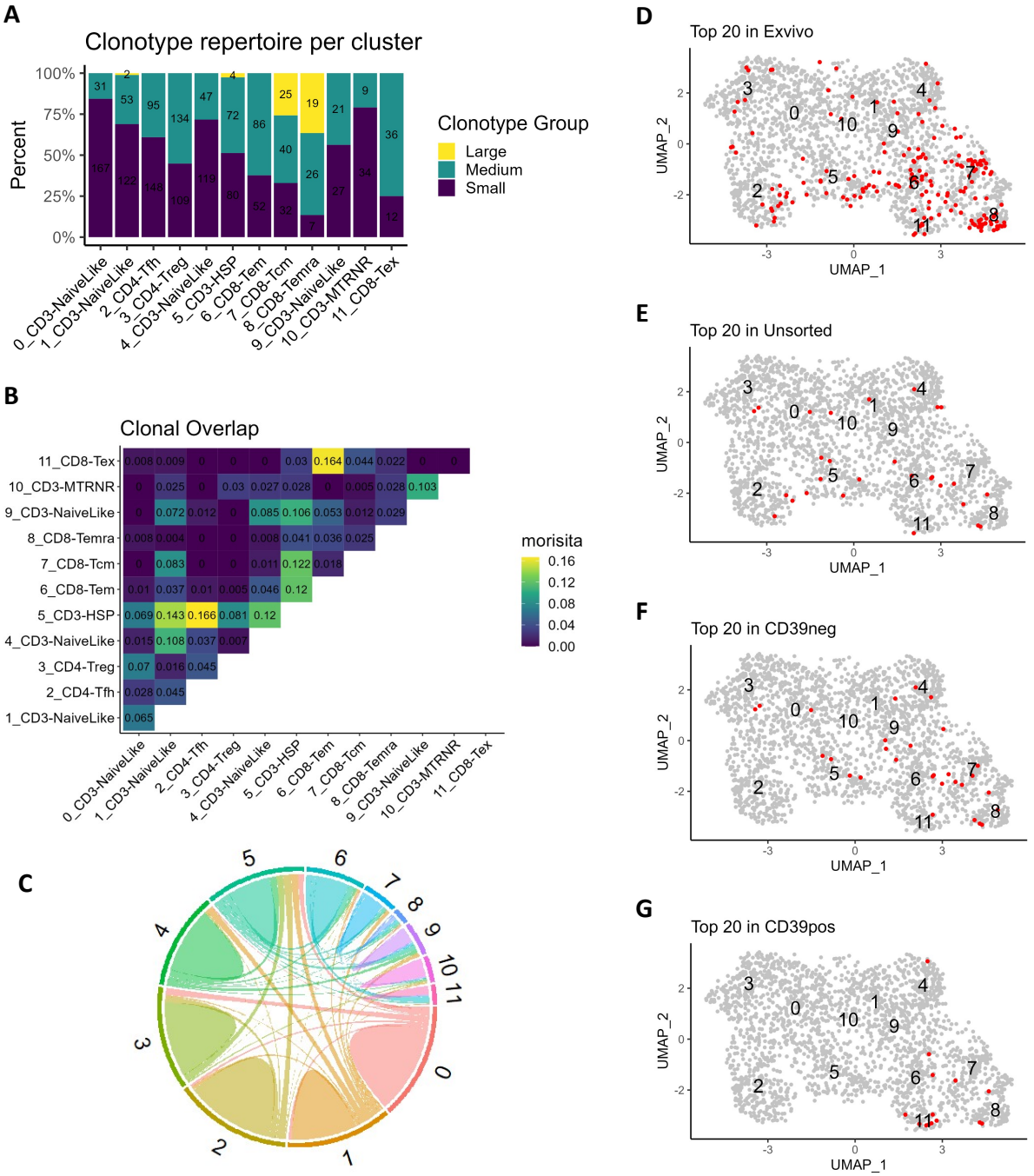

Figure 12. Combined analysis of TCR repertoire and gene expression profiles of TILs in metCRC5
(A) Relative percentage of different clonotype groups based on its dominance—large (1-10%), medium (0.1-1%), and small (0.01- 0.1%)—depicted for each TIL cluster from ovarian metastasis from colorectal cancer patient 5 (metCRC5). Numbers inside bars indicate cells within each clonotype group. **(B)** Clonal overlap between cell clusters calculated by the Morisita index, where higher coefficients indicate larger overlaps. **(C)** Chord diagram showing the TCR clonotype interconnection of clusters. Each chord represents the number of unique and shared clonotypes across colored clusters. **(D to G)** UMAP plots from Figure 11A highlighting (in red) cells expressing (D) the top 20-ranked TCRs in *ex vivo* TILs, and (E-G) TCRs within the top 20-ranked TCRs from expanded subsets (unsorted, CD39neg, and CD39pos) that were detected in *ex vivo* TILs.

3.3.2 Tumor-dominant T cell clones in an exhausted state proliferated in the unsorted and CD39$^+$ CD8$^+$ TIL subsets in patient OvCa12

In OvCa12, the TCR repertoire richness and evenness of expanded unsorted and CD39$^-$ TIL populations did not greatly differ from *ex vivo* TILs: the number of unique clonotypes per 100 cells ranged between 33 and 51, and the distribution of large, medium, and small clonotypes was comparable (Figure 13A and B). In contrast, the expanded CD39$^+$ TILs represented a more clonal population, with only 4 unique clonotypes per 100 cells, and mainly composed of large and hyperexpanded clonotypes (Figure 13A and B), similar to the CD39$^+$ T cell subset in metCRC5 (Figure 10A and B). The difference in the frequency of CD4$^+$ T cells at the end of the expansion (unsorted and CD39$^-$ TILs contained more than 70% CD4$^+$ T cells [see Figure 8B]), could explain the higher TCR diversity observed in these samples as CD4$^+$ T cells have been reported to be more diverse than CD8$^+$ T cells[176,177].

The expanded unsorted TILs had the highest TCR overlap with *ex vivo* TILs (0.317 Morisita index; Figure 13C). At the single clonotype level, they both shared the dominant clonotype at similar frequencies (1.8% and 1.1% in *ex vivo* and unsorted, respectively; Figure 13D, black arrow). When comparing the samples that showed tumor reactivity (unsorted and CD39$^+$), I observed that they shared their top two clonotypes (Supplementary Figure 6C, black and green arrows). The first TCR in CD39$^+$ TILs (14% of all cells) was also detected in the CD39$^-$ fraction (Supplementary Figure 6D, green arrow), suggesting that it might not be specific against tumor cells. On the contrary, the second TCR in CD39$^+$ TILs (6% of all cells) was the dominant clonotype previously observed in *ex vivo* and unsorted TILs, and was not detected in the CD39$^-$ population (Figure 13D to F, black arrow). Other dominant clonotypes in the CD39$^+$ CD8$^+$ TILs were also detected in the unsorted but not CD39$^-$ T subsets (Supplementary Figure 6C and D), which reflects the possibility of these clonotypes to be tumor-specific.

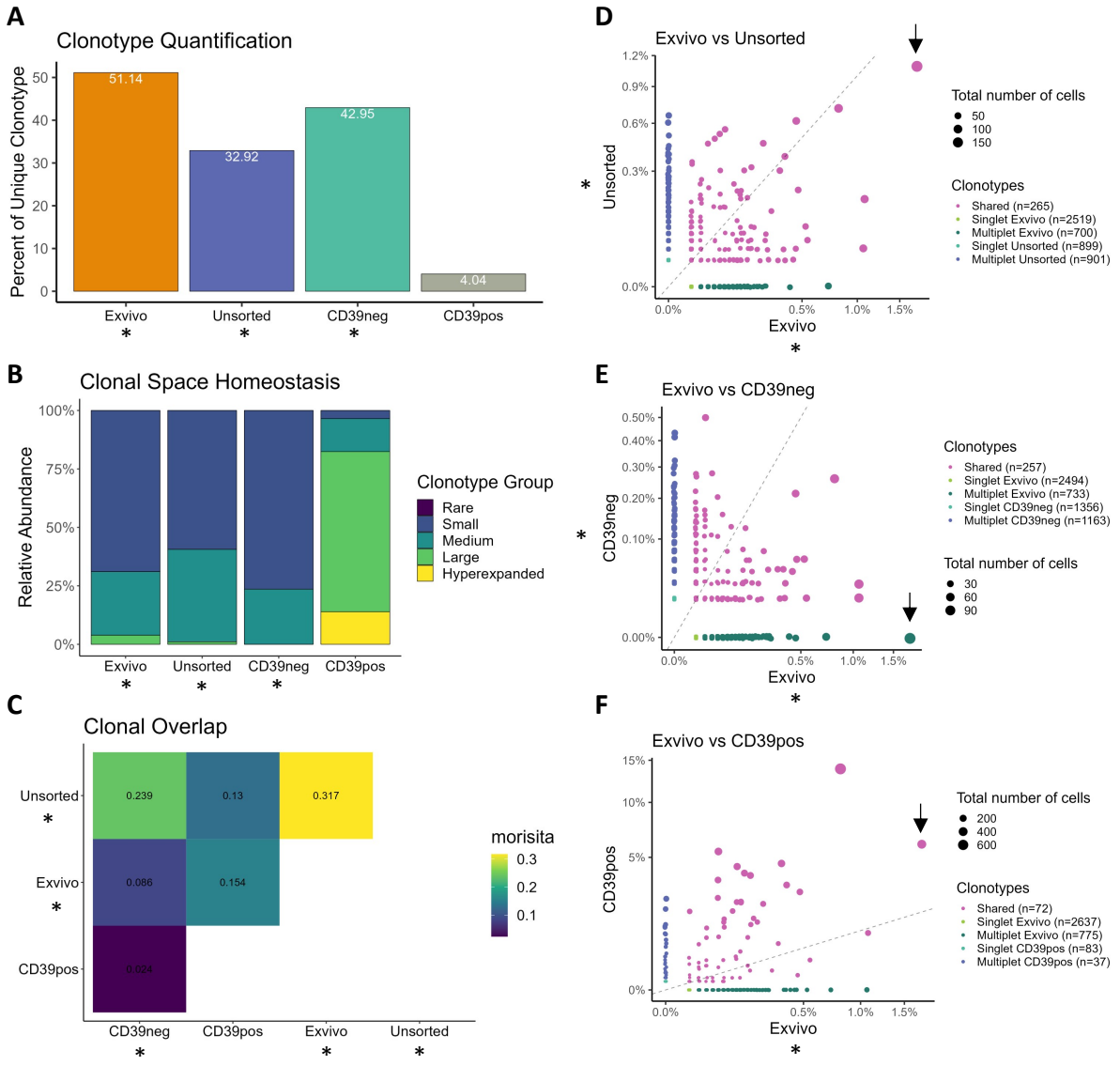

Figure 13. Characterization of the TCR repertoire in different TIL subsets from OvCa12
(A) Percentage of unique clonotypes found in different TIL populations from ovarian metastasis from colorectal carcinoma patient 5 (metCRC5), including the *ex vivo* TILs (Exvivo) and the expanded subsets (Unsorted, CD39neg and CD39pos). **(B)** The relative abundance of clonotypes grouped into classes based on its dominance in each sample: hyperexpanded (>10%), large (1-10%), medium (0.1-1%), small (0.01-0.1%) and rare (<0.01%) clones. **(C)** Clonal overlap between samples calculated by the Morisita index, where higher coefficients indicate larger overlaps. **(D to F)** Scatter plots comparing the clonotypes of *ex vivo* TILs with the expanded samples, where each dot corresponds to a unique TCR clonotype. The shared TCRs are shown in pink, the size of the circles indicates the total number of cells belonging to the clonotype, and the clonotypes closer to the diagonal are found in similar frequencies in both samples. Highlighted clonotypes are marked with arrows (black for *ex vivo* TILs). The symbol * indicates samples with 60-70% of $CD4^+$ T cells.

To understand whether these dominant clonotypes exhibited a gene expression profile characteristic of tumor-reactive $CD8^+$ T cells, I clustered and annotated *ex vivo* TILs from OvCa12 in the same manner as for metCRC5 TILs. I identified a total of 15 clusters (Figure 14A), and many of them were shared between both tumor samples.

Naive and memory-like T cell subsets (CD3-NaiveLike) were mainly identified in clusters 2, 6, 9, and 10 by ProjecTILs (Supplementary Figure 8A). I verified this annotation through the expression of genes related to naive and memory states (*CCR7*, *ANXA1*, *VIM*, *FTH1*, *IL7R*, *LMNA*, *SELL*, and *TCF7*; Supplementary Figure 8B and C) and gene signature scores for naive-like T cells[145] (Figure 14B). The main two $CD4^+$ TILs subsets found in metCRC5 were also abundant in OvCa12: $CD4^+$ T_{FH}-like cells (CD4-Tfh) in clusters 1 and 4 upregulated *CXCL13*, *BTLA*, and *CD200*; and $CD4^+$ T_{reg} cells (CD4-Treg) in clusters 0 and 8 expressed the T_{reg} marker *FOXP3* together with *IL2RA* (CD25), *ICOS*, and *TNFRSF9* (CD137) (Figure 14A and Supplementary Figure 8D).

$CD8^+$ TILs were grouped in the following five clusters, from more to less abundant: 1) cluster 3 was composed of cells defined as either T_{PEX} or T_{EX} by ProjecTILs (3_CD8-Tpex/Tex; Supplementary Figure 8A). The top differentially expressed genes in this cluster contained effector-like genes (*NKG7*, *CCL5*, *GZMB*, and *CTSW*; Supplementary Figure 8B), and I confirmed their activated/exhausted state by the expression of *HAVCR2* (TIM3), *ITGAE* (CD103), *TIGIT*, *TNFRSF9* (CD137), and *TOX* (Figure 14E). 2) Cells in cluster 5 were identified as either T_{CM} or T_{EM} cells by ProjecTILs (5_CD8-Tcm/Tem; Supplementary Figure 8A). The expression of memory-related markers (*CCR7*, *IL7R*, and *GPR183*), and effector-like genes (*GZMK*, *GZMA*, and *NKG7*) supports the presence of both T_{CM} and T_{EM} subsets (Figure 14D and Supplementary Figure 8A and B). In addition, the expression level of immune inhibitory receptors was lower in this cluster compared to cluster 3_CD8-Tpex/Tex (Figure 14E). 3) Another cluster of $CD8^+$ T_{EM} cells was identified in cluster 11 (11_CD8-Tem) and upregulated the effector molecules *CCL4*, *GZMA/B/H/K*, and *NKG7* (Figure 14D). Furthermore, this cluster had the highest expression of the cytokines *IFNG* and *TNF* (Figure 14D), indicating an activated state. 4) Cluster 13 was annotated as a small cluster of dividing $CD8^+$ T_{EX} cells (13_CD8-Tex) based on the expression of *MKI67* (Figure 14E). This cell group resembled the gene expression profile of cells in cluster 3_CD8-Tpex/Tex based on the upregulation of effector (*CCL3*, *CCL4*, *NKG7*) and exhaustion (*HAVCR2*, *LAG3*, *TOX*) genes (Figure 14D and E). 5) Last, I found a small cluster of $CD8^+$ T_{CM} (14_CD8-Tcm), which differentially expressed the cytotoxic molecule *GNLY* (Figure 14D and Supplementary Figure 8B). Among the identified $CD8^+$ TIL clusters, cluster 3_CD8-Tpex/Tex, and in particular the fraction of cells defined as T_{EX}, was the subset that expressed higher levels of tumor-reactive T cell markers, such as *CXCL13*, *PDCD1* (PD1), and *ENTPD1* (CD39). This was corroborated with the TRT signature score, which was the highest in 3_CD8-Tpex/Tex cells. The proliferating cluster 13_CD8-Tex also scored high for two out of the six TRT signatures. In short, as observed in metCRC5, $CD8^+$ T_{EX} cells best correlated with markers and gene signatures previously proposed for tumor-reactive $CD8^+$ T cells.

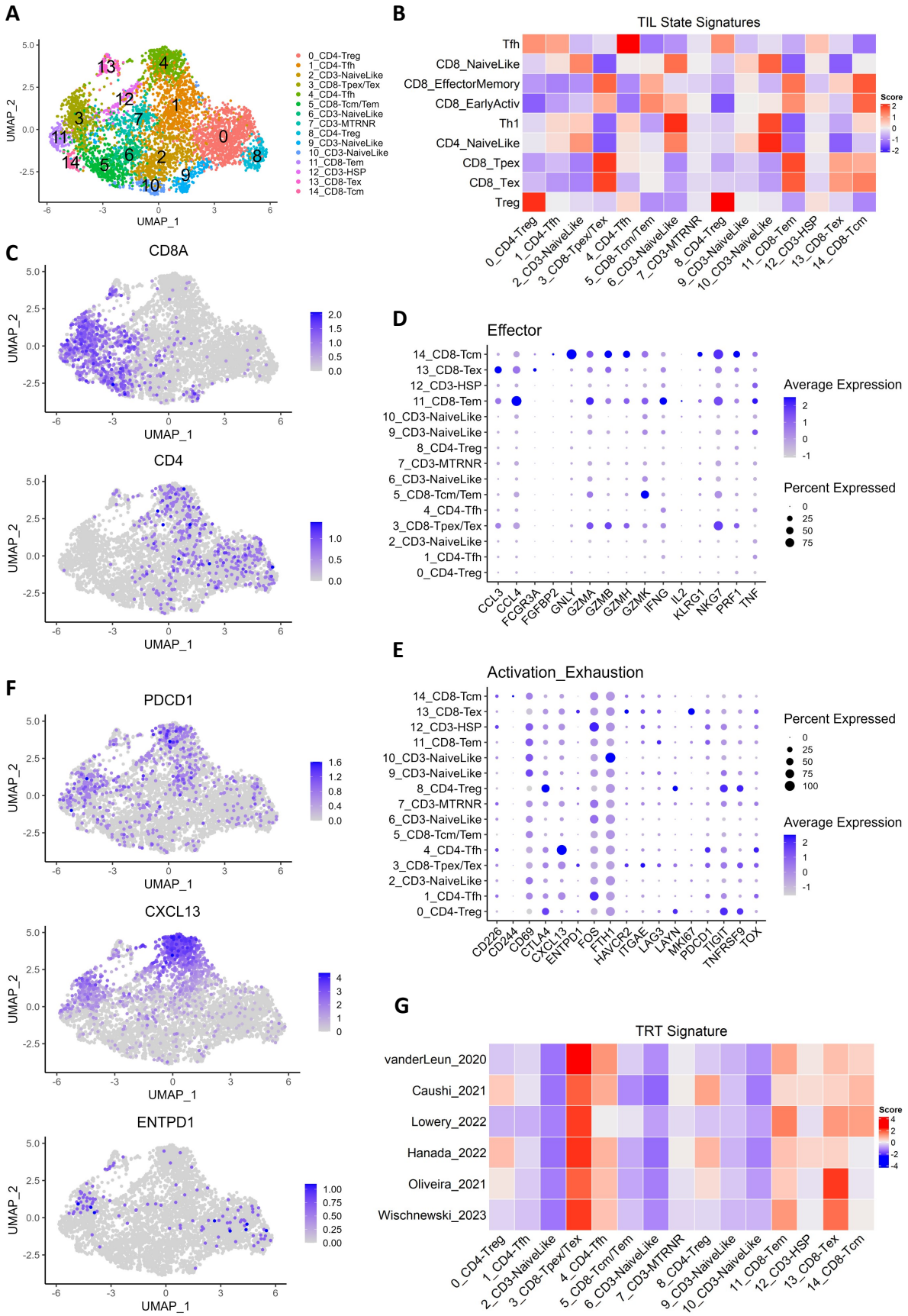
A
0_CD4-Treg
1_CD4-Tfh
2_CD3-NaiveLike
3_CD8-Tpex/Tex
4_CD4-Tfh
5_CD8-Tcm/Tem
6_CD3-NaiveLike
7_CD3-MTRNR
8_CD4-Treg
9_CD3-NaiveLike
10_CD3-NaiveLike
11_CD8-Tem
12_CD3-HSP
13_CD8-Tex
14_CD8-Tcm
UMAP_1
UMAP_2
B
TIL State Signatures
Tfh
CD8_NaiveLike
CD8_EffectorMemory
CD8_EarlyActiv
Th1
CD4_NaiveLike
CD8_Tpex
CD8_Tex
Treg
Score
C
CD8A
CD4
D
Effector
Average Expression
Percent Expressed
CCL3
CCL4
FCGR3A
FGFBP2
GNLY
GZMA
GZMB
GZMH
GZMK
IFNG
IL2
KLRG1
NKG7
PRF1
TNF
E
Activation_Exhaustion
CD226
CD244
CD69
CTLA4
CXCL13
ENTPD1
FOS
FTH1
HAVCR2
ITGAE
LAG3
LAYN
MKI67
PDCD1
TIGIT
TNFRSF9
TOX
F
PDCD1
CXCL13
ENTPD1
G
TRT Signature
vanderLeun_2020
Caushi_2021
Lowery_2022
Hanada_2022
Oliveira_2021
Wischnewski_2023

Figure 14. Gene expression profiles of TILs from OvCa12
(A) *Ex vivo* TILs from ovarian carcinoma patient 12 (OvCa12) were clustered based on gene expression profiles. **(B)** Heatmap indicating the score given to each cluster for TIL state signatures based on Andreatta et al, 2021[145]. **(C)** UMAP plots showing the expression of *CD8* and *CD4*. **(D and E)** Dot plots of selected gene sets related to (D) effector and (E) activation/exhaustion states[37,174,175] and its average expression (color gradient) by cluster. The size of the dot indicates the percentage of cells expressing the gene within each cluster. **(F)** UMAP plots showing the expression of relevant genes for tumor-reactive $CD8^+$ T cells. **(G)** Heatmap indicating the score given to each cluster for tumor-reactive T cell (TRT) signatures based on the stated publications in the figure[37,153,170–173].

The relative abundance of clonotypes per cluster showed that among $CD8^+$ TILs, clusters 3_CD8-Tpex/Tex, 11_CD8-Tem, and 13_CD8-Tex contained the higher fraction of cells with large and medium clonotypes (Figure 15A and D). The clonal overlap between these three groups was relatively high, particularly for clusters 3_CD8-Tpex/Tex and 13_CD8-Tex (0.651 Morisita index; Figure 15B). In line with this correlation, I observed that approximately one-third of clonotypes in 11_CD8-Tem and half of clonotypes in 13_CD8-Tex were shared with cluster 3_CD8-Tpex/Tex (Figure 15C). As T_{PEX} were mostly detected in cluster 3, I speculate that some clones in this group may have given rise to more differentiated cells in clusters 11 and 13.

Clonotypes within the top 20 TCRs in unsorted and $CD39^+$ TIL expanded subsets that were detected in *ex vivo* TILs (10 and 17 unique TCRs, respectively) originated from the aforementioned $CD8^+$ T cell clusters (clusters 3, 11, and 13, Figure 15E and G). Only 4 unique TCRs from the top 20 clonotypes in $CD39^-$ TILs were detected in the *ex vivo* TILs, and they were also found in cluster 3_CD8-Tpex/Tex. This analysis is in line with the overlap observed in dominant clonotypes between unsorted and $CD39^+$ $CD8^+$ TILs, and the data confirmed that these clonotypes originated in both cases from the same exhausted $CD8^+$ T cell subsets.

In conclusion, I found similar TIL phenotypes at RNA level in both metCRC5 and OvCa12 TILs. Particularly, I identified $CD8^+$ T cell clusters with activated phenotypes, including cells in cytotoxic and (pre-)exhausted states. In metCRC5, dominant clonotypes were mostly in cytotoxic states related to bystander T cells and did not greatly proliferate *in vitro*, while smaller clonotypes in exhausted states were selected and expanded in the $CD39^+$ $CD8^+$ T cell subset. In OvCa12, exhausted T cells were enriched and expanded in the $CD39^+$ but not in the $CD39^-$ fraction. They were also the predominant $CD8^+$ T cells in the tumor and had the capability to expand without any selection in the unsorted TIL population. This data further supports that exhausted $CD39^+$ $CD8^+$ TILs may contain tumor-reactive T cells, and despite their exhaustion, some clones remained capable of proliferating *in vitro*.

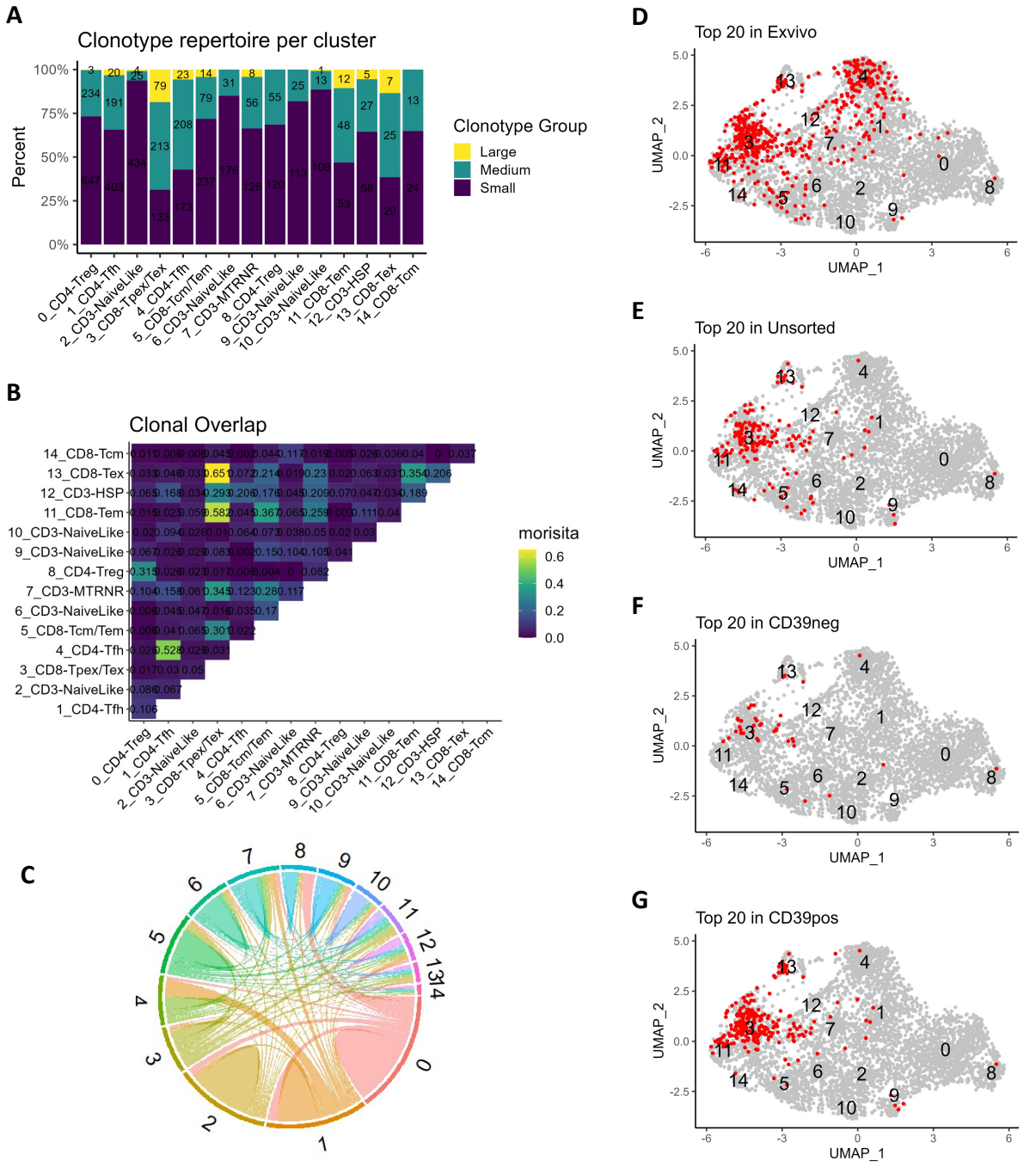

Figure 15. Combined analysis of TCR repertoire and gene expression profiles of TILs in OvCa12
(A) Relative percentage of different clonotype groups based on its dominance—hyperexpanded (>10%), large (1-10%), medium (0.1-1%), small (0.01-0.1), and rare (<0.01%)—depicted for each TIL cluster from ovarian carcinoma patient 12 (OvCa12). Numbers inside bars indicate cells within each clonotype group. **(B)** Clonal overlap between cell clusters calculated by the Morisita index, where higher coefficients indicate larger overlaps. **(C)** Chord diagram showing the clonotype interconnection of clusters. Each chord represents the number of unique and shared clonotypes across colored clusters. **(D to G)** UMAP plots from Figure 14A highlighting (in red) cells expressing (D) the top 20-ranked TCRs in *ex vivo* TILs, and (E-G) TCRs within the top 20-ranked TCRs from expanded subsets (unsorted, CD39neg, and CD39pos) that were detected in *ex vivo* TILs.

3.4 Spatial distribution of tumor-reactive CD8⁺ TILs in tumor tissues using the MICS technology

Lastly, I examined the spatial distribution and interactions of T cells within the tumor microenvironment (TME), which represent crucial aspects for the advancement of cancer immunotherapies[178]. To achieve this goal, I used our recently developed multiplexed immunofluorescent imaging platform MICS (MACSima™ Imaging Cyclic Staining) on tumor tissue sections. First, I conducted a comprehensive characterization of the composition and spatial distribution of tumor, stromal, and immune cells in the TME. Second, I investigated the proximity of T cells expressing markers linked to tumor reactivity, particularly CD39, to tumor regions, which could indicate potential interactions with or recognition of tumor cells by tumor-reactive TILs.

3.4.1 MICS as a new tool to study the tumor microenvironment

The MICS technology enables simultaneous analysis of virtually unlimited number of markers in a single tissue section at the protein level by sequential staining, image acquisition, and erasure of the fluorescent signal. Therefore, it allows multiparametric analyses of scarce biological samples[179]. A detailed description of the MICS workflow can be found in Methods sections 2.2.6. and 2.2.7. I depicted a schematic representation of this workflow in Figure 16, which shows the steps from reagent preparation to image generation and processing.

To be able to establish correlations with data generated in preceding sections of my PhD thesis, I primarily used tissue sections from the same tumor samples, such as the ovarian metastasis of colorectal cancer sample from patient 5 (metCRC5). However, due to the unavailability of certain samples for microscopic analysis, I incorporated additional samples, in this case a serous ovarian adenocarcinoma that contained tertiary lymphoid structures (TLS) (OvCa-TLS). The identification and spatial distribution of cell types within the TME for both metCRC5 and OvCa-TLS tissues were accomplished through a visual inspection of the images.

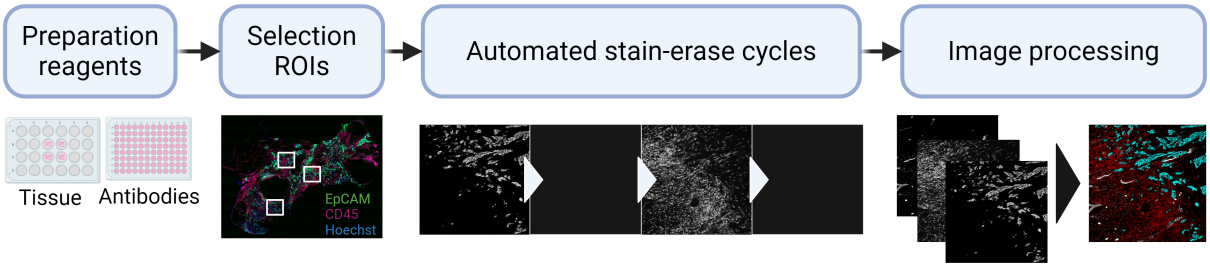

Figure 16. The MICS workflow
The MICS workflow included the preparation of reagents (tissue slices and antibodies) and the selection of regions of interest (ROIs) by the user, followed by the automatic cyclic steps (staining, image acquisition, and signal erasure) performed by the MACSima instrument. The raw images were processed by a custom pipeline (Methods section 2.2.7) to correct and align the images. Created with Biorender by Elvira Criado-Moronati.

The TME of metCRC5 is largely infiltrated by T cells and macrophages

To identify tumor regions for the analysis, I prepared hematoxylin and eosin (H&E) images (Figure 17A and B) and shared them with our affiliated pathologist, Prof. Dr. med. Philipp Ströbel (Universitätsmedizin Göttingen) who differentiated between malignant tissue from healthy tissue in the metCRC5 sample. Additionally, I identified immune-infiltrated tumor areas by staining tissues with EpCAM for tumor cells[155] and CD45 for leukocytes to facilitate the study of TIL phenotypes in proximity to cancer cells. Guided by these criteria, I selected three regions of interest (ROIs 1-3; Figure 17C). To comprehensively characterize the TME, I used a panel of 98 antibodies (Table 13 in Material section 2.1.7) that targeted markers expressed on various cell types, such as tumor cells, stromal cells, and immune cells. This extensive set of antibodies was particularly curated to include markers specific to T cells, enabling a more detailed characterization of this cell type in the following subsection 3.4.2.

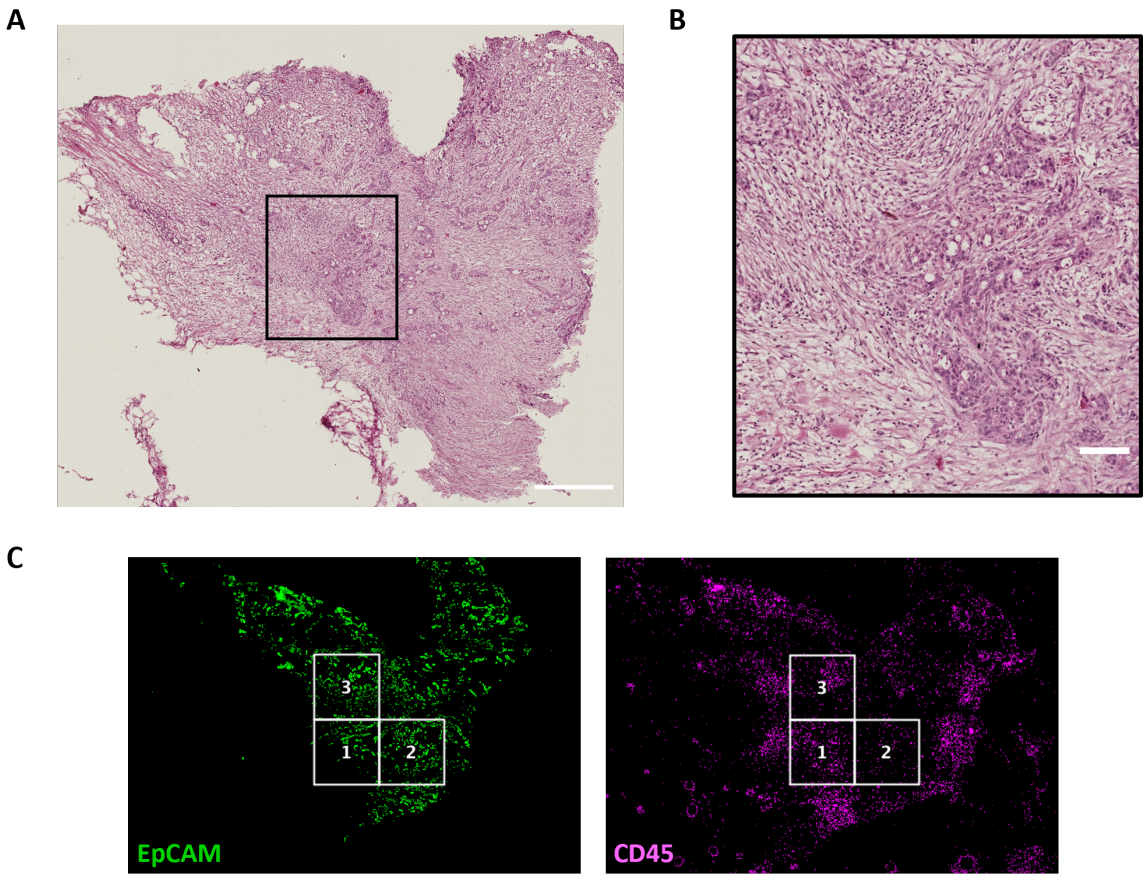

Figure 17. Whole tissue overview of the metCRC5 sample
(A) A section of the tissue was used for hematoxylin and eosin (H&E) staining for pathological evaluation. The black square indicates the magnification shown in B. **(B)** A 10x magnification of the tumor area on the H&E image. **(C)** The consecutive tissue section used for the MICS experiment was pre-stained with EpCAM (green, tumor) and CD45 (magenta, leukocytes) to choose the regions of interest (1-3 squares). Scale bars in (A): 500 µm and (B): 100 µm.

Within these regions, I analyzed the content of tumor, stromal, and immune cells, including T cells, B cells, plasma cells, and myeloid cells. In ROI 1, $EpCAM^+$ tumor cells were located in the upper right quadrant, while ROIs 2 and 3 displayed a homogenous distribution of tumor cells (Figure 18A, Figure 20A, and Supplementary Figure 9A). Furthermore, $EpCAM^+$ cells also expressed TSPAN8, a marker reported to be over-expressed in colorectal cancer cells[180] (Figure 18B, Figure 20B, and Supplementary Figure 9B). The expression of Ki67—a proliferation marker associated with tumor growth and aggressiveness[181]—was observed in cancer cells, indicating a region with dividing tumor cells (Figure 18B, Figure 20B, and Supplementary Figure 9B). Blood vessels (or endothelial cells) were identified in all ROIs by the expression of CD31, CD105, and CD34—markers that have been previously used to define endothelial cells in tumors[182] (Figure 18A and B, Figure 20A and B, and Supplementary Figure 9A and B). In addition, I identified cancer-associated fibroblasts (CAFs) by expression of the adhesion protein CD90, as previously reported[183]. Blood vessels also expressed CD90, which is in accordance with studies showing its upregulation on activated endothelial cells and its involvement in leukocytes recruitment to inflamed tissues[184] (Figure 18B, Figure 20B and Supplementary Figure 9B).

In the immune cell compartment, $CD3^+$ T cells formed a dense network in the stroma of ROI 1, whereas a smaller but distinct population of T cells infiltrated tumor-rich areas (ROIs 2 and 3; Figure 18A, Figure 20A, and Supplementary Figure 9A). ROI 1 may thus correspond to the edges of this tumor section, where immune cells accumulated. I identified both $CD8^+$ and $CD4^+$ T cell subsets and investigated relevant markers for tissue residency and activation/exhaustion, including CD103, PD1, and particularly, CD39 (Figure 18C, Figure 20C, and Supplementary Figure 9C). A detailed characterization of $CD8^+$ T cells is shown in the following subsection 3.4.2. Of note, I observed CD39 to be expressed not only in T cells, but also in other cell types, with a particularly high expression in endothelial cells. This expression pattern is in line with previous studies of various tumors, showing that CD39 is expressed by different immune cell types (including myeloid cells and regulatory T cells), CAFs, and endothelium[185].

Regarding B cell infiltration, I did not observe mature $CD19^+$ B cells in the studied ROIs. However, plasma cells defined by the co-expression of CD138 and CD38 were mainly present in ROI 1 and ROI 3 (Figure 18A and D, Figure 20A and D, and Supplementary Figure 9A and D). Additional markers further confirmed the presence of PCs, such as the absence of CD19 and expression of CD27 (Figure 19A).

These observations are in accordance with studies that describe the infiltration of B cells in specialized niches such as TLSs—not present in the studied ROIs—in contrast to plasma cells, which tend to disseminate into the tumor bed, contributing to the local secretion of antibodies against tumor antigens[186,187].

With respect to myeloid cells, the staining of CD14 revealed a large fraction of myeloid cells that accumulated in the stroma of ROI 1 and infiltrated the tumor areas of ROIs 2 and 3 (Figure 18A, Figure 20A, and Supplementary Figure 9A). The staining pattern of CD14 correlated with other monocyte/macrophage-associated markers, including CD64 and CD68, as well as the class II MHC molecule HLA-DR, which is prominently expressed by antigen-presenting cells (APCs) and has been reported on $CD14^+$ tumor-associated macrophages (TAMs)[188,189] (Figure 18D). Furthermore, $CD14^+$ myeloid cells were frequently observed in close proximity to blood vessels, consistent with their vascular-modulating function in tumors[33] (Figure 19B). Finally, the staining of CD1c revealed the presence of a minor population of $CD1c^+$ cells that co-expressed CD101 and was in close contact to tumor cells and T cells (Figure 18D, Figure 19C, and Figure 20D). These cells may correspond to a subset of conventional dendritic cells type 2 (cDC2s), which have a crucial role in the initiation of immune responses by picking up tumor antigens in tumors and presenting them to helper $CD4^+$ T cells[190,191].

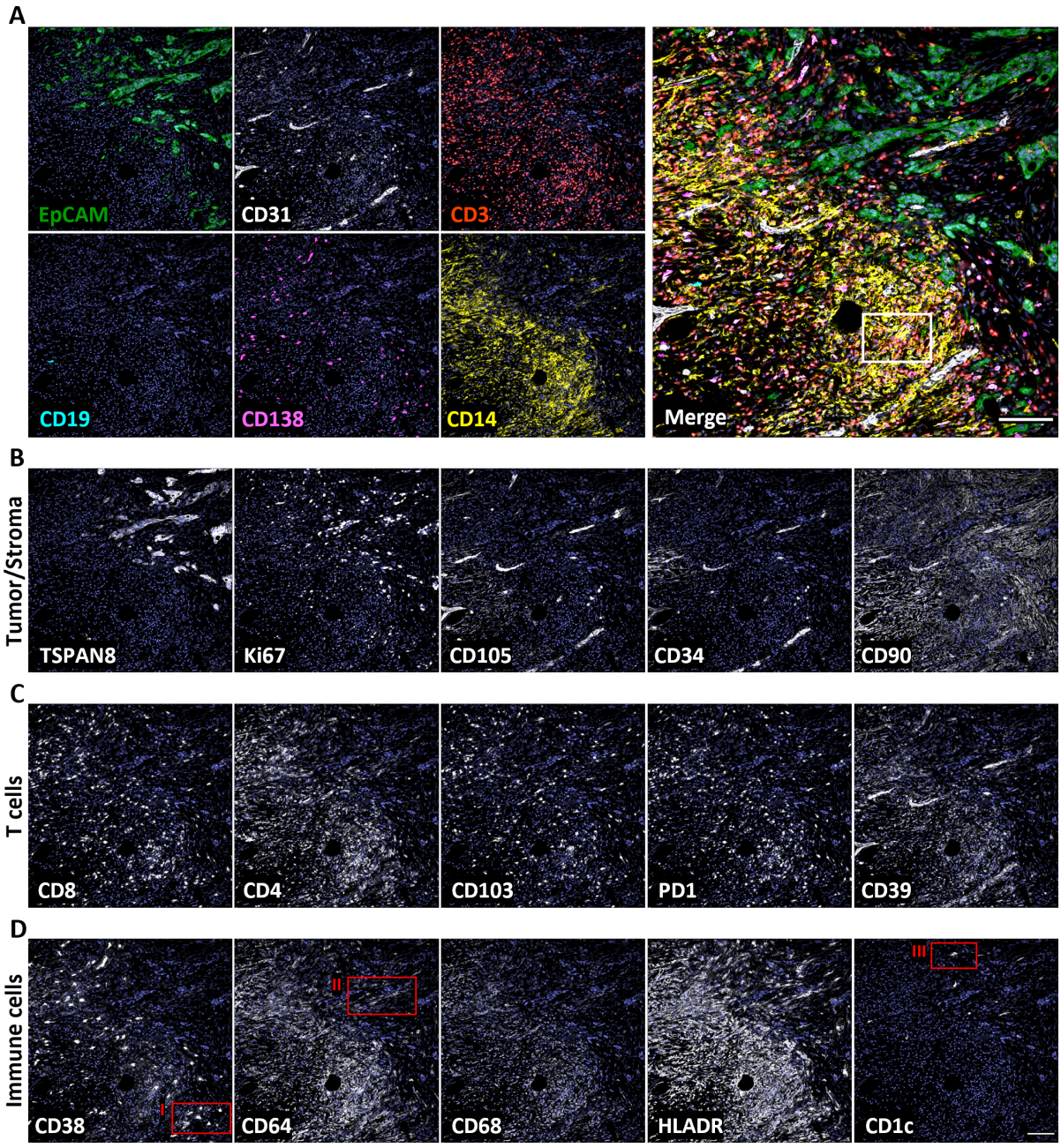

Figure 18. Visual identification of various cell types in the TME of ROI 1 from metCRC5
(A) Markers for the main cell types in the TME, such as EpCAM$^+$ tumor (green), CD31$^+$ endothelium (white), CD3$^+$ T cells (red), CD19$^+$ B cells (cyan), CD138$^+$ plasma cells (magenta), and CD14$^+$ myeloid cells (yellow), are shown on the left side, and the overlay of these stainings on the right side. White square represents the location of image magnification in Supplementary Figure 13A. **(B to D)** Representative markers found in (B) tumor/stroma, (C) T cells, and (D) several immune cell types are depicted in white. Nuclei are stained with Hoechst (blue) in all images. Red squares represent the location of image magnifications (I to III) in Figure 19. Scale bar: 100 µm.

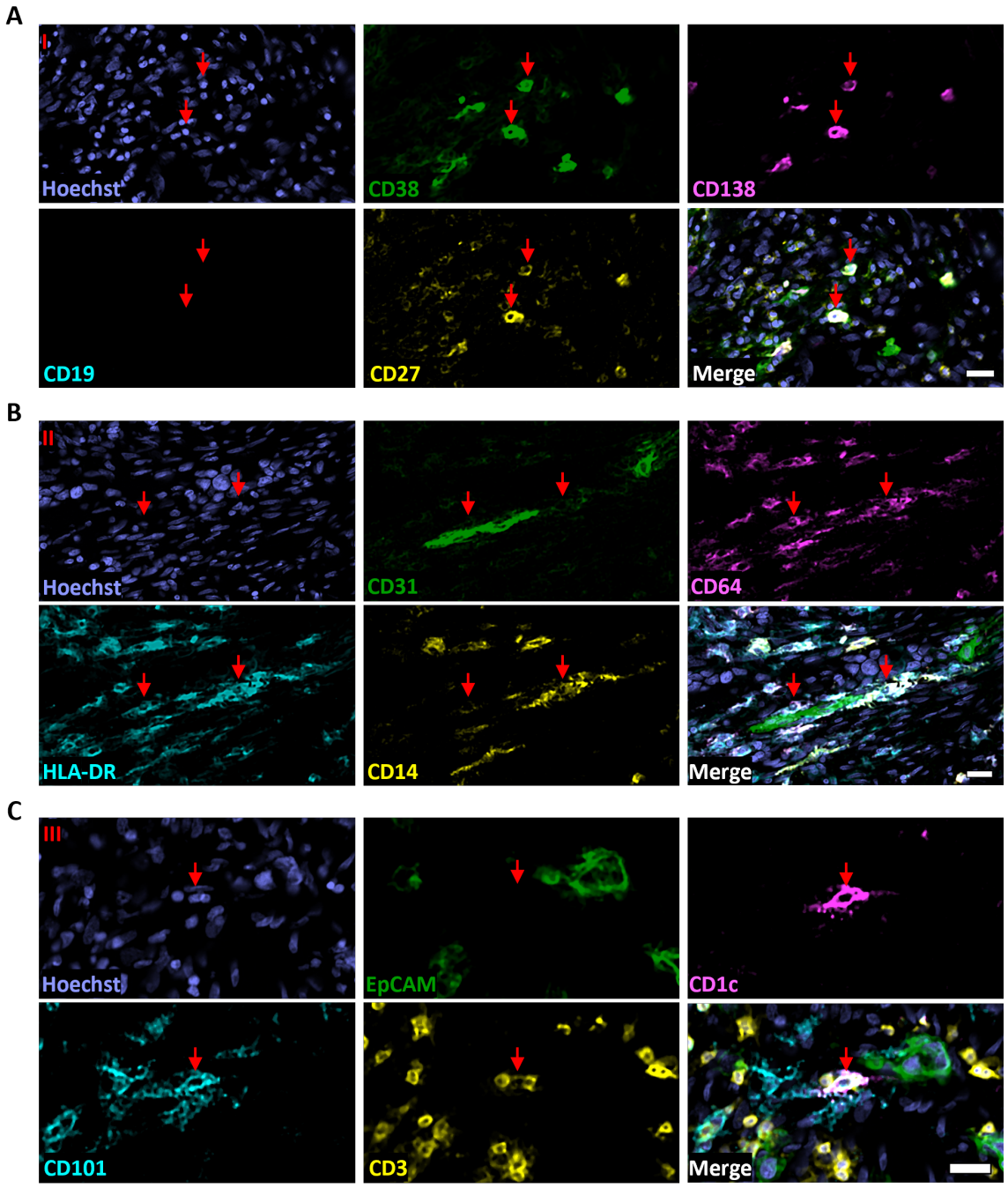

Figure 19. Marker expression patterns in different cell types in ROI 1 from metCRC5
Image magnifications from ROI 1 (Figure 18) showing co-expression of relevant markers for **(A)** $CD138^+$ plasma cells, **(B)** $CD14^+$ myeloid cells, and **(C)** $CD1c^+$ dendritic cells. Nuclei are stained with Hoechst (blue) in all images. Red arrows highlight cells of interest. Scale bar: 20 µm

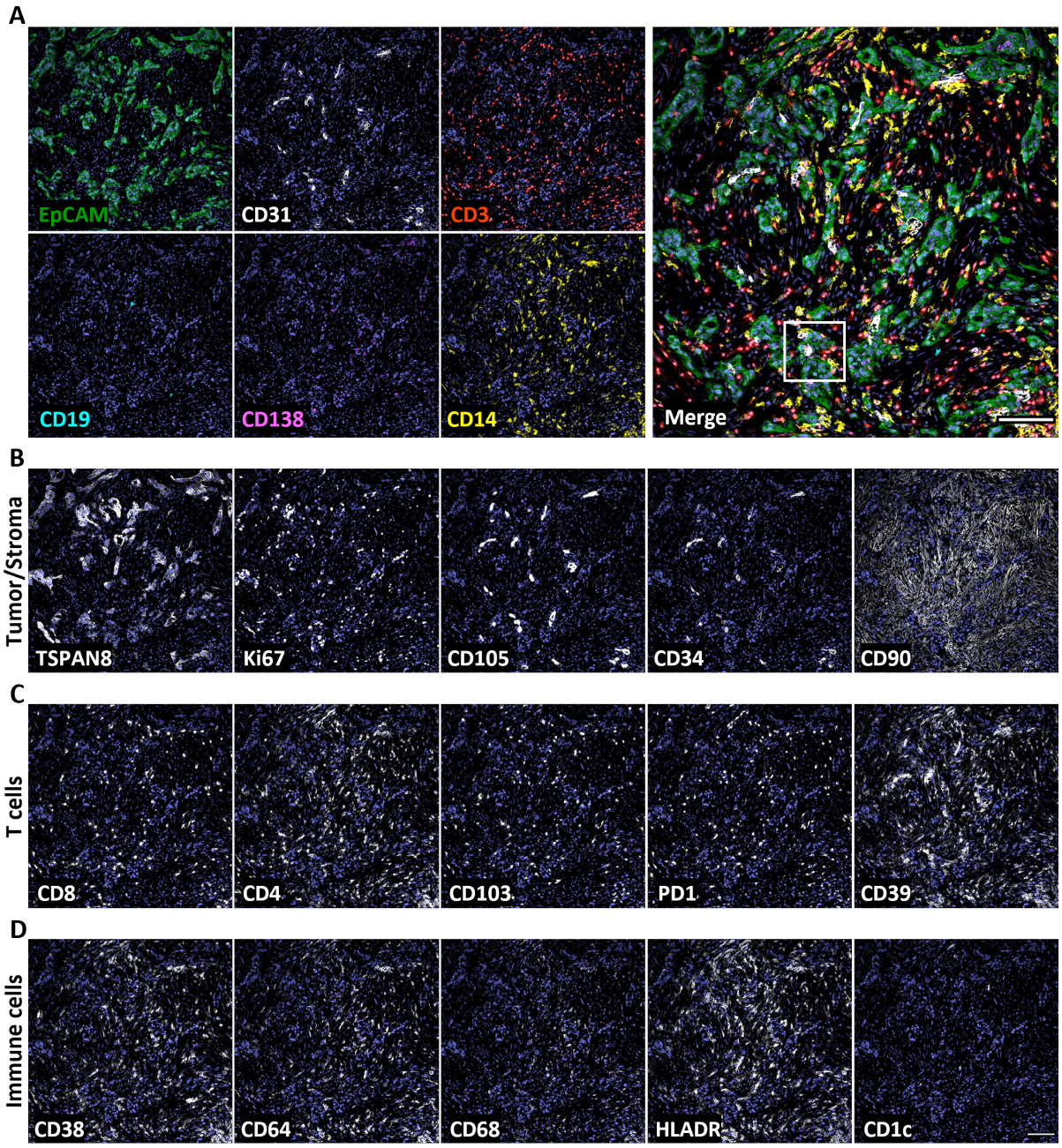

Figure 20. Visual identification of various cell types in the TME of ROI 2 from metCRC5
(A) Markers for the main cell types in the TME, such as EpCAM$^+$ tumor (green), CD31$^+$ endothelium (white), CD3$^+$ T cells (red), CD19$^+$ B cells (cyan), CD138$^+$ plasma cells (magenta), and CD14$^+$ myeloid cells (yellow), are shown on the left side, and the overlay of these stainings on the right side. White square represents the location of image magnification in Figure 26. **(B to D)** Representative markers found (B) in tumor/stroma, (C) T cells, and (D) several immune cell types are depicted in white. Nuclei are stained with Hoechst (blue) in all images. Scale bar: 100 µm.

In conclusion, the MICS technology facilitated the identification of multiple cell subsets within the three examined ROIs of this tissue section from metCRC5. The TME exhibited features indicative of a "hot" or immune-infiltrated tumor, as evidenced by the presence of T cells in tumor regions.

The TME of an OvCa sample contained tertiary lymphoid structures and exhibited poor infiltration of immune cells into the tumor mass

The second tumor tissue analyzed was a serous ovarian carcinoma (OvCa) sample. I selected a total of eight regions of interest based on the H&E and immunofluorescent images (Figure 21). These ROIs included tumor areas and immune aggregates located in the periphery of the tumor, which may correspond to tertiary lymphoid structures (TLSs). These organized ectopic structures that resemble lymph nodes are involved in initiating local immune responses[15] and have been correlated with positive prognosis in various cancer types[192,193]. Furthermore, previous studies revealed different transcriptional signatures between T cells from TLSs and tumor[194]. I thus used the MICS technology to investigate the heterogeneity and spatial organization of cells, including tumor, stromal, and immune cell subsets localized not only in TLSs (ROIs 4, 5, and 6), but also in tumor edges (ROIs 1 and 7) and tumor mass areas (ROIs 2, 3, and 6; Figure 21C).

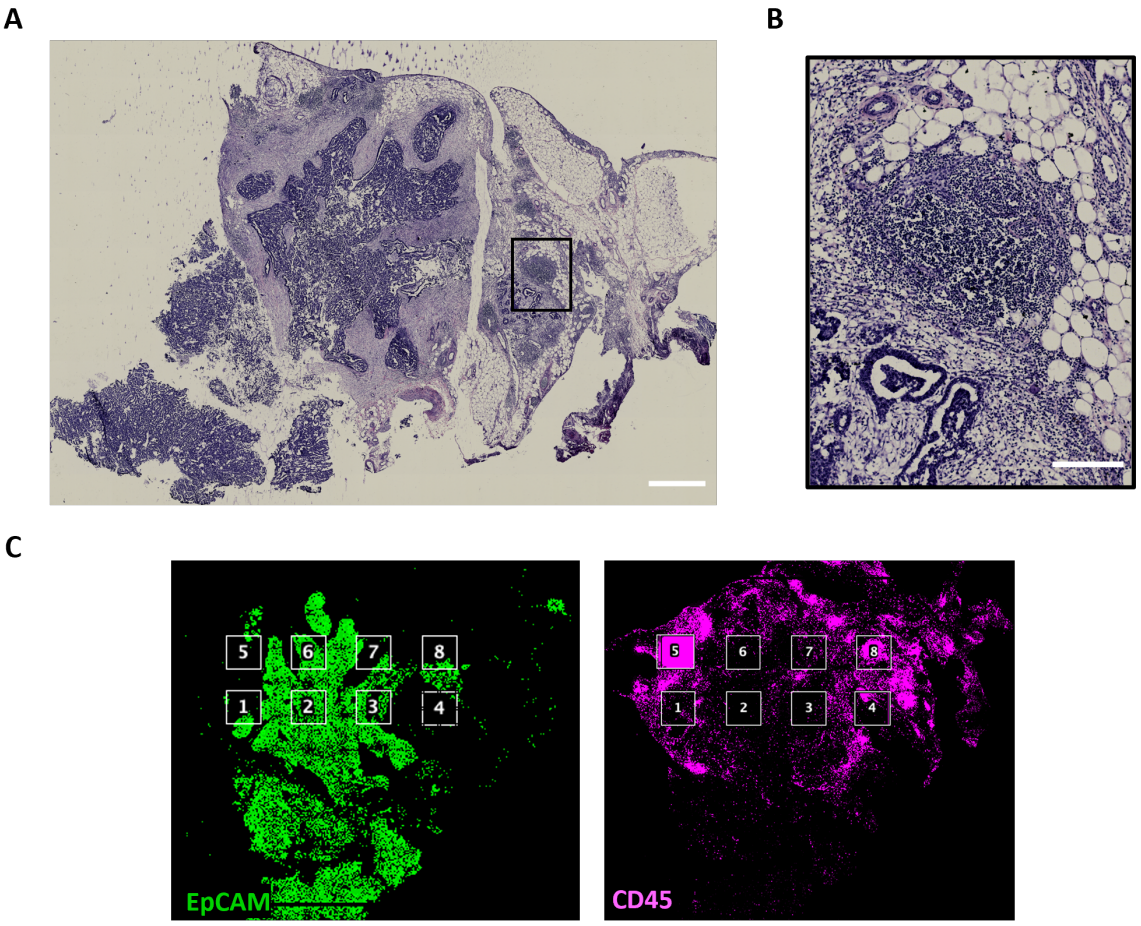

Figure 21. Whole tissue overview of the OvCa sample
(A) A section of OvCa tissue was used for hematoxylin and eosin (H&E) staining for pathological evaluation. The black square indicates the magnification shown in B. **(B)** A representative 10x magnification of a potential tertiary lymphoid structure in this tissue is shown. **(C)** The tissue section used for the MICS

experiment was pre-stained with EpCAM (green, tumor) and CD45 (magenta, leukocytes) to choose the regions of interest (1-8 squares) in the MACSima instrument. Scale bars in (A): 1 mm and (B): 200 µm.

The TLS in ROI 8, taken as a representative example, was located in the proximity of tumor cell islets that expressed EpCAM and CD56, both markers found in epithelial ovarian cancers[195,196] (Figure 22A and B). Moreover, tumor cells in this area were not actively proliferating based on the absence of Ki67 expression (Figure 22B). Blood vessels were present inside and outside the immune aggregate and co-expressed the endothelial markers CD31 and CD105 (Figure 22A and B). Additionally, I identified high endothelial venules (HEVs) within the TLS by MECA-79 expression (Figure 22B). HEVs are specialized blood vessels that facilitate the trafficking of lymphocytes from blood to secondary lymphoid organs and other lymphoid-like structures such TLSs[15]. ROI 8 did not correspond to a CAF-rich area based on the expression of CD90, which was mostly detected on endothelial cells and indicated the presence of activated blood vessels that facilitate leukocyte recruitment to the TLS (Figure 22B).

Regarding immune cells, this structure was well organized into a T cell zone enclosing a B cell zone (Figure 22A), which, together with the presence of HEVs, is a main hallmark of *bona fide* TLSs[20]. As presented in the Introduction section 1.2.1, different TLS subtypes have been described based on its developmental stage: immature or early TLSs, intermediate mature or primary follicle-like TLSs that have follicular dendritic cells (FDCs) but lack germinal center (GC) reactions, and fully mature or secondary follicle-like TLSs that contain active GC reactions. I thus determined the maturation state of this TLS based on the presence or absence of relevant cell types.

In the T cell zone, I observed a prevalence of $CD4^+$ T cells, with some T cells expressing representative markers of follicular helper T cells (T_{FH}), such as PD1 and ICOS[19] (Figure 22C and Figure 23A). The study of other T_{FH}-related markers, including the B cell attractant chemokine CXCL13 and its receptor CXCR5, the transcription factor B-cell lymphoma 6 (BCL6), and IL-21, would confirm the presence of this T cell subset that is typically present in more mature TLSs[19]. $CD8^+$ T cells were scattered throughout the T cell zone, outside the TLS, and in the B cell zone, suggesting B cell-mediated cross-presentation of antigens to $CD8^+$ T cells, as previously reported[197] (Figure 22C). A detailed characterization of $CD8^+$ T cells in TLS is shown in the following subsection 3.4.2.

In the B cell zone, the majority of $CD19^+$ B cells expressed IgD, IgM, CD23, and CD24 (Figure 22D and Figure 23B). Some B cells had low expression levels of the memory marker CD27 and no expression of the activation marker CD38. This expression pattern suggests the presence of resting naive (IgD^+ IgM^+ $CD27^-$ $CD38^-$ $CD24^+$) and unswitched memory (IgD^+ IgM^+ $CD27^+$ $CD38^-$ $CD24^+$) B cells[198]. The high proportion of unswitched B cell subsets indicates that this TLS does not contain an active GC. Additionally, the expression of CD1c, found in B cells located in the mantle zone that surrounds GCs in lymphoid organs, and the absence of both the proliferation marker Ki67 and the activation marker

CD86 on B cells are consistent with a resting state. However, the presence of large numbers of PCs, defined by the co-expression of CD38, CD138, CD19, and CD27, in the periphery of the TLS suggests that GC reactions have occurred or are currently taking place (Figure 22A and Figure 23C).

A dense network of $CD21^+$ $CD35^+$ FDCs and activated, mature $CD86^+$ $CD40^+$ DCs were present in the B cell and T cell zones, respectively (Figure 22E). The presence of these DC subsets is associated with a more mature TLS state. Therefore, even though no GC B cells have been detected in this TLS, which could indicate a primary follicle-like TLS, the existence of PCs and activated DCs suggests a more advanced maturation state. The cell composition of the other TLSs in this tissue section was similar to this TLS, but the distribution and size of the TLSs varied, probably due to their maturation and their location within the 2D tissue slice (Supplementary Figure 10).

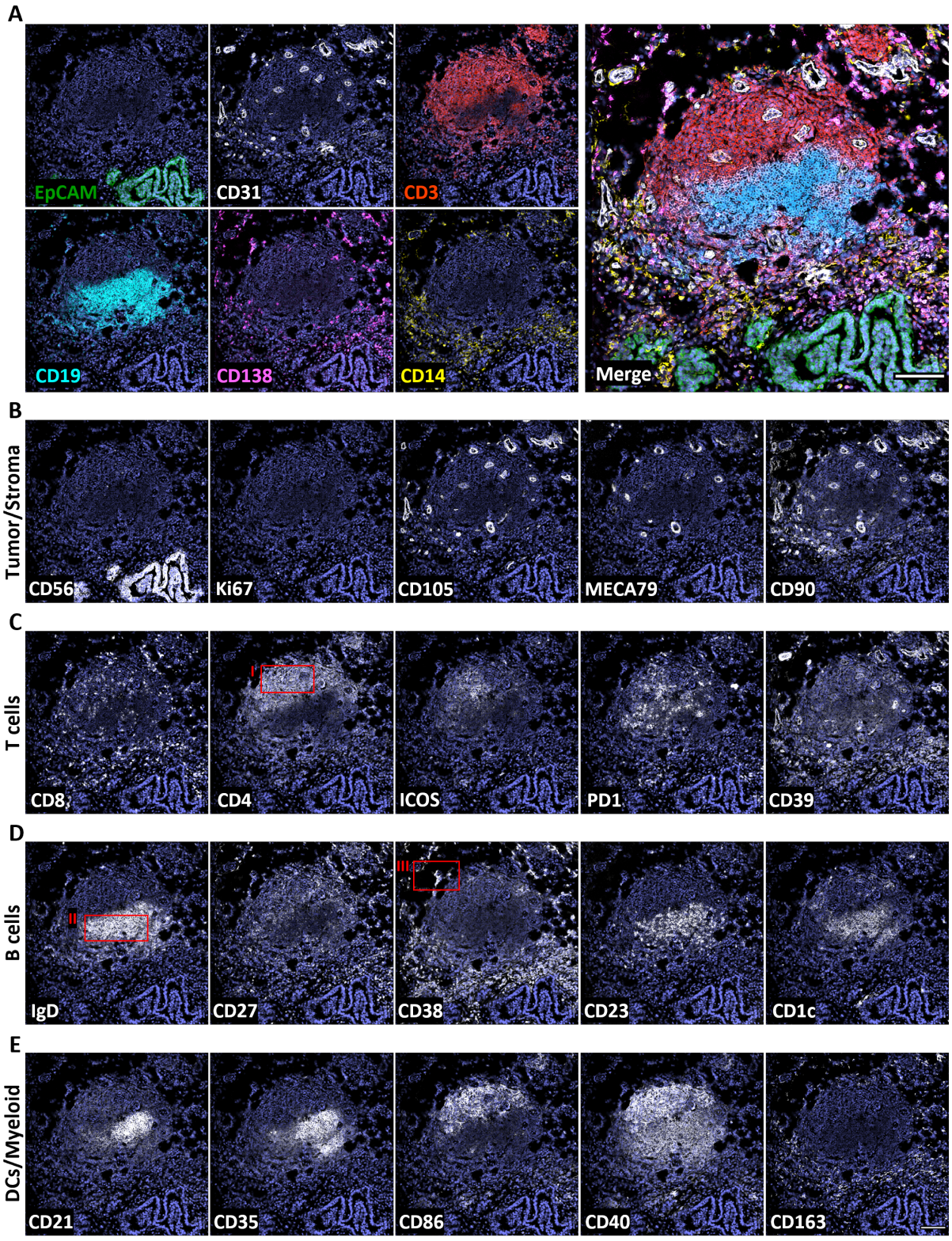

Figure 22. Visual identification of cell types in a tertiary lymphoid structure (TLS) of ROI 8 from OvCa (A) Markers for the main cell types composing the TME in ROI 8, such as EpCAM$^+$ tumor cells (green), CD31$^+$ endothelium (white), CD3$^+$ T cells (red), CD19$^+$ B cells (cyan), CD138$^+$ plasma cells (cyan), and CD14$^+$ myeloid cells (yellow), are shown on the left side, and the overlay of these stainings on the right side. **(B to E)** Several markers found in (B) tumor/stroma, (C) T cells, (D) B cells, (E) dendritic cells (DCs) and myeloid cells are

depicted in white. Nuclei are stained with Hoechst (blue) in all images. Red squares (I to III) represent the location of image magnifications in Figure 23. Scale bar: 100 µm.

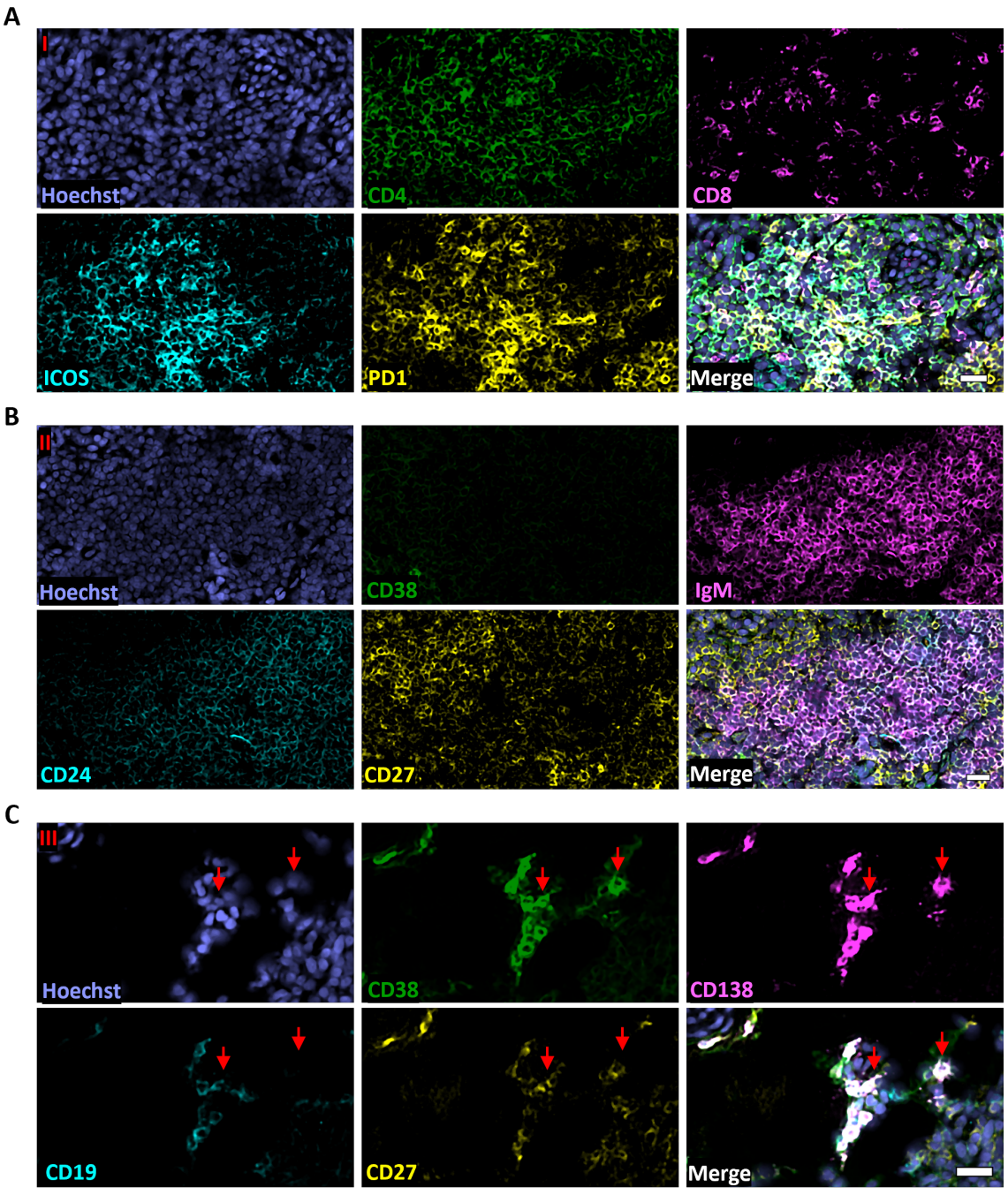

Figure 23. Marker expression patterns in different cell types in ROI 8 from OvCa
Image magnifications from ROI 8 (Figure 22) showing co-expression of relevant markers for **(A)** $CD3^+$ T cells, **(B)** $CD19^+$ B cells, and **(C)** $CD138^+$ plasma cells. Nuclei are stained with Hoechst (blue) in all images. Red arrows highlight cells of interest. Scale bar:20 µm

To study the cell composition and distribution in the tumor mass, ROI 6 was taken as a representative example. Tumor cells expressed EpCAM and CD56, and contrary to tumor cells in ROI 8, they expressed Ki67, indicating active proliferation (Figure 24A and B). Tumor cells were supported by numerous $CD31^+$ blood vessels (Figure 24A). As expected, the vasculature in the tumor did not correspond to HEVs as they did not express MECA-79. CD90 stained activated blood vessels and it revealed the presence of a dense net of CAFs surrounding the tumor bed, highlighting their function as a physical support for the tumor[13,35] (Figure 24B).

In the immune cell compartment, $CD3^+$ T cells, including both $CD8^+$ and $CD4^+$ subsets, were mainly located in the stroma and adjacent to the tumor, with only a few T cells infiltrating into the tumor bed (Figure 24A and C). I determined the presence of exhausted T cell subsets based on the expression of markers such as ICOS, PD1, or CD39. While ICOS expression was mostly restricted to a small number of cells in the stroma, PD1 was observed in $CD8^+$ and $CD4^+$ T cell subsets located in both stroma and tumor areas (Figure 24C and Figure 25A). The high expression levels of CD39 on CAFs and endothelium hindered the identification of $CD39^+$ T cells, which displayed relatively lower levels of CD39 expression (Figure 24C and Figure 25A). A more detailed characterization of $CD8^+$ T cells will be shown in the following subsection 3.4.2.

The B cell lineage marker CD19 identified plasma cells based on the co-expression of CD38, CD138, and CD27, which were detected in the stroma that surrounds the tumor (Figure 24A and D, and Figure 25B). This spatial distribution is in accordance with previous reports that describe antibody-producing PCs propagation into the tumor along fibroblastic tracks[187]. The expression of CD19 and CD138 was also observed in tumor cells (Figure 24A). Although I did not find evidence of CD19 expression in ovarian cancer cells and may thus indicate non-specific binding, CD138 expression has been previously reported in several tumor types[199].

Last, $CD14^+$ myeloid cells accumulated in the edges of the tumor and some cells penetrated into the tumor mass (Figure 24A). Other TAM-related markers corroborated their presence in this tissue, such as CD64, CD68, HLA-DR, CD40, and CD163 (Figure 24D and Figure 25C).

I also observed the exclusion of immune cells from the tumor mass in other tumor-rich ROIs, while stromal areas displayed higher levels of immune infiltration (Supplementary Figure 10).

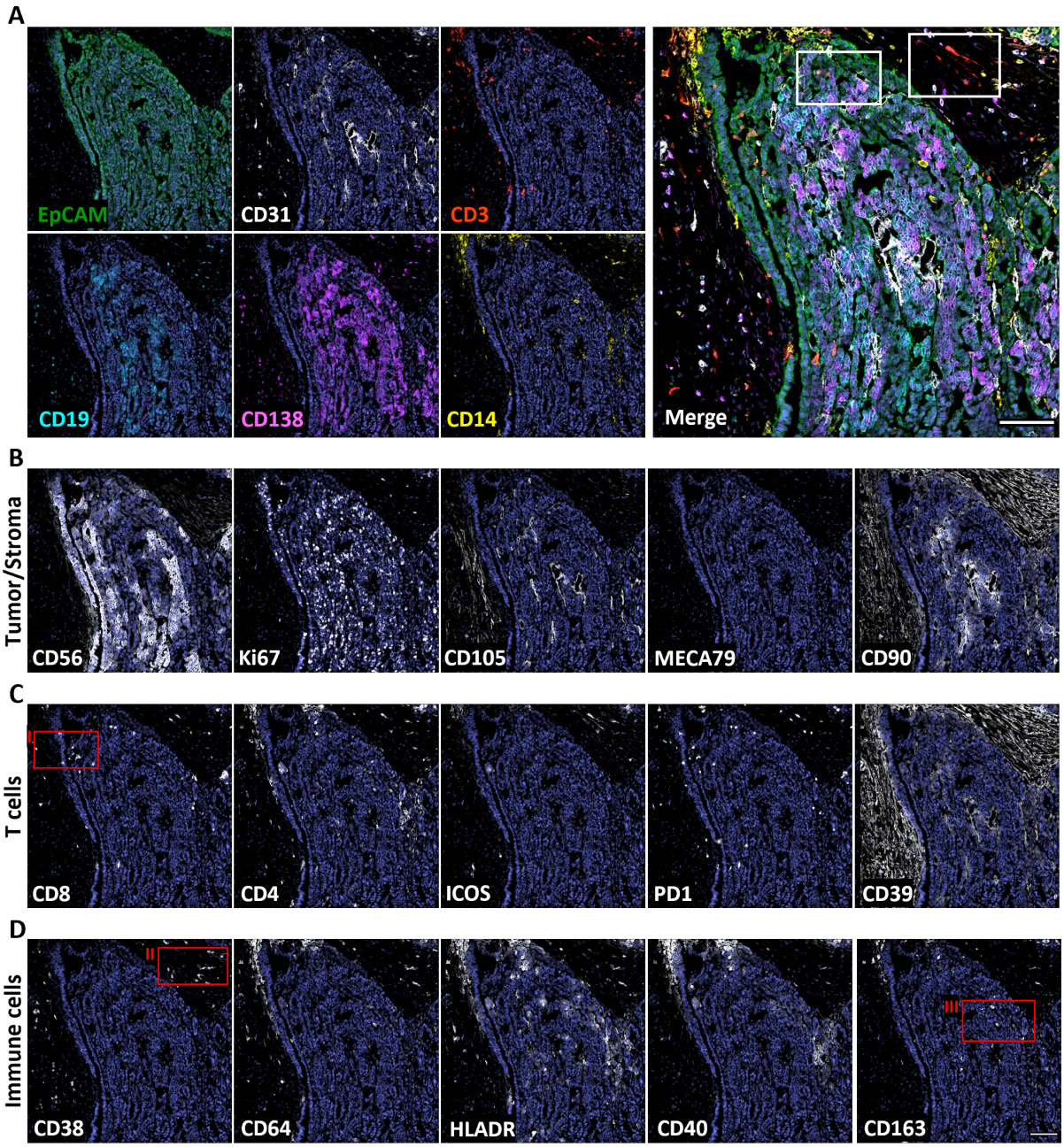

Figure 24. Visual identification of various cell types in the TME of ROI 6 from OvCa
(A) Markers for the main cell types composing the TME in ROI 6, such as EpCAM$^+$ tumor cells (green), CD31$^+$ endothelium (white), CD3$^+$ T cells (red), CD19$^+$ CD138$^+$ plasma cells (CD19, cyan; CD138, magenta), and CD14$^+$ myeloid cells (yellow) are shown on the left side and the overlay of these stainings on the right side. White squares represent the location of image magnification in Supplementary Figure 13C and D (right and left square, respectively). **(B to D)** Several markers found in (B) tumor/stroma, (C) T cells, and (D) other immune cells are depicted in white. Red squares (I to III) represent the location of image magnifications in Figure 25. Nuclei are stained with Hoechst (blue) in all images. Scale bar: 100 µm.

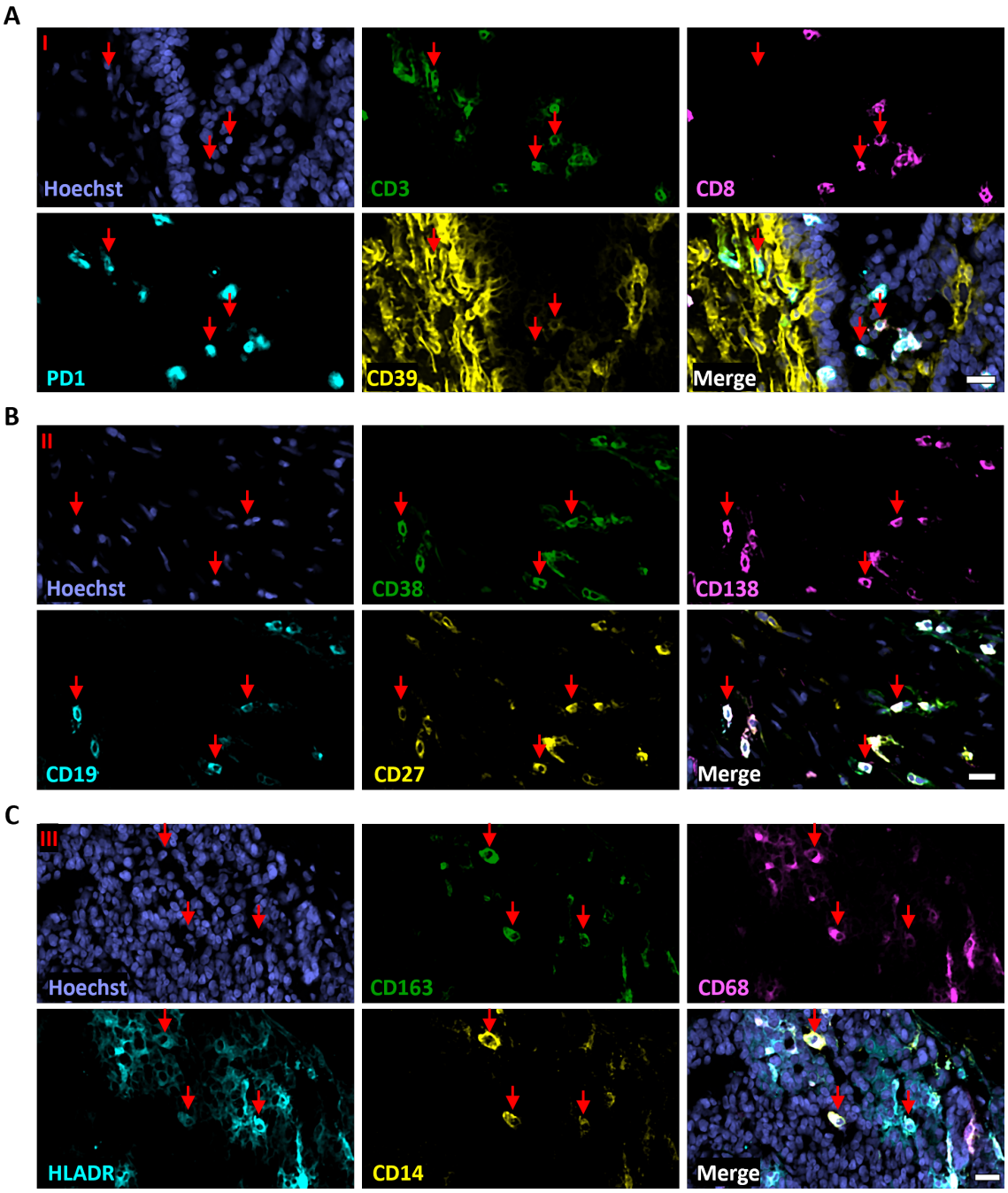

Figure 25. Marker expression patterns in different cell types in ROI 6 from OvCa
Image magnifications from ROI 6 (Figure 24) showing co-expression of relevant markers for **(A)** $CD3^+$ T cells, **(B)** $CD19^+$ $CD138^+$ plasma cells, and **(C)** $CD14^+$ myeloid cells. Nuclei are stained with Hoechst (blue) in all images. Red arrows highlight cells of interest. Scale bar: 20 µm

To conclude, this OvCa sample represented an immune-excluded TME with the presence of TLSs in the periphery of the tumor, with a cell composition and spatial organization that resembled mature TLSs with no GC reactions. The characterization of such complex structures was possible due to the multiparametric nature of the MICS technology, highlighting its power to study the tumor microenvironment.

3.4.2 Exhausted CD8⁺ TILs were found in close proximity to tumor cells

As described in the previous sections of my PhD thesis and supported by parallel investigations[107,117,118], the ectonucleotidase CD39 has the potential to identify tumor-reactive CD8⁺ TILs. To further corroborate this hypothesis with other methodologies, I analyzed the expression of CD39 and other activation/exhaustion markers on CD8⁺ T cells in tumor tissues *in situ* by MICS. The advantages of this technology are the large number of markers that can be screened at the protein level in parallel and the preservation of the spatial information, which can be relevant to study cell to cell interactions. The main disadvantage is that one cannot easily demonstrate the reactivity of T cells in tissues. Therefore, I focused on two characteristics of T cells as proxies for tumor reactivity: 1) activation/exhaustion states and 2) proximity to cancer cells. The first characteristic, extensively addressed earlier in this PhD thesis, is based on accumulated evidence in the field suggesting that tumor-reactive T cells undergo differentiation into exhausted states upon chronic antigen activation in an immunosuppressive TME[95,101,159]. As a result, tumor-reactive T cells are prone to interact with tumor cells and are thus expected to be in close proximity to them[200]. Therefore, I investigated whether CD39⁺ CD8⁺ TILs in tissues exhibited an exhausted phenotype and were located in the proximity to tumor cells using MICS. Considering that TLSs might also be a source of tumor-reactive T cells[201], I studied the phenotype of CD8⁺ T cells within these structures.

A visual inspection of the images revealed a number of CD8⁺ T cells in close contact with tumor cells (Figure 26). These T cells co-expressed CD39 and other markers related to activation (CD7, CD38, CD137, CD244, and Ki67), tissue-residency (CD69 and CD103) and exhaustion (CD101, CTLA4, ICOS, PD1, and TIM3; Figure 26), supporting my hypothesis that potential tumor-reactive CD8⁺ T cells are spatially close to tumor cells and exhibit an exhausted phenotype. However, the large number of markers and T cells in the present study made the visual inspection of images very challenging to draw conclusions about the phenotype and location of CD39⁺ CD8⁺ T cells. Consequently, I developed two different kinds of systematic approaches: gating-based and bioinformatic-based analyses.

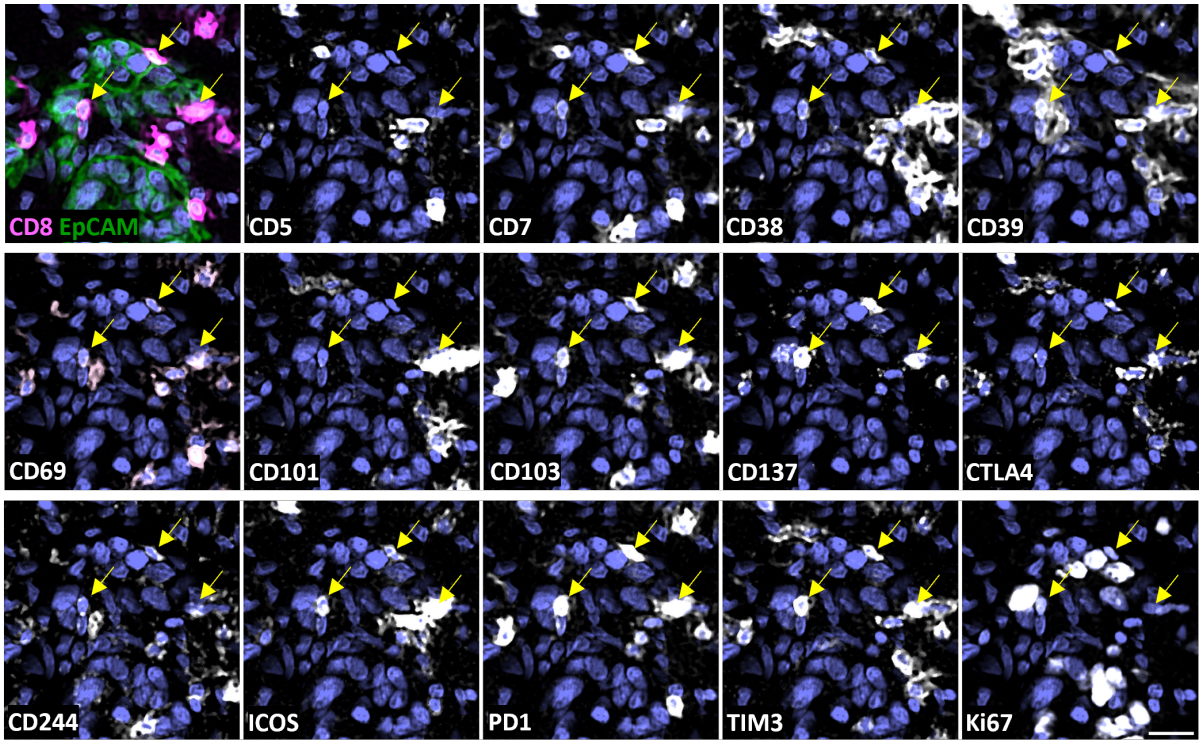

Figure 26. Representative images of marker expression on CD8⁺ TILs in tumor areas of metCRC5
Exemplary high-magnification images of CD8⁺ T cells (CD8, magenta) in tumor areas (EpCAM, green), particularly those in close contact with tumor cells (yellow arrows) and the stainings of markers of interest (white) in ROI 2 of the metCRC5 sample (white square in Figure 20). Nuclei are stained with Hoechst (blue). Scale bar: 20 µm.

In both types of analysis, the initial step involved quality control of the images by visually identifying and discarding poor-quality images and technical artifacts (Figure 27A). Afterwards, images were automatically segmented into single cells. Due to tissue complexity, cell segmentation can be imperfect and noise from neighboring or overlapping cells (also known as segmentation noise) can cause false positives (Supplementary Figure 11). To mitigate this effect, I manually corrected CD8⁺ T cell segments to accurately fit the contours of the segment to the cell morphology (Figure 27A). During this process, I also manually annotated each cell for the expression of several markers to benchmark and facilitate this analysis. Finally, the mean fluorescent intensity value of each marker per cell segment was extracted into a table. In the gating-based analysis, I used this data as flow cytometry data and developed a gating strategy to rapidly identify and quantify CD8⁺ TIL subsets (Supplementary Figure 12). In the bioinformatic-based analysis, I used different tools to study co-expression of relevant markers. Lastly, the spatial analysis was carried out by dividing the images into areas based on the location of EpCAM⁺ tumor cells (T area), its immediate vicinity partitioned into 20 µm radial areas (A1-A5), further than 100 µm (A6), and TLSs in the OvCa sample (Figure 27B to D). More details about the development of this analysis pipeline can be found in Methods section 2.2.7.

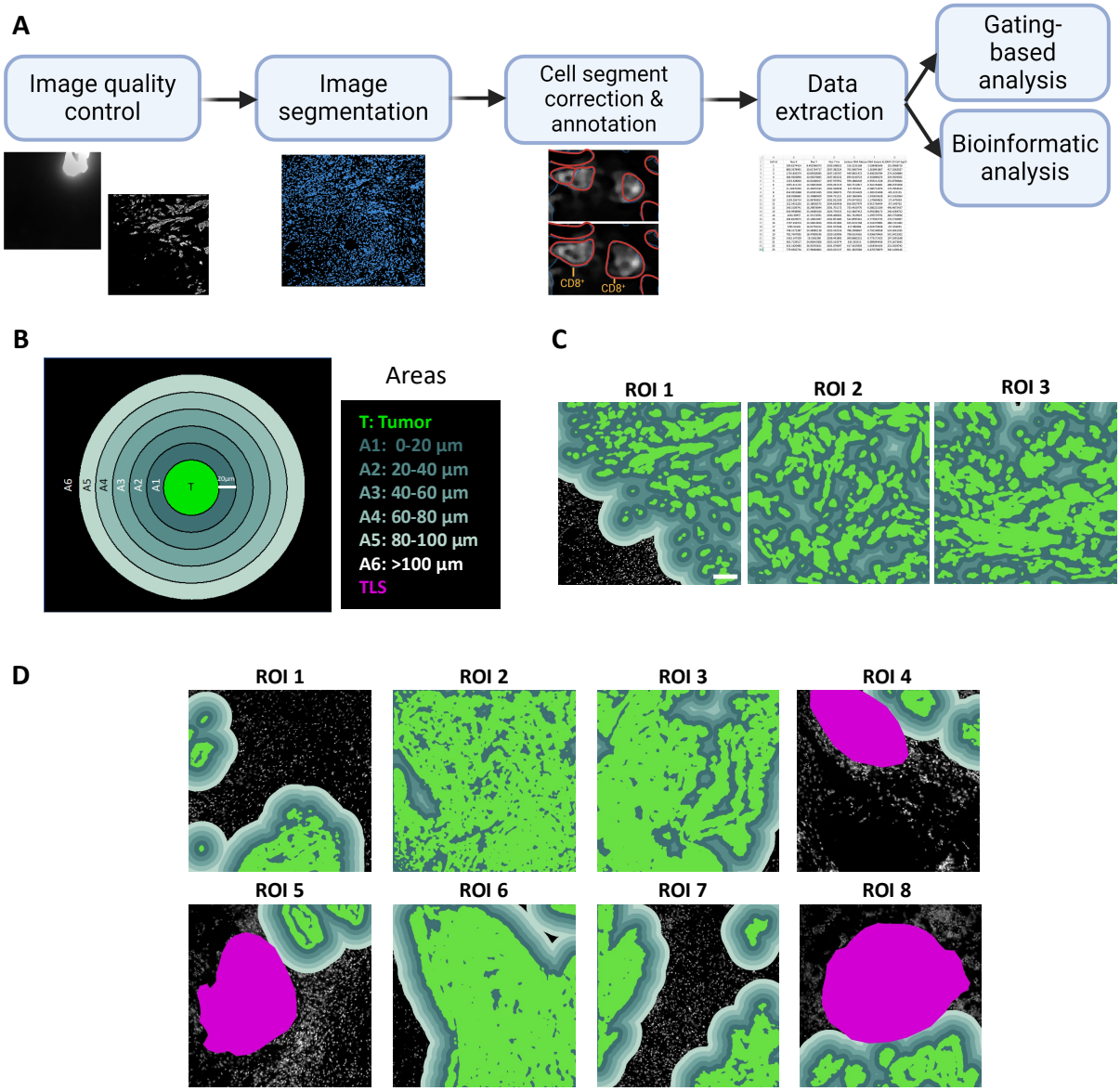

Figure 27. MICS analysis workflow for the phenotypic characterization of CD8⁺ TILs
(A) Good quality images were selected, and a systematic image segmentation was performed. Afterwards, CD8⁺ T cell segments were manually corrected and annotated. The extracted data (annotations and mean fluorescent intensity values per cell and marker) was used for gating-based and bioinformatic analyses. **(B)** Schematic representation of the division of the images into areas, starting by defining the TLS area, the tumor (T) area by EpCAM staining and its surroundings divided into 20 µm radial (A1-A5) and > 100 µm (A6) areas. **(C and D)** Division of the ROIs into the defined areas (T and A1-A6 in different shades of green, and TLS in purple) for (C) metCRC5 and (D) OvCa-TLS samples.

The gating-based quantification of CD8$^+$ TIL subsets showed that the proportions of CD137$^+$ and CD103$^+$ CD8$^+$ TILs tended to be higher in tumor areas compared to more distant sites (T vs A1 to A6; Figure 28A). Particularly for the OvCa-TLS sample, the frequencies of PD1$^+$, ICOS$^+$, and CD101$^+$ CD8$^+$ TILs were higher in tumor areas compared to stroma (A1 to A6), while the frequencies of these subsets in the tumor area were similar for both samples (Figure 28A). This suggests that while metCRC5 contained activated/exhausted T cells homogenously distributed in the studied areas, OvCa-TLS-derived activated/exhausted TILs concentrated in the tumor and its immediate vicinity. In contrast, the frequency of CD5$^+$ CD8$^+$ TILs decreased in tumor areas, which is in accordance with studies showing a downregulation of the TCR inhibitory molecule CD5 in CD8$^+$ TILs upon activation[121,202].

Regarding CD8$^+$ T cells in TLSs, I observed smaller fractions of activated T cells compared to T cells in tumor areas, for example PD1$^+$ CD8$^+$ T cells (43% vs 82% in TLS vs tumor area) and CD137$^+$ CD8$^+$ T cells (17% vs 35%, Figure 28A). CD103$^+$ CD8$^+$ T cells were also reduced in TLS vs tumor areas (16% vs 84%;). CD103 is a tissue residency marker that binds E-cadherin expressed in epithelial and tumor cells, explaining its increased expression in intratumoral T cells. Nonetheless, CD103 has also been detected in T cells residing in TLSs in lung adenocarcinoma[203] and in the surroundings of TLSs in gastric cancer[204], and has been associated with a positive prognosis. In contrast to PD1, CD137, or CD103, CD5 was upregulated in TLS-T cells compared to tumor areas, which may indicate a less differentiated state (Figure 28A).

To confirm the results obtained with the gating-based strategy, I plotted marker mean fluorescent intensity values among CD8$^+$ T cells per area in a heatmap (Figure 28B and C). This type of bioinformatic analysis revealed similar results as described above, with certain markers being more prominent in tumor areas, especially CD137, PD1, and CD103 for both patients, and ICOS and CD101 for the OvCa-TLS sample. Ki67 expression was also characteristic of CD8$^+$ TILs in tumor areas. However, this signal may also come from neighboring proliferating tumor cells, as they have been identified in the previous TME analysis (Figure 18 and Figure 24).

The expression of CD39 did not correlate with proximity to tumor areas, and I observed high frequencies of this cell subset across all areas (from 80% to 100% in metCRC5, and from 38% to 82% in OvCa-TLS; Figure 28A). This result does not support CD39 as a reliable proxy for tumor reactivity solely based on proximity to tumor cells. However, the previous TME analysis showed higher expression levels of CD39 in other cell types (e.g., CD14$^+$ myeloid cells, CD34$^+$ blood vessels, and CD90$^+$ CAFs), with CD8$^+$ TILs located in the proximity of these subsets, particularly in the stroma (Figure 25A and Supplementary Figure 13). Therefore, I hypothesize that the elevated percentage of CD39$^+$ CD8$^+$ TILs in stromal areas may result from segmentation noise originated from other CD39-expressing cells that overlapped with T cells.

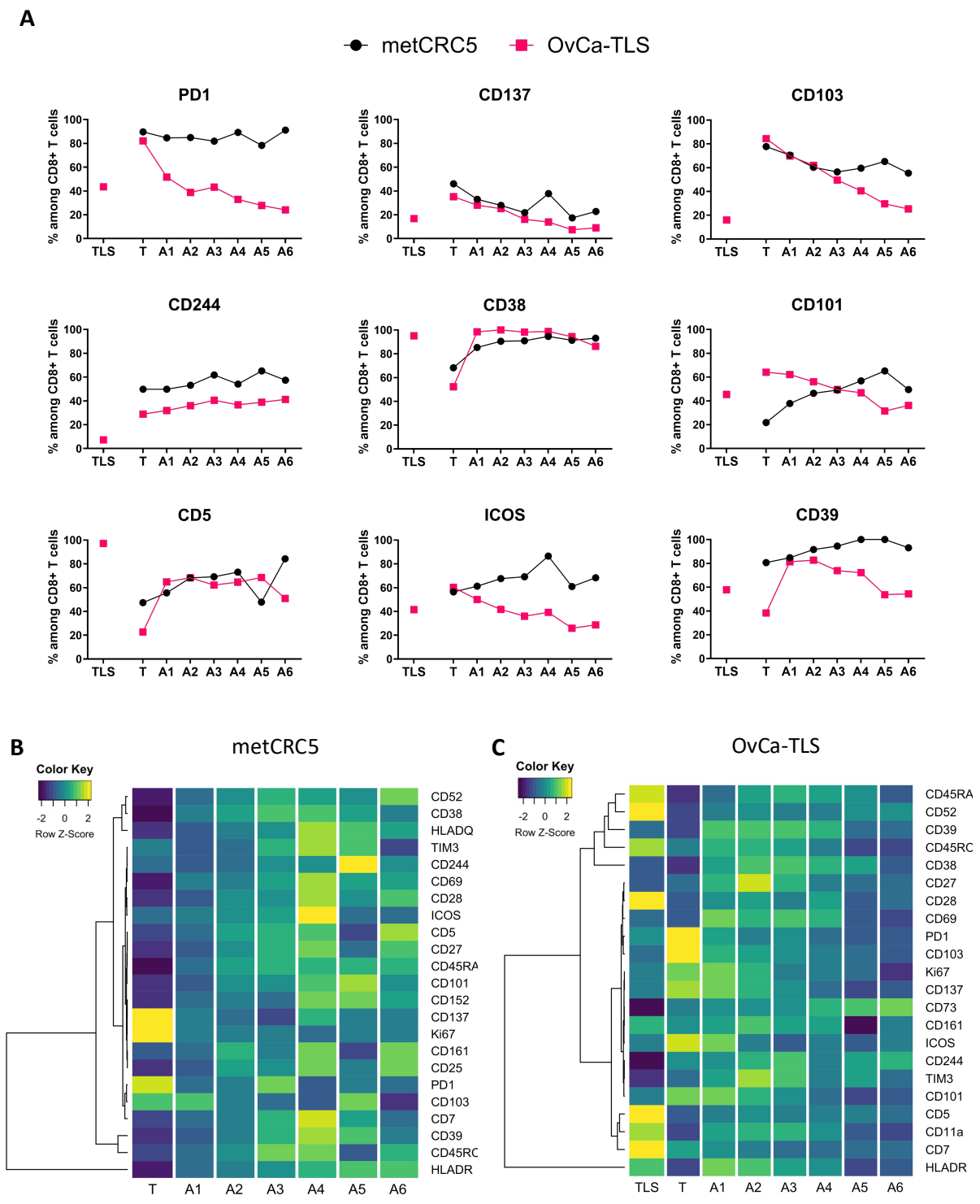

Figure 28. Phenotypic characterization of CD8⁺ TILs in different areas of tumor samples
(A) Frequency of CD8⁺ T cells expressing different markers of interest among tumor areas for both metCRC5 and OvCa-TLS samples. **(B and C)** Heatmaps representing the median expression of relevant T cell markers in CD8⁺ TILs per area for the metCRC5 (B) and OvCa-TLS (C) samples. Markers are additionally clustered in the dendrogram of the heatmaps. The images are divided into areas: tertiary lymphoid structures (TLS) (only for OvCa), tumor (T) areas (EpCAM⁺) and its surroundings: A1 (0-20 µm), A2 (20-40 µm), A3 (40-60 µm), A4 (60-80 µm), A5 (80-100 µm) and A6 (>100µm).

Based on my previous characterizations of CD39$^+$ CD8$^+$ T cells, conducted by both flow cytometry and scRNA-seq, I observed a correlation between the expression levels of CD39 and other activation/exhaustion markers, such as PD1, CD137, or CD103. To validate this co-expression patterns in MICS images, I projected the cells into a t-distributed Stochastic Neighbor Embedding (tSNE) map and visually represented the expression of relevant markers. A large proportion of PD1$^+$ CD8$^+$ TILs in the metCRC5 sample co-expressed CD103, TIM3, and CD39 (Figure 29A, red circle), with a small subset co-expressing the activation marker CD137. This observation is in alignment with previous studies showing that CD137 may be a more restricted marker of naturally occurring tumor-reactive T cells than PD1, CD103, or CD39[205]. ICOS was found on T cells co-expressing CD28 and CD4 (Figure 29A, blue circle, and Supplementary Figure 14A), suggesting close proximity to CD4$^+$ T cells. Consequently, I cannot exclude the possibility that the observed ICOS expression may result from segmentation noise from ICOS$^+$ CD4$^+$ T cells. Since most CD8$^+$ TILs in the metCRC5 sample were found nearby tumor cells (i.e., in tumor and A1 areas), the observed exhausted phenotype was exhibited by CD8$^+$ TILs that were evenly distributed in those areas (Figure 29A). In contrast, a smaller fraction of CD8$^+$ T cells corresponded to T cells in tumor areas in the OvCa-TLS sample, with a majority of T cells located in TLSs (Figure 29B). In accordance with my previous observations, PD1$^+$ CD8$^+$ TILs in OvCa-TLS were mainly found in the tumor area, and they co-expressed CD103, TIM3, and CD39 (Figure 29B, red circle), with a small subpopulation expressing CD137 and ICOS. The negative effect of segmentation noise from CD4$^+$ T cells is also highlighted in this tissue, where another subset of PD1$^+$ CD8$^+$ T cells co-expressed high levels of ICOS, CD5, CD28, and CD4 (Figure 29B, blue circle, and Supplementary Figure 14B). These cells were mainly located in TLSs, where CD4$^+$ and CD8$^+$ T cells are densely packed and the distinction between those subsets is challenging, even by an experienced user (Figure 23A).

In summary, I developed a MICS analysis pipeline for the phenotypic and spatial characterization of CD8$^+$ TILs by correcting cell segments and designing a flow cytometry-like gating strategy to identify and quantify CD8$^+$ T cell subsets. However, dealing with signal noise arising from overlapping cells posed a daunting challenge, resulting in the identification of false-positive cells for various markers of interest. This problem was particularly pronounced for markers such as CD39, which can be expressed by multiple cell types, especially in densely packed tissue areas. Despite these challenges, I observed a tendency to find activated/exhausted phenotypes in CD8$^+$ T cells located in close proximity to tumor cells. These T cells expressed markers previously reported as surrogates of tumor reactivity, and their expression correlated with the expression of CD39, providing additional support for the findings presented in this PhD thesis.

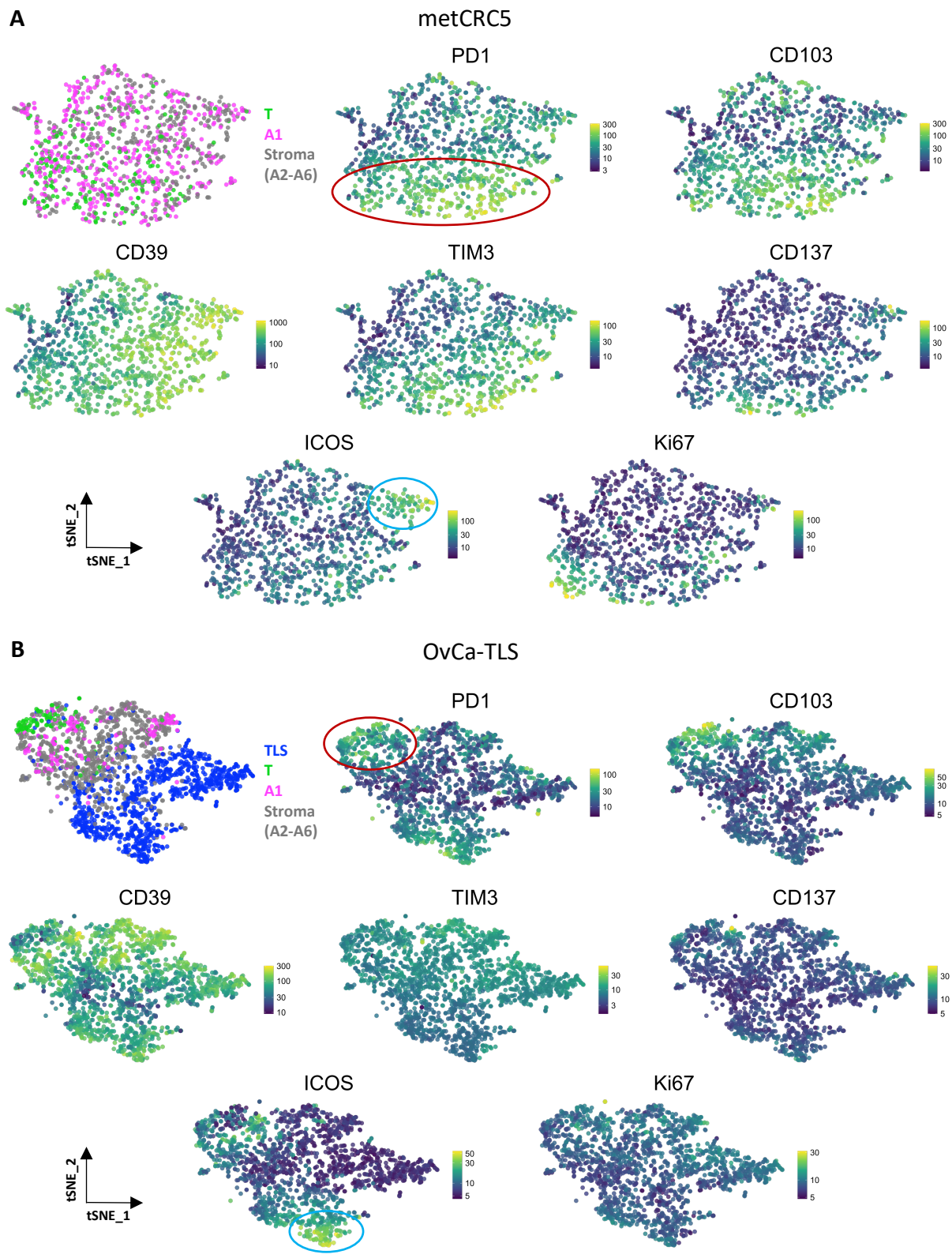

Figure 29. Co-expression of relevant markers in CD8⁺ TILs

The expression of relevant markers on CD8⁺ TILs from **(A)** metCRC5 and **(B)** OvCa-TLS samples was shown in tSNE maps, together with their corresponding area in the tissue: TLS for the OvCa sample (blue), tumor (T) area (green) and its immediate surrounding (A1 [0-20 µm], magenta), as well as stromal areas (A2-A6 [> 20 µm], grey). The red circles indicate activated/exhausted CD8⁺ T cell subsets, and the blue circles denote cells in close contact with CD4⁺ T cells. The color scale shows fluorescent mean intensity in Log10 scale.

4 Discussion

The enrichment of naturally occurring tumor-reactive T cells based on an *a priori* phenotype before the *ex vivo* expansion represents an attractive approach to improve the efficacy of adoptive cell therapy (ACT). In my PhD project, I performed a phenotypic characterization of tumor-infiltrating lymphocytes (TILs) in order to identify cell surface markers that can be used to develop enrichment strategies of tumor-reactive $CD8^+$ TILs for ACT. First, the characterization of TILs from several cancer types by flow cytometry revealed CD39 as a potential cell surface marker for isolating tumor-reactive $CD8^+$ TILs. This was evidenced by the higher levels of activation and exhaustion, two states commonly used as surrogates of tumor reactivity[159], in $CD39^+$ $CD8^+$ TILs compared to their $CD39^-$ counterparts. Second, the establishment of a pre-sorting strategy to enrich debris-free $CD8^+$ TILs from tumor digests enabled the isolation of $CD39^+$ $CD8^+$ TILs in the MACSQuant Tyto Sorter. A small fraction of expanded $CD39^+$ $CD8^+$ TILs displayed tumor reactivity *in vitro* upon co-culture with autologous tumor cells, as opposed to the $CD39^-$ T cell subset. Third, the combination of T cell receptor (TCR) sequences and transcriptome profiles of TILs confirmed that T cell clonotypes with a tumor-reactive T cell signature were capable of proliferating *in vitro* in the $CD39^+$ $CD8^+$ T cell population. Last, I used our newly developed multiplexed imaging technology MICS (MACSima™ Imaging Cyclic Staining) to confirm the presence and spatial distribution of $CD39^+$ $CD8^+$ TILs in the tumor microenvironment (TME). Despite the challenges during single-cell image analysis due to broad CD39 expression in neighboring non-T cell types, $CD8^+$ T cells expressing activation/exhaustion markers that correlated with CD39 expression (e.g., CD137, PD1, and CD103) tended to be located in close proximity to tumor cells rather than in stromal areas or in tertiary lymphoid structures (TLSs). This proximity, together with the correlation between CD39 expression and an activated/exhausted phenotype, supported CD39 as a potential marker to enrich tumor-reactive $CD8^+$ TILs.

4.1 The potential of CD39 to identify and enrich tumor-reactive $CD8^+$ TILs

The search for cell surface markers that are predictive of tumor reactivity and can be used to enrich tumor-reactive T cells before the *ex vivo* culture for ACT is a very active research field. In the last years, multiple groups have investigated the potential of activation/exhaustion markers such as PD1, TIM3, CD137, CD39, CD103, or TIGIT, which are upregulated on TILs upon (chronic) antigen stimulation in an immunosuppressive TME [95,101,107,118,123,125–128]. However, no consensus on the most suitable marker has been reached yet. In my PhD project, I joined this exciting field and aimed to contribute to the search of biomarkers for tumor reactivity by characterizing TILs using different technologies.

CD39 is an ectoenzyme that, together with CD73, converts extracellular ATP into adenosine, a potent anti-inflammatory modulator. As many other immune checkpoints, CD39 is upregulated upon prolonged TCR stimulation and is thus linked to T cell exhaustion[115]. Simoni et al. first proposed CD39 as a marker of tumor-reactive $CD8^+$ TILs since bystander T cells lacked CD39 expression in lung and colorectal cancers[118]. Duhen et al. further showed that the co-expression of CD39 and CD103 more accurately identified tumor-reactive $CD8^+$ TILs than the single positives[107], whereas Laumont et al. refined it to the $CD39^+$ $CD103^+$ $PD1^+$ T cell subset in ovarian cancer[128]. In my project, variable frequencies of $CD39^+$ $CD8^+$ TILs were observed among patients, and this population indeed co-expressed other activation/exhaustion makers, indicative of a past or ongoing immune response. Recently, Eiva et al. performed a direct comparison of CD39, CD103, CD137, and PD1 in primary ovarian tumor samples. Their findings suggest that the activation marker CD137 is a more selective marker for tumor-reactive TILs, mainly because $CD137^+$ T cells, which co-expressed all the aforementioned markers, had a higher cytotoxic effector capacity, and the secretion of IFNγ upon co-culture with autologous tumor cells was largely confined to this T cell subset[205]. However, other groups have suggested that markers such as PD1 or CD39 may define a more diverse repertoire than CD137[101], which in turn may be beneficial to mount an effective antitumor response[57]. Therefore, the investigation of different $CD39^+$ T cell subpopulations and their potential for clinical use represents an attractive goal.

For this purpose, the sorting procedure was established in the MACSQuant Tyto Sorter, which allows several, consecutive FACS sorts as well as being Good Manufacturing Practice (GMP)-compliant. One drawback of using this instrument was the necessity of developing a pre-sorting workflow, which reduced the presence of debris and increased the target population to have a faster and more efficient sort. Cell loss during this pre-sorting process was considerable, which, together with the low number of T cells in the starting material, allowed only for sorting $CD39^+$ and $CD39^-$ T cell subsets. In the future, multiple sorts may be possible by modifying the MACSQuant Tyto Sorter platform to allow direct sorting of tumor digests, omitting the pre-sorting strategy and thus minimizing cell loss. Alternatively, consecutive magnetic enrichments may be contemplated by using technologies that allow release of antibody-microbead complexes and subsequent re-staining, omitting complex FACS sorts. The success of these procedures relies on sample quality, and therefore protocols for delivery, preservation, and preparation of tumor samples need to be improved and adjusted to meet GMP-compliant clinical standards. In our laboratory, we lowered the concentration of enzyme R to prevent epitope degradation of relevant T cell markers and to mitigate potential impacts on T cell phenotyping. However, CD39 was not affected by this enzyme, which may allow future use of the recommended dose of enzymes for optimal sample dissociation and cell recovery. Unfortunately, not all tumor

samples yielded large numbers of TILs, such as in PDAC, and therefore, enriching T cell subsets from these samples may be challenging for clinical purposes. Consequently, other approaches may be considered, such as modifications of TIL culture conditions to induce the outgrowth of tumor-reactive T cells, for instance by adding tumor-specific peptides or tumor lysates for antigen-driven TIL expansions[66].

I assessed the reactivity of unsorted, $CD39^-$, and $CD39^+$ subsets after a Rapid Expansion Protocol (REP) culture, resulting in a small fraction of $CD8^+$ TILs that responded against autologous tumor cells in the $CD39^+$ subset in one out of three tumor samples tested, while the $CD39^-$ counterparts showed no reactivity in any sample. However, the advantage of an enrichment step based on CD39 was not evidently proven in this case as unsorted TILs also displayed tumor reactivity. One hypothesis is that the presence of $CD4^+$ T cells in the unselected sample may have favored the growth of tumor-reactive $CD8^+$ TILs. The beneficial role of helper $CD4^+$ T cells in cancer has been extensively studied[28] and its use in manufacturing effective TIL products will be discussed later (section 4.3). Nevertheless, the tumor reactivity was lost when $CD39^+$ T cells were depleted (i.e., in the $CD39^-$ sample). While these results support that CD39 is expressed on tumor-reactive $CD8^+$ T cells and are in accordance with recent publications[118,127,163], further validation in a larger patient cohort is necessary to obtain compelling conclusions. In addition, the frequency of cytokine-secreting, tumor-reactive $CD8^+$ TILs was very low, diminishing the prospects for a clinically effective cell product. However, our group´s findings indicate that even without cytokine secretion responses, tumor killing still occurs (data not shown), suggesting that killing assays might represent a more sensitive readout system to assess the reactivity of $CD8^+$ TILs than intracellular cytokine stainings. Furthermore, the lack of established autologous cell lines from primary tumor samples hampered the selection of proper tumor targets for these co-culture assays. The development of new culture conditions and methods may increase the success rates of establishing cancer cell lines.

Other factors may have influenced the degree of reactivity in the final product, including the frequency and differentiation state of tumor-reactive T cells in the tumor and the loss of TCR clones during the *in vitro* expansion. I evaluated these aspects on selected patients by single cell RNA sequencing (scRNA-seq). The TCR repertoire is an important metric in health and disease. Especially, increased levels of clonality can be indicative of an ongoing T cell immune response in many clinical settings such as cancer[206]. The presence of large or dominant TIL clones has been correlated with better prognosis and PD1 therapy responses[206], and several studies have identified top-ranked TCRs to be frequently tumor-specific[166,207]. In this project, I showed that the enrichment of CD39 and/or the *in vitro* expansion shaped the initial TCR repertoire towards higher clonality (or decreased diversity). Importantly, dominant clonotypes in *ex vivo* TILs (i.e., TILs before the *in vitro* expansion) were not always detected

after the REP, and vice versa, rare clones largely proliferated during the culture. Although it is a polyclonal expansion, certain T cell clones may possess a higher proliferative capacity that can compete with "unfit" clones during the culture. These findings are consistent with data provided by Poschke et al., who demonstrated that TCR profiles of TILs in melanoma and PDAC samples considerably changed during *in vitro* expansions due to different intrinsic proliferation capacities of T cells, resulting in loss of tumor-dominant clonotypes[68]. Importantly, they correlated this poor expansion ability with antigen-driven dysfunction, which suggest that relevant TCRs might be lost at the end of the culture[68]. These observations highlight the importance to maintain—or increase—the presence of tumor-reactive T cells in the final TIL product. Enrichment strategies prior to the expansion could be advantageous in this regard, which will deplete less exhausted and highly proliferative bystander T cells, allowing tumor-reactive T cells to thrive.

Recently, the explosive growth of single cell sequencing technologies has precipitated the collection of large amounts of transcriptome data of TILs, which have been correlated with relevant biological processes, including anti-tumor responses[37]. The analysis of *ex vivo* TILs from two cancer patients revealed gene expression profiles previously described by other groups, particularly the three main differentiation states in $CD8^+$ TILs: naive-like, cytotoxic, and exhausted or dysfunctional[37]. While the relation between each state is still unclear, strong evidence supports the continuum nature of the dysfunctional state[37], making the definition of each cell cluster challenging due to the presence of cells with transitioning dysfunctional states. This results in different assignations to related cell subsets across multiple scRNA-seq TIL studies[37]. However, efforts have been made to unify this classification[145,208]. To alleviate this problem, I used ProjecTILs as a computational approach to infer TIL states based on a curated reference cell atlas. Automatic cell identification methods are immensely valuable[209], with ongoing improvements such as the creation of stable reference atlases with a broader coverage of cell types and states, and the option to select diverse levels of resolution to cover transient or intermediate cell states[210]. Furthermore, trajectory inference can be integrated in future analyses to aid in the identification of differentiation states along the dysfunctional axis, as previously performed in breast[211] and pancreatic cancers[212].

Both studied tumor samples contained clusters related to exhausted or dysfunctional $CD8^+$ T cell states, and as expected, they had a marked tumor-reactive T cell profile based on recently defined gene signatures, including genes like *PDCD1* (PD1) or *CXCL13*[37,153,170–173]. Importantly, *ENTPD1*, encoding CD39, was expressed in cells within these clusters, meaning that they would be potentially enriched in the proposed process in this study. Indeed, I observed that some of these clonotypes were expanded in the $CD39^+$ TIL subset. However, not all top-ranked TCRs after the REP expansion were detectable in *ex vivo* TILs, probably due to limitations of scRNA-seq in detecting rare clonotypes or

populations[213]. New high-throughput single cell technologies can address this issue, increasing the sensitivity to detect low frequent T cell clones[214].

Overall, this data supports that potential tumor-reactive T cell clones shared an exhausted molecular profile, including the expression of CD39, and some clones were capable of proliferating *ex vivo*. To further validate this hypothesis, the specificity of these TCRs needs to be validated *in vitro* and in a larger patient cohort. Other technologies, such as DNA barcoded peptide-MHC multimers[215], could reveal the specificity of TCRs directly in the sequencing data, if predicted and/or *bona fide* tumor antigens were available[216,217]. The combination of gene expression and validated tumor-specific TCR sequences offers several opportunities. On the one hand, it can aid in the selection of better markers to enrich less differentiate tumor-reactive T cells, which are preferred for adoptive cell therapies[218]. As protein levels often correlate poorly with mRNA expression[219,220], the detection of both mRNA and protein expression in single cell sequencing experiments, for example by DNA barcoded antibodies[221], would facilitate the screening of potential markers for enrichment purposes. On the other hand, the identification of a transcriptome signature of tumor-reactive TILs can aid in the selection of tumor-specific TCRs that can be used for TCR-engineered T cell therapies, which will be later discussed in the section 4.3 regarding future clinical perspectives.

4.2 MICS as a powerful tool to study the TME

The TME plays critical roles in tumor growth and invasion, and the interaction of its components modulates important features that can affect clinical outcomes[222]. The development of multiplexed imaging technologies has offered the possibility to uncover the spatial architecture of the TME and its effects on cancer biology and therapeutic responses[129]. In this thesis, I presented the use of our highly multiplexed fluorescent imaging technology MICS to study the cell composition of the TME of two cancer patients. The use of multiple markers enabled the identification of various cell types in the TME, such as tumor cells, cancer-associated fibroblast (CAFs), endothelium, and diverse immune cell populations. The preserved spatial information of these cell groups underlined their functions in the TME. For example, CAFs were mainly found around tumor islets, which may support cancer cells and create a physical barrier for T cells to infiltrate into the tumor bed[13,35]. Similarly, activated endothelial cells were found nearby tumor areas, indicating a possible tumor-supporting role by supplying nutrients[223–225]. The study of highly organized structures such as TLSs is one of the most remarkable examples of how to exploit the power of MICS. These lymph node-like immune cell niches are formed in ectopic, inflamed tissues, such as tumors, to provide the adequate environment for immune cell interactions and local formation of antitumor responses[226]. Their presence is indicative of ongoing immune reactions and is usually associated with positive outcomes in a variety of cancer types[227]. The

MICS analysis revealed several of these structures in the periphery of the tumor mass in the OvCa sample that shared characteristics of *bona fide* TLSs.

I particularly focused on the spatial organization of potential tumor-reactive CD8$^+$ TILs in the TME. As their tumor reactivity cannot be easily determine *in situ*, I focused on TILs that exhibited an exhausted phenotype as a proxy for tumor reactivity[44] and investigated their proximity to tumor cells, which may hypothetically indicate T cells interacting with or recognizing cancer cells. *In vivo* imaging of cytotoxic CD8$^+$ T cells in a mouse tumor model could show that tumor-reactive T cells are arrested in close contact to tumor cells expressing their cognate antigens[200]. After developing an analysis pipeline, I observed a higher frequency of activated/exhausted CD8$^+$ TILs in close contact with tumor cells in both studied patients. Unfortunately, CD39 was not a distinctive marker of CD8$^+$ TILs in close proximity to tumor cells, but its expression was rather homogenous among T cells located in all studied areas in the tissue. The higher expression levels of CD39 on non-T cell types may lead to false detection of CD39 signals in T cells adjacent to those cells. Because of this, other immunofluorescent studies opted for using alternative markers, such as the co-expression of CD103 and PD1, as a redout for potential tumor specificity[153]. Bioinformatically, I confirmed that CD8$^+$ T cells in close contact with tumor cells co-expressed PD1, CD103, CD137, TIM3, ICOS, and CD39, coinciding with the flow cytometry and scRNA-seq data presented in this thesis. This highlights the importance of investigating marker co-expressions as well as spatial context to accurately identify potential tumor-reactive CD8$^+$ TILs in tissues by multiparametric immunofluorescence imaging techniques.

The possibility to use distinctive markers to identify and isolate TLS-resident CD8$^+$ T cells—possibly containing less differentiated tumor-reactive T cells—is a promising approach that can be further investigated. In this thesis, I observed differences in the marker expression profile of TLS-CD8$^+$ T cells compared to intratumoral TILs, including upregulation of CD5 and downregulation of CD103. This phenotype resembles T cells that have recently migrated into the tissue from the bloodstream rather than T cells that already reside in it, which is consistent with the proposed model for the generation and maintenance of TLSs[226]. More data is needed to delineate a possible phenotype for TLS-derived tumor-reactive CD8$^+$ T cells, although their frequency, cytotoxicity, and clinical application still remain open questions.

Several considerations need to be taken into account during the investigation of tumor-reactive T cell phenotypes using MICS. On the one hand, the proximity of cells to tumor islets above or below the imaged plane cannot be determined in 2D imaging and thus T cells in stromal areas may actually still be close to tumor cells. On the other hand, the studied regions of interest may be too small in size to see larger phenotypic differences between stromal and intratumoral TILs as they migrate through the tissue searching for their targets[200].

Furthermore, I faced other limitations during the MICS analysis that are characteristic of multiplexed imaging technologies[228]. First, I could not further subclassify certain cell types due to the lack of relevant markers in the MICS antibody panel. This can be particularly important for cells of the myeloid lineage as different subsets with either pro- or anti-inflammatory functions may co-exist in tumors[229]. One of the reasons was the absence of antibody clones at the time of this PhD project that were compatible with both the fixation method used (i.e., acetone) and the MICS technology itself (i.e., incubation times of only 10 minutes). Soluble molecules, such as cytokines and chemokines, play important modulating roles in the TME and could also be used to define cell subsets and their functions, particularly in TLSs[15,230]. In this case, aldehyde-based fixatives (e.g., formaldehyde) are preferred over organic solvents (e.g., acetone) to preserve soluble proteins[231]. Notably, components of the extracellular matrix, such as collagen and fibronectin, can have relevant functions in the TME, for example by influencing the migration of T cells in the tumor[232]. Therefore, it is important to consider the addition of markers for such molecules in future studies. Second, the quality of the segmentation was greatly affected by overlapping cells. Highly packed tissue areas, such as TLSs, represent real challenges for cell segmentation, as observed by the impossibility to systematically distinguish between $CD4^+$ and $CD8^+$ T cell subsets in the TLSs of the OvCa sample, or by the identification of markers in $CD8^+$ TILs that were expressed by neighboring cells. The combination of a systematic analysis and a visual inspection of images can help in the identification of cell types, but this requires experienced personnel and is not feasible when analyzing hundreds of images in large datasets.

New technical and computational advances may overcome the current limitations of multiplexed imaging data. These developments include: 1) selection, titration, and validation of suitable antibodies for MICS for improved quality stainings, 2) addition of positive and negative staining controls, 3) higher camera resolution, 4) the possibility of 3D imaging and whole-tissue scans in the MACSima instrument, 5) improved normalization strategies, and 6) machine learning algorithms for segmentation and cell annotation. Furthermore, cellular neighborhood analysis and cell-cell interactions may be added in future studies to achieve a deeper understanding of the TME dynamics[129].

All in all, MICS represents a powerful tool for cancer research and beyond. Although I could only present in this thesis the analysis of two patients, the investigation of larger cohorts of patients together with their clinical outcomes would generate valuable data for physicians and pathologists to better stratify and diagnose patients based on their TME composition and spatial distribution. In addition, the development of MICS for single cell suspensions will allow the investigation of liquid cancers as well. Importantly, it can be used as a screening method when material is limited, as shown by different groups at Miltenyi in the identification of tumor targets in PDAC and ovarian cancer for CAR T cell-based therapies[179,233].

4.3 Future clinical perspectives for enriched TIL subsets

The generation of effective TIL products relies on the frequency, composition, and fitness of tumor-reactive T cells. My PhD project has focused on the first aspect, advocating for the use of an *a priori* phenotype—based on CD39 expression—to enrich tumor-reactive $CD8^+$ T cells before the *ex vivo* expansion.

The second aspect refers to the composition of cell therapy products, normally including both $CD8^+$ and $CD4^+$ T cell subsets. Accumulated evidence underlines the crucial role of helper $CD4^+$ T cells in mounting and maintaining an effective anti-tumor response[28]. My project has not explored the identification of a marker that can potentially enrich both $CD8^+$ and $CD4^+$ TILs, but it would be desirable to design a process that includes both cell subsets. Fortunately, recent studies have shown that CD39 can also be used to enrich tumor-reactive $CD4^+$ TILs from lung, colorectal, breast, oropharyngeal, vulvar, and cervical cancers[127,234–236]. However, regulatory $CD4^+$ T cells are also known to express high levels of CD39[237], which may have negative effects during the generation of TIL products due to their immunosuppressive functions[238]. Other markers, such as CD137, are also under investigation[96,239,240].

The third aspect, T cell fitness, comprises key elements of T cells, such as functionality, proliferative capacity, stemness, and persistence. My project has not explored the fitness of TILs in the final product. Future studies should consider investigating these aspects, especially when enriching populations like $CD39^+$ $CD8^+$ TILs, whose levels of exhaustion may pose challenges in achieving effective clinical responses. A study in clear cell renal cell carcinoma (ccRCC) showed that high $CD39^+$ $CD8^+$ TIL frequencies correlated with poor prognosis due to their dysfunctionality[241]. Likewise, Krishna et al. analyzed TIL products of ACT responders versus non-responders and, despite finding most of neoantigen-specific TILs in the $CD39^+$ subset, ACT responders uniquely retained a $CD39^-$ $CD69^-$ stem-like T cell population containing reactive T cells[39]. These observations indicate that not all tumor-specific T cells are tumor-reactive, and it is thus important not to use these two terms interchangeably. In contrast to these studies, various publications have highlighted the cytotoxic and proliferative ability of exhausted T cell subsets[17,38,40,242]. As T cell dysfunction is a continuum, various states with diverse levels of fitness can co-exist in the tumor, explaining the differences seen among studies. Therefore, the search for markers that better define less dysfunctional states of tumor-specific TILs and can be used clinically is necessary in the future. Another approach may consist of the reprogrammability or reversibility of dysfunctional T cell states towards less differentiated and fitter cells. This aspect has been thoroughly studied by Schietinger et al., who found that terminally dysfunctional T cells expressing high levels of PD1, CD38, and CD101, together with low levels of CD5, had a locked epigenetic profile that was not therapeutically reprogrammable by immune checkpoint blockade[42,243].

Whether the dysfunctional state of CD39^{+} TILs can be reversible reminds unclear, although *in vitro* inhibition of CD39 could partially restore the function of CD39^{+} CD8^{+} TILs in ccRCC in another study[241].

Therefore, alternative sources of tumor-reactive T cells, such as blood, could be advantageous to get less differentiated cells that can proliferate and persist *in vivo*. In addition, blood constitutes a more readily available and less invasive source than tumor samples for ACT approaches. The first evidence that cell surface markers could identify circulating tumor-reactive T cells was reported by Gros et al., who showed that PD1-expressing CD8^{+} T cells from peripheral blood of melanoma patients were enriched for neoantigen reactivity[244]. Later, this finding was extended to the PD1$^{+/hi}$ T cell subset in blood from patients with gastrointestinal cancers[244]. These studies showed that peripheral blood lymphocytes contain tumor-reactive T cells with a distinctive phenotype. A recent study demonstrated that circulating, tumor-matching T cell clones had a higher activation state compared to non-matching clones in blood, but they were less dysfunctional than their tumor counterparts[245]. They proposed NKG2D, CX3CR1, and CD39 as candidate biomarkers for enrichment strategies. Similarly, Yossef et al. have recently shown that circulating antitumor T cells in metastatic cancer patients had a unique transcriptional signature with a less dysfunctional phenotype than their TIL counterparts, and they could be identified by the cell surface protein expression of CD39, HLA-DR, and CD103[246]. However, the expected frequency of tumor-reactive T cells in blood ranges between 0.0007% to 0.5% according to previous studies[66,81,246,247], posing challenges for their isolation and expansion for ACT.

The identification of a tumor-reactive phenotype, irrespective of T cell fitness, remains valuable for the next generation of cell therapies. Specifically, these phenotypes can be used to identify tumor-specific TCRs[173,246,248,249], which can be transferred into less differentiated T cells to produce TCR-engineered T cell products. This strategy overcomes limitations of traditional TIL therapies, such as the low frequency and exhaustion of tumor-reactive T cells. Although various challenges are associated with TCR-engineered T cells[250,251], ongoing research affirms the promise of this therapy as a novel and effective approach against cancer[252–254].

4.4 Concluding remarks

Collectively, the data presented in my PhD thesis provides a characterization of $CD8^+$ TILs at multiple levels and focused on the relevance of CD39 as a surrogate marker of tumor reactivity.

The potential of the MICS technology to perform analysis of spatial distribution of cells in the tumor microenvironment is highlighted in this project. New generations of MICS will offer improved technical features that, together with advanced bioinformatic pipelines, will go beyond the current limits of multiplexed imaging techniques. Importantly, the adaptation of MICS for single cell suspensions could soon become an alternative to other multiparametric cell analyses at the protein level. Other technologies, such as scRNA-seq, provide the opportunity to investigate gene expression profiles of TILs in combination with their TCR repertoire. In my PhD project, I benefited from the use of such approaches to investigate the phenotypes of TILs, which were in accordance with recent literature in the field. Multi-omics, such as the integration of TCR sequences, gene and protein expression profiles, antigen specificity, and even spatial information, will advance our understanding of antitumor responses and the development of more effective therapies.

The study of TIL phenotypes has introduced the idea of a unique marker expression profile of tumor-reactive TILs that can be exploited in different ways, including clinical application. Many tumor types, such as ovarian cancer, contain only a small fraction of tumor-reactive TILs. Therefore, their enrichment based on a cell surface marker, or combination thereof, prior to the *ex vivo* expansion may improve the efficacy of TIL products in ACT. This represents a promising approach as it generates a polyclonal T cell population without the need for prior knowledge of tumor antigens targeted, reducing the costs and time of manufacturing and making it widely applicable. CD39 has been proposed as a potential biomarker for tumor-reactive TILs and I have assessed this hypothesis by phenotypically and functionally characterizing this population. The data collected in my thesis is consistent with recent discoveries, although the feasibility of CD39 for clinical use still needs to be validated in a larger number of cancer patients and types. The development of a GMP-compliant process using CD39 in the CliniMACS Prodigy, an automated manufacturing instrument, may be considered in the future. However, the exhausted states of $CD39^+$ TILs constitute a proper reason to shift the focus to less differentiated TIL populations, such as stem-like subsets, or to alternative sources like blood. Yet, the small frequencies of tumor-reactive T cells in these subsets may present a daunting problem for enrichment approaches. Alternatively, the identification of antitumor TCRs by their specific T cell phenotype can be used to develop TCR-based therapies, overcoming the limitations of TIL treatments.

5 Supplementary Figures

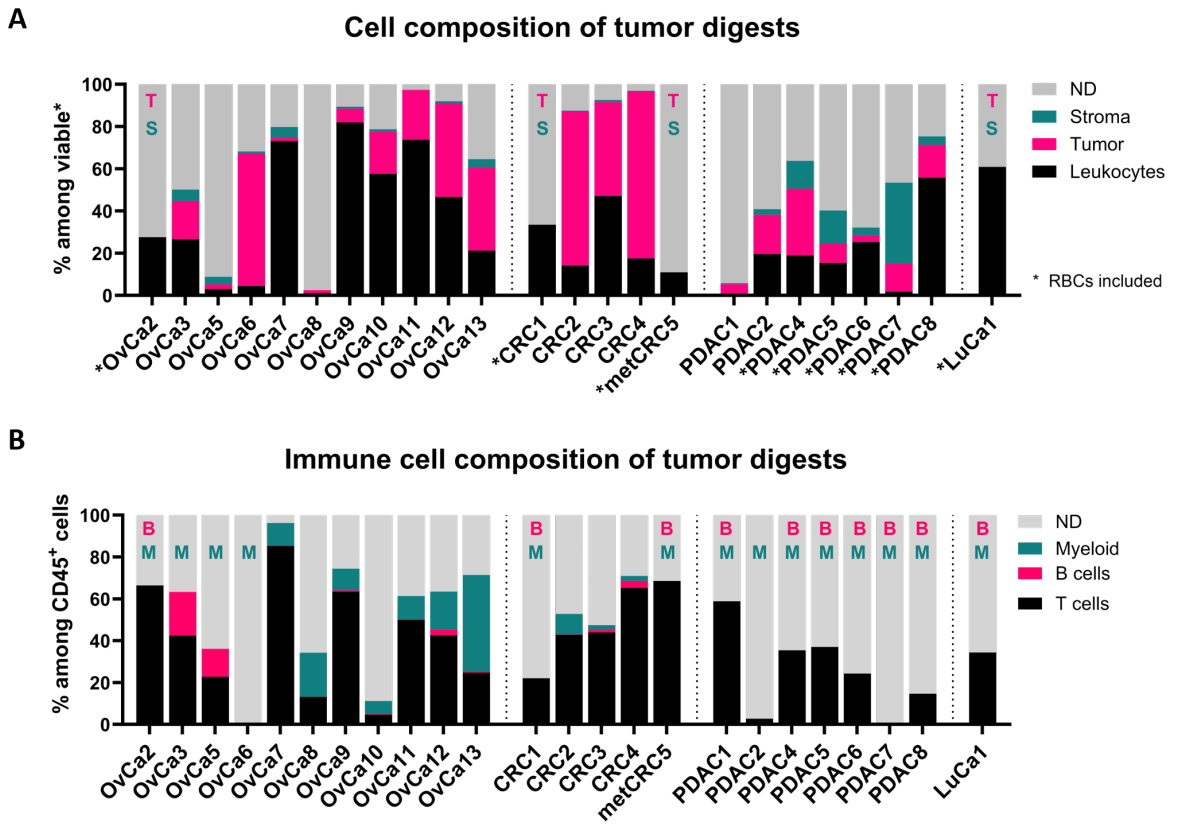

Supplementary Figure 1. Cell composition of tumor digests per cancer patient sample
(A) Percentage of leukocytes ($CD45^+$), tumor cells ($EpCAM^+$) and stromal cells ($CD31^+$ and $CD90^+$) among viable cells are depicted for each cancer patient. **(B)** Percentage of T cells ($CD3^+$), B cells ($CD19^+$) and myeloid cells ($CD14^+$) among $CD45^+$ immune cells are depicted for each cancer patient. OvCa12 data was jointly generated with Aparajita Singh, PDAC1 data with Anne Frank, and PDAC4-8 data was generated by Christina Völzke and Lisa Ehrhardt. Colored letters inside the bars (T, S, B and M) indicate that no marker for tumor, stromal cells, B cells or myeloid cells, respectively, was present in the flow panel used for the specific patient. In samples with * no red blood cell marker (RBCs) was used and thus they could not be excluded in the calculation of the frequencies among viable cells. ND: not determined. Ovarian carcinoma (OvCa), (metastatic) colorectal carcinoma ([met]CRC), pancreatic ductal adenocarcinoma (PDAC) and lung carcinoma (LuCa).

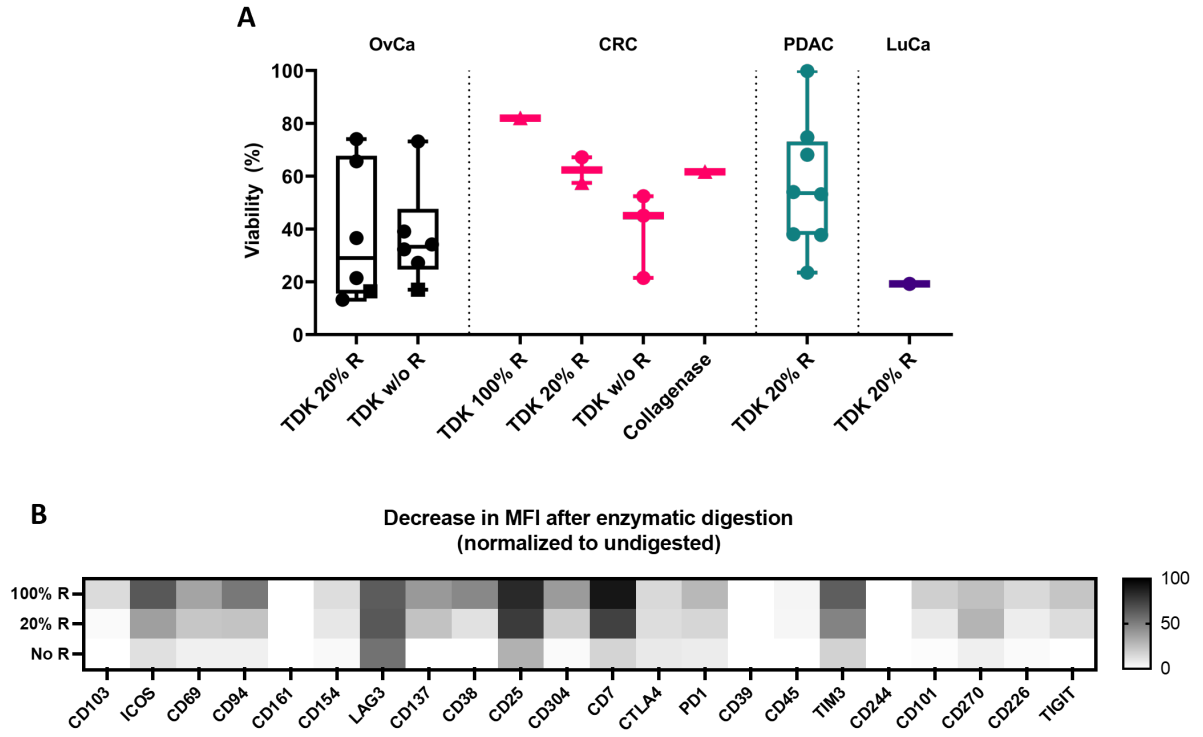

Supplementary Figure 2. Effects of enzyme R on cell viability and epitope integrity
(A) Cell viabilities of tumors digested with the tumor dissociation kit (TDK, Miltenyi) with either the recommended enzyme R concentration (TDK 100% R), a reduction of enzyme R to 20% (TDK 20% R) or no enzyme R (TDK w/o R). metCRC5 (triangle) and OvCa8 (square) samples were divided and digested with different protocols for comparison. In addition, metCRC5 was digested by replacing the enzyme H of the TDK with a collagenase IV from Sigma and without the enzyme R ("collagenase" condition), which represented a standard digestion protocol used in our group prior to the TDK development. **(B)** Relative decrease in the mean fluorescent intensity (MFI) of several markers on activated $CD3^+$ T cells from healthy PBMCs after TDK digestion with different concentrations of enzyme R. Ovarian carcinoma (OvCa, n = 12), colorectal carcinoma (CRC, n = 5), pancreatic ductal adenocarcinoma (PDAC, n = 8) and lung carcinoma (LuCa, n = 1). Bar plots show the mean (line) and standard deviation SD (error bars).

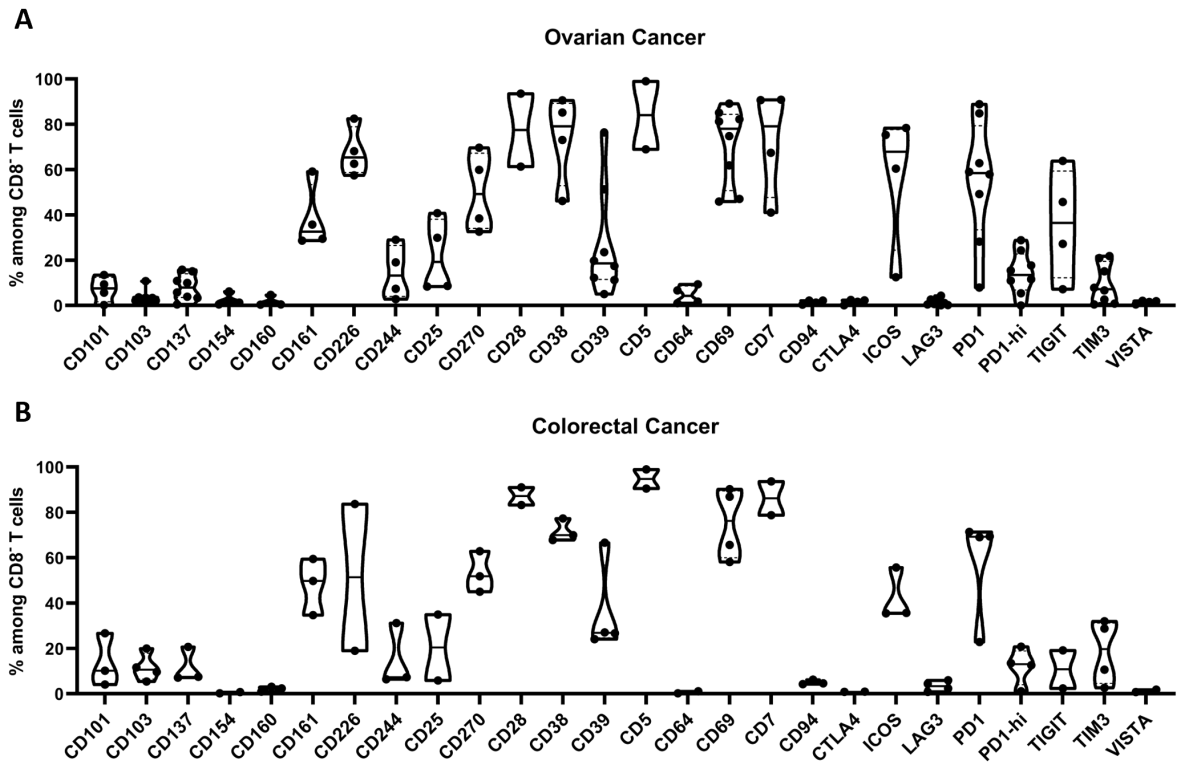

Supplementary Figure 3. Phenotypic characterization of CD8$^-$ TILs in tumor patients
Several markers related to activation/exhaustion were screened in tumor patient TILs. Percentage of marker$^+$ cells among CD8$^-$ TILs are shown for **(A)** ovarian cancer (n = 3 to 8) and **(B)** colorectal cancer (n = 1 to 4). Violin plots show the median (line) and quartiles (dotted line). Each dot represents a patient.

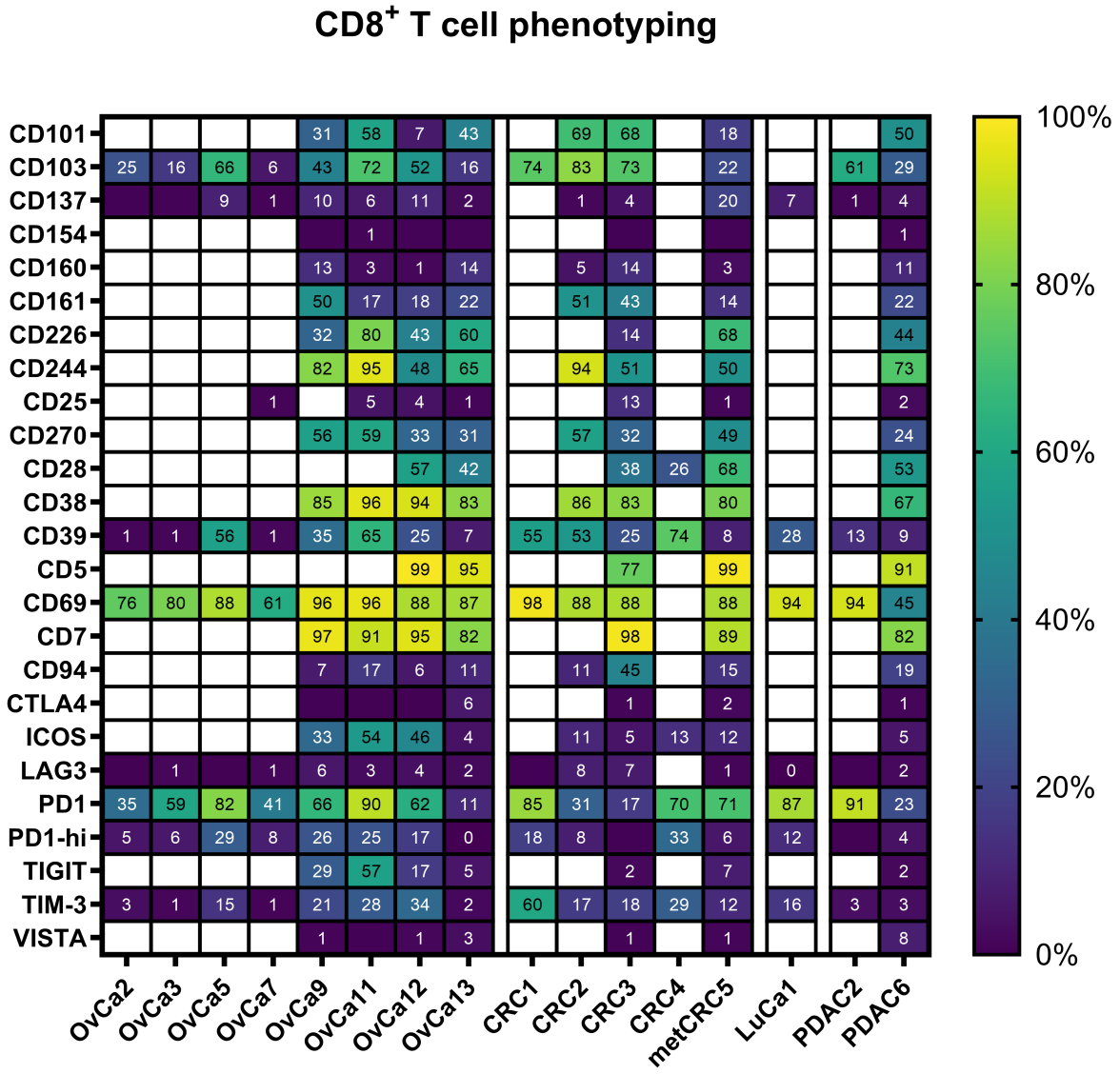

Supplementary Figure 4. Expression of relevant markers on CD8⁺ TILs per cancer patient sample
Heatmap showing the frequency of marker⁺ CD8⁺ TILs for each cancer patient. The bar color indicates the frequency among CD8⁺ TIL. Blank spaces mean that the specific marker was not included in the analysis. Ovarian carcinoma (OvCa), colorectal carcinoma (CRC), pancreatic ductal adenocarcinoma (PDAC) and lung carcinoma (LuCa).

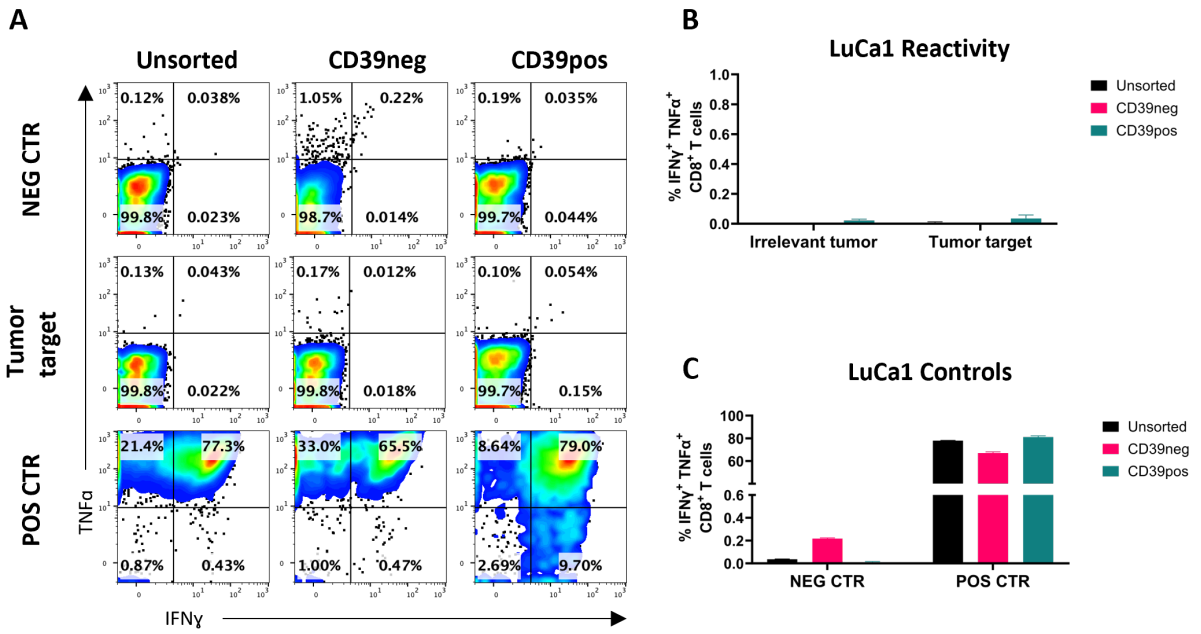

Supplementary Figure 5. Reactivities of expanded CD8⁺ TILs from LuCa1

(A) Representative FACS plots of the different expanded T cell populations from lung carcinoma patient 1 (LuCa1) (unsorted fraction, CD39⁻ [CD39neg], and CD39⁺ [CD39pos]), showing the frequency of interferon γ (IFNγ) and tumor necrosis factor α (TNFα)-secreting CD8⁺ TILs upon co-culture with tumor. TILs in only medium were used as negative control (NEG CTR), whereas TILs stimulated with PMA/Ionomycin were the positive control (POS CTR). **(B)** Quantification of the percentage of IFNγ⁺ TNFα⁺ CD8⁺ TILs upon co-culture with an irrelevant tumor (allogeneic ovarian tumor cell line) or tumor target. The background of the NEG CTR is subtracted in the graph. **(C)** Quantification of the percentage of IFNγ⁺ TNFα⁺ CD8⁺ TILs in the NEG and POS controls. Bars represent the mean and bar errors the SD of technical triplicates.

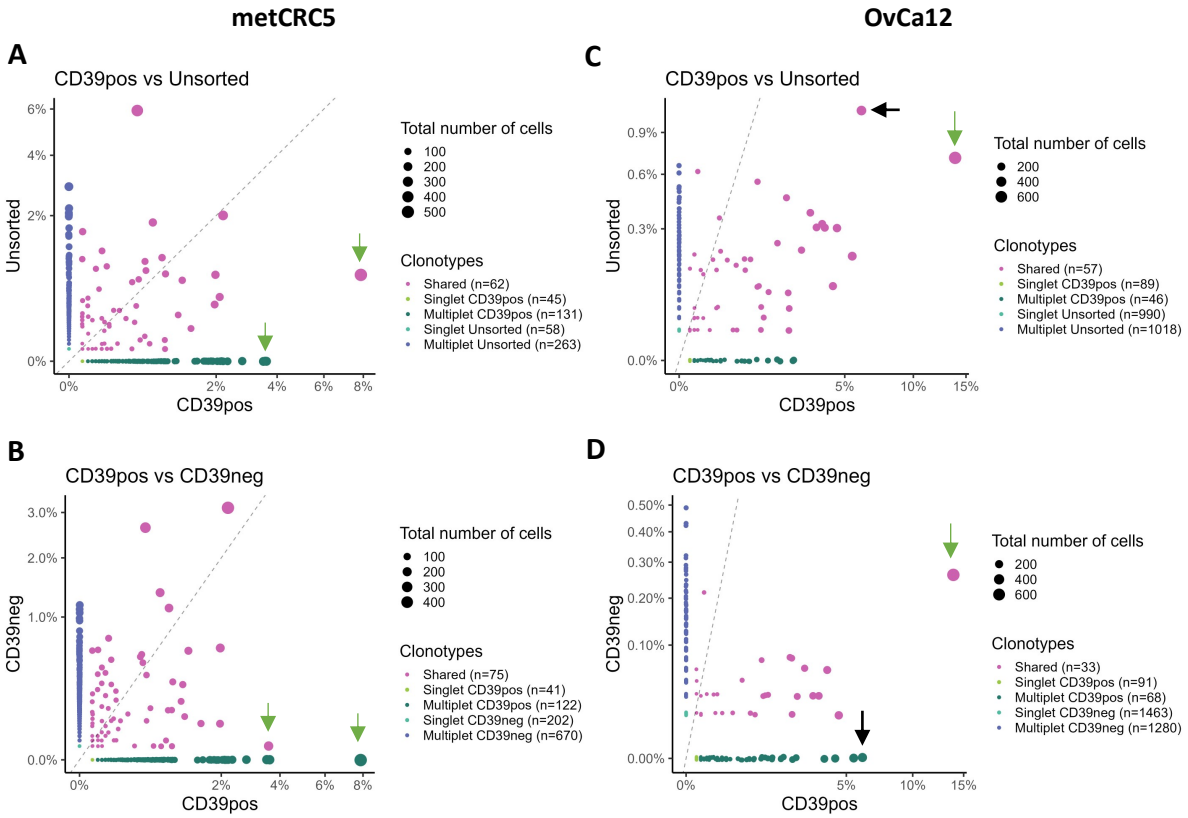

Supplementary Figure 6. Clonotype comparison between expanded CD39⁺ CD8⁺ TILs and other expanded subsets

Scatter plot comparing the clonotypes of expanded CD39⁺ CD8⁺ TILs (CD39pos) with the other expanded samples (Unsorted and CD39neg) for **(A and B)** metCRC5 and **(C and D)** OvCa12. In the scatter plots, each dot corresponds to a unique TCR clonotype. The common TCRs are shown in pink, the size of the circles indicates the total number of cells belonging to the clonotype, and the clonotypes closer to the diagonal are found in similar frequencies in both samples. s

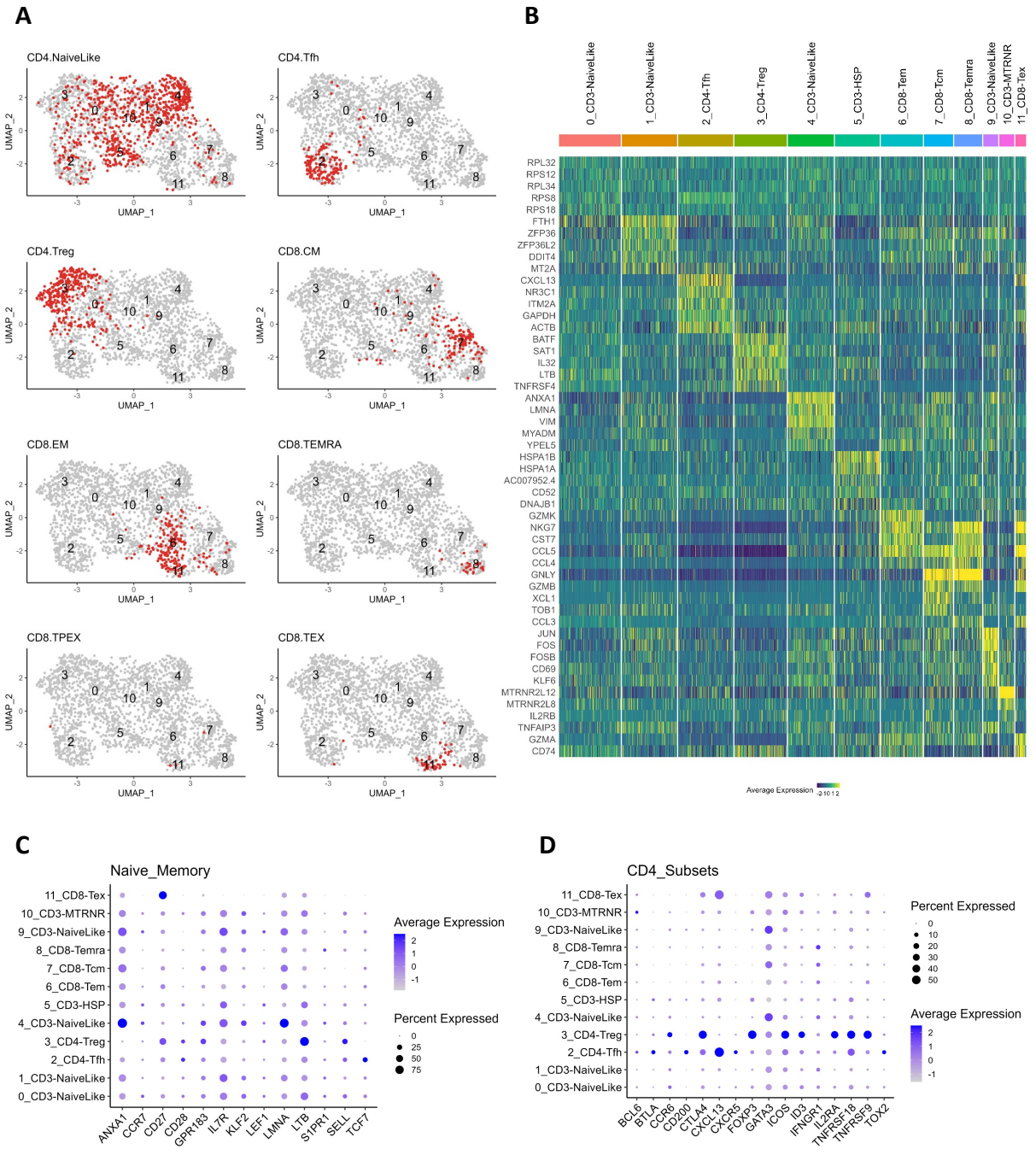

Supplementary Figure 7. Expression profiles that aided in the annotation of TILs from metCRC5
(A) UMAP plots highlighting the cells (in red) that were classified as different TIL subsets (in plot title) by ProjecTILs. **(B)** Heatmap of the top five differentially expressed genes for each cluster. **(C and D)** Dot plots of selected gene sets related to (C) naive/memory and (D) CD4 subsets, and its average expression (color gradient) by cluster. The size of the dot indicates the percentage of cells expressing the gene within each cluster.

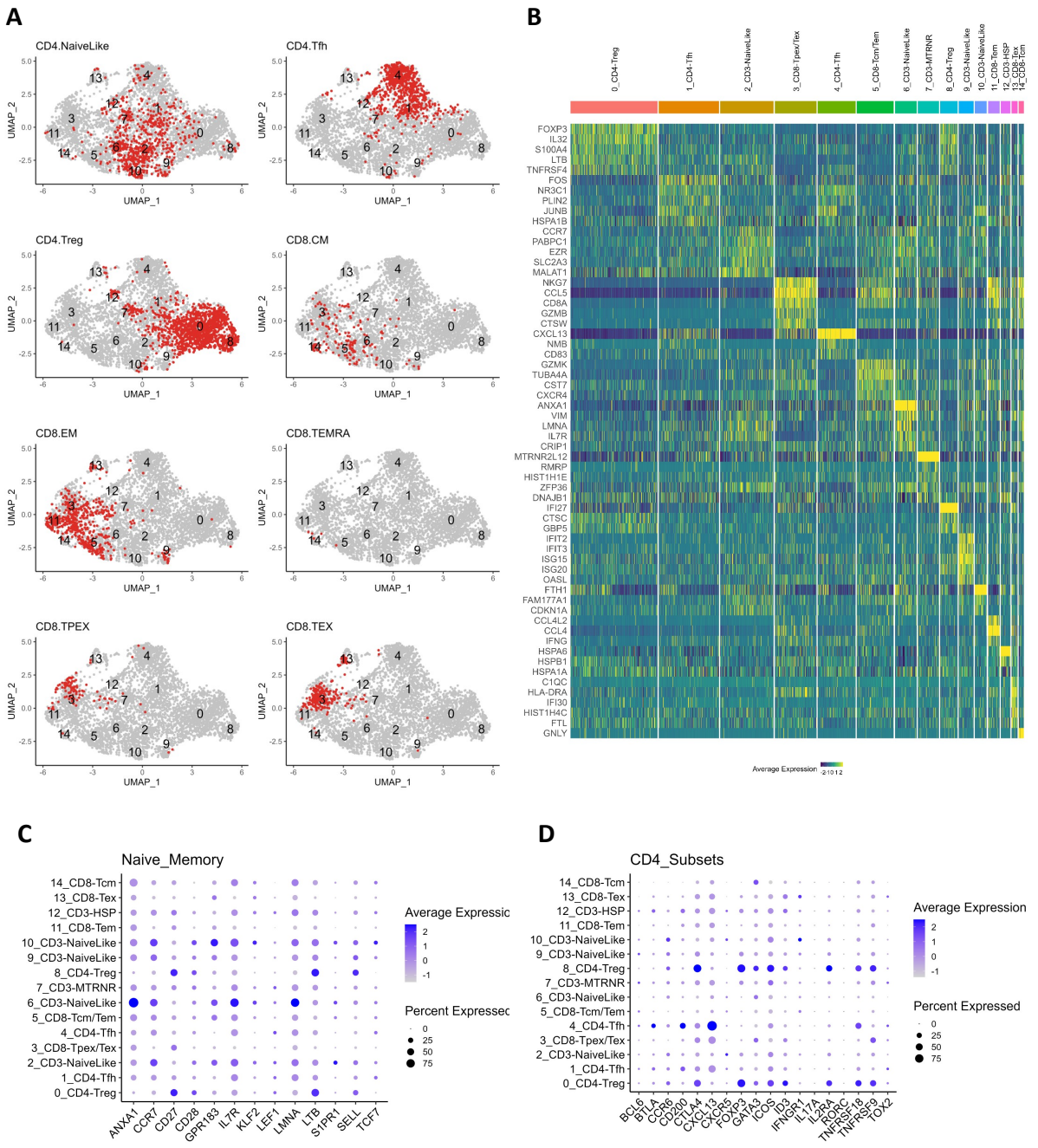

Supplementary Figure 8. Expression profiles that aided in the annotation of TILs from OvCa12
(A) UMAP plots highlighting the cells (in red) that were classified as different TIL subsets (in plot title) by ProjecTILs. **(B)** Heatmap of the top five differentially expressed genes for each cluster. **(C and D)** Dot plots of selected gene sets related to (C) naive/memory and (D) CD4 subsets, and its average expression (color gradient) by cluster. The size of the dot indicates the percentage of cells expressing the gene within each cluster.

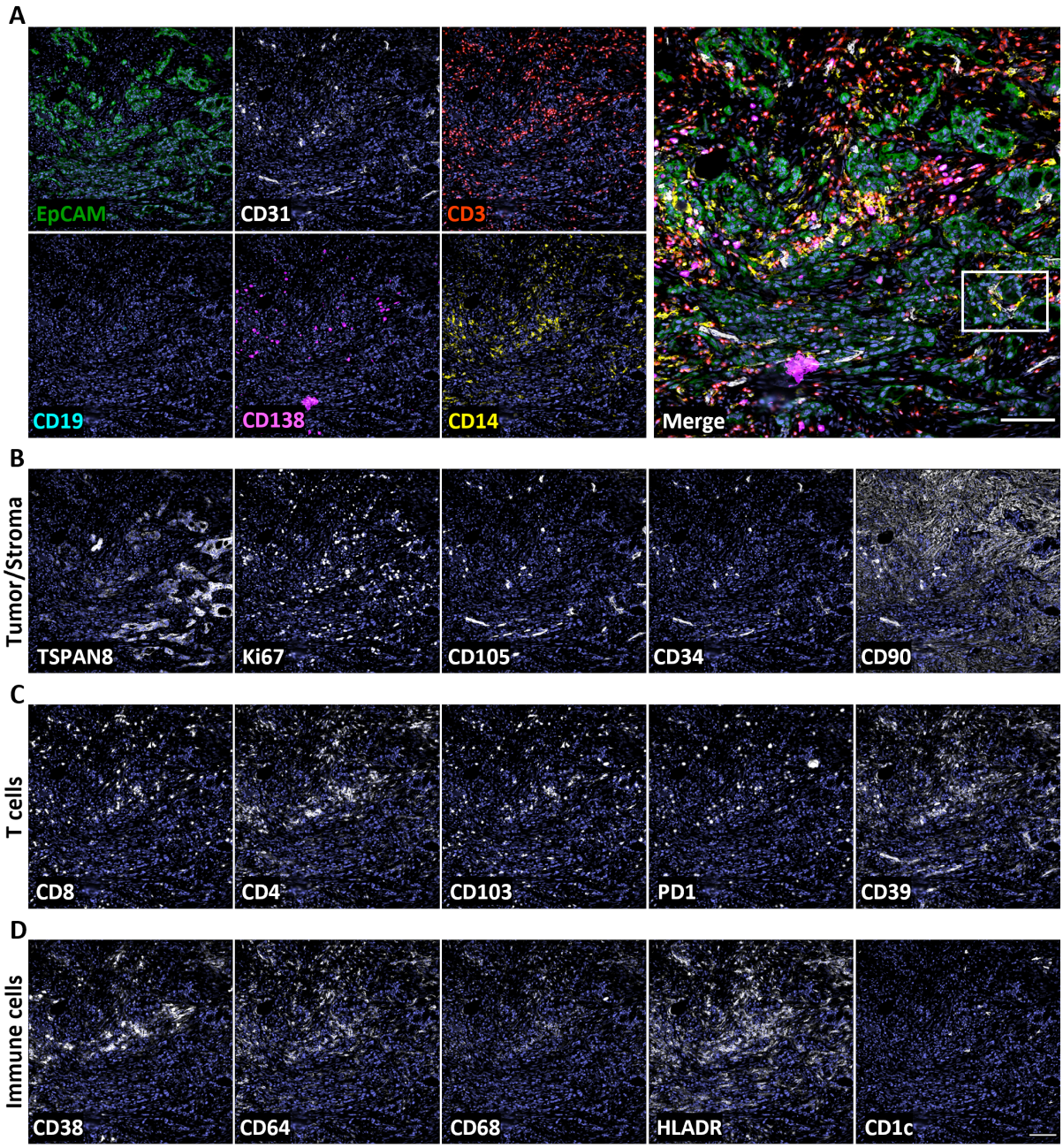

Supplementary Figure 9. Visual identification of cell types in ROI 3 from metCRC5
(A) Markers for the main cell types in the TME, such as EpCAM$^+$ tumor (green), CD31$^+$ endothelium (white), CD3$^+$ T cells (red), CD19$^+$ B cells (cyan), CD138$^+$ plasma cells (magenta), and CD14$^+$ myeloid cells (yellow), are shown on the left side, and the overlay of these stainings on the right side. White square represents the location of image magnification in Supplementary Figure 13B. **(B to D)** Representative markers found in tumor/stroma (B), T cells (C), and several immune cell types (D) are depicted in white. Nuclei are stained with Hoechst (blue) in all images. Scale bar: 100 µm.

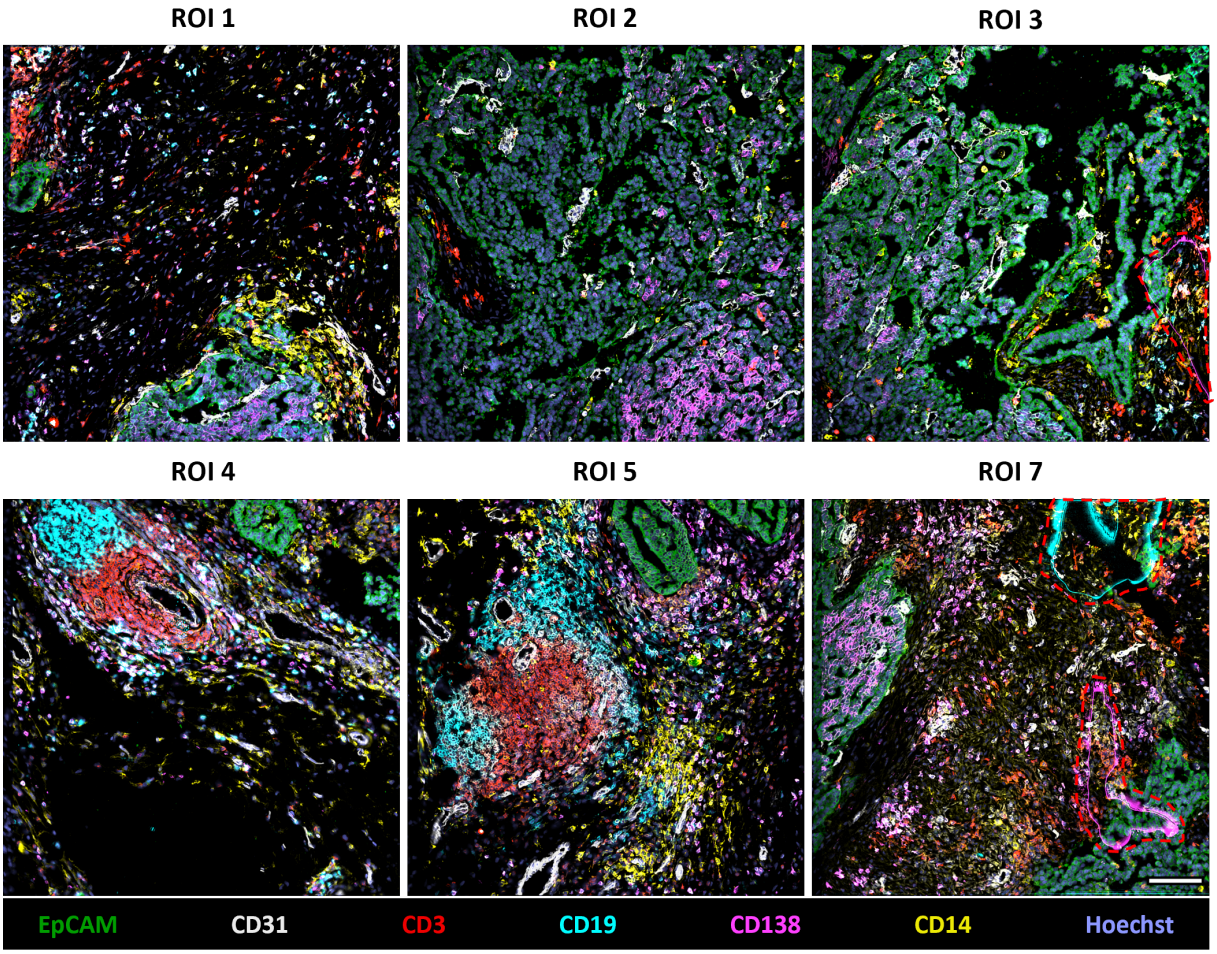

Supplementary Figure 10. Cell composition and distribution in the TME of the OvCa sample
Images from ROIs 1, 2, 3, 4, 5, and 7 from this OvCa sample showing the main cell types composing the TME, such as EpCAM$^+$ tumor cells (green), CD31$^+$ endothelium (white), CD3$^+$ T cells (red), CD19$^+$ B cells (cyan), CD138$^+$ plasma cells (cyan), and CD14$^+$ myeloid cells (yellow). Nuclei are stained with Hoechst (blue) in all images. Dotted red lines highlight staining artifacts. These areas are removed for the bioinformatic analysis. Scale bar: 100 µm.

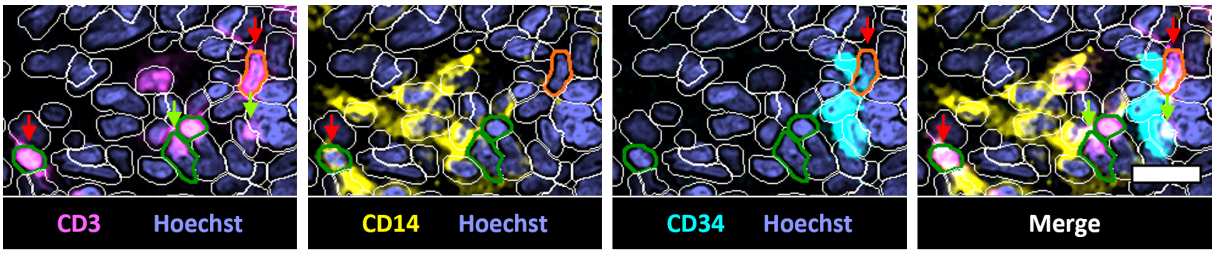

Supplementary Figure 11. Segmentation noise in multiplexed immunofluorescent images
CD4$^+$ T cells (dark green segments) and CD8$^+$ T cells (orange segments) are highlighted in the images, and the stainings of CD3 (magenta, first image), CD14 (yellow, second image), CD34 (cyan, third image), and the merge of these markers (fourth image) are shown to indicate either imperfect segmentation (light green arrows) or overlapping signals from CD14$^+$ and CD34$^+$ cells into T cell segments (red arrows) that can cause false positives (e.g., T cells expressing CD14) in MICS images. Nuclei (Hoechst) is shown in blue in all images. Scale bar: 20 µm.

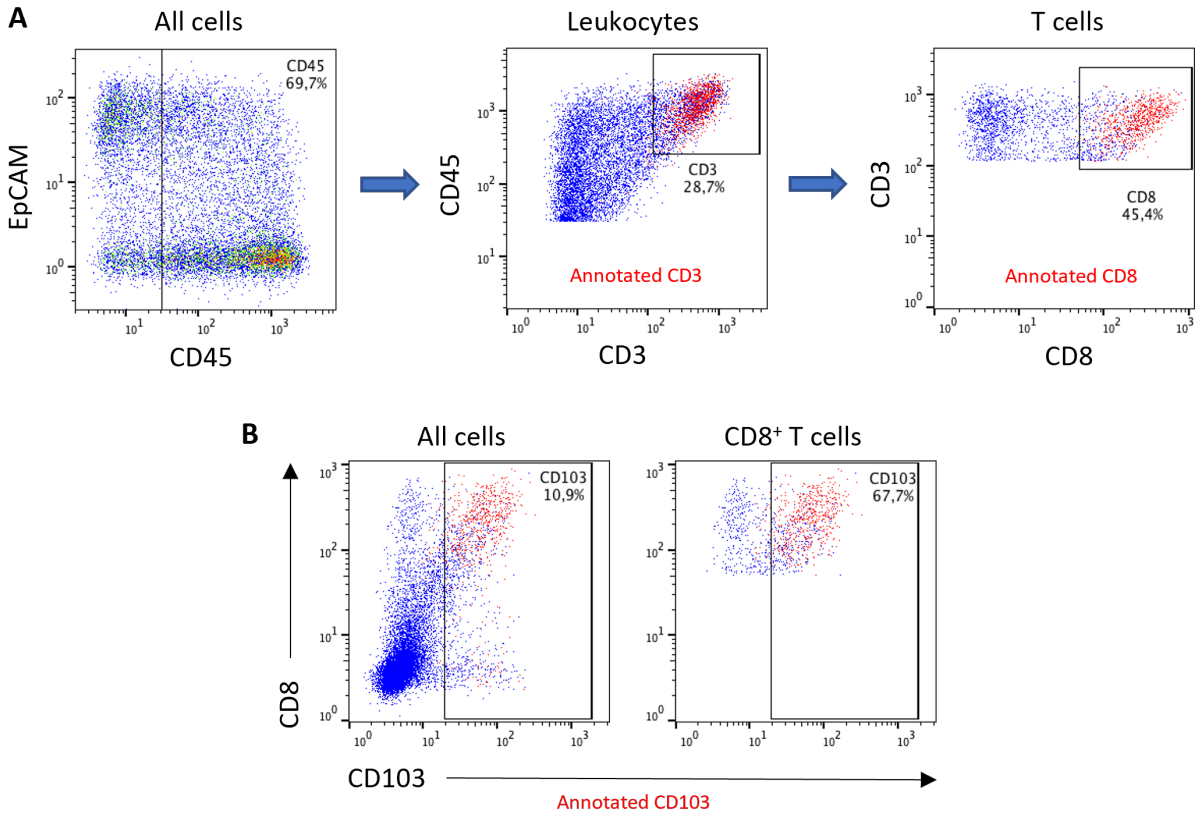

Supplementary Figure 12. Gating strategy to systematically identify CD8⁺ TIL subsets in tissues
(A) The extracted data (mean intensity values) after segmenting MICS images was analyzed in a similar manner as flow cytometry data, and a gating strategy was designed to identify CD8⁺ T cells. The gating was assisted by the manual annotation of positive cells for certain markers, such as CD3 or CD8 (dots in red). **(B)** Marker positive CD8⁺ T cells, for instance CD103⁺ CD8⁺ T cells, were gated using negative cells as a reference in the ungated population (all cells).

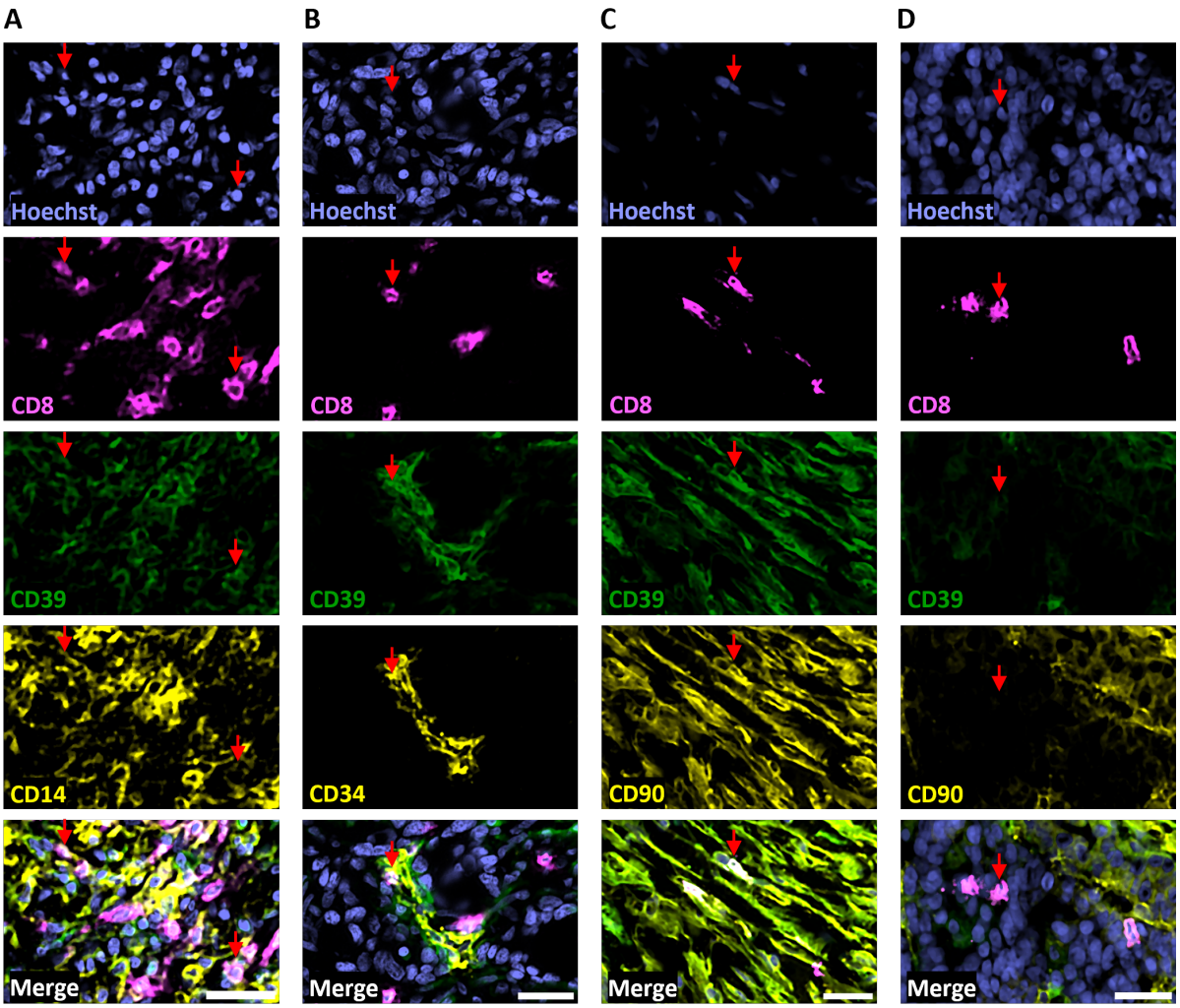

Supplementary Figure 13. Representative images of CD39 expression in tumor tissues
High-magnification images depict CD8 (magenta), CD39 (green), and CD14, CD34, or CD90 (yellow) and illustrate challenges in identifying $CD39^+$ $CD8^+$ T cells in MICS images. CD39 expression was prominent in cell types neighboring T cells, such as **(A)** $CD14^+$ myeloid cells, **(B)** $CD34^+$ blood vessels, and **(C and D)** $CD90^+$ fibroblasts. The images represent tissue areas from (A and B) patient metCRC5 ROI 1 and 3, respectively (uncropped images in Figure 18 and Supplementary Figure 9); and (C and D) patient OvCa-TLS ROI 6 (uncropped image in Figure 24). Stromal areas are represented in A and C images, whereas B and D images correspond to tumor areas. Nuclei are stained with Hoechst (blue). Scale bar: 30 µm.

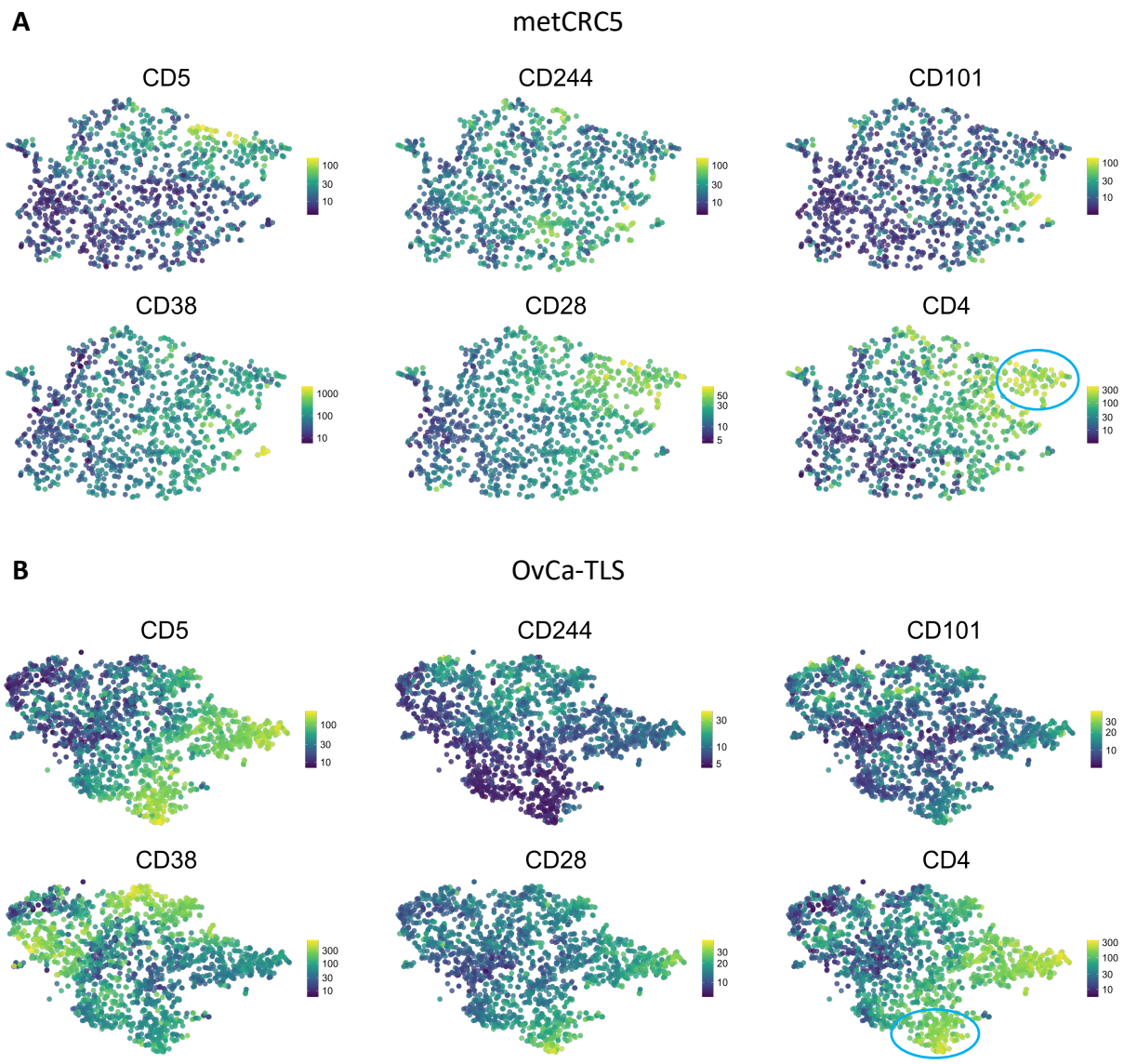

Supplementary Figure 14. Co-expression of additional relevant markers on CD8⁺ TILs
The expression of additional relevant markers on CD8⁺ TILs from **(A)** metCRC5 and **(B)** OvCa-TLS samples was shown in tSNE maps. The blue circles denote cells in close contact with CD4⁺ T cells. The tSNE color scale shows fluorescent mean intensity in Log10 scale.

6 References

1. Bray, F. *et al.* Global cancer statistics 2022: GLOBOCAN estimates of incidence and mortality worldwide for 36 cancers in 185 countries. *CA Cancer J Clin* **74**, 229–263 (2024).
2. Hajdu, S. I. A note from history: Landmarks in history of cancer, part 1. *Cancer* **117**, 1097–1102 (2011).
3. Lopez, M. J. The Evolution of Radical Cancer Surgery. *Surg Oncol Clin N Am* **14**, xiii–xv (2005).
4. Chabner, B. A. & Roberts, T. G. Chemotherapy and the war on cancer. *Nature Reviews Cancer 2005 5:1* **5**, 65–72 (2005).
5. Hunter, P. The fourth pillar. *EMBO Rep* **18**, 1889–1892 (2017).
6. McCarthy, E. F. The Toxins of William B. Coley and the Treatment of Bone and Soft-Tissue Sarcomas. *Iowa Orthop J* **26**, 154 (2006).
7. Pardoll, D. M. The blockade of immune checkpoints in cancer immunotherapy. *Nat Rev Cancer* **12**, 252–264 (2012).
8. Wang, D., Bauersachs, J. & Berliner, D. Immune Checkpoint Inhibitor Associated Myocarditis and Cardiomyopathy: A Translational Review. *Biology (Basel)* **12**, 472 (2023).
9. Haslam, A. & Prasad, V. Estimation of the Percentage of US Patients With Cancer Who Are Eligible for and Respond to Checkpoint Inhibitor Immunotherapy Drugs. *JAMA Netw Open* **2**, e192535–e192535 (2019).
10. Wei, S. C., Duffy, C. R. & Allison, J. P. Fundamental Mechanisms of Immune Checkpoint Blockade Therapy. *Cancer Discov* **8**, 1069–1086 (2018).
11. Dudley, M. E. *et al.* Cancer regression and autoimmunity in patients after clonal repopulation with antitumor lymphocytes. *Science (1979)* **298**, 850–854 (2002).
12. Morotti, M. *et al.* Promises and challenges of adoptive T-cell therapies for solid tumours. *Br J Cancer* **124**, 1759–1776 (2021).
13. Anderson, N. M. & Simon, M. C. The tumor microenvironment. *Current Biology* **30**, 905–931 (2020).
14. Binnewies, M. *et al.* Understanding the tumor immune microenvironment (TIME) for effective therapy. *Nat Med* **24**, 541–550 (2018).

15. Sautès-Fridman, C., Petitprez, F., Calderaro, J. & Fridman, W. H. Tertiary lymphoid structures in the era of cancer immunotherapy. *Nat Rev Cancer* **19**, 307–325 (2019).

16. Dai, S. *et al.* Intratumoral CXCL13+ CD8+ T cell infiltration determines poor clinical outcomes and immunoevasive contexture in patients with clear cell renal cell carcinoma. *J Immunother Cancer* **9**, e001823 (2021).

17. Thommen, D. S. *et al.* A transcriptionally and functionally distinct PD-1+ CD8+ T cell pool with predictive potential in non-small-cell lung cancer treated with PD-1 blockade. *Nat Med* **24**, 994–1004 (2018).

18. Fridman, W. H. *et al.* B cells and tertiary lymphoid structures as determinants of tumour immune contexture and clinical outcome. *Nature Reviews Clinical Oncology 2022 19:7* **19**, 441–457 (2022).

19. Niogret, J. *et al.* Follicular helper-T cells restore CD8+-dependent antitumor immunity and anti-PD-L1/PD-1 efficacy. *J Immunother Cancer* **9**, e002157 (2021).

20. Dieu-Nosjean, M. C., Goc, J., Giraldo, N. A., Sautès-Fridman, C. & Fridman, W. H. Tertiary lymphoid structures in cancer and beyond. *Trends Immunol* **35**, 571–580 (2014).

21. Ruddle, N. H. High Endothelial Venules and Lymphatic Vessels in Tertiary Lymphoid Organs: Characteristics, Functions, and Regulation. *Front Immunol* **7**, 491 (2016).

22. Domblides, C. *et al.* Tumor-Associated Tertiary Lymphoid Structures: From Basic and Clinical Knowledge to Therapeutic Manipulation. *Front Immunol* **12**, 2611 (2021).

23. Goc, J. *et al.* Dendritic Cells in Tumor-Associated Tertiary Lymphoid Structures Signal a Th1 Cytotoxic Immune Contexture and License the Positive Prognostic Value of Infiltrating CD8+ T Cells. *Cancer Res* **74**, 705–715 (2014).

24. Martínez-Lostao, L., Anel, A. & Pardo, J. How Do Cytotoxic Lymphocytes Kill Cancer Cells? *Clinical Cancer Research* **21**, 5047–5056 (2015).

25. Castro, F., Cardoso, A. P., Gonçalves, R. M., Serre, K. & Oliveira, M. J. Interferon-gamma at the crossroads of tumor immune surveillance or evasion. *Front Immunol* **9**, 847 (2018).

26. Spranger, S. & Gajewski, T. F. Mechanisms of Tumor Cell-Intrinsic Immune Evasion. *Annu. Rev. Cancer Biol* **2**, 213–228 (2018).

27. Togashi, Y., Shitara, K. & Nishikawa, H. Regulatory T cells in cancer immunosuppression — implications for anticancer therapy. *Nat Rev Clin Oncol* **16**, 356–371 (2019).

28. Tay, R. E., Richardson, E. K. & Toh, H. C. Revisiting the role of CD4+ T cells in cancer immunotherapy—new insights into old paradigms. *Cancer Gene Ther* **28**, 5–17 (2021).

29. Poncette, L., Bluhm, J. & Blankenstein, T. The role of CD4 T cells in rejection of solid tumors. *Curr Opin Immunol* **74**, 18–24 (2022).

30. Woan, K. V. & Miller, J. S. Harnessing Natural Killer Cell Antitumor Immunity: From the Bench to Bedside. *Cancer Immunol Res* **7**, 1742–1747 (2019).

31. Groth, C. *et al.* Immunosuppression mediated by myeloid-derived suppressor cells (MDSCs) during tumour progression. *Br J Cancer* **120**, 16–25 (2019).

32. Duhan, V. & Smyth, M. J. Innate myeloid cells in the tumor microenvironment. *Curr Opin Immunol* **69**, 18–28 (2021).

33. van Dalen, F., van Stevendaal, M., Fennemann, F., Verdoes, M. & Ilina, O. Molecular Repolarisation of Tumour-Associated Macrophages. *Molecules* **24**, 9 (2018).

34. Mosser, D. M. & Edwards, J. P. Exploring the full spectrum of macrophage activation. *Nat Rev Immunol* **8**, 958–969 (2008).

35. Raskov, H., Orhan, A., Gaggar, S. & Gögenur, I. Cancer-Associated Fibroblasts and Tumor-Associated Macrophages in Cancer and Cancer Immunotherapy. *Front Oncol* **11**, (2021).

36. Speiser, D. E. *et al.* T cell differentiation in chronic infection and cancer: Functional adaptation or exhaustion? *Nat Rev Immunol* **14**, 768–774 (2014).

37. van der Leun, A. M., Thommen, D. S. & Schumacher, T. N. CD8+ T cell states in human cancer: insights from single-cell analysis. *Nat Rev Cancer* **20**, 218–232 (2020).

38. Li, H. *et al.* Dysfunctional CD8 T Cells Form a Proliferative, Dynamically Regulated Compartment within Human Melanoma. *Cell* **176**, 775-789.e18 (2019).

39. Krishna, S. *et al.* Stem-like CD8 T cells mediate response of adoptive cell immunotherapy against human cancer. *Science (1979)* **370**, 1328–1334 (2020).

40. Sade-Feldman, M. *et al.* Defining T Cell States Associated with Response to Checkpoint Immunotherapy in Melanoma. *Cell* **175**, 998-1013.e20 (2018).

41. Kurtulus, S. *et al.* Checkpoint Blockade Immunotherapy Induces Dynamic Changes in PD-1-CD8+ Tumor-Infiltrating T Cells. *Immunity* **50**, 181-194.e6 (2019).

42. Philip, M. *et al.* Chromatin states define tumour-specific T cell dysfunction and reprogramming. *Nature* **545**, 452–456 (2017).

43. Vodnala, S. K. *et al.* T cell stemness and dysfunction in tumors are triggered by a common mechanism. *Science* **363**, eaau0135 (2019).

44. Thommen, D. S. & Schumacher, T. N. T Cell Dysfunction in Cancer. *Cancer Cell* **33**, 547–562 (2018).

45. Blank, C. U. *et al.* Defining 'T cell exhaustion'. *Nat Rev Immunol* **19**, 665–674 (2019).

46. Siddiqui, I. *et al.* Intratumoral Tcf1 + PD-1 + CD8 + T Cells with Stem-like Properties Promote Tumor Control in Response to Vaccination and Checkpoint Blockade Immunotherapy. *Immunity* **50**, 195-211.e10 (2019).

47. Rosenberg, S. A., Spiess, P. & Lafreniere, R. A New Approach to the Adoptive Immunotherapy of Cancer with Tumor-Infiltrating Lymphocytes. *Science (1979)* **233**, 1318–1321 (1986).

48. Rosenberg, S. A. *et al.* Use of Tumor-Infiltrating Lymphocytes and Interleukin-2 in the Immunotherapy of Patients with Metastatic Melanoma. *New England Journal of Medicine* **319**, 1676–1680 (1988).

49. Rosenberg, S. A. *et al.* Durable complete responses in heavily pretreated patients with metastatic melanoma using T-cell transfer immunotherapy. *Clinical Cancer Research* **17**, 4550–4557 (2011).

50. Pilon-Thomas, S. *et al.* Efficacy of adoptive cell transfer of tumor-infiltrating lymphocytes after lymphopenia induction for metastatic melanoma. *Journal of Immunotherapy* **35**, 615–620 (2012).

51. Radvanyi, L. G. *et al.* Specific lymphocyte subsets predict response to adoptive cell therapy using expanded autologous tumor-infiltrating lymphocytes in metastatic melanoma patients. *Clinical Cancer Research* **18**, 6758–6770 (2012).

52. Besser, M. J. *et al.* Adoptive transfer of tumor-infiltrating lymphocytes in patients with metastatic melanoma: Intent-to-treat analysis and efficacy after failure to prior immunotherapies. *Clinical Cancer Research* **19**, 4792–4800 (2013).

53. Tran, E. *et al.* T-Cell Transfer Therapy Targeting Mutant KRAS in Cancer. *New England Journal of Medicine* **375**, 2255–2262 (2016).

54. Zacharakis, N. *et al.* Immune recognition of somatic mutations leading to complete durable regression in metastatic breast cancer. *Nat Med* **24**, 724–730 (2018).

55. Stevanovic, S. *et al.* A Phase II Study of Tumor-infiltrating Lymphocyte Therapy for Human Papillomavirus-associated Epithelial Cancers. *Clin Cancer Res* **25**, 1486–1493 (2019).

56. Dudley, M. E., Wunderlich, J. R., Shelton, T. E., Even, J. & Rosenberg, S. A. Generation of Tumor-Infiltrating Lymphocyte Cultures for Use in Adoptive Transfer Therapy for Melanoma Patients. *Journal of Immunotherapy* **26**, 332–342 (2003).

57. Kishton, R. J., Vodnala, S. K., Vizcardo, R. & Restifo, N. P. Next generation immunotherapy: enhancing stemness of polyclonal T cells to improve anti-tumor activity. *Curr Opin Immunol* **74**, 39–45 (2022).

58. Alvarez-Fernández, C., Escribà-Garcia, L., Vidal, S., Sierra, J. & Briones, J. A short CD3/CD28 costimulation combined with IL-21 enhance the generation of human memory stem T cells for adoptive immunotherapy. *J Transl Med* **14**, (2016).

59. Vogelstein, B. *et al.* Cancer Genome Landscapes. *Science (1979)* **339**, 1546–1558 (2013).

60. Bobisse, S., Foukas, P. G., Coukos, G. & Harari, A. Neoantigen-based cancer immunotherapy. *Ann Transl Med* **4**, 262–262 (2016).

61. van den Berg, J. H. *et al.* Tumor infiltrating lymphocytes (TIL) therapy in metastatic melanoma: boosting of neoantigen-specific T cell reactivity and long-term follow-up. *J Immunother Cancer* **8**, e000848 (2020).

62. Van Rooij, N. *et al.* Tumor exome analysis reveals neoantigen-specific T-cell reactivity in an ipilimumab-responsive melanoma. *Journal of Clinical Oncology* **31**, e439–e442 (2013).

63. T.N., S. & R.D., S. Neoantigens in cancer immunotherapy. *Science (1979)* **348**, 69–74 (2015).

64. Johanns, T. M. *et al.* Detection of neoantigen-specific T cells following a personalized vaccine in a patient with glioblastoma. *Oncoimmunology* **8**, e1561106 (2019).

65. Liu, S. *et al.* Efficient identification of neoantigen-specific T-cell responses in advanced human ovarian cancer. *J Immunother Cancer* **7**, 156 (2019).

66. Bobisse, S. *et al.* Sensitive and frequent identification of high avidity neo-epitope specific CD8 + T cells in immunotherapy-naive ovarian cancer. *Nat Commun* **9**, 1–10 (2018).

67. Meng, Q. *et al.* Neoepitope targets of tumour-infiltrating lymphocytes from patients with pancreatic cancer. *British Journal of Cancer 2018 120:1* **120**, 97–108 (2018).

68. Poschke, I. C. *et al.* The Outcome of Ex Vivo TIL Expansion Is Highly Influenced by Spatial Heterogeneity of the Tumor T-Cell Repertoire and Differences in Intrinsic In Vitro Growth Capacity between T-Cell Clones. *Clin Cancer Res* **26**, 4289–4301 (2020).

69. Lozano-Rabella, M. & Gros, A. TCR Repertoire Changes during TIL Expansion: Clonal Selection or Drifting? *Clinical Cancer Research* **26**, 4177–4179 (2020).

70. US Patent Application for 'Expansion of tumor infiltrating lymphocytes (TILS) with tumor necrosis factor receptor superfamily (TNFRSF) agonists and therapeutic combinations of TILs and TNFRSF agonists' Patent Application (Application #20210187029 issued June 24, 2021) - Justia Patents Search. https://patents.justia.com/patent/20210187029.

71. Friese, C. *et al.* CTLA-4 blockade boosts the expansion of tumor-reactive CD8+ tumor-infiltrating lymphocytes in ovarian cancer. *Scientific Reports 2020 10:1* **10**, 1–12 (2020).

72. Kumar, R. *et al.* PD-1 blockade restores impaired function of ex vivo expanded CD8+ T cells and enhances apoptosis in mismatch repair deficient EpCAM+PD-L1+ cancer cells. *Onco Targets Ther* **10**, 3453 (2017).

73. Garcia-Garijo, A., Fajardo, C. A. & Gros, A. Determinants for Neoantigen Identification. *Front Immunol* **10**, 1–19 (2019).

74. Hao, Q. *et al.* Improvement of Neoantigen Identification Through Convolution Neural Network. *Front Immunol* **12**, 1911 (2021).

75. Zhang, X., Qi, Y., Zhang, Q. & Liu, W. Application of mass spectrometry-based MHC immunopeptidome profiling in neoantigen identification for tumor immunotherapy. *Biomedicine & Pharmacotherapy* **120**, 109542 (2019).

76. Bianchi, V., Harari, A. & Coukos, G. Neoantigen-Specific Adoptive Cell Therapies for Cancer: Making T-Cell Products More Personal. *Front Immunol* **11**, 1215 (2020).

77. Hadrup, S. R. *et al.* Parallel detection of antigen-specific T-cell responses by multidimensional encoding of MHC multimers. *Nat Methods* **6**, 520–526 (2009).

78. Newell, E. W. *et al.* Combinatorial tetramer staining and mass cytometry analysis facilitate T-cell epitope mapping and characterization. *Nat Biotechnol* **31**, 623–629 (2013).

79. Bentzen, A. K. *et al.* Large-scale detection of antigen-specific T cells using peptide-MHC-I multimers labeled with DNA barcodes. *Nat Biotechnol* **34**, 1037–1045 (2016).

80. Hansen, U. K. *et al.* Tumor-Infiltrating T Cells From Clear Cell Renal Cell Carcinoma Patients Recognize Neoepitopes Derived From Point and Frameshift Mutations. *Front Immunol* **11**, (2020).

81. Cohen, C. J. *et al.* Isolation of neoantigen-specific T cells from tumor and peripheral lymphocytes. *Journal of Clinical Investigation* **125**, 3981–3991 (2015).

82. Bentzen, A. K. & Hadrup, S. R. Evolution of MHC-based technologies used for detection of antigen-responsive T cells. *Cancer Immunology, Immunotherapy* **66**, 657–666 (2017).

83. Neudorfer, J. *et al.* Reversible HLA multimers (Streptamers) for the isolation of human cytotoxic T lymphocytes functionally active against tumor- and virus-derived antigens. *J Immunol Methods* **320**, 119–131 (2007).

84. Brosterhus, H. *et al.* Enrichment and detection of live antigen-specific CD4+ and CD8+ T cells based on cytokine secretion. *Eur J Immunol* **29**, 4053–4059 (1999).

85. Becker, C. *et al.* Adoptive tumor therapy with T lymphocytes enriched through an IFN-γ capture assay. *Nat Med* **7**, 1159–1162 (2001).

86. Jedema, I. *et al.* Early detection and rapid isolation of leukemia-reactive donor T cells for adoptive transfer using the IFN-γ secretion assay. *Clinical Cancer Research* **13**, 636–643 (2007).

87. Reissfelder, C. *et al.* Tumor-specific cytotoxic T lymphocyte activity determines colorectal cancer patient prognosis. *Journal of Clinical Investigation* **125**, 739–751 (2015).

88. Kayser, S. *et al.* Rapid generation of NY-ESO-1-specific CD4+ THELPER1 cells for adoptive T-cell therapy. *Oncoimmunology* **4**, e1002723 (2015).

89. Newell, E. W., Sigal, N., Bendall, S. C., Nolan, G. P. & Davis, M. M. Cytometry by Time-of-Flight Shows Combinatorial Cytokine Expression and Virus-Specific Cell Niches within a Continuum of CD8 + T Cell Phenotypes. *Immunity* **36**, 142–152 (2012).

90. Nakiboneka, R. *et al.* Interferon gamma (IFN-γ) negative CD4+ and CD8+ T-cells can produce immune mediators in response to viral antigens. *Vaccine* **37**, 113–122 (2019).

91. Freeman, Z. T. *et al.* A conserved intratumoral regulatory T cell signature identifies 4-1BB as a pan-cancer target. *Journal of Clinical Investigation* **130**, (2020).

92. Cannons, J. L. *et al.* 4-1BB Ligand Induces Cell Division, Sustains Survival, and Enhances Effector Function of CD4 and CD8 T Cells with Similar Efficacy. *The Journal of Immunology* **167**, 1313–1324 (2001).

93. Wolfl, M. *et al.* Activation-induced expression of CD137 permits detection, isolation, and expansion of the full repertoire of CD8+ T cells responding to antigen without requiring knowledge of epitope specificities. *Blood* **110**, 201–210 (2007).

94. Parkhurst, M. *et al.* Isolation of T-cell receptors specifically reactive with mutated tumor-associated antigens from tumor-infiltrating lymphocytes based on CD137 expression. *Clinical Cancer Research* **23**, 2491–2505 (2017).

95. Ye, Q. *et al.* CD137 accurately identifies and enriches for naturally occurring tumor-reactive T cells in tumor. *Clinical Cancer Research* **20**, 44–55 (2014).

96. Seliktar-Ofir, S. *et al.* Selection of Shared and Neoantigen-Reactive T Cells for Adoptive Cell Therapy Based on CD137 Separation. *Front Immunol* **8**, 1211 (2017).

97. Elias, G., Ogunjimi, B. & Van Tendeloo, V. Activation-induced surface proteins in the identification of antigen-responsive CD4 T cells. *Immunol Lett* **219**, 1–7 (2020).

98. Nowak, A. *et al.* CD137+CD154- expression as a regulatory T cell (Treg)-specific activation signature for identification and sorting of stable human tregs from in vitro expansion cultures. *Front Immunol* **9**, (2018).

99. Ahmadzadeh, M. *et al.* Tumor antigen–specific CD8 T cells infiltrating the tumor express high levels of PD-1 and are functionally impaired. *Blood* **114**, 1537 (2009).

100. Inozume, T. *et al.* Selection of CD8+PD-1+ lymphocytes in fresh human melanomas enriches for tumor-reactive T-cells. *J Immunother* **33**, 956 (2010).

101. Gros, A. *et al.* PD-1 identifies the patient-specific CD8+ tumor-reactive repertoire infiltrating human tumors. *Journal of Clinical Investigation* **124**, 2246–2259 (2014).

102. Salas-Benito, D. *et al.* The mutational load and a T-cell inflamed tumour phenotype identify ovarian cancer patients rendering tumour-reactive T cells from PD-1+ tumour-infiltrating lymphocytes. *Br J Cancer* **124**, 1138–1149 (2021).

103. Guo, L. *et al.* Tumoral PD-1hiCD8+ T cells are partially exhausted and predict favorable outcome in triple-negative breast cancer. *Clin Sci* **134**, 711–726 (2020).

104. Kim, Y., Shin, Y. & Kang, G. H. Prognostic significance of CD103+ immune cells in solid tumor: a systemic review and meta-analysis. *Sci Rep* **9**, 3808 (2019).

105. Wang, P. *et al.* CD103+CD8+ T lymphocytes in non-small cell lung cancer are phenotypically and functionally primed to respond to PD-1 blockade. *Cell Immunol* **325**, 48–55 (2018).

106. Ling, K.-L. *et al.* Modulation of CD103 Expression on Human Colon Carcinoma-Specific CTL. *The Journal of Immunology* **178**, 2908–2915 (2007).

107. Duhen, T. *et al.* Co-expression of CD39 and CD103 identifies tumor-reactive CD8 T cells in human solid tumors. *Nat Commun* **9**, 2724 (2018).

108. Hamid, M. A. *et al.* Self-Maintaining CD103+ Cancer-Specific T Cells Are Highly Energetic with Rapid Cytotoxic and Effector Responses. *Cancer Immunol Res* **8**, 203–216 (2020).

109. Djenidi, F. *et al.* CD8+ CD103+ Tumor–Infiltrating Lymphocytes Are Tumor-Specific Tissue-Resident Memory T Cells and a Prognostic Factor for Survival in Lung Cancer Patients. *The Journal of Immunology* **194**, 3475–3486 (2015).

110. Ganesan, A. P. *et al.* Tissue-resident memory features are linked to the magnitude of cytotoxic T cell responses in human lung cancer. *Nature Immunology 2017 18:8* **18**, 940–950 (2017).

111. Malik, B. T. *et al.* Resident memory T cells in the skin mediate durable immunity to melanoma. *Sci Immunol* **2**, (2017).

112. Wang, B. *et al.* CD103+ Tumor Infiltrating Lymphocytes Predict a Favorable Prognosis in Urothelial Cell Carcinoma of the Bladder. *Journal of Urology* **194**, 556–562 (2015).

113. Corgnac, S. *et al.* CD103+ CD8+ TRM Cells Accumulate in Tumors of Anti-PD-1-Responder Lung Cancer Patients and Are Tumor-Reactive Lymphocytes Enriched with Tc17. *Cell Rep Med* **1**, 100127 (2020).

114. De Groot, R. *et al.* Polyfunctional tumor-reactive T cells are effectively expanded from non-small cell lung cancers, and correlate with an immune-engaged T cell profile. *Oncoimmunology* **8**, e1648170 (2019).

115. Timperi, E. & Barnaba, V. CD39 Regulation and Functions in T Cells. *Int J Mol Sci* **22**, 8068 (2021).

116. Allard, B., Longhi, M. S., Robson, S. C. & Stagg, J. The ectonucleotidases CD39 and CD73: Novel checkpoint inhibitor targets. *Immunol Rev* **276**, 121–144 (2017).

117. Canale, F. P. *et al.* CD39 expression defines cell exhaustion in tumor-infiltrating CD8+ T cells. *Cancer Res* **78**, 115–128 (2018).

118. Simoni, Y. *et al.* Bystander CD8+ T cells are abundant and phenotypically distinct in human tumour infiltrates. *Nature* **557**, 575–579 (2018).

119. Harjunpää, H. & Guillerey, C. TIGIT as an emerging immune checkpoint. *Clin Exp Immunol* **200**, 108–119 (2020).

120. Leclerc, M. *et al.* Regulation of antitumour CD8 T-cell immunity and checkpoint blockade immunotherapy by Neuropilin-1. *Nat Commun* **10**, 3345 (2019).

121. Tabbekh, M., Mokrani-Hammani, M., Bismuth, G. & Mami-Chouaib, F. T-cell modulatory properties of CD5 and its role in antitumor immune responses. *Oncoimmunology* **2**, e22841 (2013).

122. Fourcade, J. *et al.* PD-1 Is a Regulator of NY-ESO-1-Specific CD8+ T Cell Expansion in Melanoma Patients. *The Journal of Immunology* **182**, 5240–5249 (2009).

123. Eberhardt, C. S. *et al.* Functional HPV-specific PD-1+ stem-like CD8 T cells in head and neck cancer. *Nature* **597**, 279–284 (2021).

124. Corgnac, S., Boutet, M., Kfoury, M., Naltet, C. & Mami-Chouaib, F. The Emerging Role of CD8+ Tissue Resident Memory T (TRM) Cells in Antitumor Immunity: A Unique Functional Contribution of the CD103 Integrin. *Front Immunol* **9**, 1904 (2018).

125. Webb, J. R., Milne, K. & Nelson, B. H. PD-1 and CD103 Are Widely Coexpressed on Prognostically Favorable Intraepithelial CD8 T Cells in Human Ovarian Cancer. *Cancer Immunol Res* **3**, 926–935 (2015).

126. Workel, H. H. *et al.* Transcriptional Activity and Stability of CD39+CD103+CD8+ T Cells in Human High-Grade Endometrial Cancer. *Int J Mol Sci* **21**, 3770 (2020).

127. Kortekaas, K. E. *et al.* CD39 Identifies the CD4+ Tumor-Specific T-cell Population in Human Cancer. *Cancer Immunol Res* **8**, 1311–1321 (2020).

128. Laumont, C. M. *et al.* Single-cell Profiles and Prognostic Impact of Tumor-Infiltrating Lymphocytes Coexpressing CD39, CD103, and PD-1 in Ovarian Cancer. *Clinical Cancer Research* **27**, 4089–4100 (2021).

129. Schürch, C. M. *et al.* Coordinated Cellular Neighborhoods Orchestrate Antitumoral Immunity at the Colorectal Cancer Invasive Front. *Cell* **182**, 1341-1359.e19 (2020).

130. Tsujikawa, T. *et al.* Prognostic significance of spatial immune profiles in human solid cancers. *Cancer Sci* **111**, 3426–3434 (2020).

131. Lewis, S. M. *et al.* Spatial omics and multiplexed imaging to explore cancer biology. *Nat Methods* **18**, 997–1012 (2021).

132. Gerdes, M. J. *et al.* Highly multiplexed single-cell analysis of formalin-fixed, paraffin-embedded cancer tissue. *Proceedings of the National Academy of Sciences* **110**, 11982–11987 (2013).

133. Goltsev, Y. *et al.* Deep Profiling of Mouse Splenic Architecture with CODEX Multiplexed Imaging. *Cell* **174**, 968-981.e15 (2018).

134. Keren, L. *et al.* MIBI-TOF: A multiplexed imaging platform relates cellular phenotypes and tissue structure. *Sci Adv* **5**, eaax5851 (2019).

135. Schulz, D. *et al.* Simultaneous Multiplexed Imaging of mRNA and Proteins with Subcellular Resolution in Breast Cancer Tissue Samples by Mass Cytometry. *Cell Syst* **6**, 25-36.e5 (2018).

136. Eisenstein, M. Seven technologies to watch in 2022. *Nature* **601**, 658–661 (2022).

137. Song, L., Hennink, E. J., Young, I. T. & Tanke, H. J. Photobleaching kinetics of fluorescein in quantitative fluorescence microscopy. *Biophys J* **68**, 2588–2600 (1995).

138. Tajiri, K., Kishi, H., Ozawa, T., Sugiyama, T. & Muraguchi, A. SFMAC: A novel method for analyzing multiple parameters on lymphocytes with a single fluorophore in cell-microarray system. *Cytometry Part A* **75A**, 282–288 (2009).

139. McQuin, C. *et al.* CellProfiler 3.0: Next-generation image processing for biology. *PLoS Biol* **16**, e2005970 (2018).

140. Mutterer, J. & Zinck, E. Quick-and-clean article figures with FigureJ. *J Microsc* **252**, 89–91 (2013).

141. Schindelin, J. *et al.* Fiji: an open-source platform for biological-image analysis. *Nat Methods* **9**, 676–682 (2012).

142. Wickham, H. *Ggplot2: Elegant Graphics for Data Analysis*. (Springer-Verlag New York, Cham, 2016).

143. Gosselink, A., Hofer, T., Criado-Moronati, E., von Haeseler, A. & Kollet, J. InspectorCell: Finding Ground Truth in Multiplexed Microscopy Images. *J Open Source Softw* **7**, 4949 (2022).

144. Demšar, J. *et al.* Orange: Data Mining Toolbox in Python Tomaž Curk Matija Polajnar Laň Zagar. *Journal of Machine Learning Research* **14**, 2349–2353 (2013).

145. Andreatta, M. *et al.* Interpretation of T cell states from single-cell transcriptomics data using reference atlases. *Nat Commun* **12**, 2965 (2021).

146. Germain, P.-L., Lun, A., Garcia Meixide, C., Macnair, W. & Robinson, M. D. Doublet identification in single-cell sequencing data using scDblFinder. *F1000Res* **10**, 979 (2022).

147. Borcherding, N., Bormann, N. L. & Kraus, G. scRepertoire: An R-based toolkit for single-cell immune receptor analysis. *F1000Res* **9**, 47 (2020).

148. Hao, Y. *et al.* Integrated analysis of multimodal single-cell data. *Cell* **184**, 3573-3587.e29 (2021).

149. Andreatta, M. & Carmona, S. J. UCell: Robust and scalable single-cell gene signature scoring. *Comput Struct Biotechnol J* **19**, 3796–3798 (2021).

150. Riddell, S. R. *et al.* Restoration of Viral Immunity in Immunodeficient Humans by the Adoptive Transfer of T Cell Clones. *Science (1979)* **257**, 238–241 (1992).

151. Choudhary, S. & Satija, R. Comparison and evaluation of statistical error models for scRNA-seq. *Genome Biol* **23**, 27 (2022).

152. Minervina, A. A. *et al.* SARS-CoV-2 antigen exposure history shapes phenotypes and specificity of memory CD8+ T cells. *Nat Immunol* **23**, 781–790 (2022).

153. Wischnewski, V. *et al.* Phenotypic diversity of T cells in human primary and metastatic brain tumors revealed by multiomic interrogation. *Nat Cancer* **4**, 908–924 (2023).

154. Andreatta, M., Gueguen, P., Borcherding, N. & Carmona, S. T Cell Clonal Analysis Using Single-cell RNA Sequencing and Reference Maps. *Bio Protoc* **13**, 4735 (2023).

155. Mohtar, M., Syafruddin, S., Nasir, S. & Low, T. Y. Revisiting the Roles of Pro-Metastatic EpCAM in Cancer. *Biomolecules* **10**, 255 (2020).

156. Hyun, S. & Park, D. Challenges in genomic analysis of model systems and primary tumors of pancreatic ductal adenocarcinoma. *Comput Struct Biotechnol J* **20**, 4806–4815 (2022).

157. Juiz, N. A., Iovanna, J. & Dusetti, N. Pancreatic Cancer Heterogeneity Can Be Explained Beyond the Genome. *Front Oncol* **9**, 446903 (2019).

158. Reichard, A. & Asosingh, K. Best Practices for Preparing a Single Cell Suspension from Solid Tissues for Flow Cytometry. *Cytometry Part A* **95**, 219–226 (2019).

159. Jiang, W. *et al.* Exhausted CD8+T Cells in the Tumor Immune Microenvironment: New Pathways to Therapy. *Front Immunol* **11**, 3739 (2021).

160. Cossarizza, A. *et al.* Guidelines for the use of flow cytometry and cell sorting in immunological studies. *Eur J Immunol* **47**, 1584–1797 (2017).

161. Gros, A. *et al.* Selection of circulating PD-1+ lymphocytes from cancer patients enriches for tumor-reactive and mutation-specific lymphocytes. *J Immunother Cancer* **3**, 1–2 (2015).

162. Wolfl, M. *et al.* Activation-induced expression of CD137 permits detection, isolation, and expansion of the full repertoire of CD8+ T cells responding to antigen without requiring knowledge of epitope specificities. *Blood* **110**, 201–210 (2007).

163. Chow, A. *et al.* CD39 Identifies Tumor-Reactive CD8 T cells in Patients With Lung Cancer. *bioRxiv* **13**, 2022.01.24.477554 (2022).

164. Marinucci, M. *et al.* Standardizing Patient-Derived Organoid Generation Workflow to Avoid Microbial Contamination From Colorectal Cancer Tissues. *Front Oncol* **11**, (2022).

165. Borst, J., Ahrends, T., Bąbała, N., Melief, C. J. M. & Kastenmüller, W. CD4+ T cell help in cancer immunology and immunotherapy. *Nat Rev Immunol* **18**, 635–647 (2018).

166. Pasetto, A. *et al.* Tumor- and Neoantigen-Reactive T-cell Receptors Can Be Identified Based on Their Frequency in Fresh Tumor. *Cancer Immunol Res* **4**, 734–743 (2016).

167. Fernandez-Poma, S. M. *et al.* Expansion of Tumor-Infiltrating CD8+ T cells Expressing PD-1 Improves the Efficacy of Adoptive T-cell Therapy. *Cancer Res* **77**, 3672–3684 (2017).

168. Winkels, H. & Wolf, D. Heterogeneity of T Cells in Atherosclerosis Defined by Single-Cell RNA-Sequencing and Cytometry by Time of Flight. *Arterioscler Thromb Vasc Biol* **41**, 549–563 (2021).

169. Gutiérrez-Melo, N. & Baumjohann, D. T follicular helper cells in cancer. *Trends Cancer* **9**, 309–325 (2023).

170. Caushi, J. X. *et al.* Transcriptional programs of neoantigen-specific TIL in anti-PD-1-treated lung cancers. *Nature 2021 596:7870* **596**, 126–132 (2021).

171. Hanada, K.-I. *et al.* A phenotypic signature that identifies neoantigen-reactive T cells in fresh human lung cancers. *Cancer Cell* **40**, 479-493.e6 (2022).

172. Oliveira, G. *et al.* Phenotype, specificity and avidity of antitumour CD8+ T cells in melanoma. *Nature 2021 596:7870* **596**, 119–125 (2021).

173. Lowery, F. J. *et al.* Molecular signatures of antitumor neoantigen-reactive T cells from metastatic human cancers. *Science (1979)* **375**, 877–884 (2022).

174. Szabo, P. A. *et al.* Single-cell transcriptomics of human T cells reveals tissue and activation signatures in health and disease. *Nat Commun* **10**, (2019).

175. Mogilenko, D. A. *et al.* Comprehensive Profiling of an Aging Immune System Reveals Clonal GZMK+ CD8+ T Cells as Conserved Hallmark of Inflammaging. *Immunity* **54**, 99-115.e12 (2021).

176. Zhang, C. *et al.* TCR repertoire intratumor heterogeneity of CD4+ and CD8+ T cells in centers and margins of localized lung adenocarcinomas. *Int J Cancer* **144**, 818–827 (2019).

177. Li, H. M. *et al.* TCR repertoire of CD4+ and CD8+ T cells is distinct in richness, distribution, and CDR3 amino acid composition. *J Leukoc Biol* **99**, 505–513 (2016).

178. Maffuid, K. & Cao, Y. Decoding the Complexity of Immune–Cancer Cell Interactions: Empowering the Future of Cancer Immunotherapy. *Cancers (Basel)* **15**, 4188 (2023).

179. Kinkhabwala, A. *et al.* MACSima imaging cyclic staining (MICS) technology reveals combinatorial target pairs for CAR T cell treatment of solid tumors. *Sci Rep* **12**, 1911 (2022).

180. Zhan, Z., Zhong, L., Feng, M. & Guo, Y. A Positive Tetraspanin 8 (TSPAN8)/β-Catenin Regulatory Loop Enhances the Stemness of Colorectal Cancer Cells. *Medical Science Monitor* **25**, 9594–9601 (2019).

181. LI, L. T., JIANG, G., CHEN, Q. & ZHENG, J. N. Ki67 is a promising molecular target in the diagnosis of cancer (Review). *Mol Med Rep* **11**, 1566–1572 (2015).

182. Guo, C. *et al.* Expression and clinical significance of CD31, CD34, and CD105 in pulmonary ground glass nodules with different vascular manifestations on CT. *Front Oncol* **12**, (2022).

183. Zeng, F. *et al.* Role and mechanism of CD90+ fibroblasts in inflammatory diseases and malignant tumors. *Molecular Medicine* **29**, 20 (2023).

184. Wetzel, A. *et al.* Human Thy-1 (CD90) on Activated Endothelial Cells Is a Counterreceptor for the Leukocyte Integrin Mac-1 (CD11b/CD18). *The Journal of Immunology* **172**, 3850–3859 (2004).

185. Allard, D., Allard, B. & Stagg, J. On the mechanism of anti-CD39 immune checkpoint therapy. *J Immunother Cancer* **8**, e000186 (2020).

186. Kroeger, D. R., Milne, K. & Nelson, B. H. Tumor-Infiltrating Plasma Cells Are Associated with Tertiary Lymphoid Structures, Cytolytic T-Cell Responses, and Superior Prognosis in Ovarian Cancer. *Clinical Cancer Research* **22**, 3005–3015 (2016).

187. Meylan, M. *et al.* Tertiary lymphoid structures generate and propagate anti-tumor antibody-producing plasma cells in renal cell cancer. *Immunity* **55**, 527-541.e5 (2022).

188. Singhal, S. *et al.* Human tumor-associated monocytes/macrophages and their regulation of T cell responses in early-stage lung cancer. *Sci Transl Med* **11**, (2019).

189. Veglia, F., Perego, M. & Gabrilovich, D. Myeloid-derived suppressor cells coming of age. *Nat Immunol* **19**, 108–119 (2018).

190. Plesca, I. *et al.* Clinical Significance of Tumor-Infiltrating Conventional and Plasmacytoid Dendritic Cells in Pancreatic Ductal Adenocarcinoma. *Cancers (Basel)* **14**, 1216 (2022).

191. Gerhard, G. M., Bill, R., Messemaker, M., Klein, A. M. & Pittet, M. J. Tumor-infiltrating dendritic cell states are conserved across solid human cancers. *Journal of Experimental Medicine* **218**, (2021).

192. He, W. *et al.* The High Level of Tertiary Lymphoid Structure Is Correlated With Superior Survival in Patients With Advanced Gastric Cancer. *Front Oncol* **10**, (2020).

193. Li, Q. *et al.* Prognostic value of tertiary lymphoid structure and tumour infiltrating lymphocytes in oral squamous cell carcinoma. *Int J Oral Sci* **12**, 24 (2020).

194. Cabrita, R. *et al.* Tertiary lymphoid structures improve immunotherapy and survival in melanoma. *Nature* **577**, 561–565 (2020).

195. Tarhriz, V. *et al.* Overview of CD24 as a new molecular marker in ovarian cancer. *J Cell Physiol* **234**, 2134–2142 (2019).

196. Tayama, S. *et al.* The impact of EpCAM expression on response to chemotherapy and clinical outcomes in patients with epithelial ovarian cancer. *Oncotarget* **8**, 44312–44325 (2017).

197. Fridman, W. H. *et al.* B cells and cancer: To B or not to B? *Journal of Experimental Medicine* **218**, (2021).

198. Sanz, I. *et al.* Challenges and Opportunities for Consistent Classification of Human B Cell and Plasma Cell Populations. *Front Immunol* **10**, 2458 (2019).

199. Kind, S. *et al.* Prevalence of Syndecan-1 (CD138) Expression in Different Kinds of Human Tumors and Normal Tissues. *Dis Markers* **2019**, (2019).

200. Boissonnas, A., Fetler, L., Zeelenberg, I. S., Hugues, S. & Amigorena, S. In vivo imaging of cytotoxic T cell infiltration and elimination of a solid tumor. *J Exp Med* **204**, 345 (2007).

201. Jansen, C. S. *et al.* An intra-tumoral niche maintains and differentiates stem-like CD8 T cells. *Nature* **576**, 465–470 (2019).

202. Alotaibi, F., Vincent, M., Min, W.-P. & Koropatnick, J. Reduced CD5 on CD8+ T Cells in Tumors but Not Lymphoid Organs Is Associated With Increased Activation and Effector Function. *Front Immunol* **11**, 584937 (2021).

203. Zhao, H., Wang, H., Zhao, Y., Sun, Q. & Ren, X. Tumor-Resident T Cells, Associated With Tertiary Lymphoid Structure Maturity, Improve Survival in Patients With Stage III Lung Adenocarcinoma. *Front Immunol* **13**, 877689 (2022).

204. Mori, T. *et al.* Tertiary lymphoid structures show infiltration of effective tumor-resident T cells in gastric cancer. *Cancer Sci* **112**, 1746–1757 (2021).

205. Eiva, M. A., Omran, D. K., Chacon, J. A. & Powell, D. J. Systematic analysis of CD39, CD103, CD137, and PD-1 as biomarkers for naturally occurring tumor antigen-specific TILs. *Eur J Immunol* **52**, 96–108 (2022).

206. Tumeh, P. C. *et al.* PD-1 blockade induces responses by inhibiting adaptive immune resistance. *Nature* **515**, 568–571 (2014).

207. Scheper, W. *et al.* Low and variable tumor reactivity of the intratumoral TCR repertoire in human cancers. *Nat Med* **25**, 89–94 (2019).

208. Pritykin, Y. *et al.* A unified atlas of CD8 T cell dysfunctional states in cancer and infection. *Mol Cell* **81**, 2477-2493.e10 (2021).

209. Pasquini, G., Rojo Arias, J. E., Schäfer, P. & Busskamp, V. Automated methods for cell type annotation on scRNA-seq data. *Comput Struct Biotechnol J* **19**, 961–969 (2021).

210. Lähnemann, D. *et al.* Eleven grand challenges in single-cell data science. *Genome Biol* **21**, 31 (2020).

211. Tietscher, S. *et al.* A comprehensive single-cell map of T cell exhaustion-associated immune environments in human breast cancer. *Nat Commun* **14**, 98 (2023).

212. Schalck, A. *et al.* Single-Cell Sequencing Reveals Trajectory of Tumor-Infiltrating Lymphocyte States in Pancreatic Cancer. *Cancer Discov* **12**, 2330–2349 (2022).

213. Nguyen, A., Khoo, W. H., Moran, I., Croucher, P. I. & Phan, T. G. Single Cell RNA Sequencing of Rare Immune Cell Populations. *Front Immunol* **9**, 1553 (2018).

214. Baysoy, A., Bai, Z., Satija, R. & Fan, R. The technological landscape and applications of single-cell multi-omics. *Nat Rev Mol Cell Biol* **24**, 695–713 (2023).

215. Bentzen, A. K. *et al.* Large-scale detection of antigen-specific T cells using peptide-MHC-I multimers labeled with DNA barcodes. *Nat Biotechnol* **34**, 1037–1045 (2016).

216. Ma, K.-Y. *et al.* High-throughput and high-dimensional single-cell analysis of antigen-specific CD8+ T cells. *Nat Immunol* **22**, 1590–1598 (2021).

217. Boutet, S. C. *et al.* Scalable and comprehensive characterization of antigen-specific CD8 T cells using multi-omics single cell analysis. *The Journal of Immunology* **202**, 131.4 (2019).

218. Ren, H., Cao, K. & Wang, M. A Correlation Between Differentiation Phenotypes of Infused T Cells and Anti-Cancer Immunotherapy. *Front Immunol* **12**, 745109 (2021).

219. Schwanhäusser, B. *et al.* Global quantification of mammalian gene expression control. *Nature* **473**, 337–342 (2011).

220. Wang, A. Z. *et al.* Glioblastoma-Infiltrating CD8+ T Cells Are Predominantly a Clonally Expanded GZMK+ Effector Population. *Cancer Discov* **14**, 1106–1131 (2024).

221. Stoeckius, M. *et al.* Simultaneous epitope and transcriptome measurement in single cells. *Nature Methods 2017 14:9* **14**, 865–868 (2017).

222. Giraldo, N. A. *et al.* The clinical role of the TME in solid cancer. *British Journal of Cancer 2018 120:1* **120**, 45–53 (2018).

223. Wikström, P., Lissbrant, I. F., Stattin, P., Egevad, L. & Bergh, A. Endoglin (CD105) is expressed on immature blood vessels and is a marker for survival in prostate cancer. *Prostate* **51**, 268–275 (2002).

224. Chiodoni, C. *et al.* Triggering CD40 on endothelial cells contributes to tumor growth. *Journal of Experimental Medicine* **203**, 2441–2450 (2006).

225. Sauzay, C., Voutetakis, K., Chatziioannou, A. A., Chevet, E. & Avril, T. CD90/Thy-1, a cancer-associated cell surface signaling molecule. *Front Cell Dev Biol* **7**, 66 (2019).

226. Schumacher, T. N. & Thommen, D. S. Tertiary lymphoid structures in cancer. *Science* **375**, eabf9419 (2022).

227. Munoz-Erazo, L., Rhodes, J. L., Marion, V. C. & Kemp, R. A. Tertiary lymphoid structures in cancer – considerations for patient prognosis. *Cellular & Molecular Immunology 2020 17:6* **17**, 570–575 (2020).

228. Hickey, J. W., Tan, Y., Nolan, G. P. & Goltsev, Y. Strategies for Accurate Cell Type Identification in CODEX Multiplexed Imaging Data. *Front Immunol* **12**, 3317 (2021).

229. Wu, K. *et al.* Redefining Tumor-Associated Macrophage Subpopulations and Functions in the Tumor Microenvironment. *Front Immunol* **11**, 1731 (2020).

230. Tokunaga, R. *et al.* 12-Chemokine signature, a predictor of tumor recurrence in colorectal cancer. *Int J Cancer* **147**, 532–541 (2020).

231. Hobro, A. J. & Smith, N. I. An evaluation of fixation methods: Spatial and compositional cellular changes observed by Raman imaging. *Vib Spectrosc* **91**, 31–45 (2017).

232. Salmon, H. & Donnadieu, E. Within tumors, interactions between T cells and tumor cells are impeded by the extracellular matrix. *Oncoimmunology* **1**, 992 (2012).

233. Schäfer, D. *et al.* Identification of CD318, TSPAN8 and CD66c as target candidates for CAR T cell based immunotherapy of pancreatic adenocarcinoma. *Nat Commun* **12**, 1453 (2021).

234. Li, S. *et al.* Bystander CD4+ T cells infiltrate human tumors and are phenotypically distinct. *Oncoimmunology* **11**, 2020.07.15.204172 (2022).

235. Hanada, K. *et al.* A phenotypic signature that identifies neoantigen-reactive T cells in fresh human lung cancers. *Cancer Cell* **40**, 479-493.e6 (2022).

236. Bossio, S. N. *et al.* CD39+ conventional CD4+ T cells with exhaustion traits and cytotoxic potential infiltrate tumors and expand upon CTLA-4 blockade. *Oncoimmunology* **12**, (2023).

237. Ahlmanner, F. *et al.* CD39+ regulatory T cells accumulate in colon adenocarcinomas and display markers of increased suppressive function. *Oncotarget* **9**, 36993–37007 (2018).

238. Sambruni, I. *et al.* Abstract 4694: Single-cell analysis of glioblastoma immune contexture identifies a subset of activated and memory tumor-reactive CD8+ TILs and a Treg signature contributing to TIL irreversible dysfunction. *Cancer Res* **83**, 4694–4694 (2023).

239. Draghi, A. *et al.* Rapid Identification of the Tumor-Specific Reactive TIL Repertoire via Combined Detection of CD137, TNF, and IFNγ, Following Recognition of Autologous Tumor-Antigens. *Front Immunol* **12**, (2021).

240. Lee, K. H. *et al. Ex vivo* enrichment of PRAME antigen-specific T cells for adoptive immunotherapy using CD137 activation marker selection. *Clin Transl Immunology* **9**, (2020).

241. Qi, Y. *et al.* Tumor-infiltrating CD39+CD8+ T cells determine poor prognosis and immune evasion in clear cell renal cell carcinoma patients. *Cancer Immunology, Immunotherapy* **69**, 1565–1576 (2020).

242. Clarke, J. *et al.* Single-cell transcriptomic analysis of tissue-resident memory T cells in human lung cancer. *Journal of Experimental Medicine* **216**, 2128–2149 (2019).

243. Schietinger, A. *et al.* Tumor-Specific T Cell Dysfunction Is a Dynamic Antigen-Driven Differentiation Program Initiated Early during Tumorigenesis. *Immunity* **45**, 389–401 (2016).

244. Gros, A. *et al.* Prospective identification of neoantigen-specific lymphocytes in the peripheral blood of melanoma patients. *Nat Med* **22**, 433–438 (2016).

245. Pauken, K. E. *et al.* Single-cell analyses identify circulating anti-tumor CD8 T cells and markers for their enrichment. *Journal of Experimental Medicine* **218**, (2021).

246. Yossef, R. *et al.* Phenotypic signatures of circulating neoantigen-reactive CD8+ T cells in patients with metastatic cancers. *Cancer Cell* **41**, 2154-2165.e5 (2023).

247. Cafri, G. *et al.* Memory T cells targeting oncogenic mutations detected in peripheral blood of epithelial cancer patients. *Nat Commun* **10**, 449 (2019).

248. Meng, Z. *et al.* Transcriptome-based identification of tumor-reactive and bystander CD8 $^{+}$ T cell receptor clonotypes in human pancreatic cancer. *Sci Transl Med* **15**, (2023).

249. Tan, C. L. *et al.* Prediction of tumor-reactive T cell receptors from scRNA-seq data for personalized T cell therapy. *Nature Biotechnology 2024* 1–9 (2024) doi:10.1038/s41587-024-02161-y.

250. Shafer, P., Kelly, L. M. & Hoyos, V. Cancer Therapy With TCR-Engineered T Cells: Current Strategies, Challenges, and Prospects. *Front Immunol* **13**, 835762 (2022).

251. Baulu, E., Gardet, C., Chuvin, N. & Depil, S. TCR-engineered T cell therapy in solid tumors: State of the art and perspectives. *Sci Adv* **9**, (2023).

252. Arnaud, M., Bobisse, S., Chiffelle, J. & Harari, A. The Promise of Personalized TCR-Based Cellular Immunotherapy for Cancer Patients. *Front Immunol* **12**, 2869 (2021).

253. Lu, Y.-C. *et al.* Direct identification of neoantigen-specific TCRs from tumor specimens by high-throughput single-cell sequencing. *J Immunother Cancer* **9**, e002595 (2021).

254. Bräunlein, E. *et al.* Functional analysis of peripheral and intratumoral neoantigen-specific TCRs identified in a patient with melanoma. *J Immunother Cancer* **9**, e002754 (2021).